McMaster University ENGINEERING

Final Report RSP-0305

"Loading of Steam Generator Tubes during Main Steam Line Breaks" – CNSC Contract No. 87055-11-0417 – R430.3

Report Authors: Ouajih Hamouda hamoudo@mcmaster.ca
David S. Weaver weaverds@mcmaster.ca

Department of Mechanical Engineering
McMaster University
Hamilton, Ontario L8S 4L7

Principal Investigator: David S. Weaver

CNSC Project Manager: Jovica Riznic

Report Recipients: Margaret Barnowski Margaret.Barnowski@cnsc-ccsn.gc.ca
Jovica Riznic jovica.riznic@cnsc-ccsn.gc.ca

Canadian Nuclear Safety Commission
280 Slater Street
P.O. Box 1046, Station B
Ottawa, Ontario K1P 5S9

February 2015

Executive Summary

The overall objective of this research is to study the effects of a postulated Main Steam Line Break (MSLB) accident and the consequent steam generator blowdown on the transient loading of nuclear steam generator tubes. An improved understanding of the physical processes involved during transient two-phase fluid blowdown across tube bundles permits the development of improved design tools to ensure steam generator safety during such events.

To perform the required experiments, an experimental facility was designed and built. The experimental apparatus was equipped such that thermodynamic phenomena could be investigated through pressure and temperature measurements. In addition, dynamic load cells were installed on a model CANDU design tube bundle test section for transient tube loading measurements.

Both this experimental rig and the instrumentation system were successfully commissioned, and, following remedial steps taken to establish instrument credibility, a two-phase experimental program was developed and initiated. Using R-134a as the working fluid, measurements of temperature, pressure and tube loading, as well as simultaneous high-speed flow visualizations, were taken in conditions simulating a full-scale commercial steam generator.

This report includes an analysis of the experimental project findings to date, as well as a discussion of the strategy formulated to develop a predictive methodology for transient blowdown loading on tube bundles based on parametric investigation techniques.

Table of Contents

List of Figures

List of Tables

List of Acronyms

AECB	Atomic Energy Control Board
AECL	Atomic Energy of Canada Limited
ATHOS	Analysis of the Thermal Hydraulics of Steam Generators
BWR	Boiling Water Reactor
CANDU	Canada Deuterium Uranium
CATHENA	Canadian Algorithm for Thermalhydraulic Network Analysis
CEA	Commissariat à l'Énergie Atomique
CFD	Computational Fluid Dynamics
CLAIR	Code for LOCA Analysis of Indian PHWRs
DBA	Design Basis Accident
EPRI	Electric Power Research Institute
FEM	Finite Element Methods
HEM	Homogeneous Equilibrium Model
LOCA	Loss-of-Coolant Accident
MSLB	Main Steam Line Break
NPP	Nuclear Power Plant
NRC	Nuclear Regulatory Commission
PHWR	Pressurised Heavy Water Reactor
PWR	Pressurised Water Reactor
RELAP	Reactor Excursion and Leak Analysis Program
SLB	Steam Line Break
SOPHT	Simulation Of Primary Heat Transport
TRAC	Transient Reactor Analysis Code
TRACE	TRAC / RELAP Advanced Computational Engine

Nomenclature

A	Flow area [m^2]
C	Flow coefficient
c	Sonic velocity [m/s]
c_P	Specific isobaric heat capacity [kJ/kg-K]
d	Diameter [m]
F	Force [N]
f	Friction factor
$F(t)$	Dimensionless discharge function
G	Mass flux [kg/m^2-s]
g	Standard gravitational acceleration [m/s^2]
H	Height [m]
h	Specific enthalpy [kJ/kg]
J	Nucleation rate [cm^3-s]$^{-1}$
k	Perfect gas specific heat ratio
L	Length [m]
m	Mass [kg]
$\dot{m}$	Mass flow rate [kg/s]
M_{mol}	Molecular mass
p	Pressure [kPa]
Re	Reynolds number
R_g	Universal gas law constant [J/kg-K]
s	Specific entropy [kJ/kg-K]
T	Temperature [K]
t	Time [s]
u	Velocity [m/s]
V	Volume [m^3]
x	Thermodynamic quality
z	Number of tube rows

Greek symbols

γ	Specific heat ratio
ε	Void fraction
η	Nucleation kinetics exponential function
θ	Angle of elevation [rad]
μ	Viscosity [Pa-s]
ξ	Pressure drop coefficient
ρ	Density [kg/m^3]
σ	Surface tension [N/m]

Subscripts

0	Stagnation
a	Ambient
c	Choked
cs	Cross-sectional
D	Discharge
d	Downstream
g	Vapour
H	Homogeneous
l	Liquid
p	Projected
sat	Saturation
T	Vessel
TP	Two-phase
u	Upstream

1. Introduction

During their normal operating life, heat exchanger tube bundles in steam generators vibrate as they are subjected to cross-flow of secondary side coolant, particularly in the U-bend region. These potentially destructive vibrations are minimised in steam generators through the installation of anti-vibration bars, which support the tubes. The anti-vibration bars are typically designed to have small clearances between the tubes and their supports to allow for manufacturing assembly and thermal expansion during operation. As a result, the tubes vibrate against the supports, often producing mechanical wear and reducing the thickness of the steam generator tube walls at the locations of contact with the tube supports. The degradation of tube wall integrity during the lifetime operation of the steam generators, due to mechanical wear and corrosion, lowers the design margin of safety against structural failure. In practice, tube wall thinning is regularly monitored during scheduled outages, and excessively worn tubes are taken out of service.

Such tube wall thinning is especially problematic in nuclear power plants because the tubes inside the steam generators represent the boundary between the irradiated primary side coolant (deuterium or heavy water, D_2O, in CANDU reactors) and the secondary side coolant (light water, H_2O). A main concern of reactor safety is to ensure that radioactive materials produced by nuclear fission during operation are safely contained, and therefore, the structural integrity of steam generator tubes is of utmost importance.

If the main steam line in a Pressurised Water Reactor (PWR) nuclear power plant were to break, the pressurised heated water in the secondary (shell) side of the steam generators would suddenly be exposed to surrounding atmospheric conditions. In the secondary side of CANDU steam generators, the operating conditions are 4.69MPa and 260°C. The rapid reduction in pressure to atmospheric conditions would cause the water to flash to vapour, or boil off very rapidly, producing what is called a 'blowdown'. This results in a high-velocity two-phase steam-water discharge out of the steam generator through the main steam pipe. A layout of the main nuclear plant components affected by this postulated Main Steam Line Break (MSLB) scenario in a CANDU design is illustrated in Fig. 1-1.

A MSLB accident would produce a very high flow rate of steam due to the substantial drop in the pressure at the point of the break. Since the tubes of a vertical U-bend type steam generator are oriented perpendicular to the direction of the flow in the U-bend region, they could be subjected to a significant and potentially dangerous transient hydraulic loading during a blowdown. The risk of structural tube failure is exacerbated if the tube wall thickness has been reduced due to long-term fretting wear and corrosion. If the structural integrity of the tubes is compromised, a leakage pathway is created that could result in the escape of radioactive materials from the primary side to the secondary side, possibly bypassing the reactor containment. Since this is unacceptable from a nuclear safety standpoint, it is essential that the structural integrity of the tubes be maintained. Thus, knowing the tube loading during such an event is an important input for safe design.

The fluid blowdown phenomenon has been the subject of much investigation in nuclear safety research, with particular attention being paid towards predicting the flow discharge properties. The analysis of blowdown loading of steam generator tubes deals with complex

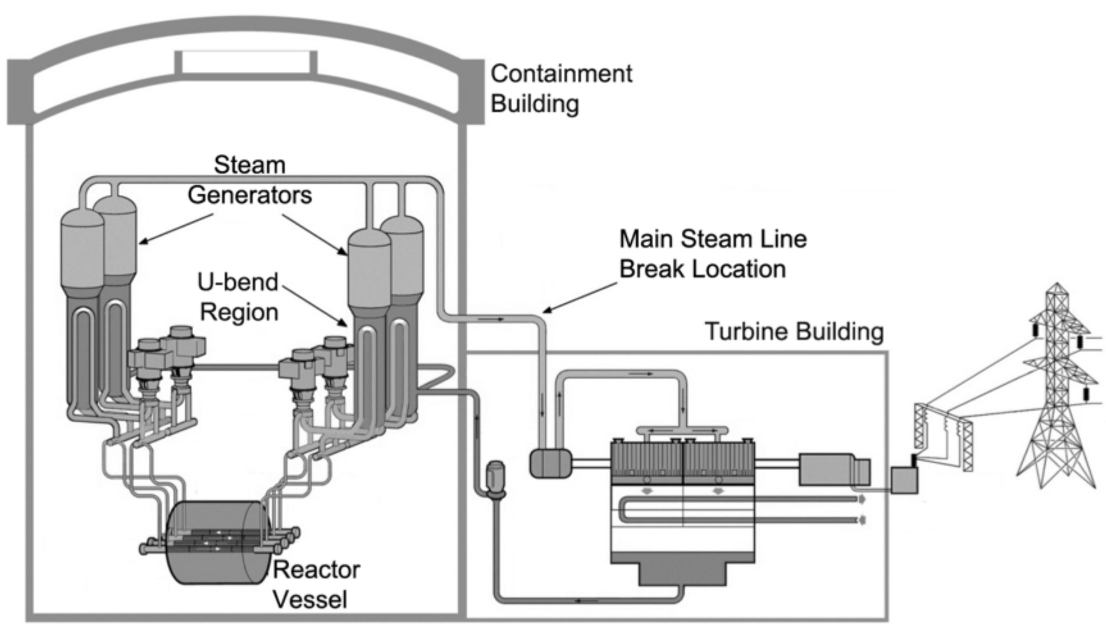

Figure 1-1. Main Steam Line Break (MSLB) accident scenario in a CANDU nuclear plant (adapted from AECL).

interactions of rapid transient two-phase flow dynamics and fluid-structural loading processes that are very difficult to model physically or numerically. Hence, tube loading during a MSLB remains difficult to predict with any precision. This report presents the results of an experimental laboratory study of the transient tube loading during a simulated blowdown.

1.1 Research objective

This experimental research program has been undertaken to simulate a MSLB, develop an understanding of the physical phenomena causing the transient loading on a sectional model of steam generator tubes, measure the loading directly, and ultimately, to develop a predictive model for tube loading. A purpose designed experimental facility has been built, which uses R-134a as the working fluid to simulate steam-water in a CANDU steam generator. The experimental blowdown rig contains a CANDU design model tube bundle test section, in which transient load measurements are obtained, which represents the main experimental novelty of the study. The sectional tube bundle model is a triangular array with a pitch ratio of 1.36.

Tests were conducted with various levels of liquid R-134a and various numbers of tube rows in the test section to improve our understanding of the nature of the transient two-phase phenomena and the mechanisms of tube loading generation. This report presents a detailed overview of the experimental facility and procedures employed, discusses instrumentation problems discovered during commissioning, explains why these occurred, and describes the remedial strategies developed and the corresponding validation methods. The results of the two-phase blowdown experiments are presented, accompanied by an analysis of the dynamic fluid transient thermal-hydraulic behaviour observed during the simulated main steam pipe rupture tests. The results include tube loading measurements during the blowdown, which are interpreted in terms of fluid transient phenomena. An empirical approach is also provided to compute the maximum tube loading during a MSLB blowdown.

The overall purpose of this investigation is to provide some physical insights and guidance for the development of predictive modelling tools. The knowledge gained has enabled the development of a better understanding of the transient loading and its prediction. The transient tube loading is explained in terms of the associated flow physics and the maximum load is compared with existing models for tube loading obtained under steady flow conditions. Ultimately, this will lead to a theoretical framework that can be used to estimate the loads on CANDU steam generator tubes during a MSLB, such that structural tube failures can be avoided.

2. Background

The US Nuclear Regulatory Commission (NRC) investigated the issue of steam generator tube vulnerability during a MSLB and classified it as Generic Safety Issue 188 in 2001 [1]. In a report published in 2009, the US NRC concluded from calculations of the dynamic response during a MSLB that the predicted loads are not expected to pose a structural integrity risk in steam generator tubes. The calculations considered short-term thermal hydraulic and acoustic effects occurring in the initial stages of steam generator blowdown, and did not incorporate the loads developed as a result of the quasi-steady flow present following the initial rapid transient effects. In addition, the analysis relied on calculations performed using one-dimensional thermal-hydraulic codes (RELAP and TRAC-M), which do not account for the three-dimensionality of the cross-flow induced forces on the tubes.

Presently, the problem continues to be the focus of some numerical investigations but, to the author's knowledge, no thorough experimental investigation has ever been performed. The following sections provide a brief overview of some of the relevant research progress made over the years, summarising the pertinent experimental and numerical studies done so far.

2.1 Experimental studies of MSLB loading of steam generator tubes

Steam generator thermal hydraulics was the focus of several large-scale nuclear safety experimental programs in the 1970s, with emphasis placed on modelling postulated critical Design Basis Accident (DBA) events. Large Steam-Line-Break (SLB) simulations were performed in scaled model facilities of typical commercial U-tube steam generators by Framatome in collaboration with CEA [2], as well as by EPRI [3]. The purpose of the tests was to develop numerical capabilities to evaluate hydraulic loading on steam generator internals during blowdown transients.

The Framatome tests were performed on a scaled facility of a Model 51 steam generator, with a total height of 3.5m, maximum cross-section of 0.2m^2, and an outlet flow restrictor area of 13.6cm^2 through which the MSLB was simulated. The transients were initiated from 'hot standby', or 0% power, initial conditions, with saturated liquid water at 7MPa. The stratified liquid free surface location was between the top of the tube bundle and the bottom of the steam separators. Transient temperature and pressure measurements were collected, and a peak pressure difference of about 70kPa was recorded at the uppermost tube support plate. It was concluded from this research that more fundamental investigations were required to study the initial transient stages of the blowdowns, during which thermodynamic non-equilibrium effects were strongly influential.

The tests at EPRI were carried out on a 1:7 scale prototypical steam generator facility, using Freon-11 as a working fluid. An in-line square tube bundle with 1:1 scale tube diameter was employed, consisting of 76 U-tubes of 0.75in (1.905cm) outside diameter and 1.05in (2.667cm) tube spacing. MSLB simulations were performed through a 4-inch diameter outlet nozzle (81.1cm^2 flow area), from subcooled liquid initial conditions, at 1013kPa and 82°C. Transient blowdown pressure and temperature measurements were obtained with a response time of 10ms and 500ms respectively. The results indicated a transient increase in the pressure drop across the steam separators, but no similar rise in pressure drop was recorded in the tube bundle. In addition, it was discovered that the build-up of back-pressure in a receiver dump tank of 2270L volume significantly influenced the transient depressurisation inside the steam generator model vessel.

The Atomic Energy Control Board (AECB) carried out an experimental program in 1995 [4] using a different approach to determine the tolerance of steam generator tubes with various defects to high cross-flow velocities. Tube bundles containing 32 tubes in a triangular pitch array, with 9 rows of 1.27cm outside diameter tubes and 0.95cm tube row spacing were placed in a water tunnel with a 50.8x13.2cm rectangular channel (670.56cm^2 flow area), in which high liquid cross-flow velocities were established, with tube gap velocities of up to 3m/s. The tubes, of which some were pre-flawed, were tested at steady state up to failure, either due to a leak or complete severance, for up to 10 minutes duration.

Typically, the hydraulic loads on tubes are computed from pressure drop measurements, using single-phase pressure drop relationships and two-phase flow corrections available in heat exchanger design guidelines [5, 6]. In the present study, it is expected that the installed sectional model of steam generator tubes will produce a realistic replication of the two-phase blowdown pressure drop in a commercial steam generator under postulated accident conditions, with a significant amount of fluid resistance imposed on the discharging flashing two-phase flow. Furthermore, a direct measurement of dynamic loading on the tubes is obtained in addition to the dynamic pressure measurements across the test section, which, to the author's knowledge, has never been done before.

2.2 Numerical studies of MSLB loading of steam generator tubes

Numerical code simulations of transient events in nuclear systems typically rely on relatively simple models that divide the system into one-dimensional flow paths. Such codes seldom contain three-dimensional flow modelling capabilities for predicting rapid transient two-phase cross-flow and radial flow conditions around steam generator tubes, which exist during blowdown. Steam generator computational codes usually model a general thermal-hydraulic network without including the detailed local behaviour within each of the segments comprising the system. Confidence in the codes is developed through comparison of the numerical predictions with experimental data, and for the past 40 years, computational methods have complemented results from scaled model experiments and prototypic tests for safety analysis and licensing purposes [7]. In the late 1980s, various attempts were made to numerically model the thermal hydraulics of Loss-Of-Coolant Accidents (LOCAs) and Steam-Line-Breaks, with the emphasis in the latter on predicting the heat transfer characteristics and fluid-structural behaviour of steam generator internal components.

A numerical simulation of a 100% MSLB from 'hot standby' conditions was performed on a 500MW U-tube PHWR (Pressurised Heavy Water Reactor) steam generator model using the Code for LOCA Analysis of Indian PHWRs (CLAIR) [8], which is a two-fluid six-equation transient two-phase flow code comparable to TRAC, RELAP, and CATHENA. In order to simplify the analysis, the steam generator tube bundle was modelled as a single U-tube, consisting only of two vertical pipes, and no horizontal segment. The simulation was performed only for the first 1000ms of the transient, and a peak pressure difference across the top tube support grid plate component was observed to be just over 100kPa.

Based on this thermal hydraulic analysis, a numerical analysis of the structural loads following a MSLB on the CANDU type steam generator internals was performed [9]. The transient drag force exerted on the tube bundle was computed by considering the outside wall friction on the entire tube bundle, which is modelled as a single tube, and the peak force was found to be 242.9kN. This value was divided by the total number of tubes in the actual steam generator, 2489 tubes, yielding a maximum drag force per tube of 98N. The maximum calculated drag force in the steam separators was 314.8kN.

A numerical simulation was also performed at EPRI for a complete SLB in a Model-F steam generator using the ATHOS3-MOD1 thermal hydraulics code [10]. The investigation was primarily concerned with the pressure imbalance across the pressure boundary, represented by the steam generator tube walls, due to the depressurisation of the steam generator. The drag pressure loading on the outer surface of the tubes was not directly addressed. Convergence problems were encountered with the ATHOS code as the simulations progressed towards ‘dry steam’ conditions, and an extrapolation of the simulation results yielded an estimated 107 seconds for the secondary side liquid to be depleted and steam generator dry-out to occur.

A similar study was performed by Ontario Hydro, which investigated tubes under transient blowdown conditions following a 100% MSLB [11]. A thermal-hydraulic analysis of a Bruce ‘B’ CANDU steam generator was carried out to estimate the transient conditions in the U-bend, using the computer code SOPHT. Instantaneous transient flow forces were then derived based on the calculated transient mass flux and pressure drop, which were obtained from the thermal hydraulic parameters: density, flow velocity, and void fraction. The transient simulation was initiated from 103% full power initial conditions, which is contrary to most other investigations of a similar nature, in which ‘hot standby’ or 0% power initially subcooled liquid blowdown is generally considered to represent the worst case scenario for conservative modelling. A flow velocity correction factor was included in the analysis to account for slip flow between the vapour and liquid phases, and the transient Reynolds numbers ranged between 10 and 10^5 for the transient blowdown duration.

The peak flow velocities, and therefore transient drag force, were established between 20 and 35 seconds following the initiation of blowdown, as shown in Fig. 2-1. A peak velocity of about 6.8m/s was obtained, corresponding to a peak pressure drop of about 4.2kPa. The simulated velocities during this time segment show large sharp fluctuations of 1 – 7m/s, and it is not clear what physical mechanisms would be responsible for such behaviour. The oscillations were not addressed in the report, and it may be that these were artefacts of numerical instabilities encountered at higher void factions. In order to derive the applied forces from the transient fluid parameters, a two-phase drag coefficient was calculated based on empirical data collected from bubbly air-water cross-flow over a single circular cylinder. The maximum drag coefficient was determined to be unity for high Reynolds number, and slightly higher than 1 for lower Reynolds number, on the order of 100.

As part of a TRAC-M (renamed TRACE) code development and validation program for the US NRC [12], code simulations were compared to experimental SLB tests carried out in the 1980s [13], focused specifically on the thermal and hydraulic loads on the steam generator

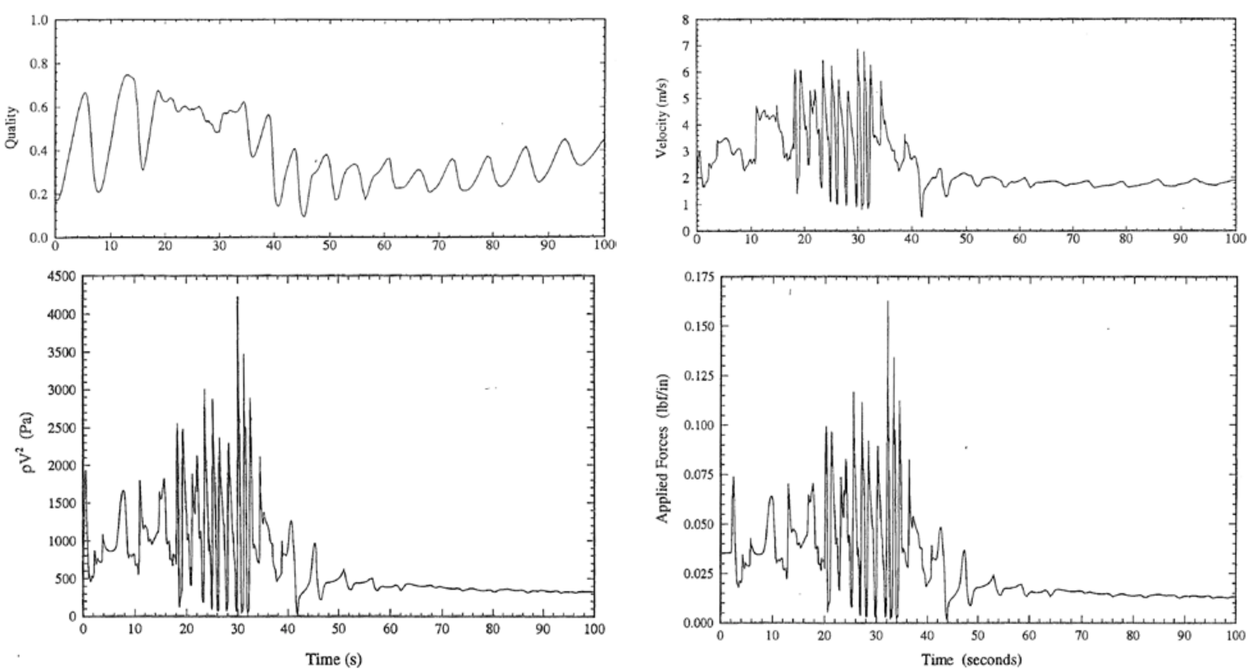

Figure 2-1. Bruce 'B' steam generator transient blowdown thermal hydraulic analysis [11].

internals. The experiments were performed on a large-scale Model Boiler (MB-2), which was a near prototypical 0.8% power-scaled facility of a Westinghouse Model F steam generator, capable of generating up to 10MW. The MB-2 contained prototypical primary and secondary temperatures, pressures, and mass flow rates, and was equipped with a tube bundle containing 54 U-tubes arranged in 4 columns and 13 rows. The bundle was 7m high, and was made with the same material, dimensions (1.75cm tube outside diameter), and tube pitch (2.49cm square pitch array) as the original steam generator design. Full 100% SLBs were simulated from 'hot standby' conditions by a quick-opening valve that opens in less than one second, using a 3.43cm throat diameter representing the steam generator flow limiter, installed in a 7.62cm diameter steam line. The initial water levels ranged between 9.91 – 12.45m, and the blowdowns were initiated from initial secondary pressure 7.591MPa to a break downstream pressure of 99.3kPa.

In the MB-2 design, the U-tube bundle occupied a cross-section of 68.4x9.96cm, and was wrapped in a rectangular channel, which was placed inside the cylindrical shell of the boiler. This tube bundle channel flow was funnelled into the steam separator and riser sections, effectively isolating it from a region inside the boiler of stagnant 'dead space', represented by the volume outside the tube bundle channel and contained inside the outer shell. The downcomer was simulated by two pipes, of 7.8cm inside diameter, which fed into the hot and cold leg openings of the wrapper box surrounding the tube bundle. The cross-sectional area of the pipes was selected to match a scaled representation of the actual downcomer annulus area in the Model F steam generator. In the numerical simulations, the flow through the tube bundle was treated using a 'hydraulic diameter' variable, which allowed for a pressure drop coefficient to be incorporated into one-dimensional flow paths between the various tube support plates.

In the first 5 seconds of the transient tests, a very fast two-phase level swell was observed, accompanied by an almost instantaneous discharge of liquid. It was also discovered that the flow in the downcomer during this initial period of the transient was reversed, such that the fluid in the tube bundle region flowed upward through the downcomer pipes, rather than through the tube bundle, riser, and separator flow path. It was concluded in the numerical study that the relative losses in the downcomer and the separator towards the steam dome were such that the differential pressures did not change significantly, and therefore, that the experiments were not well suited to determine the ability of TRAC-M to predict transient differential pressure loadings on steam generator internals during MSLBs.

Another investigation by the US NRC involved a detailed thermal-hydraulic assessment, using the numerical code TRAC-M, of the loads in a generic Westinghouse PWR steam generator during a MSLB [14]. Computer code simulations indicated that the largest forces occur during the guillotine rupture of a steam line, when the steam generator is initially in a 'hot standby' condition. The model implemented in the code simulations divides the steam generator into one-dimensional flow paths, and is not capable of predicting radial flow conditions around the steam generator tubes. The loading on the steam generator internal components was determined from the calculated thermal-hydraulic conditions, the pressure difference being primarily attributable to friction losses.

Pressure drop loss coefficients, or hydraulic drag coefficients, were incorporated into the model as 'pressure drop correction multipliers', to account for irreversible form drag losses. The peak pressure differences across the tubes and the tube support plates were calculated using the same general pressure drop equation. The drag coefficient for a single tube at each location was calculated using a correlation for the appropriate geometries from [15], and a pressure drop loss coefficient of 1.1 was used for the tube support plates, which was conservative relative to the calculated pressure loss coefficient of 0.96 for flow through a thick perforated plate from [15]. A correction for two-phase pressure drop was incorporated by using a multiplier factor of 1.2, and an additional multiplier of 1.5 was also included to account for uncertainties in the modelling.

The simulation results suggested that the largest loads were due to thermal-hydraulic and acoustic effects, related to the propagation of the initial depressurisation wave at acoustic velocity, during the first few seconds following the pipe break. Flow-induced loads, which develop as a result of the quasi-steady flow present following the initial rapid transient effects, were found to be smaller than the loads in the initial phase of the transient. Consequently, the TRAC-M analysis was only performed for the initial portion of the MSLB transient, and no extensive analysis of the quasi-steady loading on the steam generator internals was carried out.

The peak pressure difference across the primary steam generator tubes at the U-bend was found to be 7.2kPa. A higher peak pressure difference of 59.1kPa was obtained across the top tube support plate, with a peak mass flow rate of 24,000kg/s. The TRAC-M calculations were compared to hand calculations performed using analytical tools available in [16]. The pressure difference across a tube support plate, resulting from the rarefaction wave travelling from the break location to the tube support plate, was calculated at the instant where the pressure directly above the tube support plate is lowered, and the pressure directly below the tube support plate is still unaffected and remains at the original pressure value. The magnitude of the depressurisation wave entering the steam generator following a MSLB was found by determining the maximum choked flow rate and the discharge pressure at the break location in the ruptured line, obtained from the steam generator volume, the initial fluid mass, the initial stagnation pressure, the initial stagnation enthalpy, and the break line diameter and area. Friction losses and pressure wave reflections were ignored, and the pressure difference was found to be 62.1kPa.

In order to be able to properly assess cross-flow in the tube bundle region, a three-dimensional fluid model is necessary, which must be applied to the quasi-steady portion of the steam generator blowdown discharge. In the US NRC report, questions were raised concerning the potential accuracy of results obtained from a full transient analysis, and specifically, whether any existing thermal-hydraulic codes, such as TRACE and RELAP, are able to accurately predict the behaviour of liquid boiling under relatively low pressure conditions. Oscillations in the data were observed as the void fractions progressed towards higher values, and these instabilities were attributed to numerical conditions resulting from inaccuracies in the fluid-thermal correlations in the code. It was concluded that, before the accuracy of such predictions can be accepted, the ability of thermal-hydraulic codes to correctly predict quasi-steady thermal-hydraulic steam generator behaviour must be properly verified. During large-diameter SLBs, the steam generator flow restrictor is expected to choke the outlet flow, isolating the steam generator from any pressure fluctuations in the steam line. Furthermore, the fluid flow path resistances in the steam generator and the two-phase flow established during a MSLB depressurisation would mitigate the propagation of acoustic waves from the steam line into the tube bundle region.

A summary of the pressure loads on steam generator internals obtained during simulated MSLBs is presented in Table 2-1. A variety of steam generator internal components were investigated with a wide range of analysis methodologies. Pressure loss coefficients were typically included from which the drag load is computed. The sudden ‘acoustic’ hydrodynamic forces associated with the propagation of pressure waves are modelled according to a step change in pressure across the structural boundary. Flow-induced vibration was studied by simulating the flow properties and using the computed forces as input for numerical structural models. In none of these studies was the hydraulic drag on the tube bundle due to the high-velocity cross-flow directly addressed.

Table 2-1. Summary of simulated MSLB pressure loads on steam generator internals.

MSLB Research Project	**Year**	**Method of Investigation**	**Test Conditions**	**Peak Pressure Loading**	**Steam Generator Component**	**Physical Loading Mechanism**
Framatome / CEA [2]	1978	Scaled experiment	Saturated liquid H_2O – 7MPa	68kPa	Top tube support plate	Fluid-structural loading
Electric Power Research Institute [3]	1980	Scaled experiment	Subcooled liquid F-11 – 1.01MPa	1.1kPa	Steam separators	Fluid-structural loading
Bhabha Atomic Research Centre [9]	1993	CLAIR simulation	Subcooled liquid H_2O – 5.99MPa	98N (drag force per tube)	Entire tube bundle	Tube wall friction
Ontario Hydro [11]	1996	SOPHT simulation	Saturated liquid H_2O – 4.6MPa	4.2kPa	U-bend tubes	Flow-induced vibration
US NRC [14]	2004	TRAC-M simulation	Subcooled liquid H_2O – 5.47MPa	7.2kPa	U-bend tubes	Acoustic load
US NRC [14]	2004	TRAC-M simulation	Subcooled liquid H_2O – 5.47MPa	59.1kPa	Top tube support plate	Acoustic load
US NRC [14]	2004	Moody [16] analytical calculation	Saturated vapour H_2O – 5.5MPa	62.1kPa	Top tube support plate	Acoustic load

2.2.1 Computational Fluid Dynamics (CFD) MSLB simulations

The application of Computational Fluid Dynamics (CFD) codes in nuclear safety analysis is not as well established as numerical system codes. CFD codes offer the capability to include complex geometries and three-dimensional flow effects, which are not properly predicted by one-dimensional system codes. However, CFD codes are difficult to use in the evaluation of nuclear accident events due to the huge degree of sophistication inherent to transient two-phase flow phenomena.

A coupled CFD / FEM (Finite Element Modelling) study was carried out to simulate a blowdown experiment performed at FZK in Germany [17]. Single-phase predictions with fluid-structure interaction agreed with experimental data for the initial stages after the break, before phase change took place. Transient two-phase phenomena then begin to dominate, for which the simulations did not produce reliable results. A CFD analysis of a MSLB in a BWR (Boiling Water Reactor) was carried out at Forsmark NPP in Sweden [18]. The instantaneous forces obtained were approximately twice those previously estimated from simpler methods, and the results have not yet been experimentally validated.

The Korean Institute of Nuclear Safety instigated a CFD study of transient pressures in the main steam line of a PWR plant [19] following an incident at an operating plant in which a steam pressure relief valve was suddenly opened, blowing off the 7.115MPa steam to the atmosphere, and damaging some of the plant piping system components. The force caused by the rate of change of momentum in the main steam line due to the sudden change in mass flow rate propelled a 3.3m pipe elbow into a refuelling water storage tank 50m away. Using a similar theoretical modelling principle to that established in the CFD investigation, an analysis of the transient thermal-hydraulic response of a steam generator secondary side to a MSLB was performed [20], in which the steam was modelled as a real gas. The results of the CFD model suggested that the steam velocity in the steam generator region above the tube bundle accelerates to a peak velocity of about 18m/s following a MSLB. By comparing this to normal operational velocities in the U-bend of 2m/s, it was concluded that the hydraulic loading on the tubes could increase by a factor of 9.

In studies of the effects of MSLBs on tube bundles available in the literature, the issue of fluidelastic instability vibrations arising due to the increase in fluid velocities is sometimes raised. Fluidelastic instability occurs in a tube bundle when the threshold critical velocity is met, and the flow energy is then transferred at a sufficiently slow rate to the tubes, such that a significant number of seconds is required for damaging vibration levels to be established. Once these vibrations begin, a significant amount of time is needed for through wall wear or high-cycle fatigue failure to occur, as little as a few hours in extreme cases. Therefore, since the transient loading duration during steam generator blowdown is not more than a couple of minutes at most, fluidelastic instability is not likely to be a concern, and the main fluid loading mechanism to be investigated and predicted is the transient drag load due to the substantial rise in the pressure drop across the tubes.

Mechanical loading during two-phase blowdown involves complex coupled rapid two-phase flow dynamics and three-dimensional fluid-structural loading processes, which are very difficult to model numerically. As such, the development of reliable tools for the prediction of hydraulic loading during large pipe-break scenarios remains challenging. A comprehensive assessment of the state of affairs in terms of CFD applicability in nuclear safety simulations is provided in [7]. To the author’s knowledge, there are no published accounts that accurately simulate the two-phase transient blowdown pressure drop across tube banks, or that provide detailed measurements of tube loading during such events. Thus, tube loading during a MSLB remains difficult to predict with precision.

3. Experimental facility

A purpose built experimental facility was designed and constructed for this study in order to carry out the steam generator blowdown simulations. An illustration of the experimental apparatus is shown in Fig. 3-1, and a photograph of the facility is provided in Fig. 3-2. The details of the design and the instrumentation system are provided in Appendix A. The system consists of a pressure vessel serving as a static fluid reservoir that holds liquid at the bottom, with a cross-sectional area of about 186cm^2, a test section containing the sectional model of a typical CANDU steam generator tube bundle, with the same cross-sectional area, a rupture disc, and a large vacuum reservoir with an expansion ratio of about 60:1, designed such that its pressure does not rise sufficiently during a blowdown to adversely control the process. The height of the pressure vessel from the base to the rupture disc can be changed from 1.26m to 1.49m, depending on the orientation of the bottom pressurised liquid reservoir. The working fluid is refrigerant R-134a, which boils at near standard temperature and pressure and dynamically scales steam-water reasonably well for the purposes of this study.

The rupture disc was selected because it would open completely in a few milliseconds at a pressure difference of 584kPa with no obstruction to the flow. The test section is 138mm square and consists of a tube bundle of 12.7mm diameter tubes in a normal triangular array with a pitch ratio of 1.36 and 8 tubes per row. Boundary effects are minimised in the bundle by using half tubes at the side walls. Temperature and pressure measurements are taken upstream and downstream of the test section (locations 1 and 2 in Fig. 3-1 respectively), as well as downstream of the rupture disc (location 3 in Fig. 3-1). Fluid loading was obtained by summing the measurements of 4 piezoelectric load cells located on the corners of the test section (location 4 in Fig. 3-1). Sight glass windows were placed above and below the test section so that the blowdown fluid mechanics could be visually monitored using 2 synchronised digital high-speed cameras.

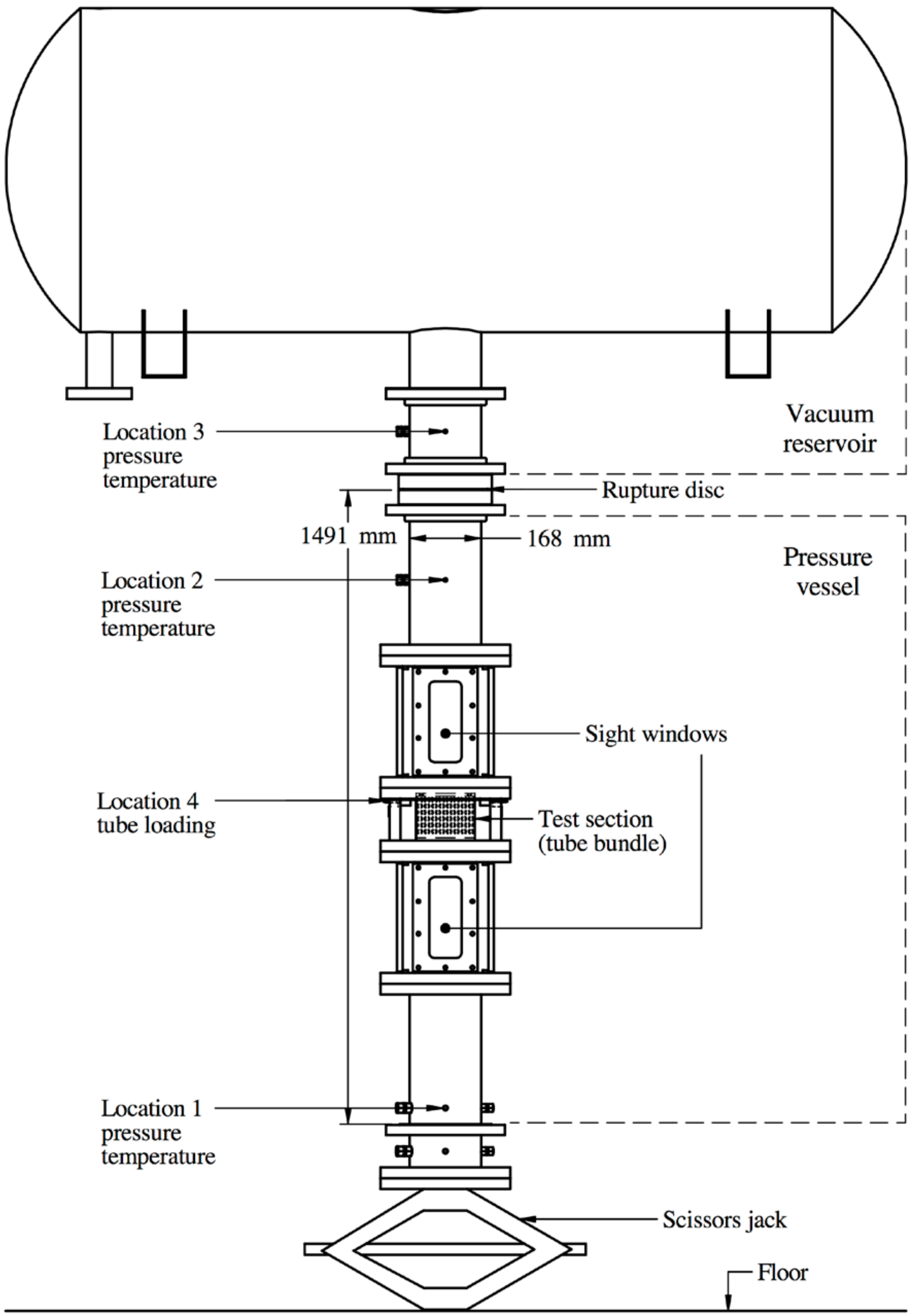

Figure 3-1. Experimental apparatus for steam generator blowdown simulations.

Figure 3-2. Photograph of the experimental facility.

3.1 Experimental procedure

For each experiment, a rupture disc was inserted and the system above and below the rupture disc was drawn to a 99.9% vacuum (about 70Pa). The fluid reservoir was then charged with R-134a until the desired fluid level and pressure was achieved. The final pressure increase was obtained using a nitrogen gas cylinder as a pressure supply, connected to a compressed gas accumulator consisting of two chambers separated by an elastic diaphragm so that the pressure could be finely controlled without introducing any foreign substance to the system and contaminating the R-134a working fluid. The burst pressure for each disc is between 555 – 613kPa (±5% manufacturer specified tolerance) so the precise rupture point cannot be determined in advance. Thus, all the instruments, including the cameras, were set to continuously capture and buffer the data before disc rupture. When the rupture disc bursts, it emits a compression wave that is registered by the dynamic pressure transducer just above the disc (location 3 in Fig. 3-1), which triggers the logging process immediately after the instant of rupture without any loss of data. This enables reliable acquisition of the rapid transient signals during the important phases of the experiment, which are over in fractions of a second.

When the experiment was complete, the R-134a was recovered from the system through a filter that removes foreign particles and dissolved moisture. Following the purging of the system, the rupture disc was removed and replaced. The entire blowdown rig is supported on a stiff steel support structure such that the pipe from the vacuum tank to the fluid reservoir is suspended above the floor with sufficient space to insert a scissors jack at the bottom of the rig, as shown in Fig. 3-1. This jack is loaded against the fluid reservoir such that the vertical transient load from the blowdown is carried largely by the floor rather than by the vacuum tank. The scissors jack facilitates the process of replacing the rupture discs by supporting the weight of the assembly below the disc and allowing it to be raised and lowered as required.

3.2 Working fluid

Experiments that are performed with water at typical nuclear reactor conditions require large-scale facilities, which are very expensive because of the high temperature and pressure conditions as well as the heat energy required. Therefore, modelling fluids that have lower boiling points and latent heats of vaporisation compared to water are often used in thermal-hydraulic testing in order to reduce costs and technical difficulties. R-134a is a reasonable substitute to scale water-steam flows, and boils at near atmospheric temperature and pressure. It was implemented as the working fluid in this study, greatly simplifying the required experimental facility and reducing the associated costs.

By using R-134a as a working fluid, the experiments could be performed at near ambient laboratory conditions, reducing the cost associated with heating and safely containing pressurised water at typical steam generator conditions. In addition, the moderately low pressures make it possible to use thin rupture discs, which open predictably and completely, without introducing any blockage to the flow area at the exit of the blowdown pipe. Also, since the saturation temperature of R-134a is close to that of atmospheric conditions, it is easy to maintain uniform initial temperatures without using any thermal insulation. Finally, direct visual liquid observation during the rapid blowdown event is facilitated since the experiments are performed at ambient temperature conditions.

In fluid-to-fluid modelling of thermal hydraulic experiments, the geometric, thermodynamic, and hydrodynamic similarities should be satisfied for both fluids. The loading on the steam generator tubes during a blowdown is basically a fluid drag force and is expected to scale with the dynamic head. Thus, fluid density and velocity are important scaling parameters and, in two-phase flows, the ratio of liquid-to-vapour densities is important. R-134a has a density ratio of about 35, at a temperature of 26°C and a pressure of 690kPa, which is very close to the density ratio of water-steam, which is about 34, at 257°C and 4.5MPa steam generator secondary side operating conditions. It also important for the sectional model tube bundle to scale the tube diameter and pitch ratio. The model used in these experiments has essentially full sized tubes with the full-scale pitch ratio, in compliance with the requirement for geometric similarity.

4. Instrumentation development

Carrying out blowdown experiments to investigate the drag loading exerted by a suddenly accelerated fluid on a tube bundle requires reliable measurements of transient pressures, temperatures, and loads. The rapidity of the transient, the significant temperature change, and the shock loading produced with initiation of the blowdown created many challenges to the instrumentation. In order to evaluate and ascertain the instrumentation and data collection system in the present experimental facility, a preliminary test phase was developed in which single-phase compressed N_2 gas blowdowns were initiated under similar initial conditions as the full-scale two-phase experiments. Clearly, reliable instrumentation is essential, but numerous problems were encountered with the use of off-the-shelf instruments. In some cases, the data was so severely compromised, that the measurements were of little quantitative value.

Rather than accepting the results without attempting to correct them, it was considered important in this experimental investigation to identify the underlying causes, and remove these shock effects from the signals as much as possible by eliminating the spurious measurement sources. This required a re-evaluation of all of the instruments: static and dynamic pressure transducers, load cells, and thermocouples. The remedial actions taken resulted in much improved instrumentation reliability. In particular, the dynamic pressure transducers were mounted in custom designed and fabricated shock and vibration isolation devices, which effectively reduced the noise and ringing in the measurements. Erroneous measurements produced by thermal loading were also addressed, and corrective measures were developed and implemented. The instrument shock and vibration isolation designs are described in detail in Appendix B.

Following the implementation of the shock and vibration isolation designs developed for the instruments, additional commissioning tests were carried out, the results of which established confidence in the modified instrumentation and data collection system. A comprehensive examination of sensor behaviour and response under various input conditions provided evidence that all of the undesired external effects were effectively resolved. The following sections briefly explain the strategies and tests carried out to validate the results and establish confidence in the instrumentation, demonstrating that erroneous signals due to unwanted external effects have been properly resolved.

4.1 Pressure measurement validation

The accurate measurement of transient blowdown pressures was one of the biggest challenges encountered in this experimental study. Indeed, it was found that the vibration 'ringing' and thermal loading obscured some of the pressure changes of interest in this study, and that some means of eliminating these unwanted signals needed to be found. By using custom designed and manufactured shock isolation devices, the shock and vibration-induced artefacts in the measurements were successfully eliminated. Transient thermal shock effects were also resolved for the relevant time segments of the blowdown, rendering the dynamic pressure measurements quantitatively reliable for the duration of the rapid pressure wave propagation portion of the transient blowdowns. The methods used to eliminate these effects from the measurements were developed during single-phase compressed N_2 gas commissioning blowdown tests, and the procedures are discussed in detail in Appendix B.

Figure 4-1 shows transient pressure measurements obtained directly upstream and downstream of the rupture disc, from locations 2 and 3 (refer to Fig. 3-1), during a single-phase N_2 blowdown test. The results demonstrate the successful elimination of undesired artefacts in the pressure signals. The dynamic pressure transducers accurately capture the rapid pressure changes in the first few milliseconds following disc rupture, as shown in Fig. 4-1. This performance is expected since the dynamic pressure transducers were chosen based on the specified upper frequency response limit of 200kHz. However, given that such sensors do not measure static pressures, static pressure sensors were used to establish the upstream and downstream initial steady-state conditions required to initiate the blowdowns. Interestingly, it was discovered that the static sensors also offered some dynamic capabilities, as seen in the pressure measurements shown in Fig. 4-1. The static sensors have a time constant of about 160μs, which gives a response time of 0.8ms. This is about two orders of magnitude slower than the dynamic pressure transducer response. As such, the static pressure sensor signals represent a smooth low-pass filtered set of measurements, with average transient pressure behaviour, but not the details of the dynamics, which occur in fractions of milliseconds.

The transient pressure measurements at all of the points of interest along the blowdown rig (identified in Fig. 3-1) are provided by a combination of dynamic pressure transducer as well as static pressure sensor signals, both sensors having been installed on the pipe walls at the same axial locations. A complete pressure measurement for the entire transient duration is reliably obtained by synchronising the two sets of signals and acquiring simultaneous pressure measurements, starting from the initial rapid depressurisation stage, until equilibrium steady-state. The dynamic pressure transducers provide pressure wave propagation and phase information, and the relatively slower quasi-steady transient pressure profile is completed by the static pressure sensor measurements.

The instrumentation performance in the single-phase N_2 commissioning tests can be quantitatively evaluated by comparing the measurements with predicted values of pressure in the rig. The mass flow rate through a discharge plane for the release of a compressible gas initially at a uniform stagnation pressure to lower ambient pressure surroundings can be derived from the

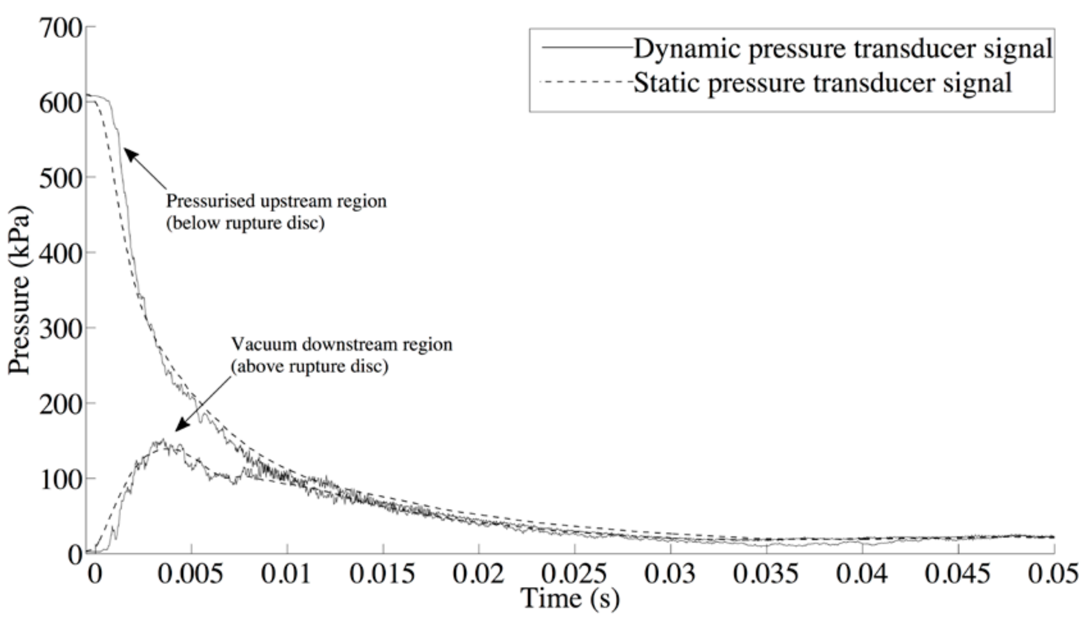

Figure 4-1. Validated pressure measurements for N_2 blowdown, obtained using dynamic pressure transducers and static pressure sensors, above and below the rupture disc location.

continuity equation. The analysis assumes isentropic and adiabatic discharge, and treats the compressed N_2 as a perfect gas discharging through a perfect nozzle. The one-dimensional flow at the exit location during vessel blowdown is expressed in Eq. (4-1),

$$\dot{m}^2 = G^2 A^2 = A^2 \left[\frac{2k}{k-1} \right] \rho_0 p_0 \left(\frac{p}{p_0} \right)^{\frac{2}{k}} \left[1 - \left(\frac{p}{p_0} \right)^{\frac{k-1}{k}} \right], \tag{4-1}$$

where $\dot{m}$ is the mass flow rate, G is the mass flux, A is the flow area, k is the perfect gas specific heat ratio, ρ_0 is the gas density, p_0 is the gas pressure, and p is the exit pressure. Equation (4-1) can be expanded to accommodate sonic as well as subsonic discharge rates,

$$\text{sonic (critical) discharge: } \dot{m} = -A_D C_D \left[k p_T \rho_T \left(\frac{2}{k+1} \right)^{\frac{k+1}{k-1}} \right]^{\frac{1}{2}}, \tag{4-2}$$

$$\text{subsonic discharge: } \dot{m} = -A_D C_D \left[\left(\frac{2k}{k-1} \right) p_T \rho_T \left(\frac{p_a}{p_T} \right)^{\frac{2}{k}} \left[1 - \left(\frac{p_a}{p_T} \right)^{\frac{k-1}{k}} \right] \right]^{\frac{1}{2}}, \tag{4-3}$$

where A_D is the discharge area, C_D is the discharge coefficient, p_T is the vessel pressure, ρ_T is the gas density, and p_a is the ambient pressure. The mass remaining in the uniform constant volume vessel can then be calculated as a function of time by determining the mass discharged according to Eq. (4-4),

$$m(t) = m_{T_0} \left[1 - F(t) \right]^{\frac{2}{k-1}}, \tag{4-4}$$

where $m(t)$ is the mass discharged as a function of time, m_{T_0} is the mass of gas in the vessel, and $F(t)$ is defined by Eq. (4-5),

$$F(t) = \left[1 + \frac{\dot{m}_0 (k-1)}{2 m_{T_0}} t \right]^{-1}. \tag{4-5}$$

The instantaneous gas temperature, pressure, and density can be derived from Eq. (4-4) and the respective relationships are shown in Eqs. (4-6), (4-7), and (4-8),

$$\frac{T_2}{T_0} = \left[F\left(t\right)\right]^2, \tag{4-6}$$

$$\frac{p_2}{p_{T_0}} = \left[F\left(t\right)\right]^{\frac{2k}{k-1}}, \tag{4-7}$$

$$\frac{\rho_2}{\rho_0} = \left[F\left(t\right)\right]^{\frac{2}{k-1}}, \tag{4-8}$$

where T is the gas temperature.

This analysis implicitly assumes that the gas does not condense during depressurisation, and that the pressure in the discharging vessel is uniform. In Fig. 4-2, a theoretical estimate of single-phase N_2 blowdown pressure is compared with the pressure measured just below the rupture disc (location 2 in Fig. 3-1) for a N_2 blowdown test. The theoretical pressures are calculated from Eq. (4-7) based on the initial experimental conditions, the experimental vessel volume, and ideal gas discharge through the rupture disc flow area. Therefore, the theoretical prediction in Fig. 4-2 is an average transient pressure, which assumes uniform conditions inside the pipe, and does not account for the pressure gradient along the pipe axis, unsteady wave propagation effects, or local pressure perturbations. Despite these simplifications, the measured pressure amplitudes and the rate of the depressurisation directly upstream of the rupture disc show good agreement with the theoretical predictions. The instrument uncertainties and modelling assumptions result in small differences between the theoretical and measured pressures, but the overall results satisfactorily validate the pressure instrumentation.

Following the sudden opening of a rupture disc, pressurised gas in an upstream pipe is exposed to a downstream region of lower pressure. The initial acoustic wave propagation velocity in the pipe can be determined based on compressible gas dynamics theory. Simple one-dimensional steep-fronted planar waves propagating at sonic velocity along the length of the pipe are assumed, and head losses and viscous effects are ignored. The gas properties are assumed to be radially uniform along the pipe flow axis, and the flow equations are uncoupled from the pipe

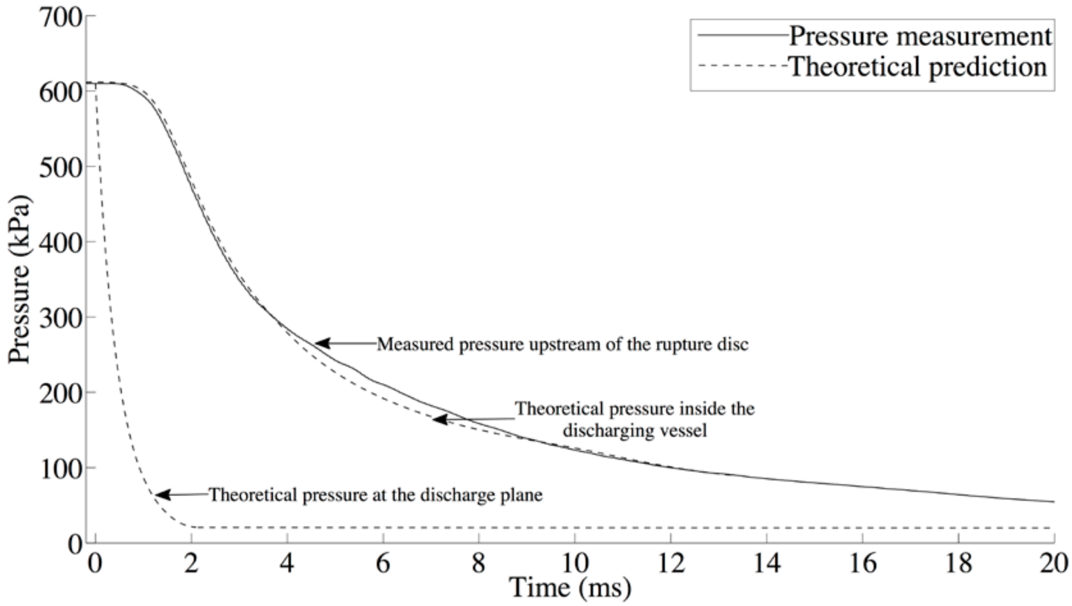

Figure 4-2. Comparison of theoretical N_2 vessel discharge pressure with actual blowdown measurement.

walls. This is justified for gas-filled pipes, where the fluid-structure interaction is insignificant because the gas densities are negligible compared to those of solid steel pipes. Finally, it is also assumed that the temperature remains above the saturation temperature during blowdown, such that there is no liquid condensation. The acoustic propagation velocity, c, is calculated according to Eq. (4-9),

$$c = \sqrt{\gamma R_g T}\ , \tag{4-9}$$

where γ is the specific heat ratio, R_g is the universal gas law constant, and T is the temperature.

Figure 4-3 shows the dynamic pressures measured following the initiation of blowdown in a N_2 gas test. The measurement locations are indicated on the right of Fig. 4-3. The graph shows the pressure measurements immediately after rupture, compared with the predicted timings of pressure wave propagation. The calculated wave propagation velocity in N_2 gas from Eq. (4-9) is 343m/s. The results confirm that the pressure transducers accurately capture the passage of the waves. The timings of the arrival of the pressure waves at the measurement locations are consistent with theory, which validates the measurements of the initially rapidly changing transient pressures, as well as the signal capture and synchronisation system.

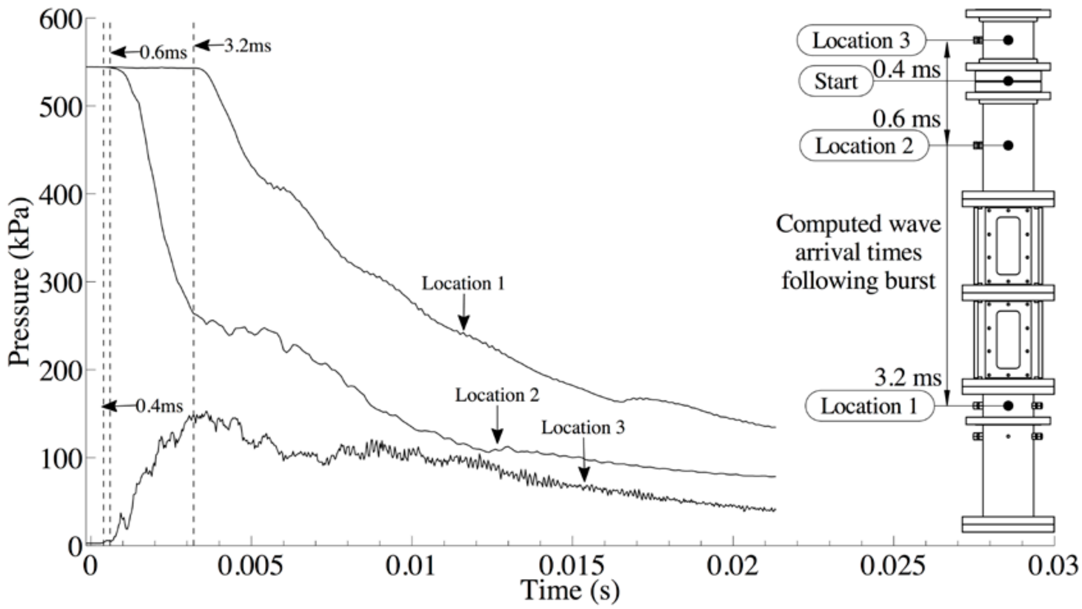

Figure 4-3. Comparison of computed wave propagation timings with blowdown pressure measurements.

4.2 Temperature measurement validation

In the previous section, it was demonstrated that during the first few milliseconds following rupture, when the pressure changes are extremely rapid, the shock-isolated dynamic pressure transducers provide accurate pressure measurements. For the remainder of the blowdown, from quasi-steady state until the end of the transient, the static pressure sensors provide reliable pressure measurements. During this quasi-steady discharge stage, a single-component two-phase fluid mixture at thermal equilibrium will exist at its saturated thermodynamic state. The temperature and pressure measurements can therefore be validated in the current blowdown experiments by comparing the acquired transient pressure measurements to the computed saturated vapour pressures, which are based on the temperature measurements. In Fig. 4-4, local pressure measurements are plotted against computed saturation pressures based on temperature measurements obtained in a two-phase blowdown test. Overlapping measured and computed pressures indicate saturated thermodynamic fluid conditions, which validates the measurement system.

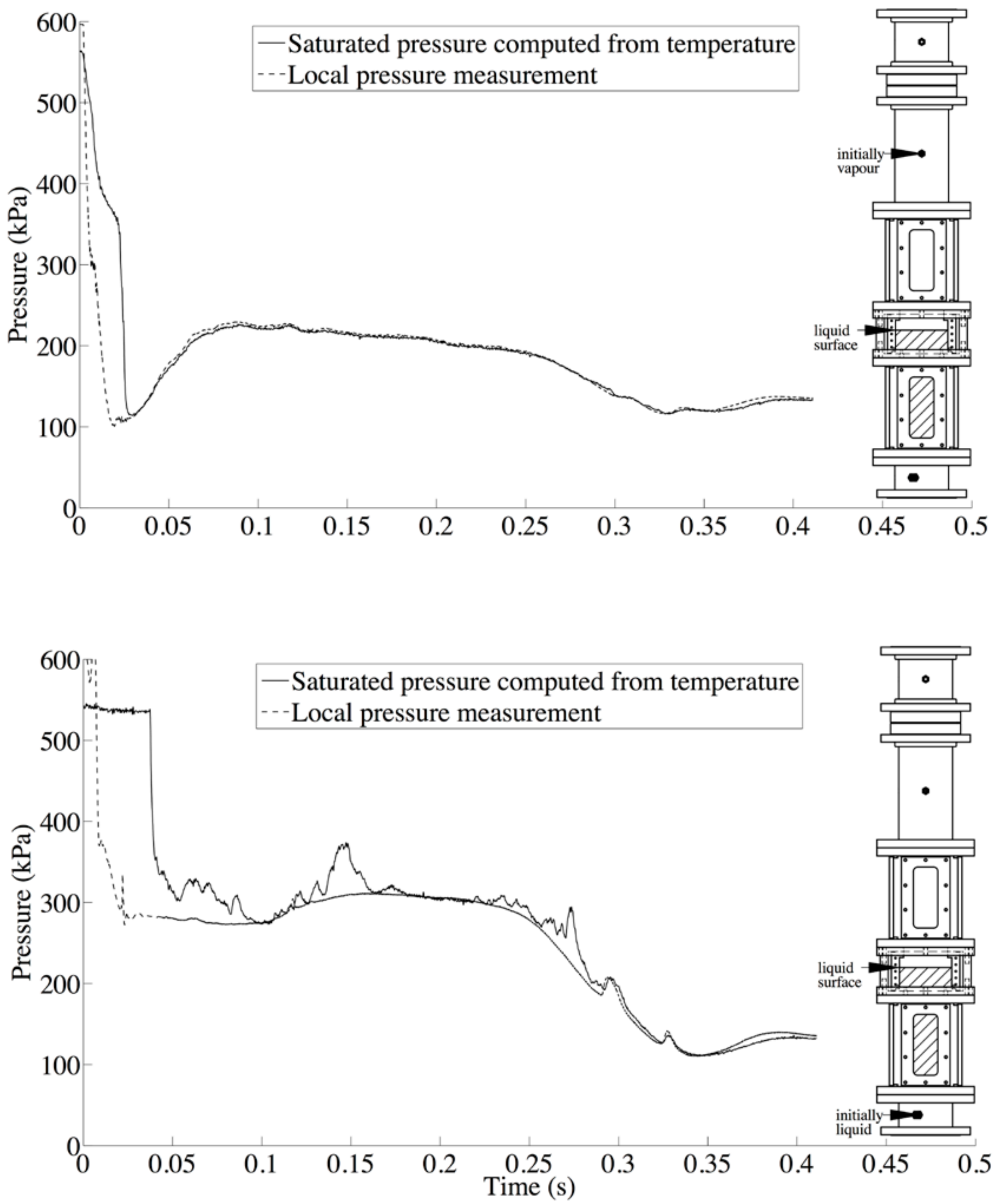

Figure 4-4. Validation of temperature measurements through a comparison of local pressure measurements and computed saturated vapour pressures. Initial conditions: (a) vapour (top), (b) liquid (bottom).

The agreement between the measured pressures and computed saturation pressures is clearly demonstrated in Fig. 4-4, especially in Fig. 4-4(a), which represents measurements obtained in the region initially filled with pressurised vapour R-134a. The vapour temperature almost immediately proceeds towards saturated thermodynamic conditions following the initiation of the transient blowdown. When a fluid is superheated, its temperature would be higher than the theoretically predicted saturation temperature computed from an instantaneous pressure measurement. This is seen during the first 30ms in Fig. 4-4(a).

The results obtained in the region initially filled with liquid R-134a, shown in Fig. 4-4(b), suggest that the liquid remains superheated for about 40ms during the initial stages of the transient. After this constant temperature period, the measured and predicted pressures converge towards each other, indicating that the fluid is near a saturated thermodynamic state. The irregular upward spikes represent local measurements of superheated liquid at the thermocouple locations. The measured temperature during blowdown never drops below the saturation temperature, which is in agreement with the expected behaviour since liquid subcooling is not possible during flashing. As the superheated boiling continues, saturation conditions are approached, until the transient depressurisation in the rig is complete, at about 330ms. This duration depends to some extent on the initial volume of pressurised liquid. The agreement between the measured pressures and the computed saturation pressures based on the temperatures validates the temperature measurements for the time segments in which the two-phase mixture is in a saturated thermodynamic state. The fluid thermodynamic properties can therefore be established with confidence.

4.3 Tube loading measurement validation

The extent of signal distortion due to shock-induced loading of the original test section design during commissioning was such that the measured dynamic loads could not be directly related to the fluid drag loading phenomena being investigated. These issues therefore needed to be resolved, particularly the detrimental initial shock effects and load cell cross-sensitivity. An experimental commissioning program was initiated, specifically developed for the validation of the dynamic tube loading measurement system. Dynamic measurements of blowdown loading were collected for various blowdown configurations: with and without the tube bundle installed, using single-phase and two-phase fluids, and with a wide range of initial liquid volumes. These commissioning tests allowed the structural and hydraulic forces on the test section frame during blowdown to be evaluated, which enabled alternate load paths to be eliminated and the tube loading measurement system reliability to be established. The final design, including the integrated mechanical shock and vibration isolation mechanism, is discussed in detail in Appendix B.

Figure 4-5 shows a two-phase blowdown load signal obtained using the shock-isolated design. The general behaviour observed in Fig. 4-5 was consistent across all of the experiments that were performed. Initially, momentum pressure drop dominates as the fluid is rapidly accelerated towards the vacuum reservoir. Following these transient inertial effects, which last for about 50ms, the measured pressure drop becomes dominated by the two-phase fluid form drag across the tube bundle. After the initial 50ms, in which the inertial effects are significant, the transient distribution of the drag loading on the tubes follows the trend of the measured pressure drop very well. If the pressure sensors were located closer to the tube bundle, then the pressure drop along the blowdown pipe axis between the tube bundle and the rupture disc would not be measured, and the momentum component of the total pressure drop would be smaller. A detailed analysis of the pressure drop across the tube bundle is presented in section 6.7. The results shown in Fig. 4-5 demonstrate that the spurious measurements caused by sudden blowdown shock loading have been eliminated. Hence, by anticipating and mitigating the

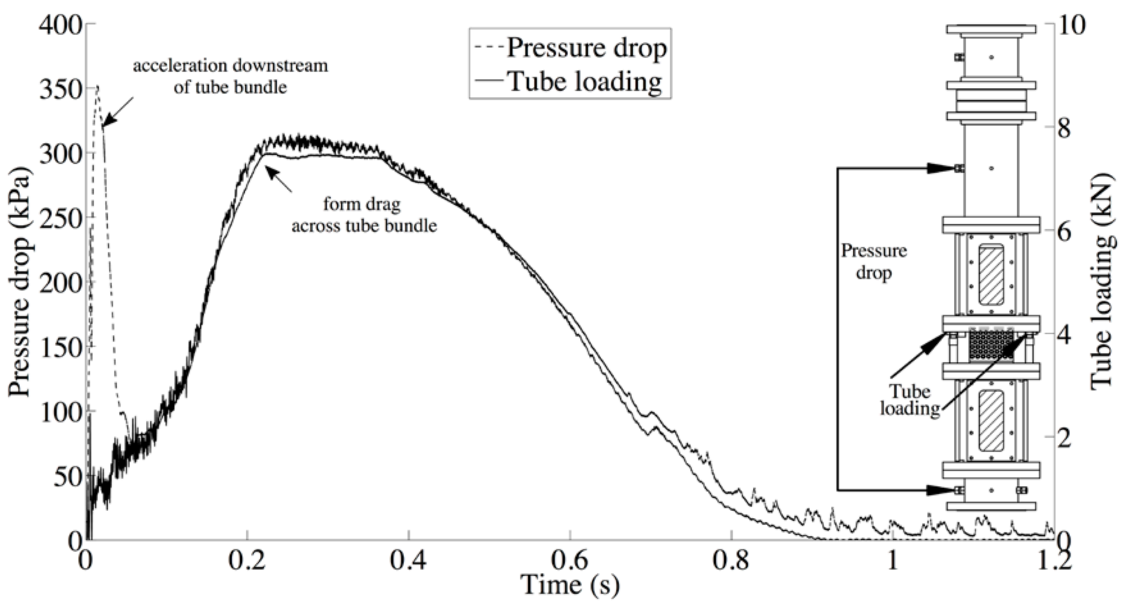

Figure 4-5. Transient tube loading and tube bundle pressure drop showing all measurement issues resolved.

negative effects of the shock loading on the measurements, problematic issues in the signals have successfully been addressed, and the dynamic loads measured can be related to the desired fluid drag loading phenomena.

5. Description of blowdown experiments

A number of experiments were performed with varying initial volumes of liquid R-134a, ranging from 0.8 – 15.4L (3 – 65% of the pressurised reservoir volume), to determine the effect of the initial liquid volume on the blowdown process and tube loading. The number of tube rows was also varied from 0 to 6 rows to determine the effect on the pressure drop and loading. In all, data were collected for 12 experiments. A complete list of the experiments performed is provided in Appendix E including all of the relevant information. Five preliminary commissioning tests are also included in Appendix E, denoted by the prefix C. The results of these tests contain some reliable transient pressure and temperature data but, unfortunately, no reliable dynamic tube loads were obtained. Data collected from the preliminary commissioning tests has already been presented in [21], and additional tests performed using compressed N_2 gas, for instrumentation validation purposes, will not be discussed here.

This section of the report explains the main thermal hydraulic phenomena observed in the experiments, enabling the attendant effects on the dynamic structural loading of a tube bundle subjected to transient two-phase cross-flow to be understood. The particular graphs used to illustrate the phenomena discussed are from a variety of the experiments. While the detailed timings of the events vary significantly with the initial liquid levels and number of tube rows in the bundle, the general phenomenological behaviour observed was common to all experiments. The initial thermodynamic conditions prior to blowdown initiation were similar across all tests. The liquid R-134a pressure and temperature ranges were 554 – 616kPa and 287 – 294K (14 – 21°C) respectively.

5.1 Initial conditions

The initial steady-state conditions of the pressurised R-134a must be accurately determined in order to enable a proper analysis of the transient fluid depressurisation following the sudden opening of the rupture disc, which initiates the blowdown. The initial fluid properties such as the speed of sound and the liquid volume in the pressure vessel are determined from the initial thermodynamic state of the R-134a. By assuming a quiescent pool of subcooled liquid below a region of uniform saturated vapour, the corresponding volumes of the liquid and vapour domains in the pressure vessel can be calculated from the fluid pressure and temperature measurements. Once the fluid properties and the height of the liquid surface are established, the subsequent transient phenomena that begin with blowdown initiation can be investigated.

5.1.1 Calculation of the initial liquid volume

The pressures and temperatures of the liquid and vapour phases are assumed to be uniformly distributed throughout the respective domains, and a uniform density is computed based on the measurements at the sensor locations. The liquid density is determined from the subcooled pressure and temperature measurements, and the vapour density is determined by assuming saturated vapour, corresponding to the pressure measurement. The temperature readings in this region were slightly lower than the saturation temperatures of the vapour, influenced by heat transfer from the colder pipe surroundings and liquid condensation on the inside pipe walls. The range of initial liquid and vapour densities in the experiments varied between 1222 – 1248kg/m^3 and 26.6 – 29.4kg/m^3 respectively. From the liquid and vapour densities, ρ_l and ρ_g, the initial volume of liquid in the pressurised reservoir, V_l, can be calculated according to Eq. (5-1),

$$V_l = \frac{m_T - \rho_g V_T}{\rho_l - \rho_g}, \tag{5-1}$$

where V_T is the total volume of the pressure vessel below the rupture disc, and m_T is the total mass of R-134a introduced into the system. The initial liquid surface height from the bottom of the reservoir, H_l, can then be readily found by dividing the liquid volume, V_l, by the cross-sectional area of the vessel, A_{cs}, which is 0.01864m^2, as shown in Eq. (5-2),

$$H_l = \frac{V_l}{A_{cs}}. \tag{5-2}$$

A compressed gas accumulator with a total volume of 0.0028m^3 was used to pressurise the fluid below the rupture disc in order to trigger the blowdowns. The accumulator contains an elastic diaphragm, which separates the compressed gas driver from the pressurised fluid R-134a in the system. During pressurisation, the introduction of compressed N_2 gas into the driver section of the accumulator results in the expansion of the elastic diaphragm, which compresses the R-134a in the receiver section, steadily drives it out of the accumulator, and boosts the pressure of the pressurised fluid in the pressure vessel below the rupture disc. At some point during this process, usually after most of the R-134a in the accumulator has already been driven out, the pressure required to burst the rupture disc is attained.

For the purposes of calculating the initial conditions in the pressurised reservoir, the volumes of the accumulator and the connecting lines are neglected. Essentially, the assumption, which is supported by experience gained during testing, is that the accumulator is almost completely filled with compressed N_2 gas at the point when the blowdown is initiated. In the worst-case scenario, the accumulator is completely filled with liquid R-134a, and the liquid volume in the reservoir is 0.0028m^3 less than the calculated value. The experiments were carried out with different reservoir volumes depending on the length of the pressure vessel section used below the rupture disc. The list of experiments in Appendix E is arranged from smallest to largest percentage fill of the pressure vessel, which can be divided into four main liquid volume fills: minimum (3 – 10%), small (21 – 23%), moderate (39 – 56%), and large (62 – 65%).

5.1.2 Calculation of the rupture disc opening instant

It is important to establish a precise and repeatable method of determining the instant of rupture disc opening, given the significance of the phenomena that occur in the first few milliseconds of the blowdowns. The procedure developed for setting the instant of blowdown initiation, at time t = 0, is based on the initial thermodynamic conditions of the R-134a in the pressurised reservoir, below the rupture disc, just before the disc opens. When the rupture disc opens, compression and rarefaction waves propagate simultaneously upwards and downwards, respectively, originating at the point of the rupture disc. A positive rise in pressure is signalled by the arrival of the compression wave above the disc (downstream), and a negative pressure wave is signalled below the rupture disc (upstream). The rarefaction wave, which travels downwards opposite the direction of fluid acceleration, is described and analysed in detail in section 5.3. The compression wave, which travels upwards towards the vacuum tank, is used to determine the time t = 0. This is because the wave propagation through the vacuum reservoir occurs at a velocity that is consistent for all of the experiments, making this method universally applicable to all of the tests performed.

The velocity of propagation of the wave, which is equivalent to the speed of sound from Eq. (4-9), can be readily evaluated from the initial thermodynamic state of the saturated vapour in the pressurised reservoir. The calculated velocity for the entire range of initial experimental conditions is 145m/s. This velocity, together with the distance of the pressure transducer from the rupture disc, 138mm, determines the time required for the pressure wave to travel between the two locations. Thus, the instant of rupture disc opening is set to occur 0.95ms before a rise in pressure is observed in the transducer signal.

Figure 5-1 shows a sample pressure signal obtained for test T02 at location 3, just above the rupture disc (refer to Fig. 3-1). The instant of the opening of the rupture disc is set to occur at t = 0, which is 0.95ms before the pressure rise is detected in the signal. Since the opening pattern of the disc produces a pressure wave front that is not a perfect square wave, the pressure signal in the boundary layer does not show an ideal step rise in pressure. The slope of the rising pressure signal increases sharply about 0.5ms after signal detection. The pressure transducer signal noise is about ±0.03kPa, and the observed signal rise is of the order of 0.3kPa. The sampling resolution and transducer diameter result in an uncertainty in the calculation of t = 0. The 30kHz sampling rate error is ±0.033ms, and the pressure wave, travelling at 145m/s, travels across the face of the 5.5mm diameter transducer in 0.038ms. The combined uncertainty is therefore ±0.05ms, about 5% of the duration of the wave propagation from the rupture disc to the transducer location.

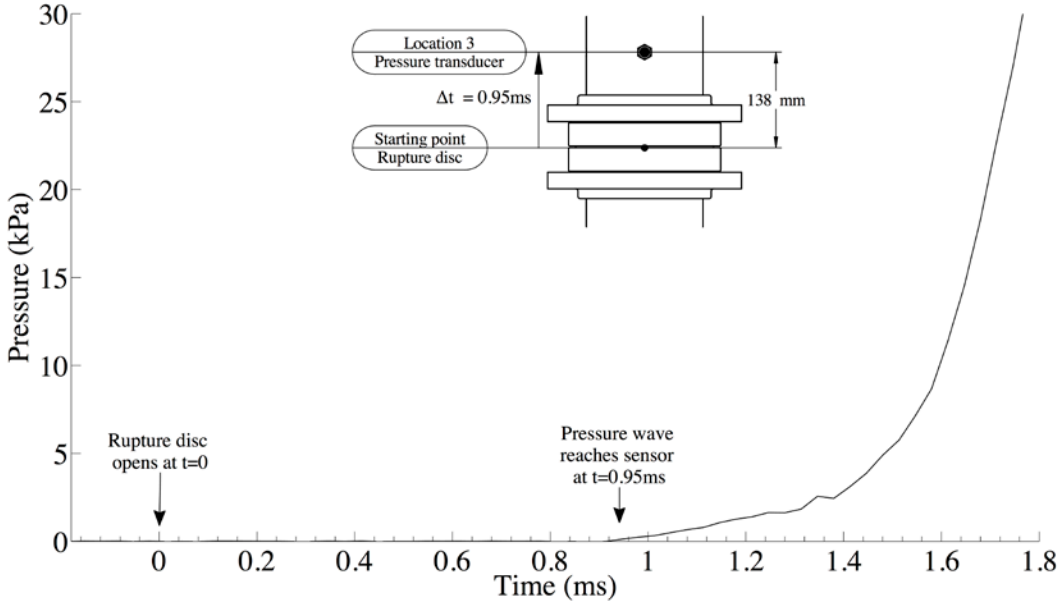

Figure 5-1. Rupture disc opening instant at time *t* = 0 (test T02).

5.2 Thermal-hydraulic phenomena observed during blowdown

A sample set of transient pressures measured for blowdown test T08 at the 3 sensor locations along the pipe axis are shown in Fig. 5-2. This test was performed with 6 rows of tubes mounted in the test section, and with 51% of the reservoir filled with liquid R-134a. The pressure sensors at locations 1 and 2, below the rupture disc, are in the regions initially filled with subcooled liquid and saturated vapour respectively. Initially, the liquid is at 581.6kPa and 18.3°C, and the vapour is at 570.2kPa and 18.7°C. Location 3, above the rupture disc, is initially in a vacuum. The general transient behaviour shown in Fig. 5-2 was typically observed in all of the two-phase blowdown tests carried out. The pressure amplitudes and event durations varied from test to test due to the changes in the initial conditions and the reservoir and test section geometries.

In general, the transient pressure traces show distinct features that can be split into 3 main segments, which in Fig. 5-2 are observed to occur between 0 – 10ms, 10 – 600ms, and from 600ms onwards. In the first 10 milliseconds of the test, pressure waves propagate rapidly at the speed of sound, originating at the point of the rupture disc. This is followed by a period of

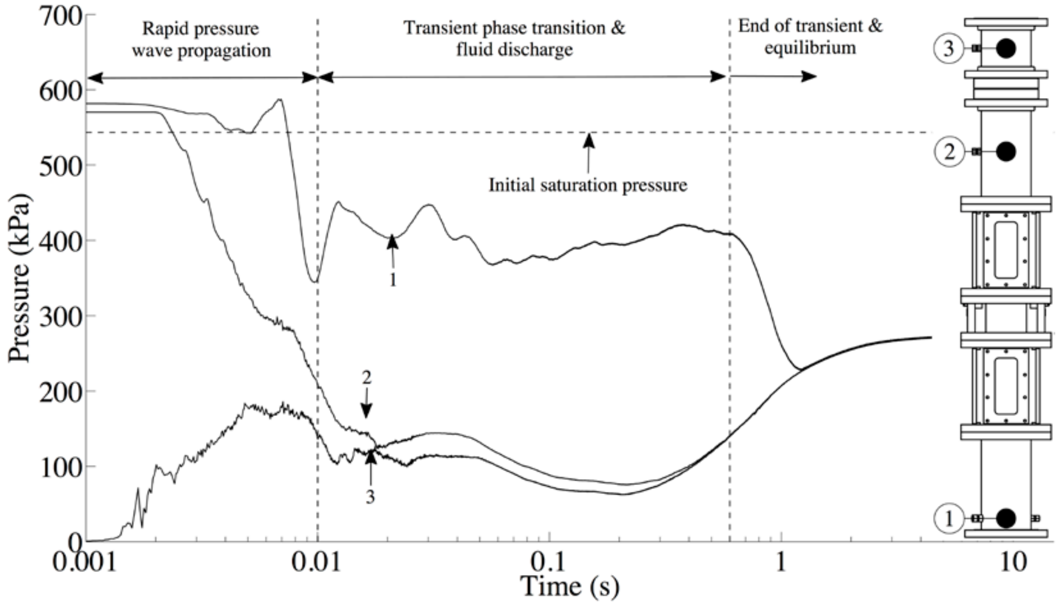

Figure 5-2. Sample transient blowdown pressure measurements (test T08).

vigorous phase transition, in which the ratio of vapour to liquid in the pressure vessel increases rapidly. At the same time, the two-phase fluid mixture is discharged from the outlet above the open rupture disc due to the pressure difference between the pressure vessel and the vacuum tank. At about 600ms, the pressures everywhere in the system begin to equalise at a relatively slower rate, until equilibrium conditions are established, signalling the end of the transient.

When the rupture disc opens, the fluid is suddenly exposed to the downstream vacuum reservoir. The pressure relief is transmitted upstream of the rupture disc (towards the bottom of the pressure vessel) as a rarefaction pressure wave, with the liquid's inertia limiting its initial flow rate. The rapid rates of depressurisation (or pressurisation at location 3) in Fig. 5-2 are typical of large-amplitude pressure waves propagating at acoustic velocity. The time delay to depressurisation does not begin at the pressure measurement points until the rarefaction wave arrives, and can be computed using the speed of sound in the vapour and liquid. This explains the difference seen in times for the depressurisation to begin at the points above and below the tube bundle. The details of the initial transient wave propagation effects are discussed in section 5.3. The small pressure variations measured at location 1 below the tube bundle between 2 – 8ms (before the arrival of the rarefaction pressure wave) are associated with fluid-structural interactions between the stagnant liquid pool and the enclosing steel pipe, caused by the propagation of a stress wave and shock loading along the pipe walls immediately following disc rupture. The stress waves propagate through the steel pipe at about 6100m/s, which is more than 40 times greater than the propagation speed in vapour R-134a. This explains their appearance before sudden depressurisation, and their rapid attenuation following the formation of compressible vapour in the vicinity of the pressure transducer.

At about 7ms, the liquid pressure at this point drops to a value lower than its initial saturation pressure of 543kPa. The rapidly decreasing liquid pressure is halted by the initiation of boiling at about 9ms. The ensuing phase transition results in the vigorous generation of vapour and produces a recovery in the pressure amplitude, at about 0.2s, to a value that remains substantially lower than the initial saturation pressure. The two-phase fluid mixture simultaneously flashes and discharges through the tube bundle with the pressure difference across the bundle remaining nearly constant until about 0.4s into the blowdown. As equilibrium conditions are approached, the void fraction in the pressure vessel continues to increase until the majority of the liquid has boiled off. Once the pressure vessel liquid inventory is depleted, about 1s into the blowdown, the system pressures equalise everywhere and the pressure amplitude is determined by the accumulation of vapour R-134a in the vacuum reservoir.

5.2.1 Description of visual blowdown fluid dynamics

Flow visualisation was acquired for test T08 using two synchronised digital high-speed cameras. The images were taken through the sight windows above and below the test section (refer to Fig. 3-1), and were synchronised to the data acquisition system. By obtaining high-speed images of the transient flow, the behaviour of the fluid mixture as it enters and exits the tube bundle can be monitored. This provides valuable insights into the mechanisms of phase transition, vapour growth, and transient fluid regime development. By relating the visual phenomena to the physical measurements, a fundamental understanding of the governing flow phenomena is developed. In Figs. 5-3 and 5-4, high-speed image sequences of the transient two-phase flow pattern development are shown above and below the tube bundle, respectively.

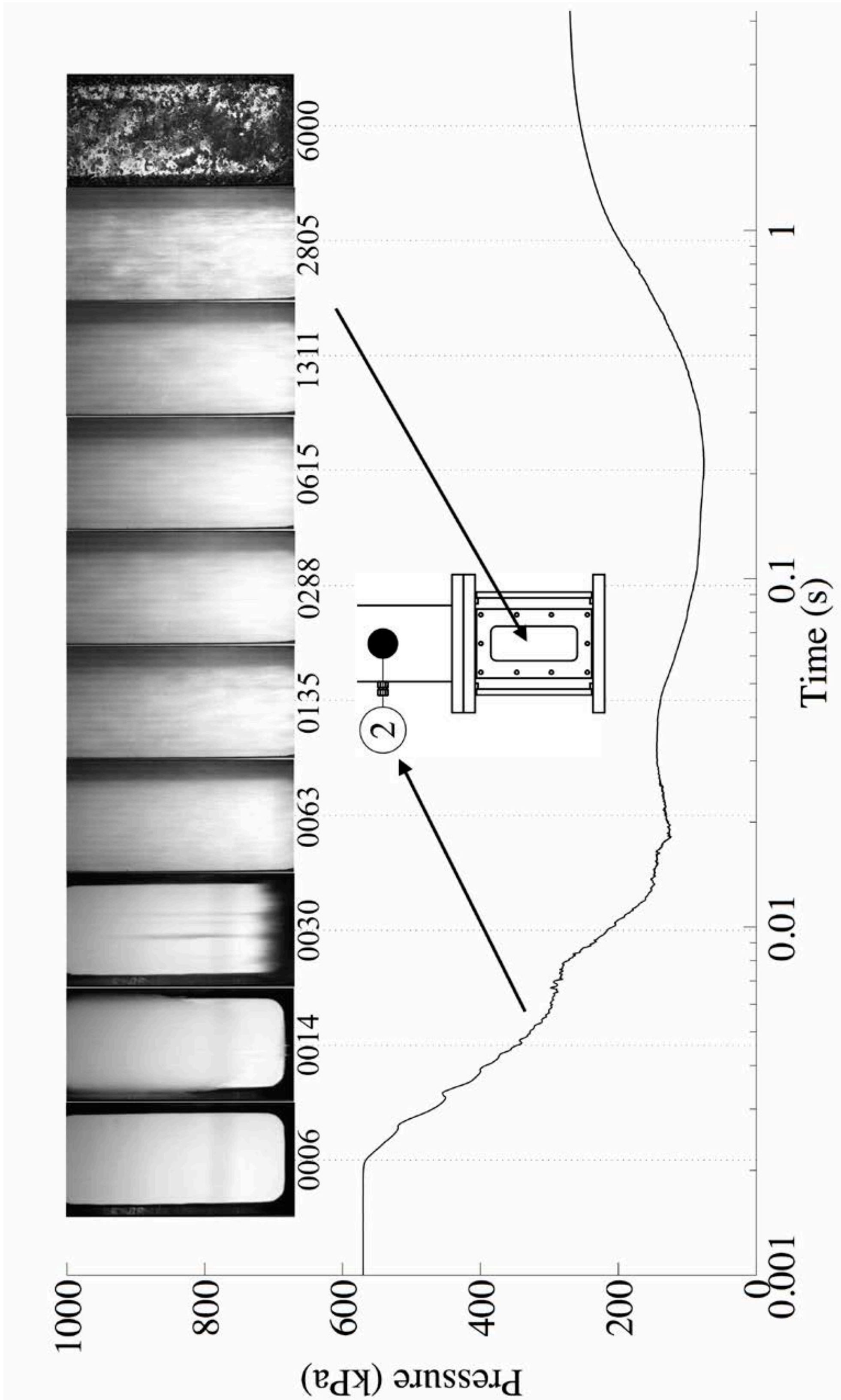

Figure 5-3. Synchronised high-speed images and transient pressure at location 2 (test T08).

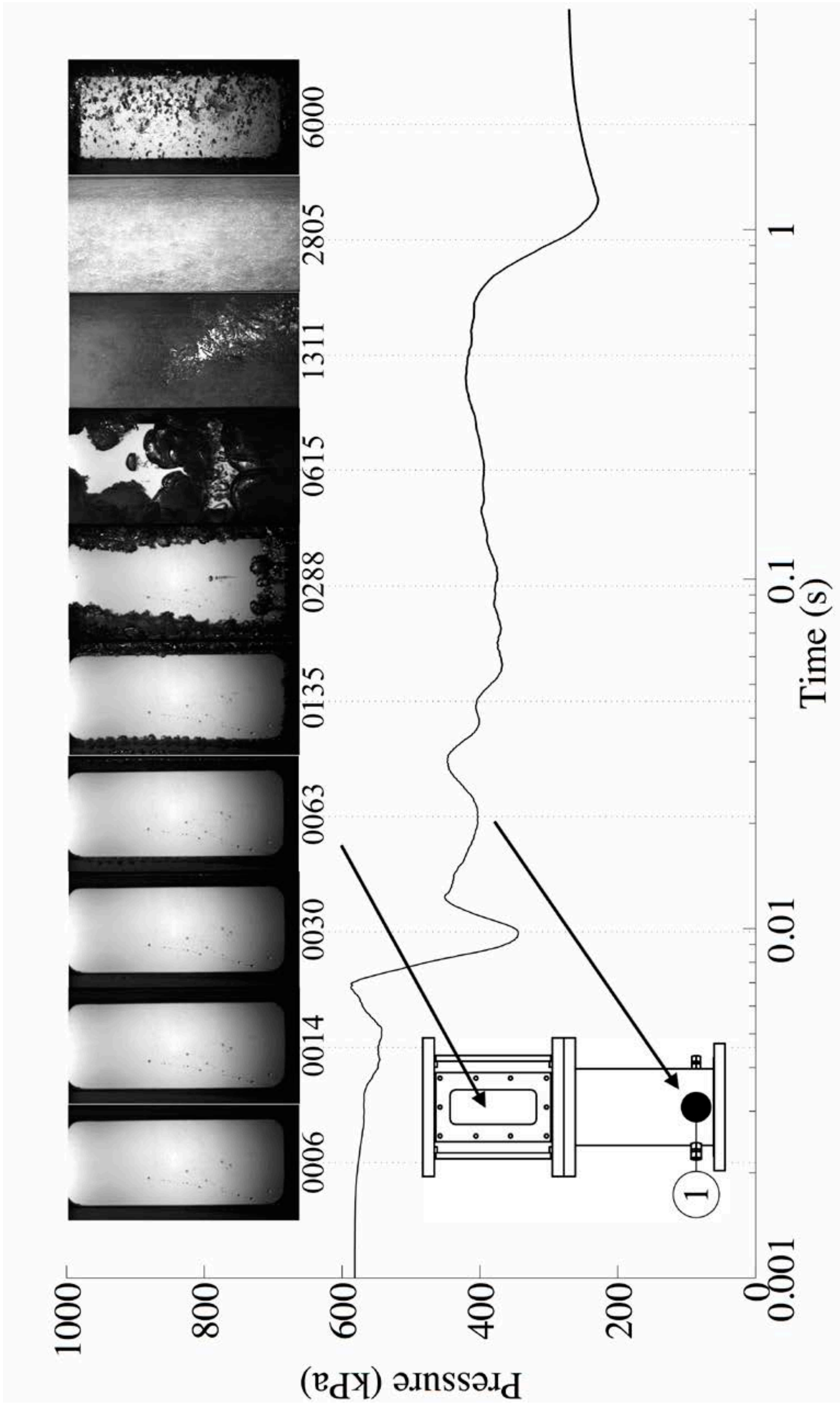

Figure 5-4. Synchronised high-speed images and transient pressure at location 1 (test T08).

The images are presented along with the corresponding transient pressures measured at the transducer locations. Figure 5-3 shows the saturated vapour region, which correlates with the pressure measurement at location 2. Figure 5-4 shows the subcooled liquid domain, compared to the pressure at location 1. Figures 5-3 and 5-4 depict the main phenomena observed in the majority of the two-phase blowdown tests, starting from the opening of the rupture disc to the completion of the transient. In both Figs. 5-3 and 5-4, the time $t = 0$ refers to the instant when the rupture disc opens, which is set to frame 0000. At a filming rate of 3000fps, each increment of 3 frames represents 1ms of elapsed time. 500W halogen spotlights were used to direct light into the sight windows through the fully transparent liquid and vapour media and into the camera lenses. The liquid surface in test T08 lies between the two windows and the images initially show the regions fully occupied by pressurised vapour and liquid in Figs. 5-3 and 5-4 respectively. In some tests, the liquid level is visible through the window and the opaque liquid surface interface appears as a thin dark line in the captured images. Once phase transition begins, the generated liquid-vapour interfaces block the light from being transmitted through the windows, casting a shadow that appears as a darker shade than the surrounding lit regions in the high-speed photographs. An additional light source was used to provide front lighting, which reflects off the liquid-vapour interfaces back into the lenses. This must be dim in order not to saturate the image brightness.

Between frames 0006 and 0014 in Fig. 5-3 (t = 2 – 4.7ms), the rarefaction wave originating at the rupture disc passes the viewing section downwards towards the base of the pressure vessel, leaving condensed vapour in its wake. This explains the faintly discernible blurriness at the bottom of frame 0014, caused by condensed liquid droplets. In frame 0030 (t = 10ms) the expanding two-phase mixture accelerating upwards appears at the bottom of the frame. By frame 0063 (t = 21ms), the two-phase mixture covers the entire viewing area. As the transient progresses from t = 45 to t = 437ms (frames 0135 to 1311), the two-phase mixture concentration is substantially increased, and a high void fraction can be seen in the corresponding images. The flow patterns during these stages are difficult to distinguish due to the significant amount of light blocked by the generation of vapour, which degrades the image quality. The images seem to show a uniform distribution of homogeneous two-phase fluid. Despite the photographic challenges associated with the extremely rapid nature of the transient and the significant change in the void fraction during this time (from 0% to 100% in about 1 second), viewing the images as an animated film provides valuable information about the flow velocity and the heterogeneity or uniformity of the two-phase distribution. By frame 2805 (*t* = 935ms) the flow is decelerating. In frame 6000, 2 seconds after blowdown initiation, the image shows films of liquid on the glass surface and small droplets falling by gravity at the end of the transient once the pressures in the reservoir have equalised.

In Fig. 5-4, there is no visible change in the liquid from the original conditions up until frame 0030 (*t* = 10ms) despite that the pressure has been reduced by the passing rarefaction wave. In frame 0063 (*t* = 21ms) vapour being generated towards the right of the image begins to enter the viewing area. The bubble growth is much more visible in frame 0135 (*t* = 45ms), and in frame 0288 (*t* = 96ms) the bubbles continue to occupy a larger portion of the viewing area. In addition, rising bubbles originating from below the window appear at the bottom of the image. The darker regions in these images represent the expanding two-phase plumes. The images in the first 200ms of the transient show vigorous liquid boiling creating densely populated vapour clouds that rise and expand simultaneously. Similar to the previous set of images shown in Fig. 5-3, the darker regions in Fig. 5-4 indicate a high interfacial density between the two phases due to phase transition. This is clearly visible in frame 0615 (*t* = 205ms) in which the bottom half of the image is highly populated with bubbles and vaporised plumes. At the same time, the liquid bulk in the top half of the image appears to remain largely unperturbed. By frame 1311 (*t* = 437ms) the interfacial density increases to the extent that most of the light transmitted through the window is blocked. The flow continues to develop non-uniformly as it discharges upwards and in frame 2805 (*t* = 935ms) the image is brighter, indicating that most of the liquid has boiled off by this time. The transient is complete in frame 6000 (*t* = 2s) and falling liquid is visible on the glass surface as well as in the centre of the flow area cross-section.

The velocity of distinct fluid interfaces such as dispersed bubbles or entrained droplets can be estimated during the transient by digitally imposing a scaled grid on the viewing area and visually tracing the time-stamped flow development. Figure 5-5 presents an example of this methodology. The image sequence in Fig. 5-5 shows a rising bubble shortly after blowdown initiation, filmed during test T02 through the window below the test section. The grid super-imposed on the images is 10mm square, and the frames are shown in 10ms time-steps. The darker portions on the sides represent expanding two-phase plumes, and the inside lighter region

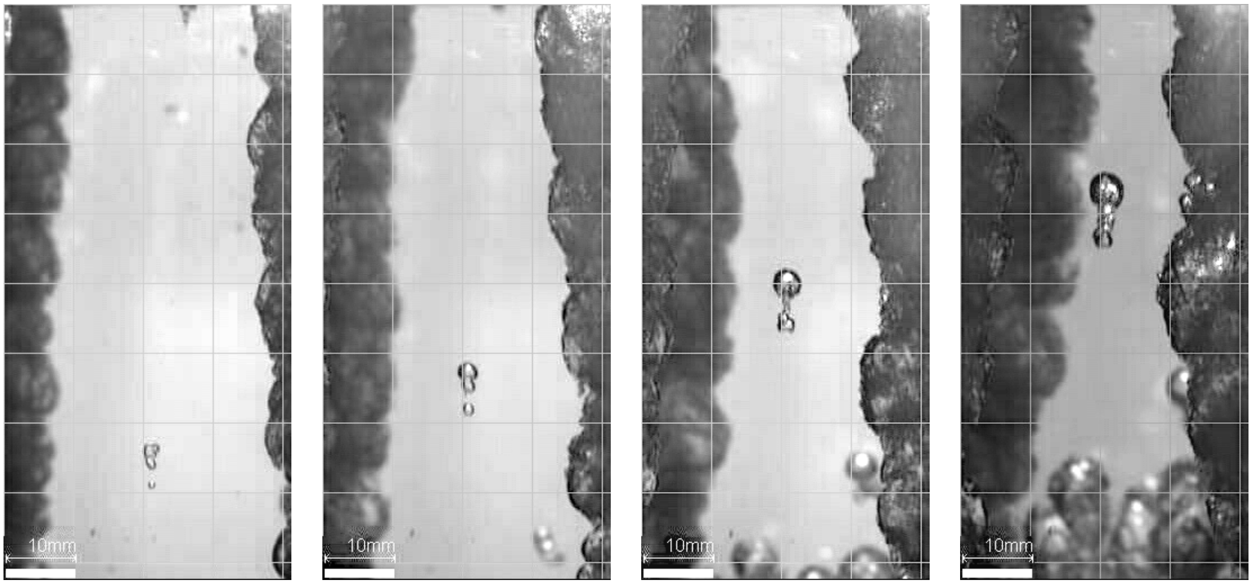

Figure 5-5. High-speed images of rising bubble for estimating velocity (10ms time-step, test T02).

is the relatively undisturbed liquid. The rising vapour bubbles in the centre of the images accelerate upwards as their volume expands. The average bubble velocity can be estimated from the distance covered, about 35mm, in the elapsed time of 30ms. The estimated average rising bubble velocity is about 1.2m/s.

By employing this technique, the images can be used to evaluate the transient flow velocity below and above the tube bundle. The two-phase fluid velocity is related to the pressure drop across the tube bundle, and its evaluation assists in developing an understanding of the two-phase transient tube bundle loading. For illustration purposes, Fig. 5-6 shows the flashing two-phase front discharging from the tube bundle in test T04 immediately after the initial rarefaction wave has passed. A 10mm square grid is super-imposed on the images, which are provided in 2.7ms increments. The flashing two-phase mixture downstream of the tube bundle enters the bottom of the image in the second frame and travels a distance of about 75mm in 8ms, with an estimated average velocity of 9.4m/s. By monitoring the fluid velocities in the images, the observed flow regime development in the high-speed visualisations can be related to the transient measurements. This is useful for developing a fundamental interpretation of the governing phenomena during transient two-phase tube loading.

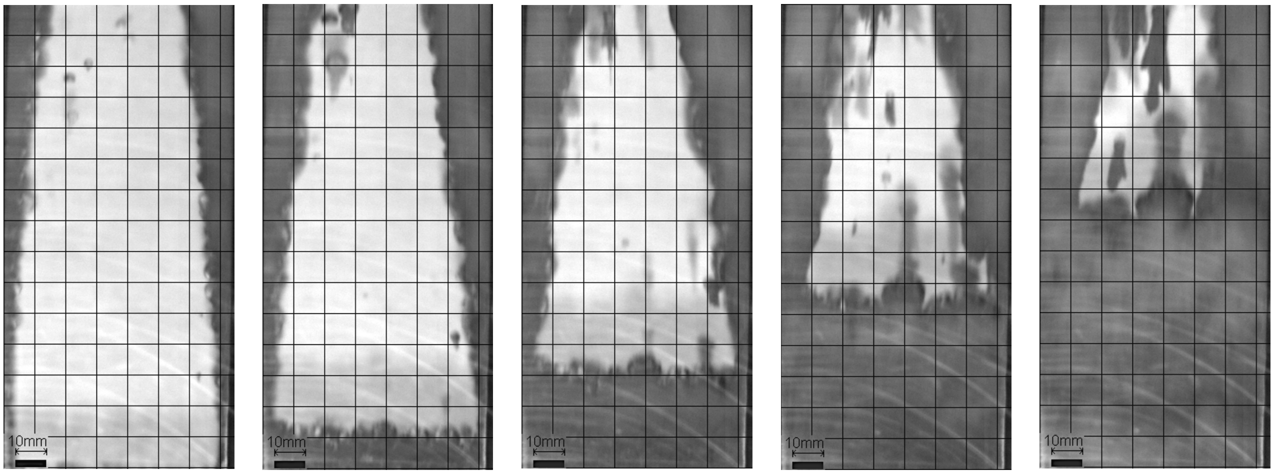

Figure 5-6. Flashing two-phase mixture front downstream of the tube bundle (2.7ms time-step, test T04).

5.3 Transient pressure wave propagation

Under steady-state conditions, before blowdown, the reservoir contains distinct liquid and vapor domains, the interface being the free liquid surface. When the rupture disc opens, fluid depressurisation is initiated and the pressure relief is transmitted along the pressure vessel as a rarefaction wave, propagating away from the rupture disc breakage location towards the bottom of the pressure vessel. The wave initially propagates through the compressed saturated vapour region below the rupture disc. Following the arrival of the rarefaction wave at the liquid surface, it propagates through pressurised subcooled liquid. The transmission of the wave through this liquid-vapour interface is accompanied by complex partial wave reflection phenomena, which are quickly attenuated.

Figure 5-7 shows a set of pressure signals obtained for tests T05 and T07 immediately following rupture, at locations 1 and 2 (refer to Fig. 3-1). In both tests, the rarefaction wave travels a distance of 211mm from the rupture disc to the measurement station at location 2 under similar thermodynamic conditions (saturated vapour). The wave propagation time of 1.6ms is therefore the same for both tests at this location. The steepness of the rarefaction wave is identical, confirming the uniformity and reproducibility of the rupture disc opening behaviour. In the case of single-phase compressible gas, the propagation velocities of compression and decompression waves are the same, and can be calculated from Eq. (4-9). However, a decompressive disturbance in saturated vapour may result in liquid condensation, which affects the wave front propagation velocity. The theoretical speed of sound in vapour R-134a at standard temperature conditions is 145m/s, and the measured velocity in the present tests, verified by calculated timings shown in Fig. 5-7, is 135m/s. The phase change accompanying the rarefaction wave propagation through saturated vapour results in a slightly reduced acoustic velocity.

The respective liquid level heights from the bottom of the reservoir are 650mm and 129mm in tests T05 and T07. In test T05, the rarefaction wave travels 612mm through vapour and 612mm through liquid before arriving at location 1, whereas in test T07, the propagation occurs through 1133mm of vapour and 91mm of liquid. The speed of sound in liquid R-134a is 542m/s, which is about 4 times faster than in vapour. Therefore the rarefaction wave takes longer to arrive at location 1 in test T07, when the liquid level is lower, compared to test T05. Interestingly, the tube bundle does not seem to have any discernible influence on the propagation of the rarefaction waves.

The condensation effect caused by the propagation of the rarefaction wave through the saturated vapour domain is observable in the high-speed flow visualisations. Figure 5-8 shows a high-speed image sequence taken through the upper window in test T06 in which the

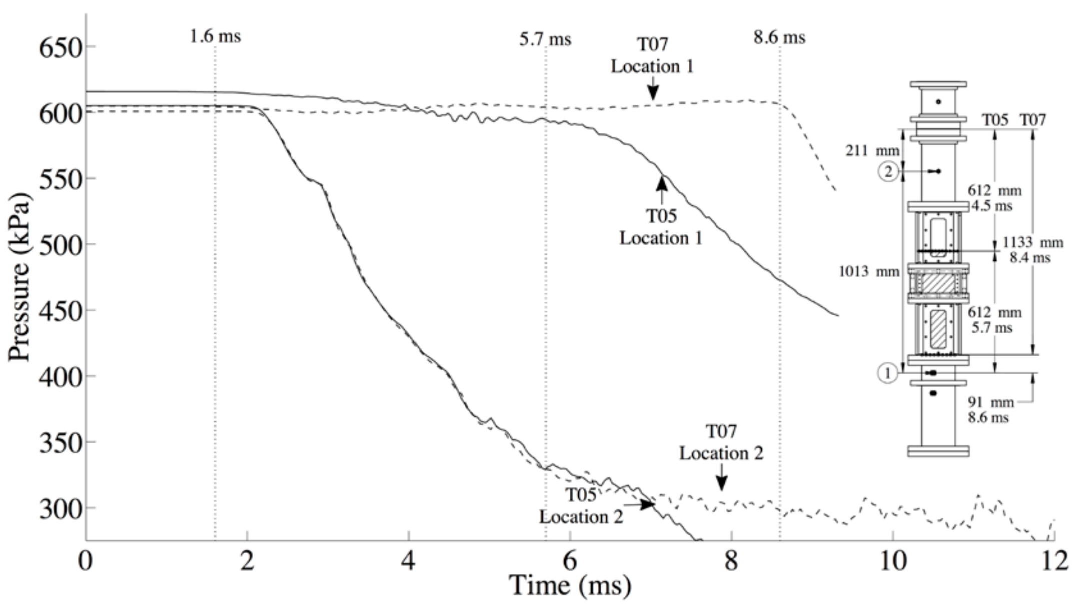

Figure 5-7. Rarefaction wave propagation comparison (tests T05 & T07).

condensation wave front is traced, providing a reasonable estimate of the rarefaction wave position with respect to time. In the images, the ‘condensation’ wave front travels a distance of about 190mm in 4 frames, which is 1.33ms. The corresponding estimated speed of the rarefaction wave traced in the images is about 140m/s. This estimated velocity is within 4% of the 135m/s velocity computed from the pressure signals, which confirms the quality of the data, as well as the adequacy of the high-speed images for obtaining quantitative velocity estimates.

The speed of sound in a two-phase medium cannot be determined by simple thermodynamic state properties as in single-phase fluids. In fact, analytical descriptions of wave propagation phenomena in two-phase flows do not exist, apart from the simplified extreme cases of perfect homogeneous equilibrium, or ‘frozen’ conditions, where the mass, momentum, and energy transfer terms between the two phases disappear [22]. In a two-phase mixture, the speed of sound depends on the flow regime, the frequency of the pressure wave, whether it is a pulse or continuous wave, and the nature of the disturbance (compressive or decompressive). The computed velocity estimates in Fig. 5-7 are therefore only valid for a brief period of time directly following disc rupture, during which the fluid states are in single-phase. The rapid dynamic vapour generation that ensues substantially changes the speed of sound. The sound velocity is typically lower in a two-phase mixture than in a pure liquid or vapour phase.

A common observation made in blowdown tests with more than 10% of the pressure vessel filled with liquid R-134a was the almost immediate appearance of oscillations after disc rupture in the pressure signals at the lowermost measurement station. Figure 5-9 shows pressure fluctuations measured in three separate tests, beginning about 1ms after the rupture disc has

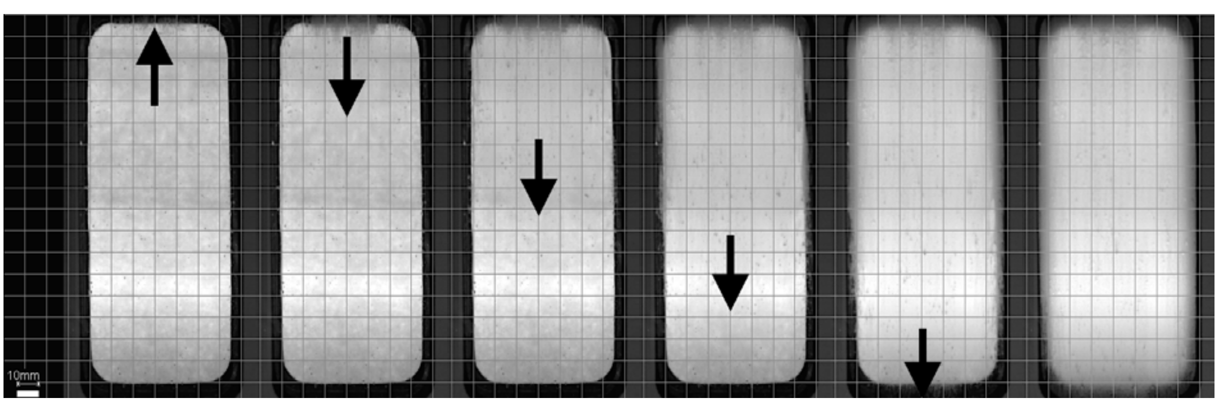

Figure 5-8. Propagating ‘condensation’ wave front (0.33ms time-step, test T06).

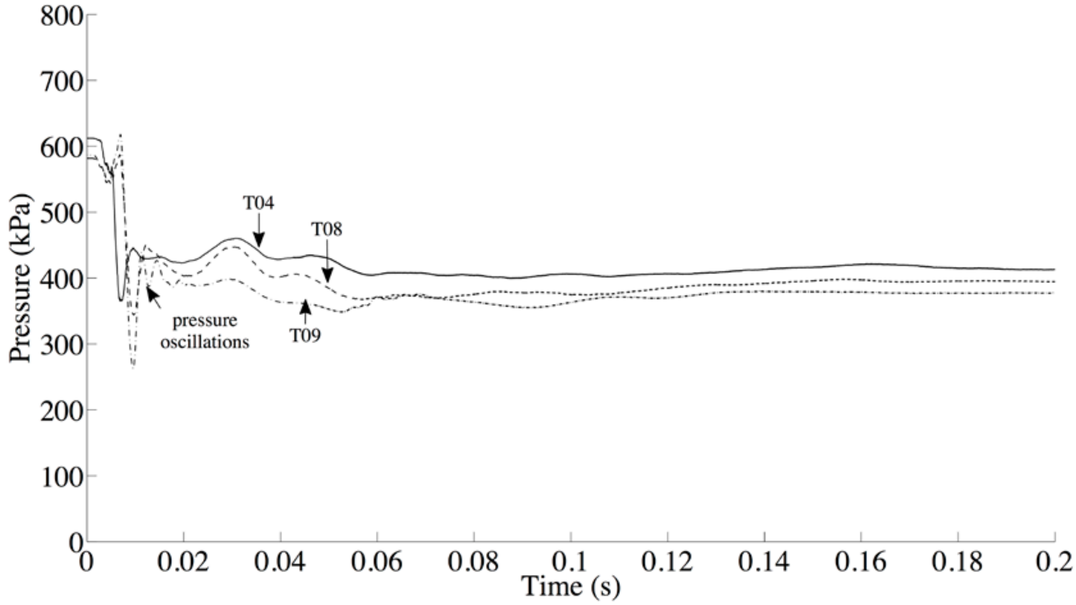

Figure 5-9. Rapid pressure fluctuations at location 1 (tests T04, T08, & T09).

opened. At this point in time, the rarefaction wave has only travelled about 140mm away from the rupture disc, and has not yet arrived at the measurement location. The sound velocity in the steel pipes of about 6100m/s is more than 40 times faster than that in vapour R-134a. Therefore, stress waves induced in the pipe by the opening of the rupture disc propagate along the pipe walls well ahead of the pressure waves in the fluid. An analysis of the shock loading effects on the reservoir is provided in Appendix B. It seems that the shock loading produces pressure disturbances in the liquid R-134a, which give rise to the fluctuations observed in the pressure transducer signals 5 – 15ms after rupture. Following the propagation of the initial rarefaction wave along the length of the pipe reservoir, liquid boiling increases the compressibility of the R-134a. The vapour phase growth is very rapid, and develops at the pipe walls, near the pressure transducers (refer to Fig. 5-4). This increase in fluid compressibility results in a rapid attenuation of the pressure fluctuations, which explains the broadening of the oscillations between 15 – 45ms in Fig. 5-9, and their subsequent disappearance shortly afterwards. The fluctuations do not affect the transient pressure amplitudes that follow, which are mainly influenced by the reservoir volume, the amount of liquid fill, the rate of phase change and vapour growth, and the two-phase discharge rate through the test section.

5.4 Vapour choking

When the rupture disc opens, the pressure vessel contains separate liquid and vapour phase domains and the initial discharge through the rupture disc is single-phase vapour R-134a. Since the pressure ratio between the pressure vessel and the downstream reservoir (initially in a vacuum) is very high, the accelerating vapour phase rapidly becomes choked at the pressurised reservoir exit. Flow choking occurs when the fluid velocity reaches the speed of sound, at which point small flow disturbances cannot propagate upstream and any further reduction in downstream pressure has no effect on the flow rate. When choking occurs, the ratio of the pressure at the choked plane, p_c, to the upstream pressure, p_0, is defined as the critical pressure ratio. For an isentropic single-phase flow, the critical pressure ratio is given by Eq. (5-3),

$$\frac{p_c}{p_0} = \left(\frac{2}{\gamma+1}\right)^{\frac{\gamma}{\gamma-1}}, \tag{5-3}$$

where γ is the specific heat ratio. For vapour R-134a at 20°C, γ = 1.2, and the critical pressure ratio calculated from Eq. (5-3) is 0.564. Therefore, the single-phase vapour R-134a discharge at 20°C will be choked as long as the upstream pressure is at least 1.8 times the downstream pressure. The speed of sound of vapour R-134a at 20°C is 145m/s, and the maximum mass flux through the rupture disc flow area, G, is therefore about 4,205kg/m^2-s.

Figure 5-10 shows transient pressure measurements obtained in test T07 at locations 2 and 3, upstream and downstream of the rupture disc respectively (refer to Fig. 3-1). Test T07 was carried out with 10% of the pressure vessel filled with liquid R-134a and all of the tubes removed from the test section. The initial liquid and vapour pressures and temperatures were 604.7kPa and 17.3°C, and 600.7kPa and 19.7°C respectively. In the first 12 milliseconds, the pressure upstream of the disc drops to about 300kPa and the pressure downstream of the disc increases from vacuum to about 170kPa. This gives a pressure ratio of 0.567, sufficiently close to the theoretical critical pressure ratio of 0.564 computed from Eq. (5-3) to suggest that the single-phase vapour R-134a discharge is choked during this time. This also explains why the pressure difference remains approximately the same for about 4ms. Both pressures then decrease, indicating that the discharge flow transitions to subsonic at about 12ms.

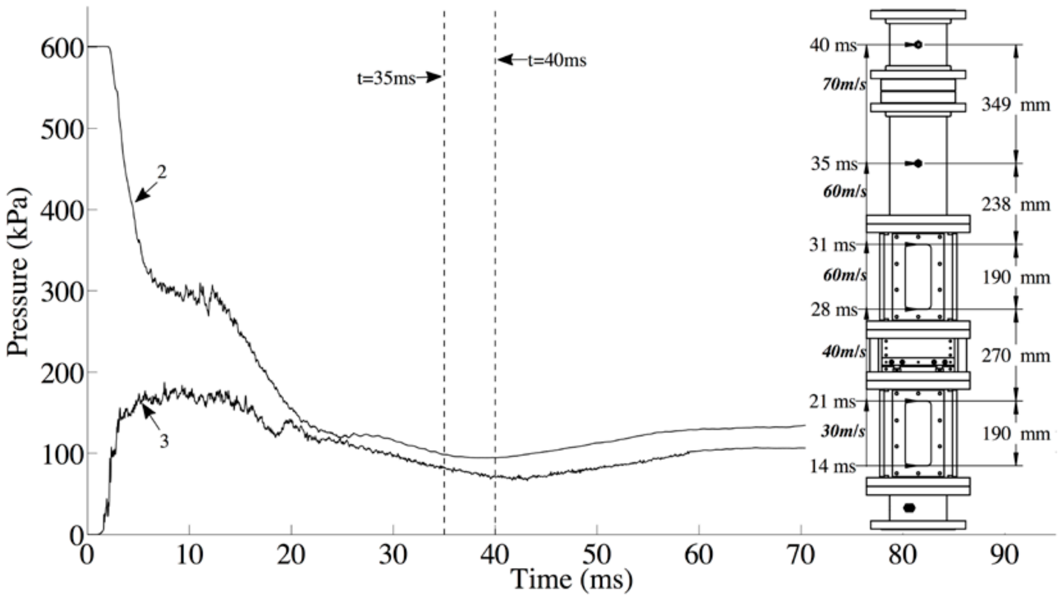

Figure 5-10. Pressure measurements at locations 2 & 3 (test T07).

The pressure continues decreasing at location 2 until about 35ms, and at location 3 until about 40ms, after which both pressures begin to climb at a similar rate. The increase in pressure is due to the arrival of the accelerating two-phase fluid mixture originating at the liquid level surface. A high-speed image sequence showing the acceleration of the flashing two-phase mixture is shown in Fig. 5-11. The top images show the two-phase front propagation at the lower window 14 – 21ms after rupture, and the bottom images show the front propagation at the upper window 29 – 32ms after rupture. The position of the flashing front with respect to time, as determined from the high-speed images and the pressure transducer measurements, is included in Fig. 5-10 on the right, with estimated average velocities at each successive segment.

The top image sequence in Fig. 5-11(a) shows the two-phase front propagating upwards at the lower window. The initial liquid surface is just below the window frame. In Fig. 5-11(b), the first frame shows two separate two-phase mixture concentrations. The top half of the frame shows a liquid-vapour mixture that had originated at the transition section between the windows due to steady-state condensation on the steel walls before disc rupture. At the bottom of the frame, the two-phase front that had originated at the liquid surface, shown in Fig. 5-11(a), is seen entering the viewing area. The velocity of the flashing two-phase mixture increases as it

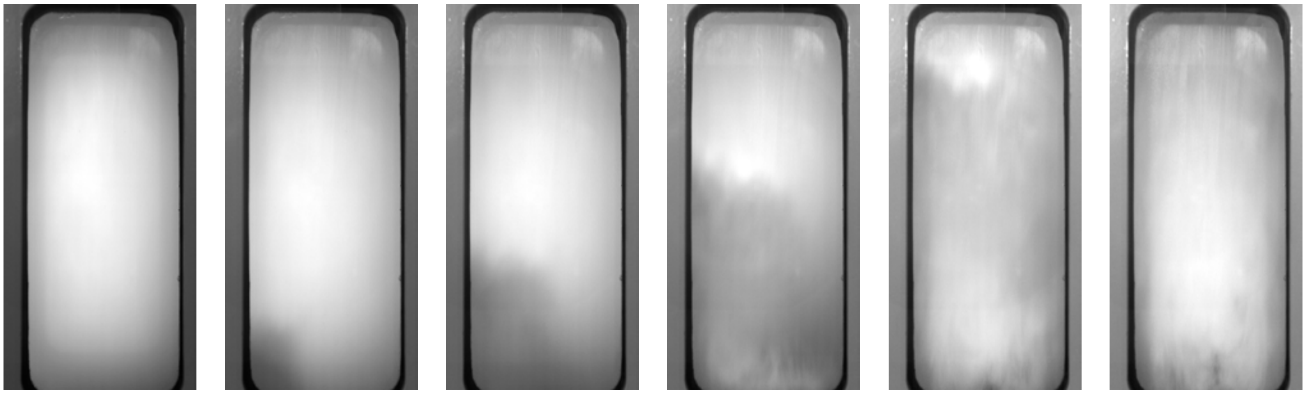

(a) Lower window: *t*=13.67-22ms (1.67ms time-step).

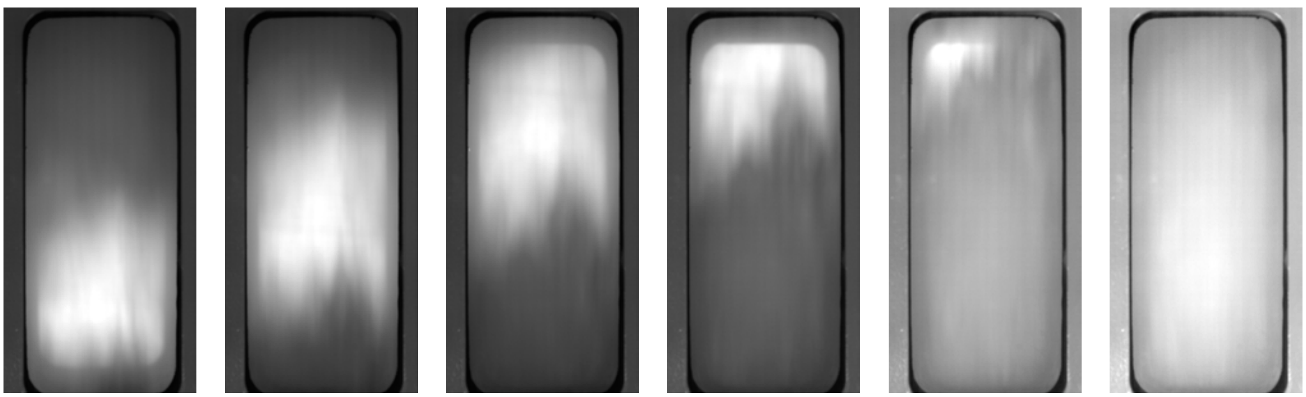

(b) Upper window, *t*=27.67-31ms (0.67ms time-step).

Figure 5-11. High-speed images of flashing two-phase front (test T07): (a) lower window, (b) upper window.

accelerates towards the vacuum reservoir. The average velocity is about 30m/s at the lower window, about 60m/s at the upper window, and about 70m/s discharging into the downstream vacuum reservoir.

Choked flow in single-phase compressible fluids has been widely investigated and is well understood. The introduction of a second phase however, substantially increases the phenomenon's complexity. There is no theoretical model available that completely describes all aspects of two-phase critical flow. While a basic understanding of the main flow mechanisms exists, complex physical behaviour at the liquid-vapour interfaces makes the accurate prediction of two-phase critical flow a difficult task [23]. When a flowing two-phase mixture flashes, the vapour generated reduces the average density of the fluid, thereby reducing the overall mass flow rate. The local speed of sound is also influenced substantially, as discussed in section 5.3. While the choked and sonic velocities are equal in compressible single-phase flows, the presence of critical flow conditions in a two-phase mixture does not necessarily indicate that the maximum choked mass flow rate of the mixture has been attained. The presence of significant interfacial heat and mass transfer processes can produce maximum mass discharge at subsonic flow conditions [22]. The simplest available model for predicting two-phase critical flow is the Homogeneous Equilibrium Model (HEM), which assumes that the two phases are always in mechanical (no-slip) and thermal (no temperature difference) equilibrium.

For choked two-phase flow in short pipes, the liquid and vapour phase velocities do not have sufficient time to equalise, and the slip effects result in an under-prediction of the choked flow velocity by the HEM. Conversely, the assumption of thermal equilibrium can greatly overestimate the density of a two-phase mixture at the discharge plane, and the net effect is that the HEM over-estimates the choked flow rate for large discharge areas [24]. The HEM produces reasonable choked flow rate predictions in long pipes with small discharge areas, in which the assumptions of mechanical and thermal equilibrium are justified [16, 25].

An analysis of the accelerating two-phase mixture in test T08 is presented in Fig. 5-12. The initial liquid surface is inside the tube bundle, in which 6 tube rows were mounted. Similar to Fig. 5-10, the ratio between the initial pressures of 170kPa and 300kPa in Fig. 5-12 indicates that single-phase choked flow conditions exist at discharge during this time. The transition to subsonic discharge occurs at about 7ms. Figure 5-12 also shows a high-speed image sequence of the front propagation at the upper window. The fluid enters at the bottom of frame 0030 (t = 10ms) and travels the window length by frame 0041 (t = 13.67ms). The corresponding timing of the arrival of this mixture at the transducers at locations 2 and 3, determined by the rise in pressure, are indicated on Fig. 5-12. The average velocity of the two-phase mixture increases from about 52m/s at the window to about 58m/s at discharge. The velocities are in the same range as those observed from test T07 in Fig. 5-10.

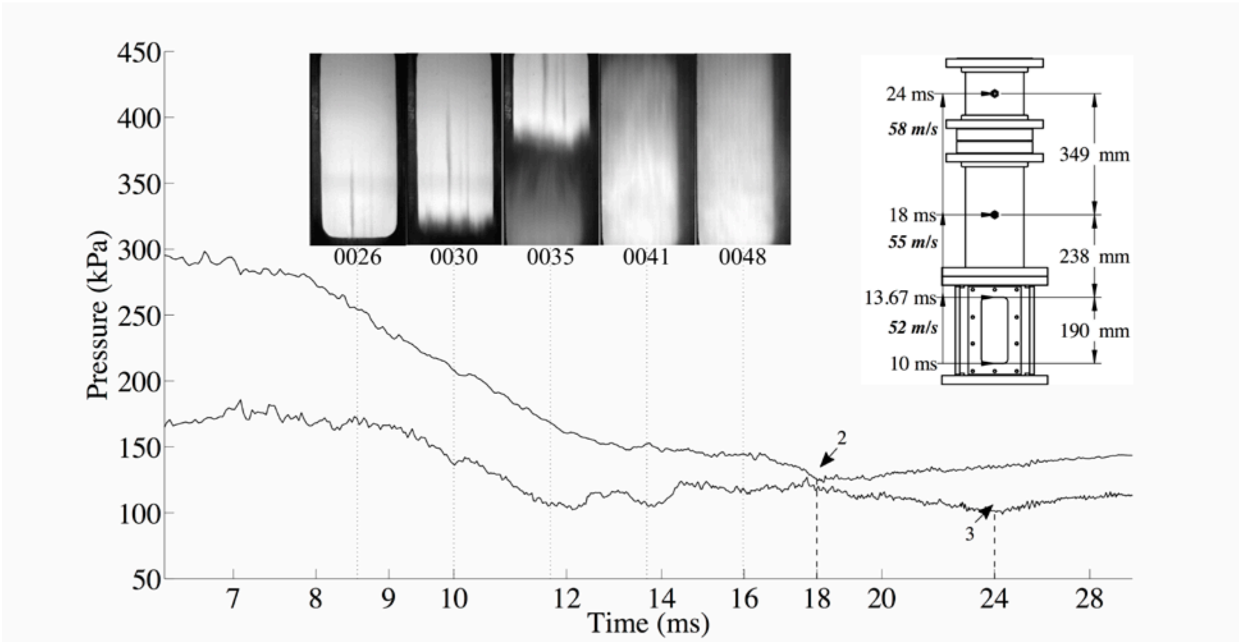

Figure 5-12. Accelerating two-phase mixture front propagation (test T08).

5.5 Phase transition and vapour growth

In all of the tests performed, the pressure measurements in the liquid region (location 1 in Fig. 3-1) indicate that the initial rapid depressurisation of the liquid R-134a proceeds to a minimum pressure that is lower than the initial saturation pressure, as shown in Fig. 5-2. Following the minimum pressure point, the pressure recovers due to the rapid expansion and growth of the vapour phase. Figures 5-2 and 5-4 show that the quasi-steady pressure at location 1 remains fairly constant for about 0.4s in test T08, and that the pressure during this stage is also well below the initial saturation pressure of the liquid. The high-speed flow pattern visualisations provide interesting insights into the physical mechanisms of vapour generation and growth in the liquid immediately following the rapid depressurisation. Figure 5-13 shows an image sequence of the rapid vapour growth seen through the lower window, filmed in test T09 at 3000fps. Also shown is the transient pressure measurement at location 1, below the window. Test T09 was performed with 5 rows of tubes in the test section, and with the liquid R-134a initially at 586.4kPa and 17.7°C.

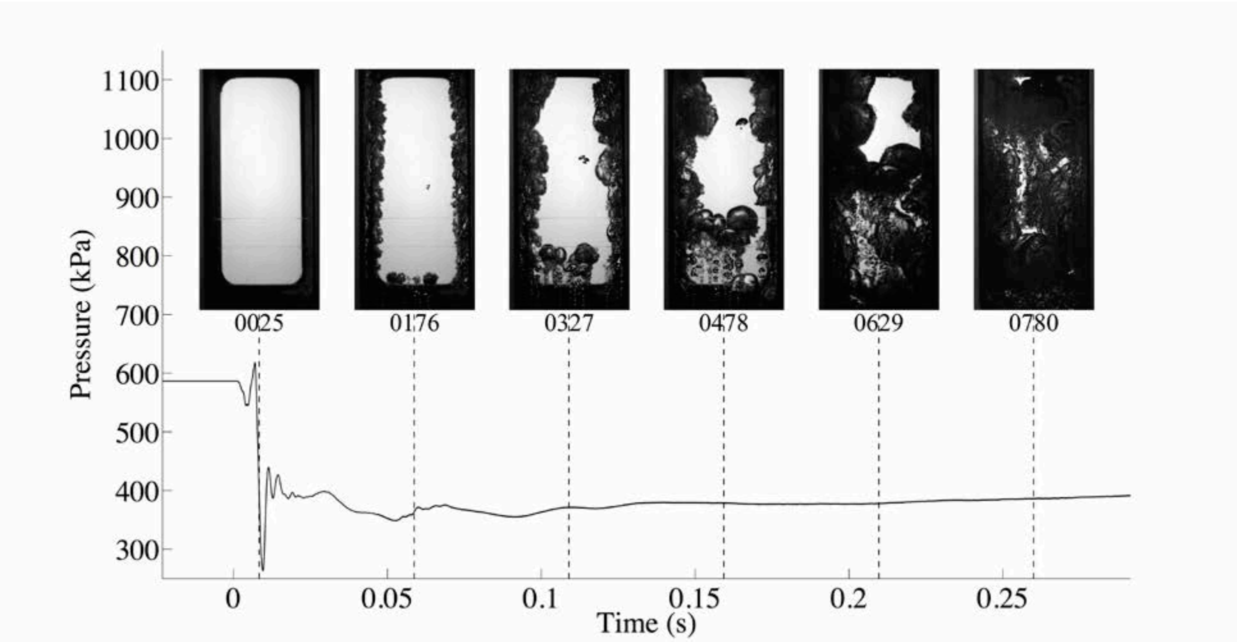

Figure 5-13. High-speed visualisation of vapour growth with corresponding pressure measurement (test T09).

The images in Fig. 5-13 show that the generation of vapour primarily originates at the solid-liquid interfaces on the pipe walls. The expanding bubbles can be seen developing on both sides of the glass frames, which are surrounded by steel, as well as from below the window, in the bottom steel pressure reservoir. The vapour that is generated grows radially into the liquid bulk and rises upwards towards the vacuum reservoir. After about 0.25s the two-phase mixture covers most of the viewing area and the dark regions in frames 0629 and 0780 indicate that the void fraction is significantly increased by about 200ms after blowdown initiation. The study of bubble nucleation in superheated liquids is well established in the field of boiling heat transfer [26]. The mechanisms of bubble nucleation are related to the degree of liquid superheat and are classified into two types: homogeneous and heterogeneous nucleation. In a perfectly homogeneous system, nucleation arises spontaneously in the liquid bulk due to molecular interactions and density fluctuations. Heterogeneous nucleation takes place at liquid-vapour interfaces and liquid-solid boundaries where the bubble nucleation activity is promoted by system imperfections such as cavities in rough surfaces, fluid impurities, dissolved gases, and foreign particles suspended in the liquid.

In Fig. 5-13, a group of small bubbles developing in the liquid bulk is visible near the middle in frames 0176 and 0327. Although the bubbles appear to be nucleating spontaneously in the liquid bulk, such behaviour might possibly result from heterogeneous nucleation on suspended microscopic particles or micro-bubbles of non-condensable foreign gas in the liquid, which would not be distinguishable in the images due to the resolution limitations. The nucleation phenomena shown in Fig. 5-13 were consistently observed in all of the experiments for which high-speed images were taken. The primary bubble activation and growth mechanism appears to be heterogeneous nucleation at the solid metal boundaries. Bubbles growing in the liquid bulk were occasionally observed, which may have originated at microscopic nucleation sites suspended in the liquid, although this cannot be visually confirmed.

The level of superheat required for homogeneous nucleation to occur in a superheated liquid can be determined by considering the kinetics of bubble formation. The kinetic limit of superheat predicts the theoretical point at which spontaneous and random density fluctuations arising from molecular interactions result in the formation of small vapour embryos. By assuming a nucleation rate of vapour nuclei, J, as being representative of ‘spontaneous nucleation’, the temperature at which pure liquid substances undergo homogeneous nucleation can be predicted from Eq. (5-4),

$$J = 1.44\times10^{40}\left[\frac{\rho_l^2\sigma}{M_{mol}^3}\right]^{\frac{1}{2}}\exp\left\{\frac{-1.213\times10^{24}\sigma^3}{T_l\left[\eta p_{sat}\left(T_l\right)-p_l\right]^2}\right\}, \tag{5-4}$$

with the threshold value of J = 10^{12} vapour nuclei per second per cubic centimetre of liquid, where ρ_l is the liquid density, σ is the surface tension, M_{mol} is the molecular weight, T_l is the liquid temperature, $p_{sat}(T_l)$ is the saturation pressure at the liquid temperature, p_l is the liquid pressure, and η is calculated from Eq. (5-5),

$$\eta = \exp\left[\frac{p_l - p_{sat}\left(T_l\right)}{\rho_l R_g T_l}\right], \tag{5-5}$$

where R_g is the ideal gas constant per unit mass. Equation (5-4) can be applied directly to the present R-134a blowdown experimental conditions, as well as secondary side light water in operating steam generators, in order to determine whether there is sufficient liquid superheat available to promote homogeneous bulk nucleation during a sudden depressurisation.

The minimum liquid R-134a pressure observed in test T09 during the initial rapid depressurisation stage shown in Fig. 5-13 is 260kPa. The corresponding R-134a equilibrium saturation temperature is -3°C. In order for homogeneous nucleation to occur at this pressure, the predicted initial liquid R-134a temperature from Eq. (5-4) is 63.5°C. In the present blowdown tests, the initial liquid temperature is no greater than 20°C, which is more than 40°C short of the calculated superheat required. This indicates that the conditions in these experiments were not favourable for homogeneous nucleation in the liquid bulk, which is in agreement with the nucleation patterns observed in Fig. 5-13.

In an operating steam generator, the maximum theoretical initial water superheat possible during blowdown to atmospheric conditions occurs if the liquid pressure is assumed to fall very rapidly to atmospheric pressure, 101.3kPa. By assuming that the pressurised secondary side liquid is suddenly dropped to atmospheric pressure, the required superheated liquid temperature for homogeneous nucleation calculated from Eq. (5-4) is 305°C, which is higher than the typical 260°C operating temperature in the secondary side of a CANDU steam generator. Therefore, even under conservative assumptions, homogeneous nucleation is unlikely to occur in the secondary side of a steam generator during blowdown. These predictions confirm that the current experiments adequately replicate the phenomena that would occur in a full-scale CANDU steam generator during a postulated Main Steam-Line-Break.

The role of surface roughness in nucleate boiling has been widely researched and is well recognised [26]. The surface roughness governs the active nucleation site density at liquid-solid boundaries, which influences the number of bubbles that form during boiling. Blowdown experiments performed from smooth acrylic vessels have shown that the pressures recover to a lower level during the quasi-steady stage compared to steel vessels, and that the durations of the blowdowns are longer [27]. The increased presence of nucleation sites on the steel surfaces promotes a more vigorous phase transition resulting in greater superheat relief, which produces higher pressure amplitudes and shorter blowdown durations. In the present experiments, there was no evidence of nucleation visible on the quartz glass window surfaces. Figure 5-14 shows a high-speed image sequence taken through a vertical glass tube 12.7mm in diameter during a commissioning test performed at a reduced pressure of about 310kPa. The blowdown was initiated using cooled R-134a at a saturation temperature of about 0°C, and the full tests are described in [21]. The initial formation and growth of the vapour phase in the liquid shown in Fig. 5-14 was restricted to a single bubble slug originating at the bottom closed end steel surface, with no nucleation occurring on the polished glass surface.

Another feature occasionally observed in the flow visualisations was nucleation at pre-existing liquid-vapour interfaces. Since a compressed gas accumulator was used to pressurise the R-134a reservoir, vapour pockets of R-134a gas were driven into the pressurised liquid in the pressure vessel through the connecting lines during pressurisation. Figure 5-15 presents a high-speed image sequence filmed through the lower window in test T05. The first couple of frames captured before the opening of the rupture disc show a collection of R-134a bubbles that had been introduced into the pressure vessel through the pressurising line, which subsequently grow rapidly upon blowdown initiation and act as nucleation sites for further bubble generation and growth. Based on such experimental observations, it is expected that a blowdown through the main steam pipe in a commercial steam generator would result in vigorous vapour generation at sizeable surface imperfections in the liquid-metal boundaries, suspended foreign particles in the secondary side water, and any pre-existing liquid-vapour interfaces in the liquid bulk.

In test T06, the liquid surface separating the subcooled liquid domain at the bottom of the reservoir and the saturated vapour domain below the rupture disc was filmed during blowdown in order to monitor the behaviour of the liquid-vapour interface in this region. A sequence of high-speed images acquired from the bottom window during test T06 is shown in Fig. 5-16. In

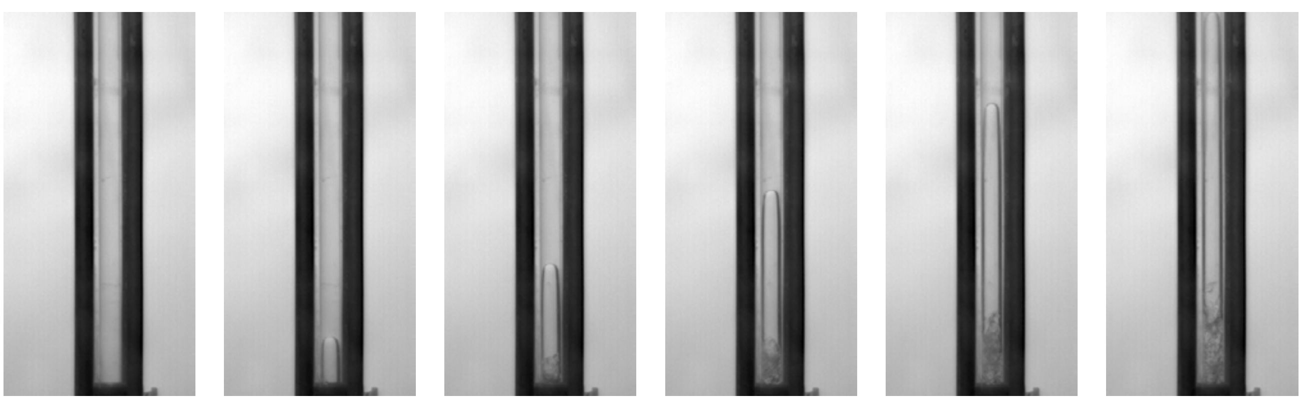

Figure 5-14. Vapour generation during vertical tube blowdown (commissioning test at 310kPa, 78.5ms time-step.

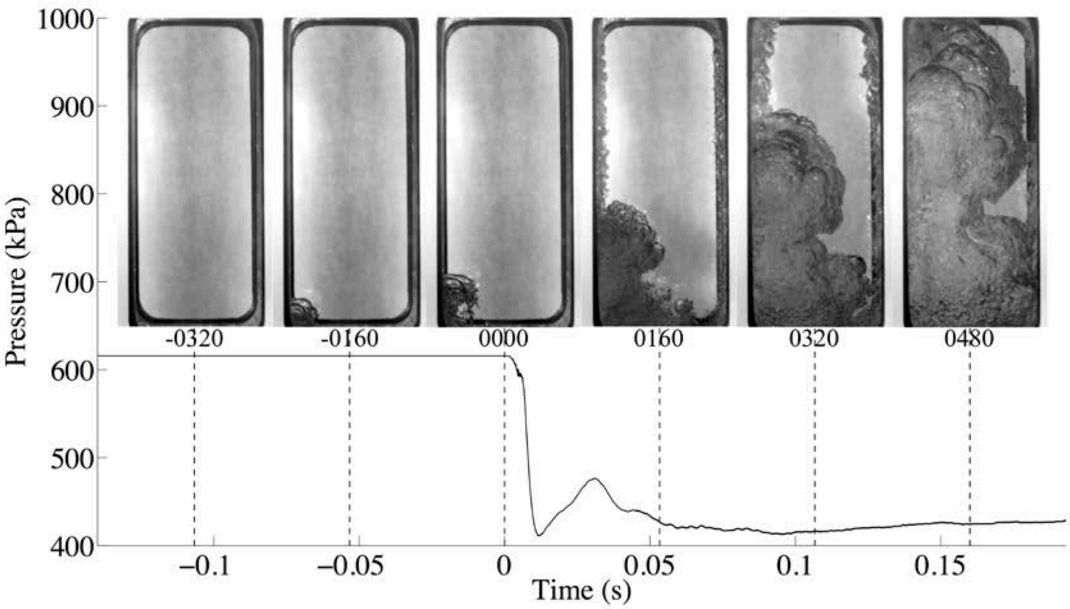

Figure 5-15. High-speed images of pre-existing bubble interfaces acting as nucleation sites (test T05).

frames 0048 and 0064 (t = 16 – 21.3ms), it appears that the liquid remains fairly stationary, and that the expanding vapour phase slips through the liquid free surface towards the top of the reservoir. The two-phase plumes that are formed by the dynamic phase transition apparently accelerate at a much faster rate than the liquid bulk during these initial stages of the vapour growth. This can be explained by the large difference in inertia between the two phases, the vapour density being about 45 times less than the liquid density. The flow pattern above the initial liquid surface position in frames 0064 and 0080 (t = 21.3 – 26.7ms) seems to be a mixed vapour-droplet flow regime, which is well established by the end of the image sequence.

In frame 0048 (t = 16ms) there appears to be some evidence of two-phase flashing at the interface between the liquid and the vapour, which occurs in a narrow zone at the surface. It is possible that turbulence due to agitation, foreign particles such as trapped dust suspended at the liquid surface, or local low pressures caused by complex rarefaction wave-interface interactions produce local conditions at the liquid surface that are conducive to the nucleation of vapour bubbles in this region. Bubbles originating below the window in the steel pipe reservoir can be seen propagating upwards in frames 0064 to 0080 (t = 21.3 – 26.7ms). The rate of vapour generation observed in Fig. 5-16 is extremely rapid. Once the rarefaction wave propagating from

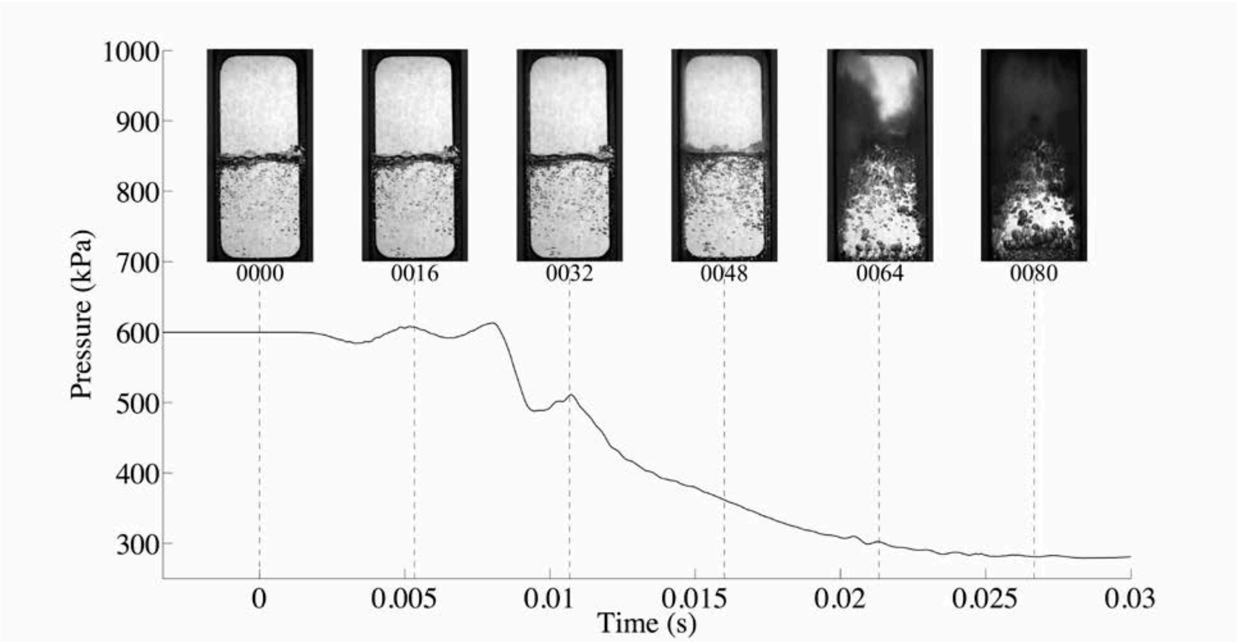

Figure 5-16. Liquid-vapour phase transition visualisation at the liquid surface (5.3ms time-step, test T06).

the rupture disc arrives at the bottom reservoir, it is reflected at the closed end of the pipe reservoir, and propagates back up through the flashing two-phase fluid mixture. Since the compressibility of the R-134a increases rapidly with the rate of vapour formation, the rarefaction wave reflection is rapidly attenuated. This effectively dampens any 'water-hammer' type of pressure oscillations, which explains why there are no strong pressure fluctuations visible in the pressure measurement at the bottom of the reservoir.

The general phase transition features observed in the high-speed flow visualisations can be summarised as follows. Vapour formation begins around the time at which the measured pressure rapidly decreases to a minimum value. The generation of vapour bubbles occurs primarily on the pipe walls and also on liquid-vapour interfaces in the fluid. Some nucleation was observed in the liquid bulk, which is probably due to the presence of suspended microscopic foreign particles or gas bubbles. No vapour nucleation was seen to occur on the glass windows through which the high-speed images were taken. The bubble growth proceeds from the outside walls towards the fluid in the centre of the pressure vessel. The velocity of the flashing vapour phase initially seems to have a vertical component towards the rupture disc at the top, as well as a radial component towards the undisturbed superheated liquid at the centre of the cross-sectional flow area. The growth of the vapour phase proceeds very rapidly, with bubble coalescence producing continuous two-phase plumes that accelerate towards the vacuum reservoir. About 30 – 40ms after disc rupture, the images show a dense two-phase concentration suggestive of a high void fraction, which develops early in the transient blowdowns.

5.6 Quasi-steady blowdown

The rate of the change in pressure during a two-phase blowdown is determined by the net effect of the rate of vapour generation, which produces an increase in pressure due to fluid expansion, and the discharge fluid flow rate, which results in a decrease in pressure. Figure 5-17 compares the transient pressure measured at the bottom measurement station of the pressure vessel for test T06 with 6 rows of tubes and test T03 with no tubes mounted in the test section respectively. Both tests were performed with similar initial liquid levels, 21% and 23% of the pressure vessel filled with liquid R-134a respectively.

The rate of the depressurisation during the initial stage of the transient (t = 0 – 20ms) is very rapid. The restriction to the discharging flow imposed by the tube bundle in test T06 results

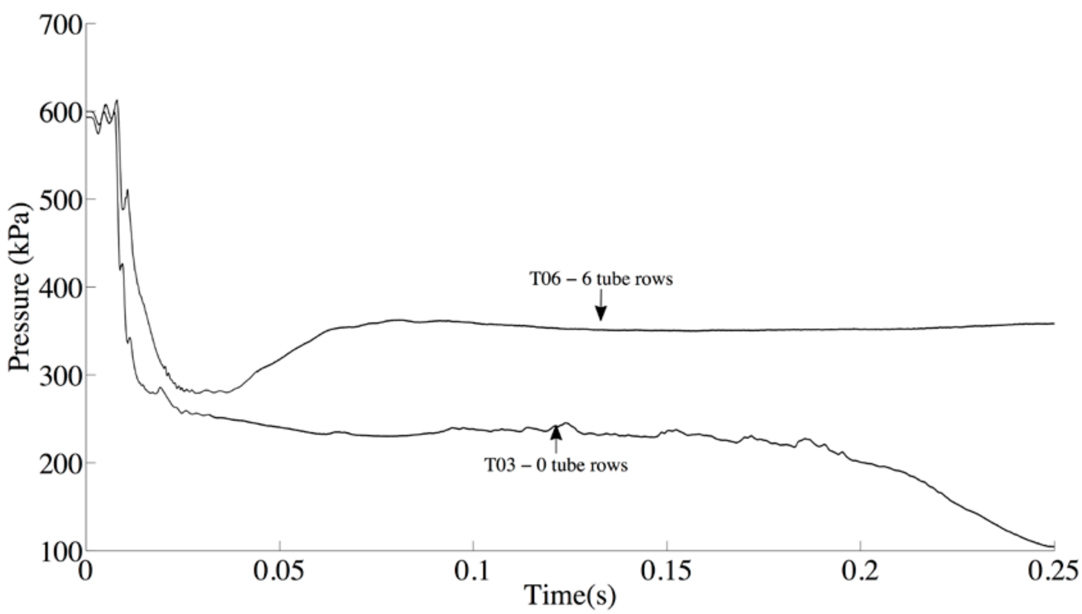

Figure 5-17. Comparison of pressure measurements at location 1 (tests T06 & T07).

in the upstream pressure being a little higher than the case with no tubes. At about 35ms, the generation of vapour and acceleration of the two-phase flow produces an increase in the pressure upstream of the tube bundle until about 75ms, whereupon the upstream pressure remains constant for the next few hundred milliseconds. When there are no tubes mounted in the test section, in test T03, the initial rate of fluid discharge is significantly higher because of the much lower downstream resistance to the flow. As a result, the initial rate of vapour generation cannot be sustained and the more rapid depletion of the liquid inventory results in a monotonically decreasing pressure as well as a much shorter duration of the blowdown.

High-speed flow visualisation images of the final stages of the blowdown transient filmed in test T07 are presented with the pressures measured at locations 1 and 3 in Fig. 5-18. The experiment was performed with 10% of the pressure vessel filled with liquid and no tubes mounted in the test section. The two-phase flow towards the end of the blowdown at t = 0.12 – 0.14s appears to be fairly homogeneous. At t = 0.16s, entrained liquid droplets are visible in the flow, and the droplet concentration is greatly reduced by t = 0.18s as the liquid inventory depletion is basically complete by this time. At this point in the transient, the liquid phase has lost most of its sensible heat. The temperature of the liquid drops sufficiently to limit the occurrence of further flashing and phase transition. As the blowdown transient proceeds towards

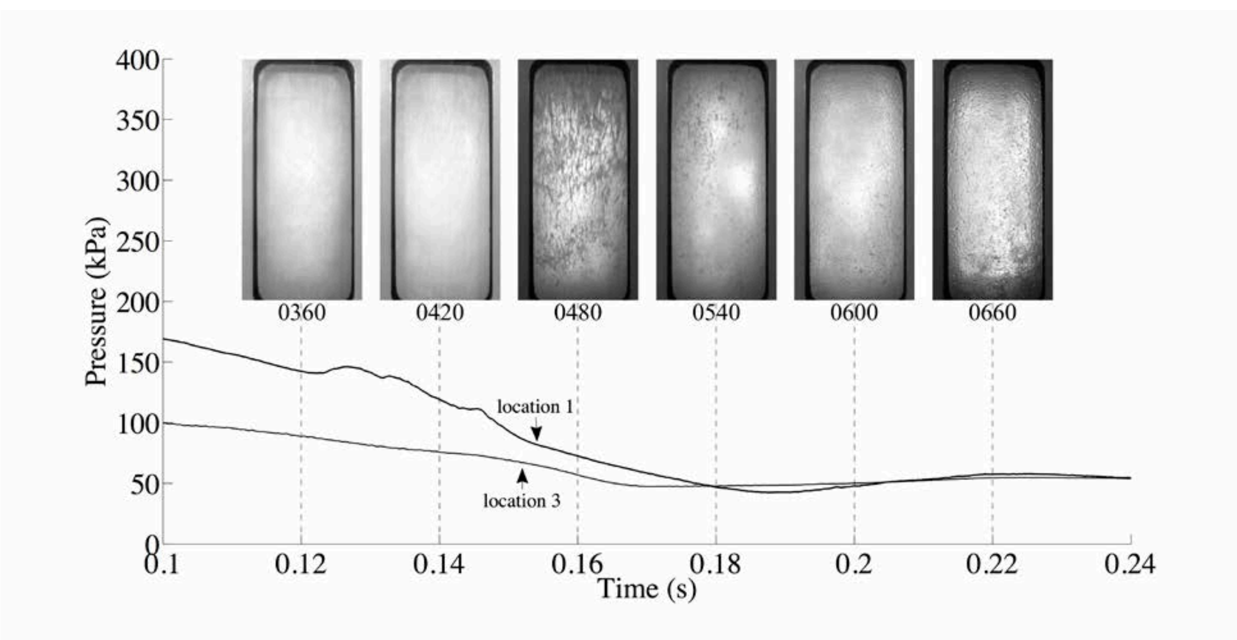

Figure 5-18. High-speed images of end of blowdown transient (20ms time-step, test T07).

completion, equilibrium is established in the reservoir at about t = 0.18s, and relatively slowly evaporating liquid films and droplets are visible on the glass window surface at t = 0.2 – 0.22s.

6. Analysis and discussion of experimental results

The general thermal hydraulic phenomena observed in all of the experiments carried out can be summarised as follows. For the first 15ms or so following the rupture of the disc, the transient is dominated by acoustic phenomena, the specific details of which depend on the initial liquid levels in the pressure vessel. A few milliseconds later, significant liquid flashing to vapour develops and the mass flow rate of the discharging fluid increases rapidly. Subsequently, the upstream pressure appears to stabilise and remain constant for a few hundred milliseconds, which suggests that the two-phase flow is choked during this time. The duration of this quasi-steady discharge segment of the blowdown depends strongly on the initial liquid level in the reservoir and the restriction to the flow imposed by the tube bundle in the test section. The blowdown tapers off when the liquid inventory is reduced sufficiently that the pressure level cannot be maintained by the vapour generation in the pressure vessel.

6.1 Reproducibility of the blowdown results

The measurement reproducibility of the R-134a blowdown tests is shown in Fig. 6-1. The results shown were obtained at locations 1 and 3 (refer to Fig. 3-1) in tests C03, C04, and T06, which were all performed with 6 tube rows in the test section and similar initial conditions. Figure 6-1(a) shows the measurements over the full transient duration and Fig. 6-1(b) shows the initial 100ms of the transient. The reproducibility of the measurements over the full transient duration shown in Fig. 6-1(a) is reasonably good. The rates of the change in pressure are similar and the deviations in the pressure amplitudes during the quasi-steady stage of the blowdowns are small. These slight variations in the measurements may be partly attributed to the differences in the initial conditions. The initial liquid pressures in the tests varied from 569kPa to 600kPa, the initial liquid temperatures varied from 17.6°C to 18.8°C, and the liquid surface heights from the bottom of the pressure vessel ranged from 265mm to 295mm. Although the timings of the transient pressure signals in all three tests are consistent, the amplitude discrepancies between the measurements are greater during the initial stages of the transient, shown in Fig. 6-1(b), and are more pronounced at location 1 than at location 3.

Figure 6-1(b) shows that the minimum pressure amplitude of the liquid following the initial rapid depressurisation, the rate of pressure recovery during liquid flashing, and the

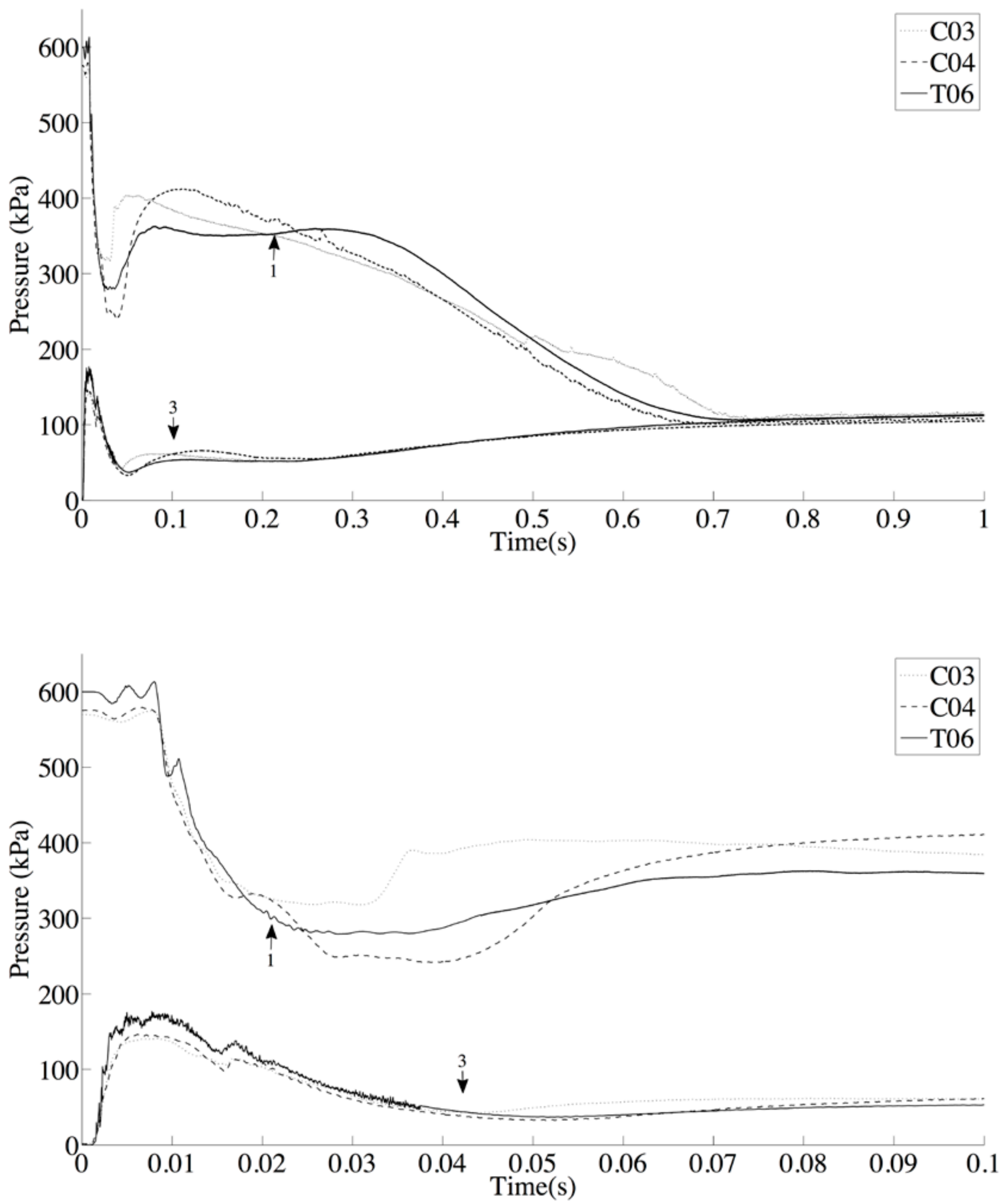

Figure 6-1. Pressure at locations 1 and 3 (tests C03, C04, & T06): (a) t = 0 – 1s (top), (b) t = 0 – 100ms (bottom).

amplitude of the pressure ‘plateau’ during quasi-steady blowdown all varied between the three tests. Potentially influential factors, such as nucleation site density and precise blowdown initiation pressure, are difficult to control experimentally. The rupture disc burst pressure tolerance of ±5%, for instance, ranges from 555kPa to 613kPa. The nucleation mechanisms filmed in tests C03 and T06 are compared in Fig. 6-2. In the high-speed image sequences, it is observed that the phase transition appears to be stronger in test C03. This can be explained by the higher initial concentration of vapour bubbles distributed in the pressurised R-134a liquid, which results in a relatively faster rate of superheat relief and vapour generation. This could be the cause of the quicker rise in pressure and the higher pressure amplitude observed in Fig. 6-1(b). In addition, the local pressure measurements are highly sensitive to three-dimensional transient effects, especially in the initial stages of the blowdown, before average uniform conditions are established across the pressure vessel cross-sectional flow area. Generally, the variations in the details of the pressures during the initial stages had no discernible influence on the average transient measurements over the full blowdown duration.

6.2 Effect of the initial pressure

Figure 6-3 shows the transient pressure measurements acquired at location 1 in tests C05 and T05. The initial test conditions are almost identical for both tests, save for the initial pressures, which are 572kPa and 615.7kPa in tests C05 and T05 respectively. In particular, the initial liquid temperatures (and therefore saturation pressures) are practically the same, with 0.1°C variation between the two. Figure 6-3 demonstrates that the transient trends, the rates of pressure reduction, and the amplitudes at the end of the transient are the same in both tests. The main difference between the two tests is that the minimum pressure following the initial rapid depressurisation in the liquid is higher in test T05. The amplitude of the subsequent quasi-steady pressure in the reservoir during the blowdown is also higher in test T05, by about the same amount.

Apart from the difference in the quasi-steady pressure amplitude between both tests in the first 250ms of the transient of about 40kPa, the results are practically identical and the deviations

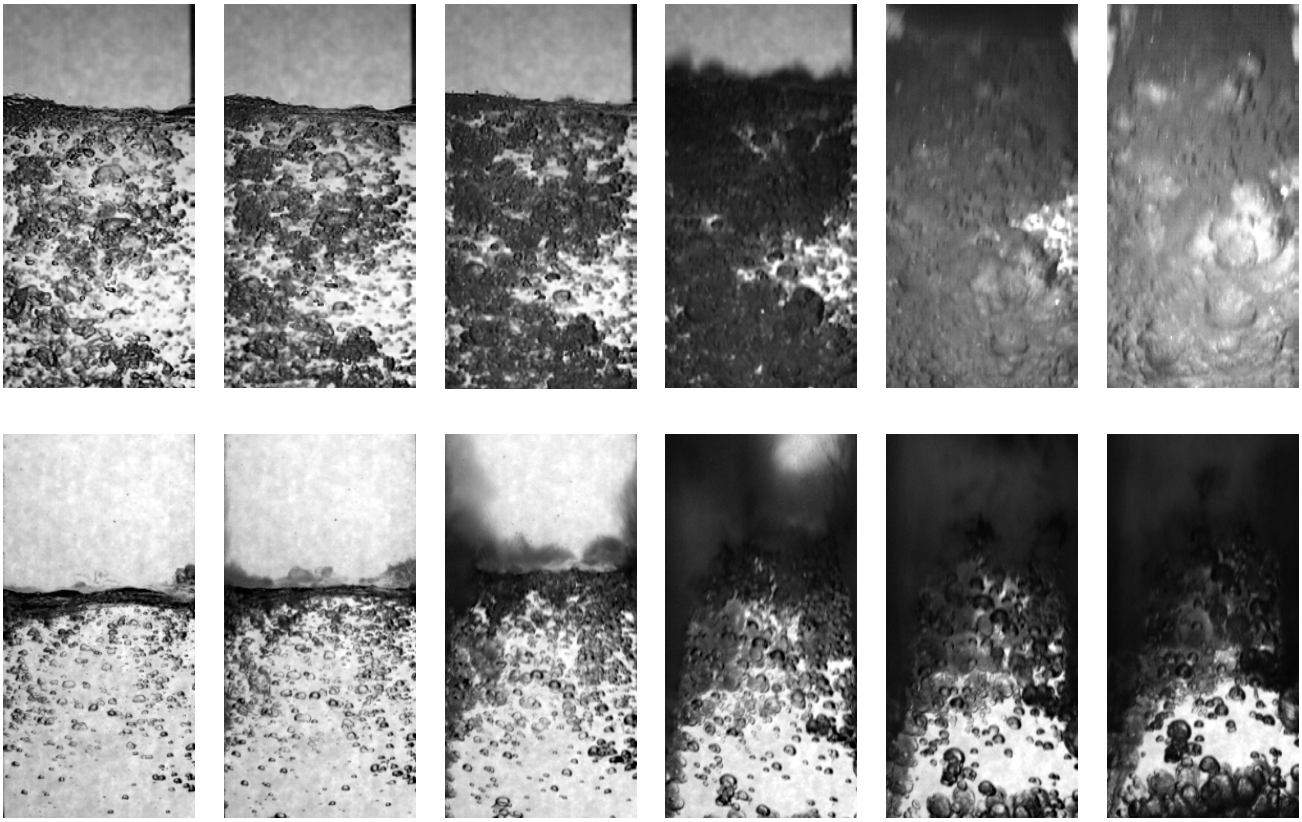

Figure 6-2. Comparison of initial rapid phase transition (3ms time-steps): (a) test C03 (top), (b) test T06 (bottom).

in the pressure trends in the first 50ms and between 650 – 850ms can be attributed to the limitations in test reproducibility discussed in section 6.1. If the effect of the initial pressure on the transient blowdown pressure amplitude were indeed important, then the transient pressure amplitudes for test T06 in Fig. 6-1, which is at an initial pressure of 599.8kPa, would be expected to be higher than tests C03 and C04, which are at initial pressures of 569kPa and 575kPa respectively. In fact, the opposite was observed, which may be explained by the difference in the rate of vapour formation shown in Fig. 6-2. It is also shown in Fig. 6-1 that the discrepancies in the pressure amplitudes can be even greater than the 40kPa difference observed in Fig. 6-3.

Figure 6-4 presents a visual comparison of the vapour generation mechanisms observed in the high-speed flow visualisations of tests C05 and T05. In test T05, vapour bubbles exist in the liquid before blowdown, which promote a more vigorous phase transition and faster vapour growth than in test C05, in which the bubble nucleation was restricted to the pressure vessel wall

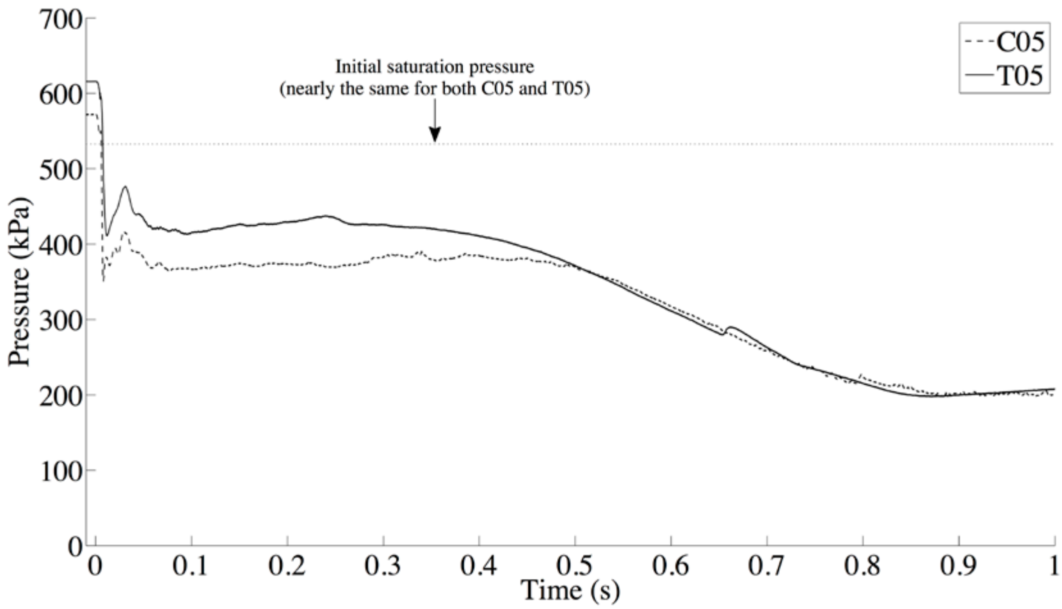

Figure 6-3. Comparison of pressure measurements at location 1 (tests C05 & T05).

boundary. It is therefore entirely plausible that this greater nucleation and vapour growth activity is responsible for the difference in pressure amplitude seen in Fig. 6-3.

6.3 Effect of the initial temperature

A comparison of the transient pressure measurements at location 1 in tests C05 and T04 is presented in Fig. 6-5. The initial liquid temperatures are 17.6°C and 21.1°C in tests C05 and T04 respectively. Unlike the comparison in Fig. 6-3 in which the initial saturation pressures were nearly the same, the 3.5°C initial temperature difference results in different initial liquid saturation pressures, 531.7kPa and 592.3kPa in tests C05 and T04 respectively. The results shown in Fig. 6-5 demonstrate that the pressure amplitude in test T04 is consistently higher than in test C05 throughout the entire duration of the blowdown transient. The overall trends in both tests are very similar and the minor deviations in the local measurement details can be attributed to the reproducibility limitations discussed in section 6.1. No significant nucleation mechanism differences were discernible in the high-speed visualisation images captured for both tests. The

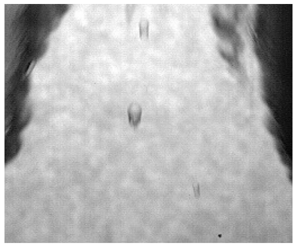

(a) C05: nucleation on steel walls

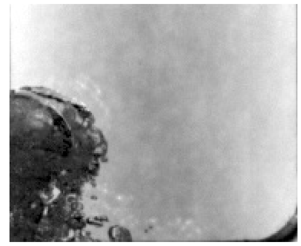

(b) T05: nucleation in liquid bulk

Figure 6-4. Comparison of vapour nucleation mechanism: (a) test C05, (b) test T05.

liquid R-134a in both cases was initially quiescent and the bubble nucleation was largely restricted to the pipe walls as shown in Fig. 6-4(a).

The results shown in Fig. 6-5 suggest that, the vapour nucleation mechanisms being relatively similar, a 3.5°C increase in initial liquid temperature, which corresponds to a 60.6kPa increase in the initial saturation pressure, may influence the transient pressure amplitude during blowdown. This initial temperature influence is not surprising, since the initial liquid saturation pressure, which only depends on the temperature, determines to some extent the level of liquid superheat permissible during rapid depressurisation before liquid to vapour transition begins. The liquid temperature also plays an important role in the rate of vapour generation and growth, which is controlled by heat and mass transfer between the liquid and vapour phases during non-equilibrium phase transition. The experimental results suggest that the initial liquid pressure, which determines the level of initial liquid subcooling, seems to have little influence on the transient blowdown pressures. Similar initial pressure and temperature effects during blowdown were also observed in previous experimental blowdown investigations in [27] and [28].

A comparison of the transient pressures measured at location 1 in tests C01 and T03 is presented in Fig. 6-6. Both tests were initiated with similar liquid inventories (22 – 23%) in the pressure vessel. The main difference is that the liquid in test C01 was initially saturated while the liquid in test T03 was initially 88.2kPa subcooled. The pressure transients in Fig. 6-6 are practically the same, save for the duration of the blowdown discharge, which lasts about 180ms in test C01 and 200ms in test T03. Since the tube bundle was removed in both tests, the rate of initial fluid discharge through the full pipe cross-sectional flow area in both tests is very rapid.

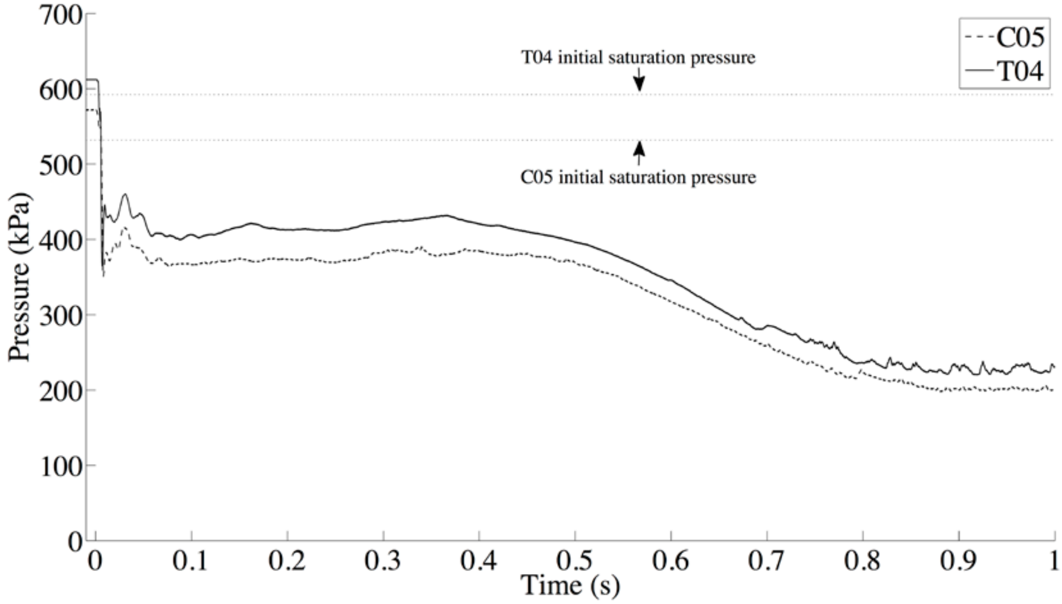

Figure 6-5. Comparison of pressure measurements at location 1 (tests C05 & T04).

Therefore, the initial liquid inventory cannot sustain the rate of vapour generation required to produce a recovery in pressure following the initial rapid transient depressurisation and the fluid pressure decreases monotonically until the end of the blowdown. Starting at about 80ms, the rates of vapour generation and fluid discharge cancel each other out, the net effect being a temporary nearly constant pressure amplitude. Following this quasi-steady period, once the majority of the liquid inventory is depleted, the pressure drops to equilibrium conditions.

If the effect of the initial liquid pressure were significant, then test T03, which is subcooled with an initial pressure of 593.2kPa, would produce more rapid liquid flashing and a shorter blowdown duration. The opposite is observed in Fig. 6-6. Higher temperatures promote faster phase transitions, which produce more rapid depletion of the superheated liquid. This may explain the shorter duration of the transient, shown in Fig. 6-6, for test C01, in which the liquid temperature is initially higher. The liquid inventory in test C01 is also slightly smaller than test T03, which would also shorten the duration of the blowdown. The vapour formation mechanisms observed in tests C01 and T03, which are shown in Fig. 6-7, are remarkably similar. The liquid is initially observed to be quiescent and the phase transition occurs largely at the pressure vessel

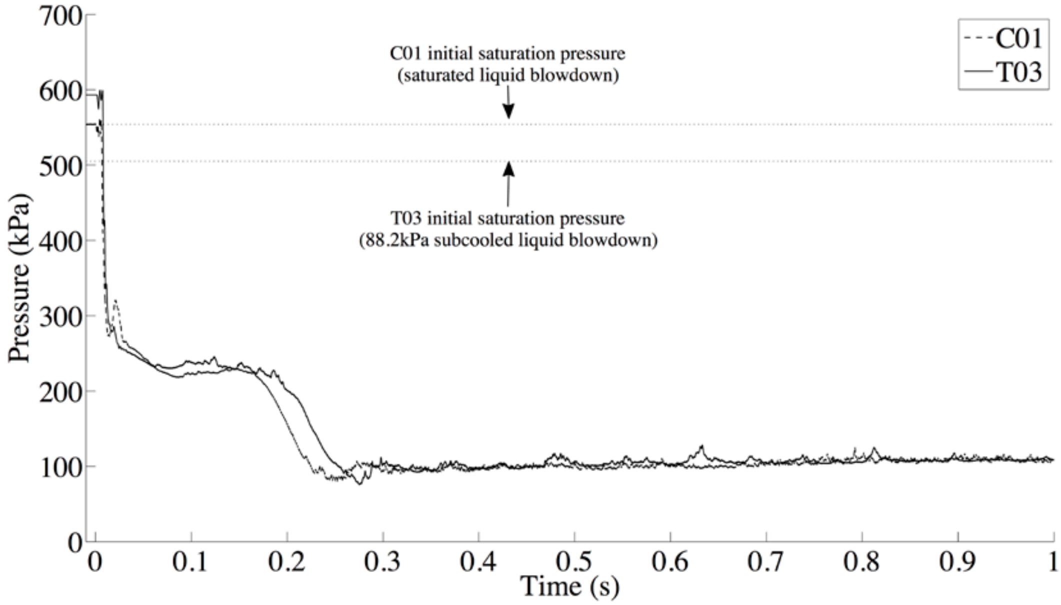

Figure 6-6. Comparison of pressure measurements at location 1 (tests C01 & T03).

walls. Image saturation occurs in the photographs obtained in test C01 due to excessive front lighting brightness and the bright portions represent two-phase plumes.

The interpretation of the above results can be summarised as follows. The main factors that influence the rate of phase transition and the amplitude of pressure recovery in these experiments are related to the rate and mechanism of vapour generation. Pre-existing liquid-vapour interfaces in the liquid before blowdown initiation promote faster phase transitions and higher pressure recovery amplitudes due to the larger initial interfacial surface area available for phase transition, which results in higher heat and mass transfer between the liquid and vapour phases. When the vapour nucleation mechanisms are similar, the rate of liquid to vapour phase transition increases with temperature, due to the increase in the thermal energy available in the liquid for heat transfer.

In these experiments, there is inevitably a variability in the initial liquid pressure from one test to another due to the rupture disc burst pressure tolerance, the hydrostatic head, and the compressed gas pressure boost. Due to the insufficiency of experimental data and lack of precise control over the parameters discussed above, the direct individual contribution of each independent parameter is difficult to establish with absolute certainty. It seems that the vapour

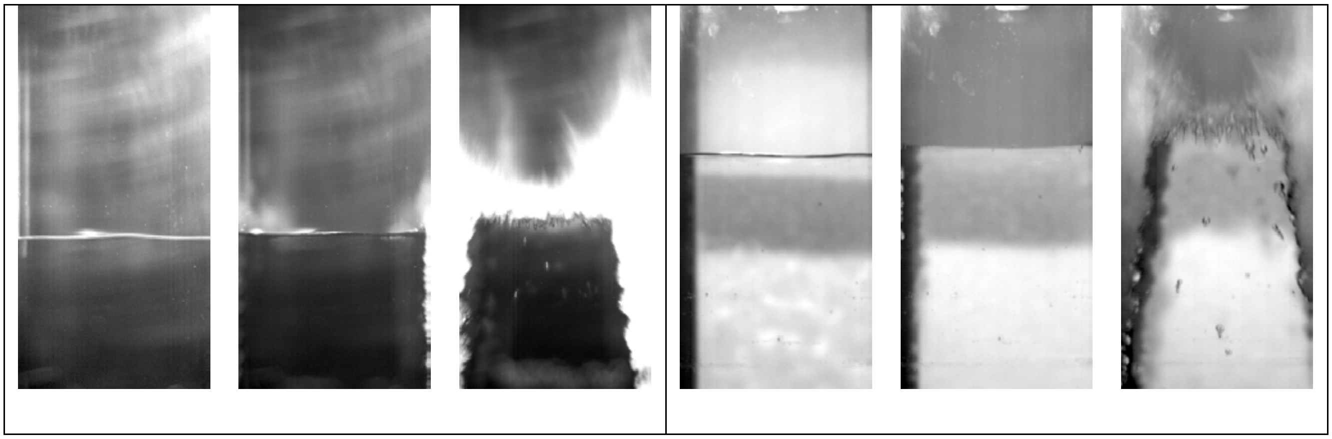

Figure 6-7. Rapid phase transition mechanisms (4ms time-steps): (a) test C01 (left), (b) test T03 (right).

nucleation mechanisms in the initial stages of blowdown play a significant role in determining the subsequent pressure amplitudes. When trapped vapour pockets are introduced into the pressure vessel from the accumulator, the increased availability of nucleation sites due to the increase in the interfacial surface area promotes a more vigorous phase transition and higher pressure amplitudes. The initial temperature of the liquid also seems to affect the phase transition phenomena to some extent. However, the degree of liquid subcooling appears to have no influence on the transient blowdown pressures.

6.4 Effect of the initial liquid volume

A comparison of the pressures measured in the pressure vessel below the rupture disc in tests T02, T03, and T07 is provided in Fig. 6-8. Figure 6-8(a) shows the measurements obtained at location 2, initially in vapour, and Fig. 6-8(b) shows the measurements at location 1, initially in liquid. The three tests were performed with similar initial thermodynamic conditions, identical pressure vessel dimensions, and all of the tubes removed from the test section. The liquid surface heights from the bottom of the reservoir were 499mm, 290mm, and 129mm in tests T02, T03, and T07 respectively. These heights correspond to pressure vessel liquid volume fills of 39%, 23%, and 10% respectively.

By performing the tests with different initial liquid levels, the influence of the initial liquid volume on the transient blowdown pressures can be examined. A main difference

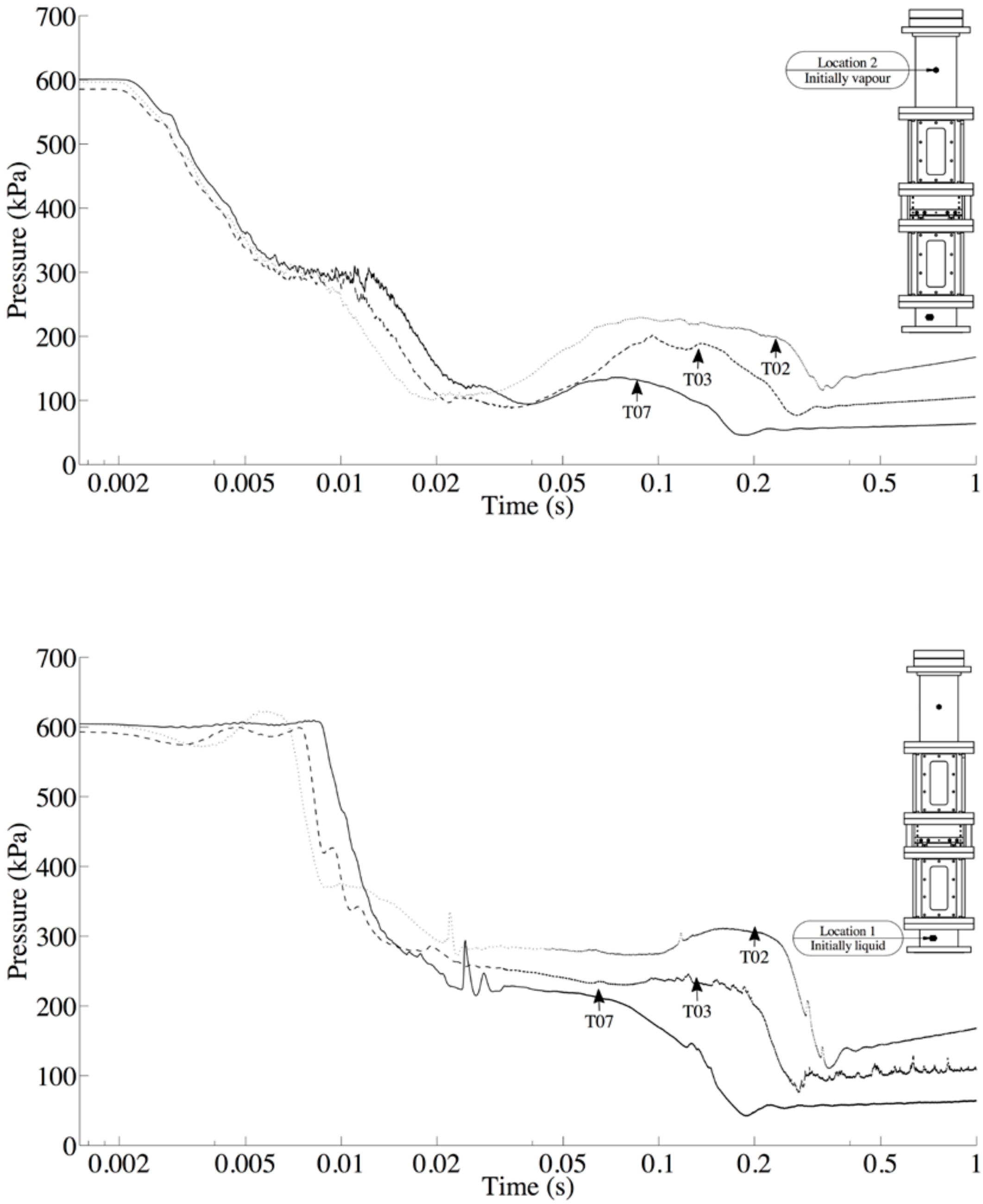

Figure 6-8. Transient pressure comparison (tests T02, T03, & T07): (a) location 2 (top), (b) location 1 (bottom).

observed between the pressures at both locations is that the depressurisation in Fig. 6-8(a) begins at the same time in the vapour region, whereas the delay time for depressurisation in Fig. 6-8(b) in the liquid region increases with decreasing liquid volume. This is due to the wave propagation velocity, which is about 4 times faster in liquid than in vapour. A higher liquid surface results in faster wave propagation towards location 1 and the depressurisation therefore begins earlier when the liquid surface in the pressurised reservoir is higher. This was also demonstrated in section 5.3 in Fig. 5-7.

The volume of liquid in the pressure vessel determines to a certain extent the transient pressure amplitudes and the duration of the blowdown discharge. When the initial liquid inventory is smaller, less vapour is generated, and the overall pressure amplitudes are therefore lower. Similarly, smaller liquid inventories produce shorter blowdowns. However, since the discharge flow area in all of the experiments is the same when the tube bundle is removed from the test section, the discharge rates are similar. In Fig. 6-8, it is observed that the quasi-steady pressure 'plateau' is less flat when the initial volume decreases since the rate of vapour generation cannot be sustained to match the rate of fluid discharge.

The effect of the initial liquid volume on the blowdown pressure can be quantitatively investigated by averaging the transient pressure amplitudes with respect to the blowdown durations. An average blowdown pressure can be computed by numerically integrating the area under the transient pressure curve and dividing the integral by the time required for the pressure at both ends of the pressure vessel to equalise. Figure 6-9 shows the three pressure measurements at location 1 from tests T02, T03, and T07 correlated with the calculated average pressures. Unsurprisingly, the average blowdown pressure increases with increasing initial liquid volume. The average blowdown pressures calculated for tests T02, T03, and T07 are 271kPa, 219kPa, and 185kPa respectively. The average blowdown pressure computed in this manner is sensitive to the accumulation of the R-134a discharged from the pressure vessel into the vacuum reservoir. The final equilibrium pressure is higher when the initial liquid volume is larger.

In Fig. 6-10, the transient pressure drop across locations 1 and 3 (the bottom of the vessel and above the rupture disc) is plotted for tests T02, T03, and T07, along with the corresponding average pressure drop calculated based on the procedure presented above. The transient pressure drop across locations 1 and 3 is obtained simply by subtracting the pressure at location 3 from the upstream pressure at location 1. Since the pressure downstream of the rupture disc is initially nearly 0kPa, the initial pressure drop at $t = 0$ is the same as the initial pressure inside the pressure vessel. The pressure drop at the end of the transient, once the pressures at the two locations have equalised, converges to 0kPa.

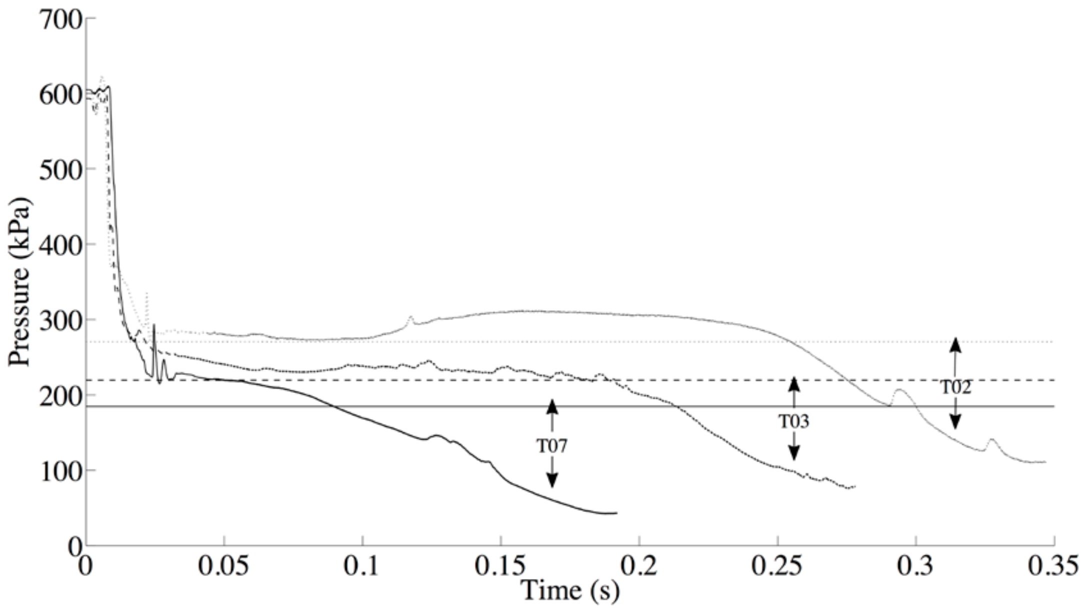

Figure 6-9. Transient pressure measurements and calculated average pressures at location 1 (tests T02, T03, & T07).

The calculated average pressure drops are 121kPa, 107kPa, and 96kPa for tests T02, T03, and T07 respectively. The pressure drop in the pipe during blowdown is mainly due to viscous losses along the inside walls of the pipe. Since the geometry and dimensions of the pressure vessel and the initial fluid conditions are practically the same for the 3 tests being compared, the frictional pressure drop depends mainly on the fluid mass flow rate during discharge. The calculated average pressure drop is normalised with respect to the duration of the discharge, which means that the average pressure drop will be directly proportional to the initial R-134a liquid inventory in the pressure vessel if the average flow rate does not change. Accordingly, the relationship between the initial liquid inventory (39%, 23%, and 10%) and the average pressure drop (121kPa, 107kPa, and 96kPa) is approximately linear.

In order to better investigate the transient pressure during blowdown quantitatively, it is more instructive to plot the pressure drop, Δp, across locations 1 and 3, normalised by the upstream pressure, p_u, according to Eq. (6-1),

$$\frac{\Delta p}{p_u} = \frac{p_u - p_d}{p_u} = 1 - \frac{p_d}{p_u}, \tag{6-1}$$

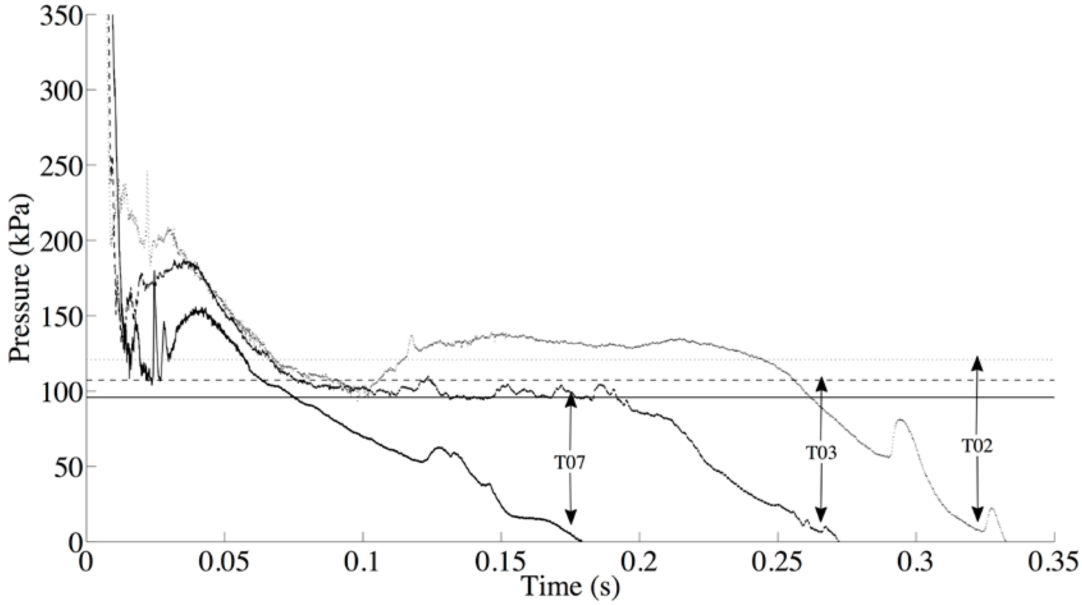

Figure 6-10. Transient pressure drop and calculated average pressure drop across locations 1 & 3 (tests T02, T03, & T07).

where p_d is the downstream pressure. The transient non-dimensional pressure ratio obtained from Eq. (6-1) is plotted in Fig. 6-11 for tests T02, T03, and T07. The pressure downstream of the rupture disc is initially 0kPa and the pressure ratio is therefore equal to 1 at t = 0. The pressure ratio converges to 0 when the upstream and downstream pressures approach each other towards the end of the blowdown.

The computed average normalised pressure ratio for each of the three tests is also shown in Fig. 6-11. The value of the average normalised pressure ratio is about 0.42. This gives a downstream to upstream pressure ratio of 1 – 0.42 = 0.58. This value of the average downstream to upstream pressure ratio is close to the 0.56 choked pressure ratio calculated in section 5.4 from Eq. (5-3) for single-phase vapour R-134a. This suggests that the R-134a discharge occurs at the critical (choked) flow rate with a high void fraction during the quasi-steady discharge period of these unobstructed pipe blowdown transients.

If it is assumed that most of the liquid R-134a is discharged during the quasi-steady portion of the transient at a constant flow rate, then an average mass flow rate can be computed by dividing the initial mass of R-134a in the pressure vessel by the duration of the quasi-steady

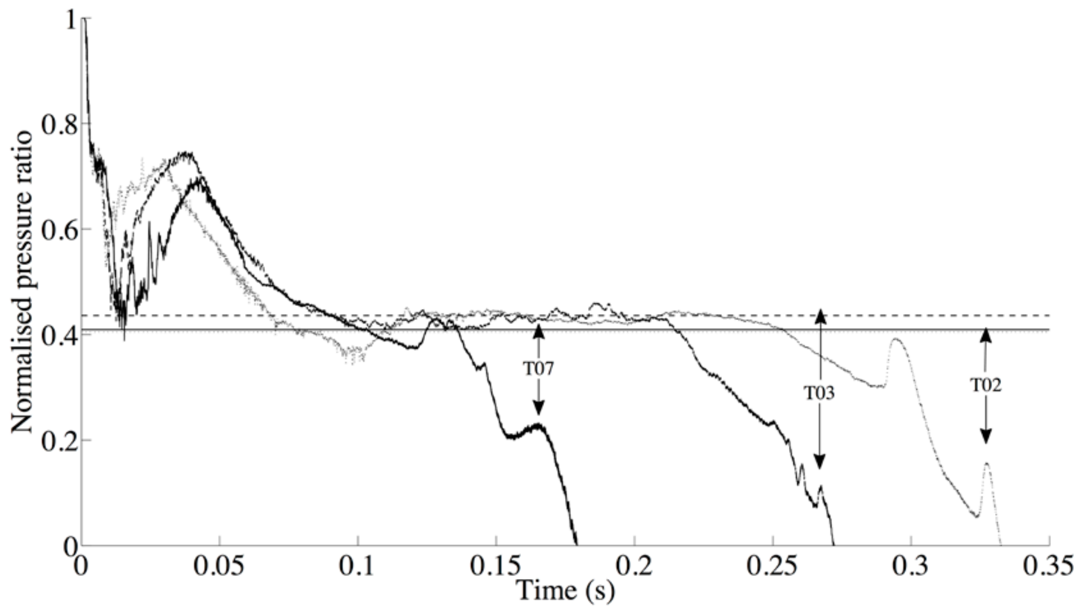

Figure 6-11. Non-dimensional transient pressure ratio and computed average pressure ratio across locations 1 & 3 (tests T02, T03, & T07).

segment of the transient. Based on Fig. 6-9, the quasi-steady discharge occurs between 90 – 250ms in test T02, 90 – 200ms in test T03, and 70 – 120ms in test T07. The initial mass is 11.9kg, 7.2kg, and 3.6kg in tests T02, T03, and T07, giving an average mass flow rate of 74kg/s, 66kg/s, and 72kg/s respectively. The computed average mass flow rates are close to the theoretical choked mass flow rate of single-phase vapour R-134a, 78kg/s, further corroborating the choked pressure ratio results presented above. The results of the quantitative investigation of the influence of the initial liquid volume on the blowdown pressure are summarised in Table 6-1.

6.5 Analysis of the blowdown thermodynamics

In the present blowdown experiments, the blowdown discharge always occurs through the opened rupture discs, which all have the same uniform diameter and opening pattern. The size of the discharge area was identified in several previous experimental two-phase blowdown investigations to have a significant effect on the extent of thermal non-equilibrium between the two phases during blowdown [27, 28, 29, 30]. When a rapid transient blowdown occurs under

Table 6-1. Effect of the initial liquid volume on the transient blowdown properties.

Test	Initial liquid volume	Transient blowdown duration	Average pressure	Average pressure drop	Average pressure ratio	Average mass flow rate
T02	39%	347ms	271kPa	121kPa	0.41	74kg/s
T03	23%	278ms	219kPa	107kPa	0.43	66kg/s
T07	10%	192ms	185kPa	96kPa	0.41	72kg/s

thermal non-equilibrium conditions, the temperature of the liquid before it transitions to vapour remains higher than the saturation temperature corresponding to the local pressure conditions. The temporarily superheated liquid is defined to be in a 'meta-stable' state [26].

Larger blowdown discharge areas produce greater departures from thermodynamic phase equilibrium. The reason for this behaviour is that the rate of depressurisation is limited by the size of the vessel discharge area. Small discharge areas allow relatively more time for the two phases to achieve thermal equilibrium during transient discharge, whereas large discharge areas result in faster depressurisation and discharge rates, promoting higher levels of thermodynamic non-equilibrium. Similarly, blowdowns initiated from pipes with identical diameters and discharge areas were found to exhibit greater departures from thermal phase equilibrium when shorter pipes were used. Smaller vessel volumes produce higher rates of depressurisation and discharge, resulting in greater departures from thermal equilibrium. These thermodynamic non-equilibrium phenomena were also observed in the present experiments. This section presents an analysis of the fluid thermodynamics in the two-phase blowdown experiments.

The analysis of the transient thermal phenomena in the current tests was made possible by the temperature measurements obtained from rapid response thermocouples. Figure 6-12 presents sample temperature measurements obtained for two different tests, T02 and T03, at locations 1 and 2, in the regions initially filled with liquid and vapour respectively. The measurements shown in Fig. 6-12 indicate that the transient temperatures of the liquid and vapour phases during blowdown were significantly different. The thermocouple signal fluctuations at location 1 at 50 – 280ms in test T02 and 30 – 160ms in test T03 represent temperature discrepancies between the boiling liquid and expanding vapour phases during blowdown. A quantitative representation of the degree of thermodynamic non-equilibrium during transient blowdown can be obtained by comparing the equilibrium saturation pressures computed from the local temperature measurements to the measured transient pressures.

When a two-phase fluid is at thermodynamic equilibrium, its pressure is the same as the saturation pressure corresponding to its temperature. The computed saturation pressure of a superheated fluid is higher than the actual saturation pressure that corresponds to the fluid's temperature under thermodynamic equilibrium conditions. In Fig. 6-13, the computed transient saturation pressure is compared to the measured transient pressure in tests T02 and T03. Measurements from location 1, which is initially submerged in liquid, are plotted in Fig. 6-13(a), and from location 2, initially in vapour, are shown in Fig. 6-13(b). The comparisons in Fig. 6-13 demonstrate that in both cases, the fluid temperature approaches and then follows the saturation temperature corresponding to the local pressure.

The liquid temperature trace in Fig. 6-13(a) shows that the liquid retains its initial pre-blowdown temperature during the initial rapid phase of the depressurisation. After a brief time period of 17ms in test T03 and 37ms in test T02 following the initiation of the rapid liquid to

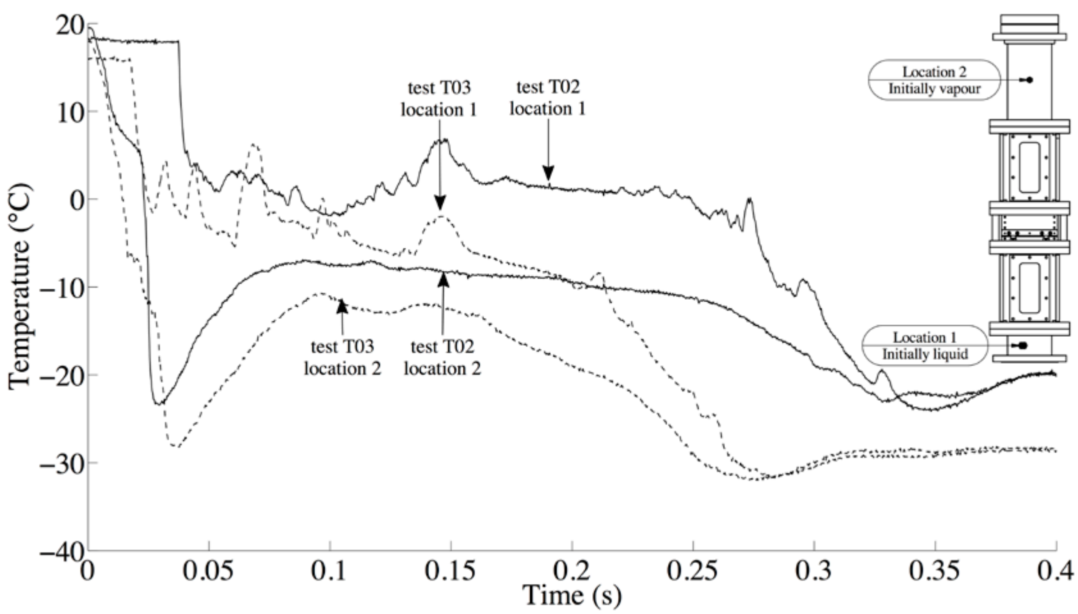

Figure 6-12. Temperature measurements at locations 1 & 2 (tests T02 & T03).

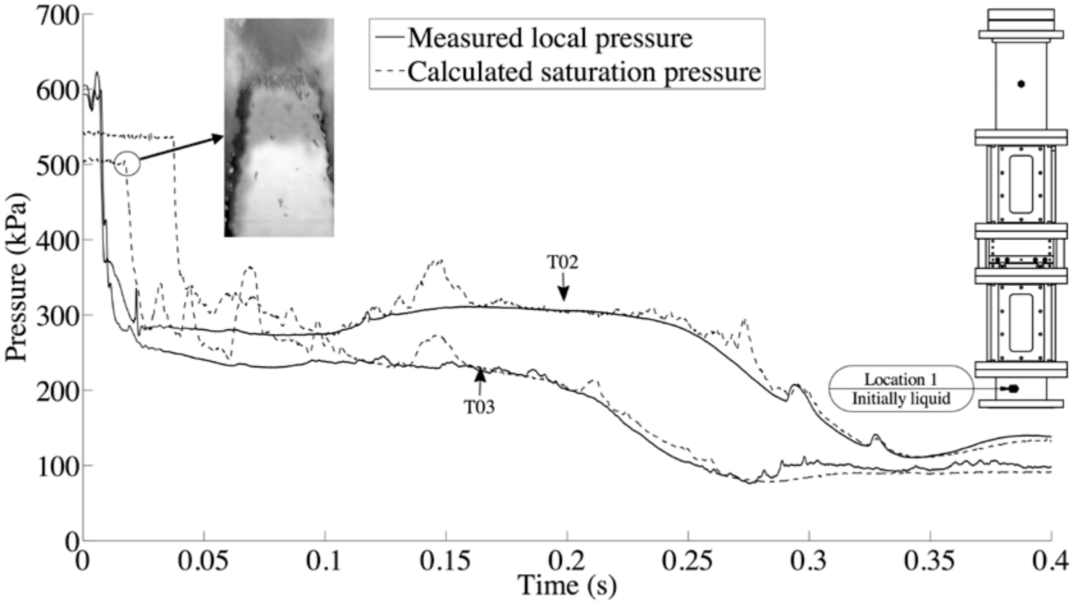

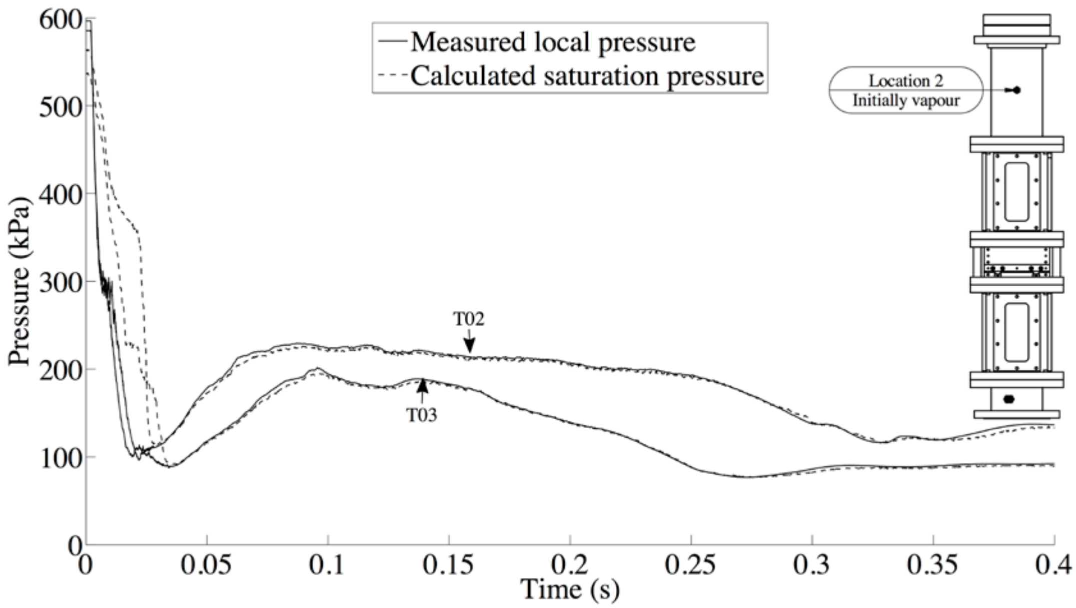

Figure 6-13. Comparison of measured pressure and calculated saturation pressure (tests T02 & T03): (a) location 1 (top), (b) location 2 (bottom).

vapour phase transition, the temperature measurement drops rapidly and approaches the saturation temperature corresponding to the local pressure. The flow visualisation snapshot captured at t = 17ms confirms that the rapid drop in temperature occurs around the same time as the liquid begins flashing vigorously to vapour. These observations can be explained through a physical interpretation of the signals by considering the thermocouple measurement point of contact. The thermocouple hot junction is surrounded by superheated liquid, which is in a non-equilibrium ‘meta-stable’ thermodynamic state, during the initial rapid transient phase of the depressurisation. Once the liquid in the thermocouple vicinity boils off, the temperature measurement rapidly drops towards the temperature of the vapour generated by liquid flashing, which is at the saturation temperature corresponding to the local pressure conditions. The response of the thermocouples during the rapid temperature drop is very fast.

In contrast, the temperature in the vapour region shown in Fig. 6-13(b) does not display any isothermal behaviour at the start of the transient blowdown. The initial temperature measurement drops rapidly immediately following the passage of the depressurisation wave as the single-phase superheated vapour expansion results in a significant reduction in its temperature. The temperature then stabilises briefly once the transient pressure reaches its minimum amplitude, after which the temperature drops rapidly towards saturation conditions at 28ms in test T02 and 34ms in test T03. It was shown in Fig. 5-12 that this point in the transient during which the pressure is observed to begin rising coincides with the timing of the arrival of the two-phase flashing mixture front accelerating upwards. The agreement between the local pressures and computed saturation pressures measured at this moment as shown in Fig. 6-13(b) indicates that the flashing two-phase fluid mixture is at saturated thermal equilibrium. Thermodynamic equilibrium with respect to the system saturation pressure is approached relatively quickly at this location compared to the liquid region at the bottom of the pressure vessel, and is maintained for the remaining duration of the blowdown transient.

The rapid liquid depressurisation process can be idealised as an incompressible saturated liquid undergoing an isentropic expansion. In the test case of T02, the change in the specific enthalpy of the liquid R-134a, dh_l/dt, can be determined from the energy equation according to Eq. (6-2),

$$\frac{dh_l}{dt} = T_l \frac{ds}{dt} + \frac{1}{\rho_l} \frac{dp}{dt}, \tag{6-2}$$

where T_l is the liquid temperature, ds/dt is the change in entropy, which is 0 for an isentropic expansion, ρ_l is the liquid density, which is 1233kg/m^3 at the initial liquid temperature of 18.2°C, and dp/dt is the rate of depressurisation, which was experimentally found to be 115.8MPa/s. Thus, from Eq. (6-2), dh_l/dt is determined to be 93.9kJ/kg-s. The change in the liquid temperature, T_l, can be determined from Eq. (6-3),

$$c_P = \frac{dh_l}{dT_l}, \tag{6-3}$$

where c_P is the specific isobaric heat capacity of the liquid R-134a, which is 1.4kJ/kg-K. The liquid temperature change associated with the isentropic expansion process is therefore determined to be 0.14°C.

The relatively small temperature change calculated for the rapid isentropic depressurisation of an incompressible liquid corroborates the interpretation of the measurements in the first 37ms of Fig. 6-12 for test T02, where the rapid depressurisation in the liquid region is initially observed to be isothermal and the liquid remains superheated. This also confirms that the substantial rapid temperature drop occurring at 37ms cannot be due to a change in the temperature of the liquid, and is instead caused by the rapid liquid phase transition to vapour. The subsequent deviations from the saturation temperature in the measurements appear in the form of upward spikes, which suggests that the thermocouple hot junction during these periods is in contact with superheated liquid flowing towards the vacuum reservoir downstream of the pressure vessel. Due to the response time characteristics of the thermocouple and the transient nature of the event, it is not possible to confirm whether the temperatures recorded in these fluctuations are the actual liquid temperatures or somewhere in between the temperatures of the vapour and liquid phases.

6.6 Effect of the tube bundle on the transient blowdown phenomena

The introduction of a tube bundle in the test section imposes a significant restriction to the flow during the transient blowdowns. The effect of this flow restriction in the pressure vessel on the transient fluid thermodynamics is shown in Fig. 6-14, which presents a comparison of measured pressures and calculated saturation pressures in test T02, without the tubes, and T05, with 6 rows of tubes. Aside from the presence of the tube bundle, all of the experimental parameters and initial conditions are similar in tests T02 and T05. The initial pressures are 605kPa and 615.7kPa and the initial temperatures are 18.2°C and 17.7°C in tests T02 and T05 respectively.

The main influence of the tube bundle is the significant reduction in the discharge rate of the R-134a below the tubes, which results in increased mass hold-up. The result, which can be observed in Fig. 6-14, is a higher pressure amplitude during fluid discharge, a longer transient blowdown duration, and an extended quasi-steady pressure 'plateau' during discharge with a slower rate of depressurisation towards final equilibrium conditions. During this quasi-steady stage of the blowdown, which lasts until about 400ms into the blowdown, the rate of pressure increase due to vapour generation and expansion matches the rate of fluid discharge through the tube bundle. When the tube bundle is removed from the test section, the quasi-steady discharge condition exists for only about 200ms, after which the rate of vapour generation cannot be sustained to match the higher rate of fluid discharge.

The reduced rate of fluid discharge through the tube bundle in test T05 is responsible for the increase in the transient blowdown duration. Since the tubes limit the depressurisation rate, the rate of vapour formation is also slower when the tube bundle is inserted in test T05 compared

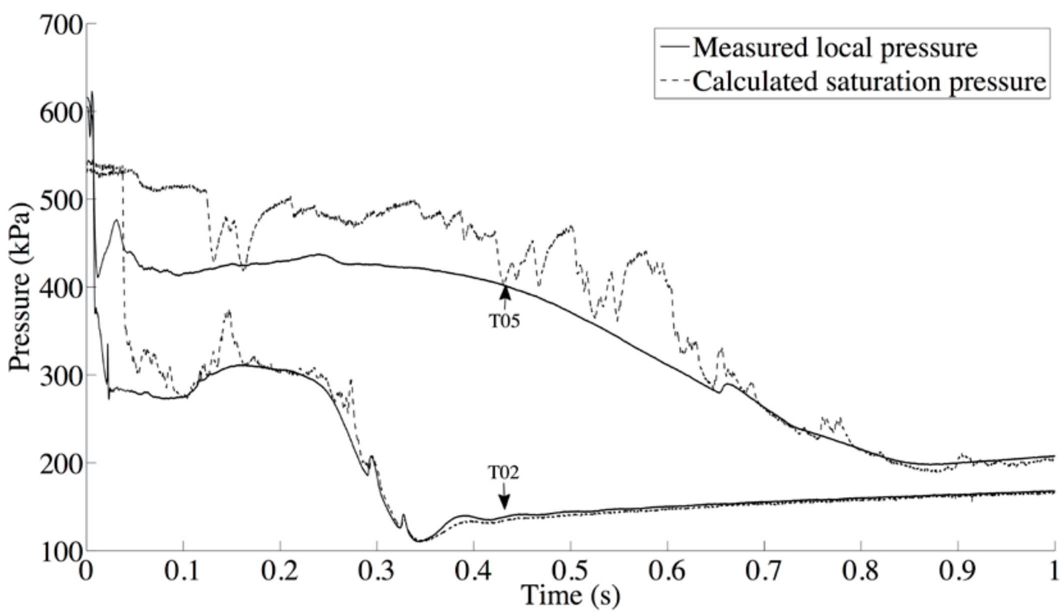

Figure 6-14. Comparison of measured pressure and calculated saturation pressure at location 1 (tests T02 & T05).

to the unobstructed pipe blowdown case of test T02. As a result of the reduced rate of vapour generation, the thermocouple in test T05 seems to remain in contact with superheated liquid for longer periods throughout the transient. The temperature dips recorded in the measurements from test T05 at 162ms, 430ms, 525ms, and 647ms match the computed saturation temperature, which indicates that the vapour generated below the tubes during the transient is in a saturated thermodynamic state.

In some cases, the amplitude of the dips in temperature is not sufficient to reach the saturation temperature, which is observed to occur at 131ms, 467ms, and 548ms. The most probable explanation for this behaviour is that the thermocouple junction acts as a nucleation site, and the dips in temperature represent vapour bubble growth on the thermocouple junction itself. In the event that the nucleated bubble departs before the measured temperature drops to saturation, the temperature recovers towards the superheated liquid temperature before reaching the saturation point. This would also explain the better agreement between the measured and calculated pressures in test T02, since the higher rate of vapour formation increases the likelihood of vapour bubbles nucleating at the thermocouple junction, and the temperature remains at saturation for longer periods of the transient with occasional upward spikes representing contact with flowing superheated liquid. The temperature measurement never drops below the corresponding saturation temperature since it is impossible for either of the two phases to become subcooled during rapid depressurisation.

Vapour nucleation is an inherently random phenomenon and in some cases the temperature in the liquid region did not converge towards the saturation temperature until after the end of the transient blowdown, indicating that no nucleation took place at the thermocouple junction. Figure 6-15 shows an example of a liquid temperature measurement, obtained in test T08, which corresponds to a superheated thermodynamic state for the entire blowdown duration. It was shown in the high-speed flow visualisations in Figs. 5-3 and 5-4 that the two-phase flow composition below and above the tubes during the transient blowdown is remarkably different. A two-phase mixture, which is apparently in saturated thermodynamic equilibrium, is rapidly established downstream of the tube bundle, as demonstrated by the agreement between the measured and calculated pressures at location 2 in Fig. 6-15. Below the tubes, the liquid remains superheated throughout the transient. This indicates that even with the reduction of the discharge rate due to the flow restriction imposed by the tube bundle, the extent of the departure from thermal equilibrium between the liquid and vapour phases is significant in these experiments. The physical modelling of this type of transient non-equilibrium two-phase phenomena is very difficult and beyond currently available numerical modelling capabilities.

A high-speed image sequence of the blowdown discharge flow filmed above the tubes in test C05 is presented in Fig. 6-16, which provides insight into the two-phase mixture composition at the exit of the tube bundle during the quasi-steady stage of the transient. The images from t = 0.47s to t = 0.71s show the presence of entrained liquid streams in the discharging two-phase fluid mixture, which splash against the glass windows as the fluid mixture flows rapidly towards the downstream vacuum reservoir. It appears that by limiting the rate of vapour generation during the transient blowdown, the fluid mixture maintains a distinct liquid-vapour composition, which passes through the tube bundle and emerges with the flow pattern observed in Fig. 6-16. At t = 0.83s, the two-phase mixture seems to have an increased void fraction, and towards the end of the transient, at t = 0.95s, the two-phase mixture appears to consist mainly of high-quality vapour flow, with dispersed liquid droplets visible mostly towards the outside perimeter of the cross-sectional flow area. The continuous medium in this region throughout the transient is observed to be the vapour phase, which explains the saturated

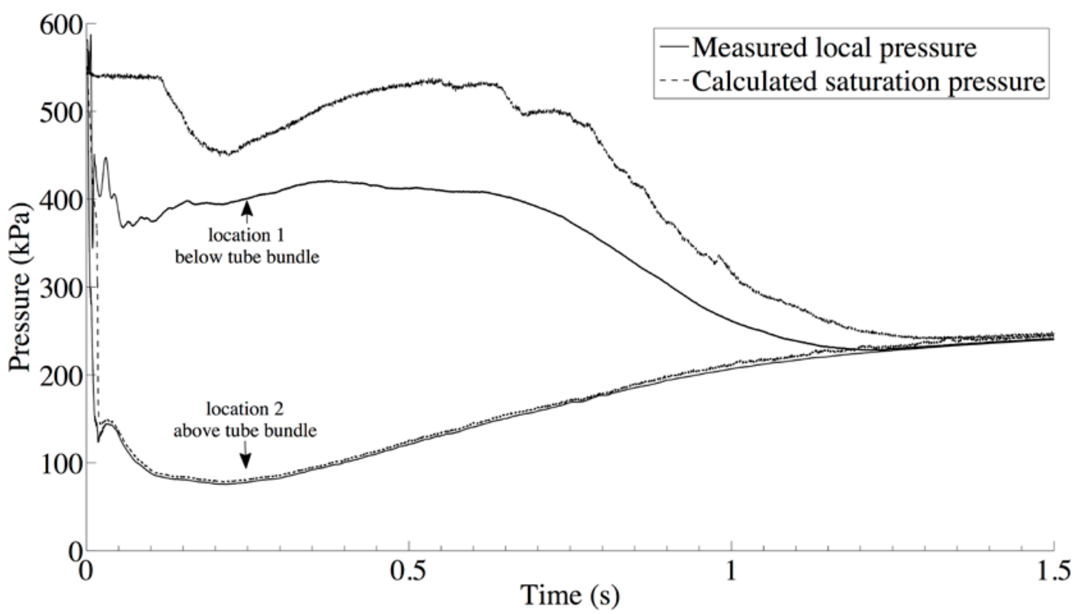

Figure 6-15. Comparison of measured pressure and calculated saturation pressure at locations 1 & 2 (test T08).

equilibrium thermocouple measurements downstream of the tube bundle. The presence of entrained liquid streams also explains the significant thermal non-equilibrium measured below the tubes, where the liquid phase is the continuous medium.

Figure 6-17 presents a comparison of the rates of vapour formation and growth observed in the high-speed flow visualisations filmed in test T03, without the tube bundle installed, and test T06, with 6 rows of tubes. The high-speed image sequences are shown in 6ms time-steps, starting with the point of phase transition initiation. In both tests, the liquid surface is initially visible through the lower window, below the tube bundle test section location in the pressure vessel. The images demonstrate the influence of the presence of the tube bundle on the rate of vapour growth. The two-phase plumes in Fig. 6-17(a) develop quickly, covering the entire viewing area by the 5th frame. The rate of vapour growth is faster than that in Fig. 6-17(b). Even with the pre-existing vapour bubbles distributed in the liquid shown in the 1st and 2nd frames of Fig. 6-17(b), which provide an increased interfacial surface area for phase transition, the rate of vapour growth over the 30ms segment shown does not keep up with that observed without any obstruction to the flow in the pressure vessel. This provides further evidence that the tube bundle controls the rate of discharge and vapour formation in the region upstream of the tubes.

Figure 6-18 presents high-speed image sequences showing the rates of vapour generation observed through the upper window when the initial liquid free surface is above the tube bundle in both tests C05 and T05. The images are shown in 6ms time-steps beginning with the initiation

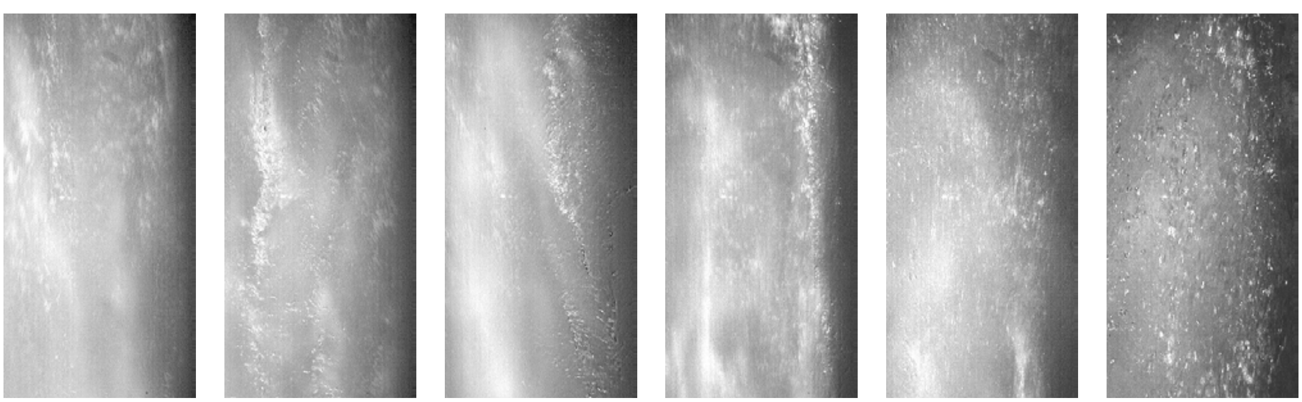

t = 0.35s *t* = 0.47s *t* = 0.59s *t* = 0.71s *t* = 0.83s *t* = 0.95s

Figure 6-16. High-speed image sequence of transient two-phase mixture downstream of the tube bundle (test C05).

of phase transition, and 6 rows of tubes were mounted in the two experiments shown. Since the liquid R-134a in this region was directly exposed to the full break area of the downstream rupture discs without any obstruction to the flow in between, the vapour generation rates are virtually identical in the image sequences shown in Fig. 6-18. An accelerating two-phase mixture appears at the bottom of the 3rd frame in both tests, which seems to have originated at the surface of the tubes in the tube bundle. The rate of vapour growth in this region downstream of the bundle does not appear to be influenced by the presence of the bundle, further validating that the tube bundle only affects the pressure drop across the tubes and the vapour generation rate upstream.

Figure 6-19 shows pressure and temperature measurements obtained at location 1 in tests T03 and T06. These measurements lend further support to the interpretations of the high-speed

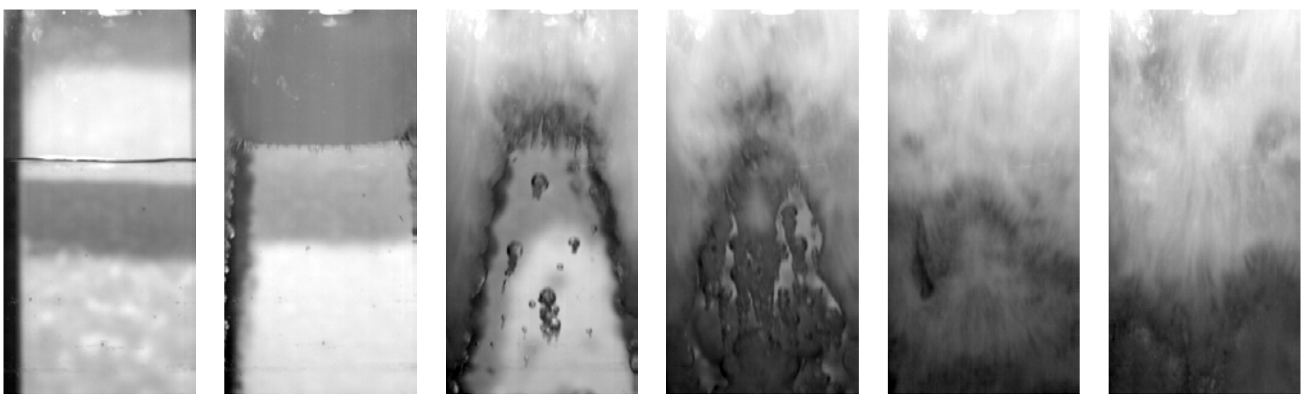

(a) Test T03: lower window, 0 rows of tubes downstream

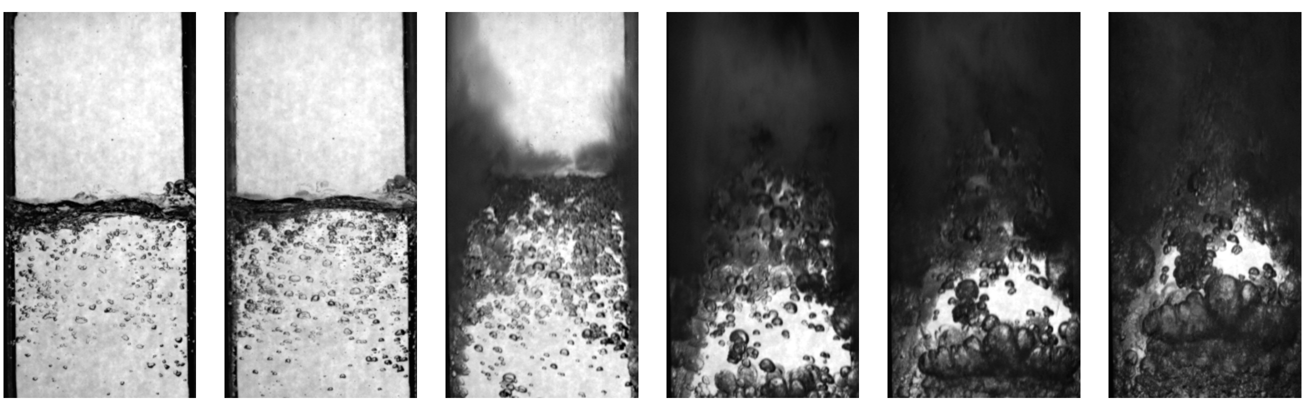

(b) Test T06: lower window, 6 rows of tubes downstream

Figure 6-17. High-speed image sequence of vapour growth rate (6ms time-steps): (a) test T03, (b) test T06.

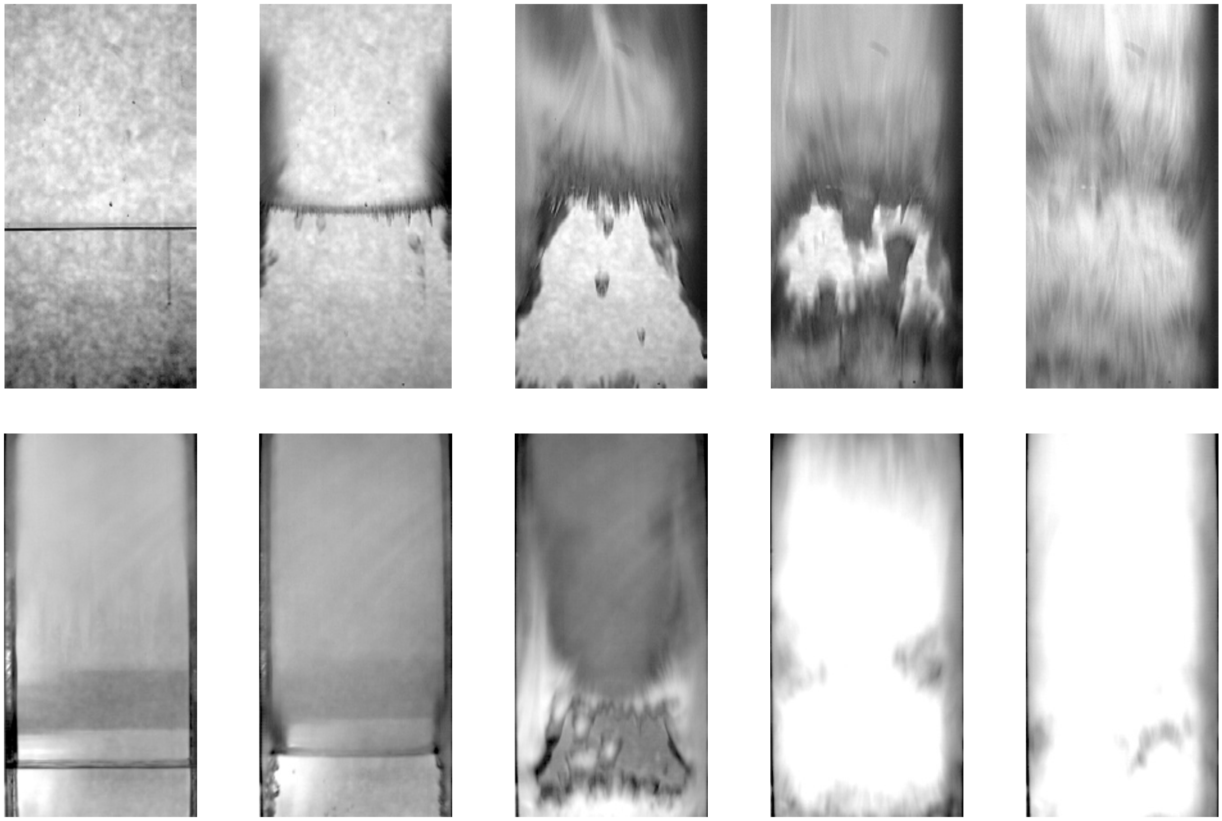

Figure 6-18. Comparison of vapour growth rates downstream of the tube bundle (6ms time-step): (a) test C05 (top), (b) test T05 (bottom).

image observations above. When the tube bundle is removed in test T03, the transient blowdown duration is shorter and the rate of vapour generation is higher. The temperature measurements indicate increased phase transition and vapour nucleation activity at the thermocouple junction in test T03. In contrast, the thermocouple trace for test T06 appears to remain in contact with superheated liquid for a longer period of time. Nucleation at the thermocouple junction is observed to be less pronounced in test T06 when the rate of depressurisation and phase transition is limited by the flow restriction of the downstream tube bundle. The pressure upstream of the tubes increases starting at about 35ms when the fluid accelerates through the tube bundle and the pressure drop across the tubes is subsequently controlled by the tube bundle for the remainder of the transient blowdown.

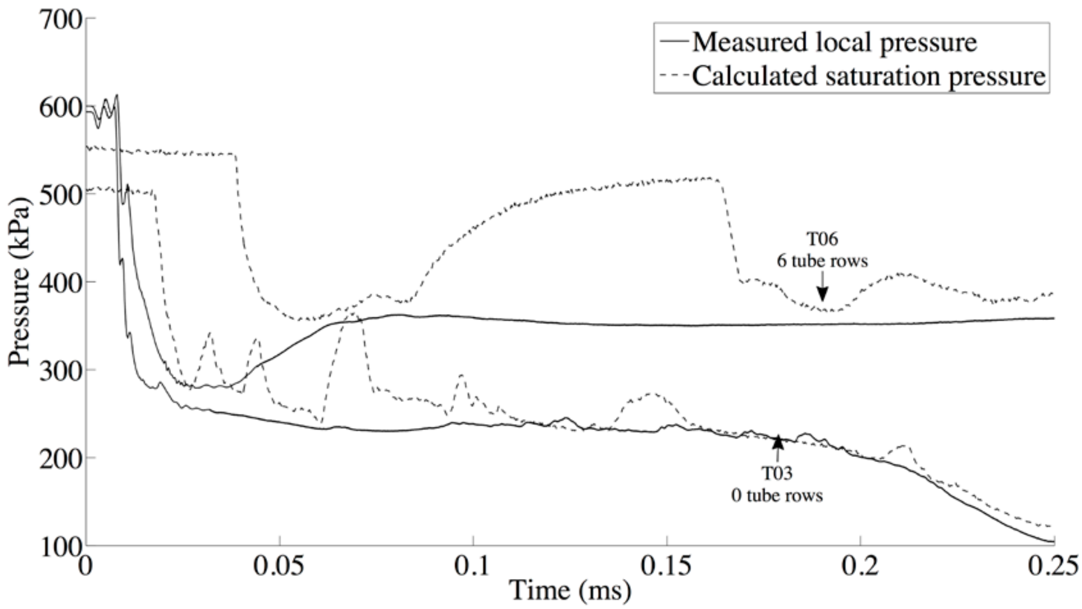

Figure 6-19. Comparison of measured pressure and calculated saturation pressure at location 1 (tests T03 & T06).

6.7 Analysis of the transient pressure drop across the tube bundle

The total pressure drop of a two-phase fluid flowing in cross-flow over a tube bundle is composed of the total changes in the potential energy, the kinetic energy, and the skin friction or form drag pressure losses. The steady pressure drop can be analytically formulated using the homogeneous model, which assumes that the liquid and vapour phases are in thermal and mechanical equilibrium such that the velocity and density can be averaged across the cross-sectional flow area. The total two-phase pressure drop, Δp_{total}, is the sum of the elevation head, Δp_{static}, the acceleration or momentum component of the pressure drop, Δp_{mom}, and the frictional or form drag pressure drop, $\Delta p_{friction}$ or Δp_{drag}, as given by Eq. (6-4),

$$\Delta p_{total} = \Delta p_{static} + \Delta p_{mom} + \Delta p_{drag} . \tag{6-4}$$

For a homogeneous two-phase fluid, the static pressure drop, Δp_{static}, is determined according to Eq. (6-5),

$$\Delta p_{static} = \rho_H g H \sin\theta , \tag{6-5}$$

where ρ_H is the homogeneous density, g is the gravitational acceleration, H is the total height of the flow channel, and θ is the angle of the elevation. The homogeneous density can be determined from Eq. (6-6),

$$\rho_H = \rho_l\left(1-\varepsilon\right)+\rho_g\varepsilon\,, \tag{6-6}$$

where ρ_l and ρ_g are the liquid and vapour phase densities respectively, and ε is the two-phase mixture void fraction, which is given by Eq. (6-7),

$$\varepsilon = \frac{1}{1+\left(\frac{u_g}{u_l}\frac{\left(1-x\right)}{x}\frac{\rho_g}{\rho_l}\right)}\,, \tag{6-7}$$

where u_g and u_l are the gas and liquid phase velocities respectively, and x is the thermodynamic quality. At very low void fractions, the static pressure drop for non-zero angles approaches the liquid hydrostatic head, and at high void fractions and flow rates, the static pressure drop is usually negligible due to the relatively low vapour densities.

The momentum pressure gradient per unit length, $(dp/dz)_{mom}$, which reflects the change in the kinetic energy of the flow due to the dynamic change in the vapour quality, is determined from Eq. (6-8),

$$\left(\frac{dp}{dz}\right)_{mom} = \frac{d\left(\frac{\dot{m}_{total}}{\rho_H}\right)}{dz}\,, \tag{6-8}$$

where $\dot{m}_{total} = \rho u$ is the overall two-phase mixture mass flow rate. The homogeneous momentum pressure drop between the flow inlet and outlet planes, Δp_{mom}, is given by Eq. (6-9),

$$\Delta p_{mom} = \dot{m}_{total}^2\left\{\left[\frac{\left(1-x\right)^2}{\rho_l\left(1-\varepsilon\right)}+\frac{x^2}{\rho_g\varepsilon}\right]_{outlet}-\left[\frac{\left(1-x\right)^2}{\rho_l\left(1-\varepsilon\right)}+\frac{x^2}{\rho_g\varepsilon}\right]_{inlet}\right\}. \tag{6-9}$$

If there is no change in two-phase flow quality along the length of the conduit and through the tube bundle, and no resultant change in the homogeneous density, then the contribution of the momentum pressure drop to the overall pressure drop reduces to zero.

The two-phase frictional pressure drop along a pipe, $\Delta p_{friction}$, is given by Eq. (6-10),

$$\Delta p_{friction} = \frac{2 f_{TP} L}{d} \rho_H u_H^2 , \tag{6-10}$$

where f_{TP} is the two-phase friction factor, L is the total length of the flow conduit, and d is the hydraulic diameter. The frictional pressure drop can also be given by Eq. (6-11),

$$\Delta p_{friction} = \frac{2 f_{TP} L}{d} \frac{\dot{m}_{total}^2}{\rho_H} . \tag{6-11}$$

The two-phase friction factor is empirically determined, and is a function of the Reynolds Number, Re, which is given by Eq. (6-12),

$$\mathrm{Re} = \frac{\dot{m}_{total} d}{\mu_{TP}} , \tag{6-12}$$

where μ_{TP} is the two-phase viscosity, given by Eq. (6-13),

$$\mu_{TP} = x\mu_g + \left(1 - x\right)\mu_l , \tag{6-13}$$

where μ_g and μ_l are the single-phase vapour and liquid viscosities respectively. The form drag pressure drop of an external two-phase flow past a bluff body, such as a bank of tubes is related to the flow dynamic head according to Eq. (6-14),

$$\Delta p_{drag} = \frac{C_{drag} A_p}{2} \rho_H u_H^2 , \tag{6-14}$$

where C_{drag} is the flow drag coefficient, and A_p is the projected area.

Figure 6-20 demonstrates the transient pressure drops measured in test T04 between the pressure transducers at locations 1 and 2 (labelled as the test section pressure drop), and between locations 2 and 3 (labelled as the rupture disc pressure drop). The initial steady-state pressure drop of 14kPa across the test section consists of the elevation head of the R-134a, which is 10kPa, and the pressure boost supplied by the compressed gas accumulator just before disc rupture, which is 4kPa. This static pressure drop decreases with the initiation of the blowdown as the pressure is relieved through the rupture disc and the fluid density is reduced by rapid phase transition from liquid to vapour. The initial pressure drop across the rupture disc is equivalent to the absolute vessel pressure of 598kPa since the region downstream of the rupture disc is initially in a vacuum, with a pressure of nearly 0kPa, when the rupture disc is closed. The opening of the rupture disc results in a very rapid discharge of the saturated vapour directly upstream. The propagation of the rarefaction wave upstream decreases the pressure drop across the rupture disc to a minimum at about 13ms, at which point most of the single-phase saturated vapour has been discharged through the rupture disc.

The downward propagation of the rarefaction wave produces an unsteady pressure drop across the test section, which is labelled as the 'acoustic' pressure drop term in Fig. 6-20. The transient pressure drop begins to rise at about 2ms, when the rarefaction wave passes location 2, and peaks at about 5ms, when the wave arrives at location 1, after which the pressure drop begins to drop due to liquid depressurisation. Following the arrival of the rarefaction wave, the liquid R-134a flashes to vapour and accelerates upwards, resulting in a rise in the two-phase fluid momentum pressure drop. The rise in the momentum pressure drop is observed to begin at about 7ms at the test section, and about 13ms at the rupture disc. The peak in the momentum pressure drop at the test section also occurs at 13ms. This indicates that the flashing two-phase fluid front originating at the liquid surface above the tubes and accelerating upwards towards the vacuum

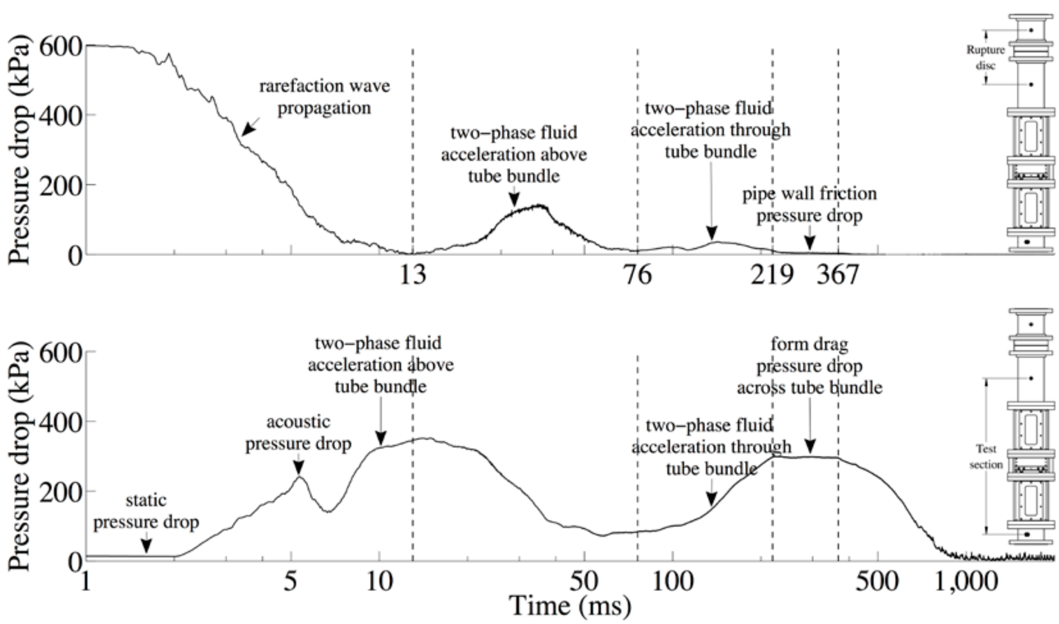

Figure 6-20. Transient pressure drop measured along the pressurised pipe with the tube bundle installed (test T04).

reservoir passes the pressure transducer at location 2 at 13ms.

The flow restriction imposed by the tube bundle limits the rate of the depressurisation and discharge upstream, and the acceleration of the liquid below the tubes is limited by its inertia. Once the average mass flow rate downstream of the tube bundle begins to equalise and the momentum pressure drop component begins to drop at about 21ms and 37ms across the test section and rupture disc respectively, the blowdown discharge begins in earnest and a significant acceleration of the two-phase fluid below the tubes occurs upwards through the tube bundle. Viscous effects then become dominant beginning at about 76ms and proceeding until the end of the transient. During this time, the pressure drop across the rupture disc is comparatively negligible since the friction at the pipe wall is small relative to the hydraulic drag pressure drop across the tube bundle. The form drag pressure drop across the tube bundle equalises at about 219ms, and a quasi-steady discharge is established at a maximum velocity with a pressure drop across the tube bundle that is greater than 300kPa. The wall friction downstream of the tube bundle basically disappears when the discharge flow reaches this quasi-steady state.

When the tube bundle is removed from the test section, the viscous fluid resistance (friction) along the pressure vessel wall boundary becomes uniquely responsible for the pressure drop during quasi-steady discharge. An example is shown in Fig. 6-21 from test T02. The trends in the pressure drop across the test section and rupture disc regions are similar to those observed in Fig. 6-20, the difference being that the form drag losses in the tube bundle do not appear in the measurements. The transient pressure difference across the rupture disc remains fairly constant at 9 – 12ms with a pressure drop of about 130kPa, which was demonstrated in section 5.4 to be associated with single-phase vapour choking. The peak in the ‘acoustic’ pressure drop occurs at about 7ms, the instant at which the rarefaction wave passes location 1. The acceleration pressure drop across the test section rises shortly afterwards, starting at 9ms, and peaks at 16ms. Once again, this coincides with the timing of the increase of the momentum pressure drop across the rupture disc, as was previously observed in Fig. 6-20, indicating that the accelerating two-phase front passes location 2 at 16ms.

The amplitude of the momentum pressure drop is greater in magnitude in Fig. 6-20 (350kPa at t = 13ms) compared to Fig. 6-21 (200kPa at t = 16ms). This is because the rate of change of momentum, which is related to the fluid inertia, is greater in test T04 than in test T02.

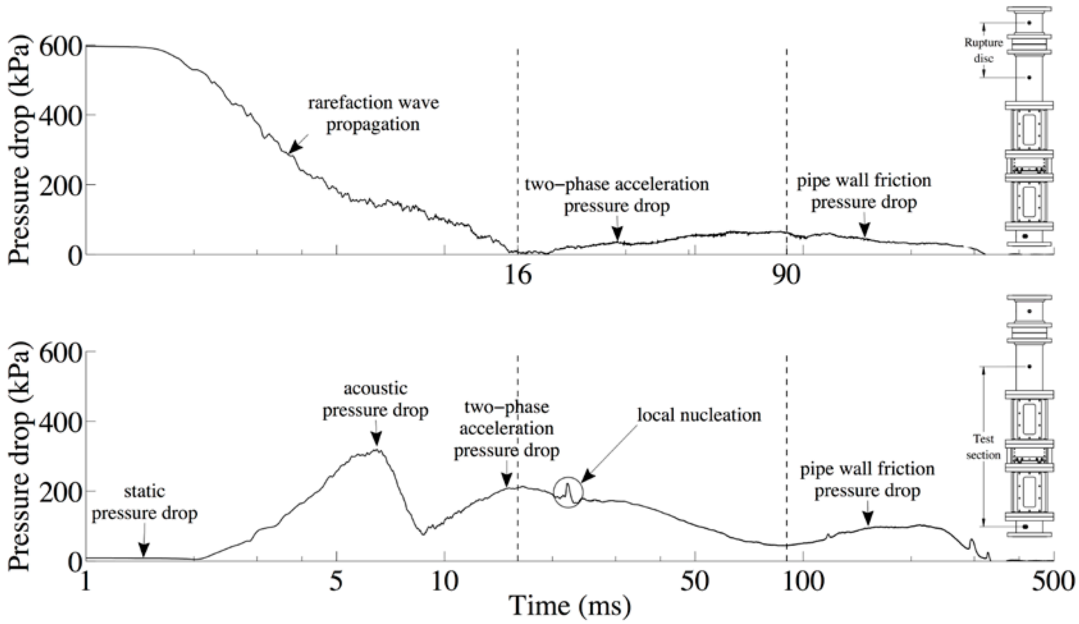

Figure 6-21. Transient pressure drop measured along the pressurised pipe with the tube bundle removed (test T02).

Test T04 was performed with 15.4L of liquid R-134a, while test T02 was performed with only 9.3L of liquid R-134a. The small pressure spike observed in Fig. 6-21 at 22ms is presumably due to local nucleation effects on the surface of the pressure transducer. The rapid generation of vapour and the acceleration of the two-phase fluid continues to contribute to the momentum pressure drop until about 90ms, after which the average mass flow rate equalises and a pressure gradient is established along the pipe due to friction at the inside walls for the remainder of the blowdown transient. The amplitude of the frictional pressure drop during this stage is considerably smaller than the form drag pressure drop amplitude shown in Fig. 6-20.

A comparison of the pressure drop measured across the test section (locations 1 and 2) with and without the tube bundle installed (tests T06 and T03 respectively) is shown in Fig. 6-22. The initial liquid volumes in these two tests were similar (21% in test T06 and 23% in test T03). The initial unsteady acoustic pressure drop is observed to be very similar for both tests and does not appear to be influenced by the presence of the tube bundle. The wave propagation timings depend on the initial liquid level and the peak acoustic pressure drop is therefore slightly delayed in test T06 due to the slightly lower liquid free surface level (265mm in test T06 and 290mm in test T03).

Following the initial unsteady pressure wave propagation effects, the pressure drop across the test section rises due to the acceleration of the two-phase fluid. The peak momentum pressure drop of about 250kPa at 11ms in test T06 is lower than the peak of about 350kPa obtained in test T04 shown in Fig. 6-20. This is because the liquid level in test T06 is below the tubes, which means that the region between the transducers is occupied by a greater amount of single-phase vapour, which has a considerably lower inertia than the liquid. The peak in the momentum pressure drop observed at 11ms in test T06 is produced by a small amount of flashing liquid, which had collected on the steel surfaces in the tube bundle prior to the initiation of the transient due to steady-state condensation.

The observations in the measurements are supported by the high-speed flow visualisations shown in Fig. 6-23. A two-phase fluid mixture can be observed accelerating upwards in the upper window at t = 10ms while the liquid in the lower window has not yet began flashing to vapour. This two-phase mixture cannot have originated anywhere other than between the two windows, which is where the tube bundle is located. By t = 20ms, the accelerating two-phase mixture has disappeared, and the liquid below the tubes begins rapidly transitioning to vapour. The two-phase mixture that originates at the liquid level surface can be seen entering the bottom frame of the upper window at t = 30ms, after which a continuous two-phase flashing

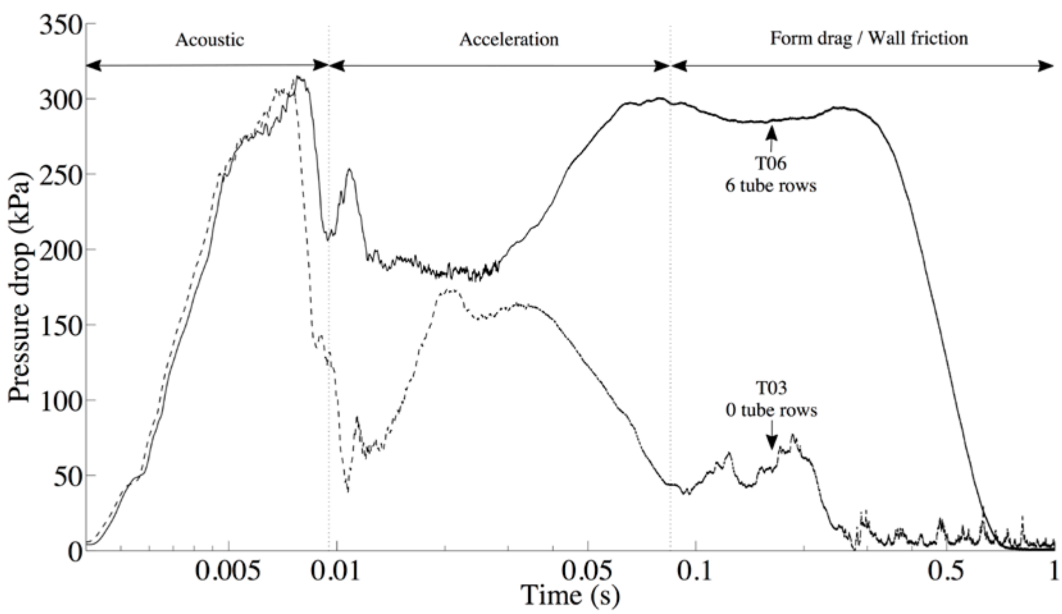

Figure 6-22. Transient pressure drop across the test section with and without the tube bundle (tests T03 & T06).

mixture persists for the entire duration of the blowdown transient. The timing of the acceleration of this two-phase front (t = 30 – 40ms) coincides with the beginning of the rise in the acceleration pressure drop through the tube bundle observed in Fig. 6-22 for test T06. Therefore, the peak at t = 11ms must be caused by a flashing two-phase mixture that had originated on the surface of the tubes in the tube bundle.

A peak in the pressure drop can also be observed in Fig. 6-22 for test T03 at 11ms, similarly caused by steady-state condensation at the steel side-walls of the test section. Since the tubes were removed in this experiment, the surface area available for condensation is smaller, and a lower amplitude is observed for the momentum pressure drop peak. The pressure drop rises to a maximum of about 170kPa at 21ms and then drops briefly. At about 25ms, rapid vapour generation in the pressure vessel produces a temporary recovery in the pressure. The mass flow

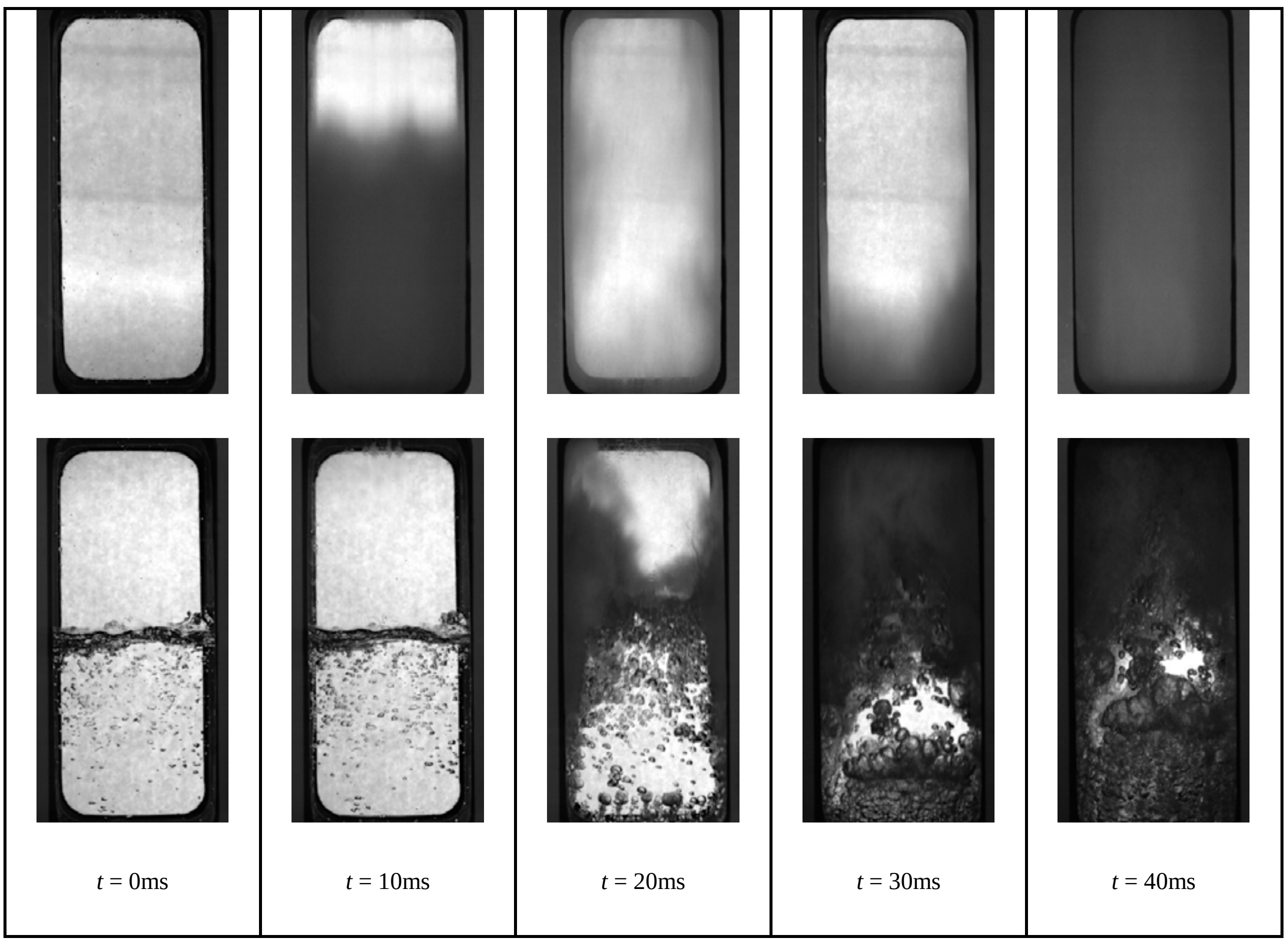

Figure 6-23. High-speed flow visualisation of accelerating two-phase fluid front (test T06): (a) upper window (top), (b) lower window (bottom).

rate then begins to drop, reducing the pressure drop to about 50kPa, which remains fairly steady for the remainder of the transient until the liquid inventory is depleted.

In Fig. 6-24, the transient pressures at the three transducer locations along the blowdown pipe are shown for tests T03 and T06. It has been demonstrated in Fig. 6-22 that the form drag losses in the tube bundle create the maximum transient pressure drop across the tubes. Looking at the pressure gradients in Fig. 6-24, it can be observed that the pressure drop across the tube bundle in test T06 significantly contributes to the overall pressure drop, whereas in test T03, a pressure gradient is established due to viscous losses at the pipe walls. The transient pressure drop measurement across the tube bundle depends largely on the fluid flow rate during the transient blowdown. The upstream pressure in test T06 rises at about 30ms due to the acceleration of the flashing two-phase fluid. At about 75ms the pressure drop across the tube bundle in test T06 reaches its maximum amplitude and remains fairly constant until about 300ms. This quasi-steady condition suggests that the two-phase flow through the tube bundle is choked during this time. The upstream pressure remains constant while the two-phase mixture is being discharged through the tube bundle at maximum velocity, until the liquid inventory is reduced to the point that the vapour generation can no longer maintain the critical pressure ratio through the tube bundle. In terms of fluid drag on the tubes, the maximum drag is established

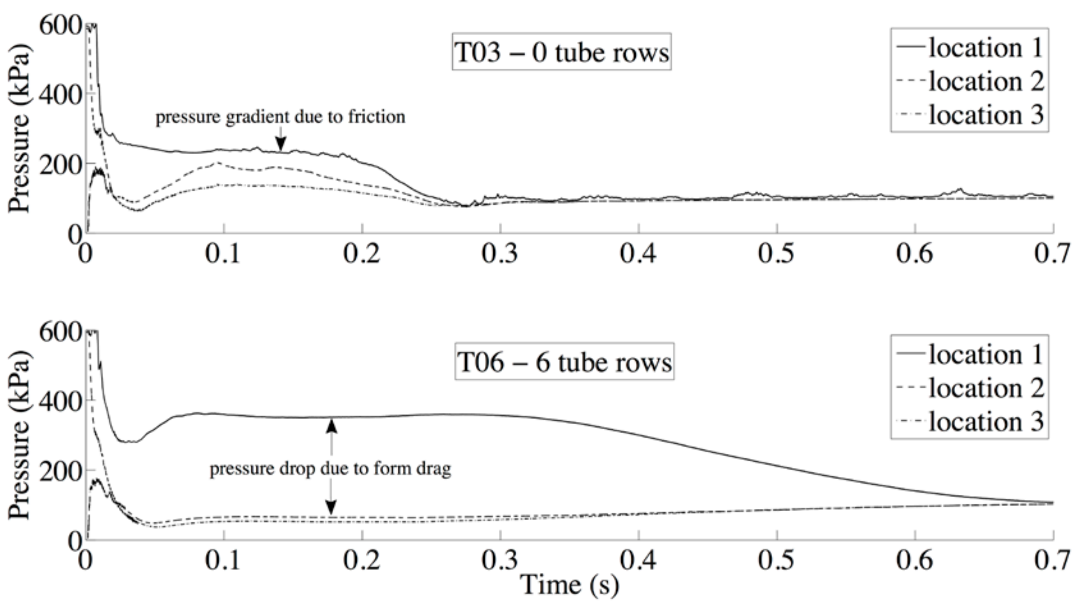

Figure 6-24. Transient pressure comparison in the pressure vessel with and without the tubes (tests T03 & T06).

when the fluid flow rate through the tube bundle is maximum, which occurs when the two-phase flow is choked.

7. Analysis of the dynamic tube loading

The overall objective of the dynamic tube loading analysis in this section is to develop a physical understanding of the relationship between the transient hydraulic drag loads and the two-phase flow development in the experiments, which can then be used to predict the expected dynamic loads in an industrial steam generator tube bundle during blowdown. Figure 7-1 presents a sample transient load measurement obtained from test T05, which was performed with a tube bundle containing 6 rows of tubes. The initial volume of liquid in the pressure vessel for test T05 was 12.1L, which corresponds to a liquid column height of 650mm with the liquid free surface level visible at the upper window in the pressure vessel. The physical mechanisms of fluid transient tube loading during the blowdown were determined based on the thermal hydraulic phenomena described in chapters 5 and 6 as well as the synchronised high-speed flow visualisations observed through the sight windows located below and above the tube bundle. The oscillations that appear in the first 0.1s of the signal in Fig. 7-1, which persist throughout the remainder of the transient at reduced amplitudes, are caused by the vibrations of the pressure vessel at its natural axial frequency. The frequency of the oscillations is supported by accelerometer measurements obtained at the test section, and the vessel vibrations were also identifiable in the high-speed flow visualisations.

The tube loading trends shown in Fig. 7-1 represent the general tube loading behaviour observed in all of the tests performed with multiple tube rows mounted in the test section. The initial stage of the transient is characterised by a large rate of change in the fluid's momentum. The load signal rises rapidly as the pressurised vapour downstream of the tube bundle accelerates away from the tubes and the two-phase fluid below the tubes accelerates through the tube bundle. At about 150ms, the tube loading begins to level off at about 8kN as the flow rate through the tube bundle becomes established, and the tube bundle loading reaches a maximum value of about 8.5kN. This persists at a nearly constant amplitude for about 100ms, after which the two-phase mixture flow rate begins to decrease once enough of the liquid inventory below the tubes has been depleted to the point that the initial rapid rate of vapour generation cannot be sustained. As the two-phase flow through the bundle begins to decelerate, the load signal tapers off and

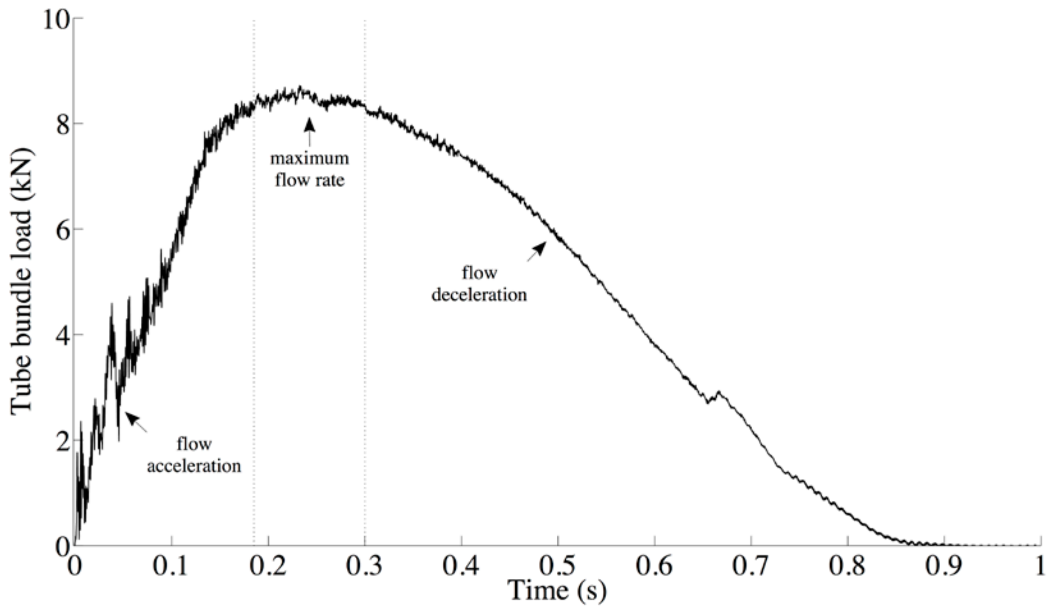

Figure 7-1. Sample tube bundle load transient (test T05).

asymptotes towards 0kN. It is observed in Fig. 7-1 that the maximum tube loading occurs when the two-phase fluid flow rate through the tube bundle is a maximum during the ‘quasi-steady’ discharge phase of the transient associated with choked flow through the tubes.

7.1 Effect of the initial liquid level on tube loading

The influence of the liquid level in the pressure vessel, or more specifically the location of the liquid free surface with respect to the tube bundle, on the transient loading of the tubes was investigated by varying the initial amount of liquid R-134a inside the pressure vessel and performing experiments with identical pressure vessel dimensions and tube bundle geometry. Industrial steam generators are typically designed such that the tube bundle is submerged in water at all times during operation, but the tubes may become uncovered if the water level falls sufficiently. In addition, the quality of the saturated steam-water mixture varies at different locations in the steam generator and with different amounts of heat transferred from the tubes. Figure 7-2 shows a comparison of transient tube loads measured in tests T06 and T04 with the initial R-134a liquid free surface below and above the tube bundle respectively. The transient tube bundle load comparison presented in Fig. 7-2 shows that the initial liquid level does not significantly affect the maximum load amplitude of about 8kN during the blowdown.

When the region inside and downstream of the tube bundle is initially occupied by vapour (liquid initially below the tubes), the maximum load plateau across the tubes is established much more quickly. As the liquid inventory is much smaller in this case, 4.9L of liquid R-134a in test T06 compared to 15.4L in test T04, the blowdown time is shorter. When the liquid is initially above the tube bundle, the fluid acceleration through the tube bundle is limited by the inertia of the liquid, resulting in a slower rise in the load signal and a time delay of about 0.2s before maximum tube loading is established. Since the rates of vapour generation and fluid discharge below the tubes are controlled primarily by the resistance to the flow of the tube bundle, the fluid load on the tube bundle during quasi-steady discharge depends mainly on the upstream thermodynamic conditions and the tube bundle geometry, and is not influenced by the initial liquid volume.

When the liquid free surface is initially below the tube bundle, the rarefaction wave originating from the rupture disc location is observed to exert a sudden impulsive ‘acoustic’ load with a peak of nearly 5kN on the tubes as it propagates through the tube bundle towards the bottom of the pressure vessel. The magnitude of the load can be estimated conservatively by

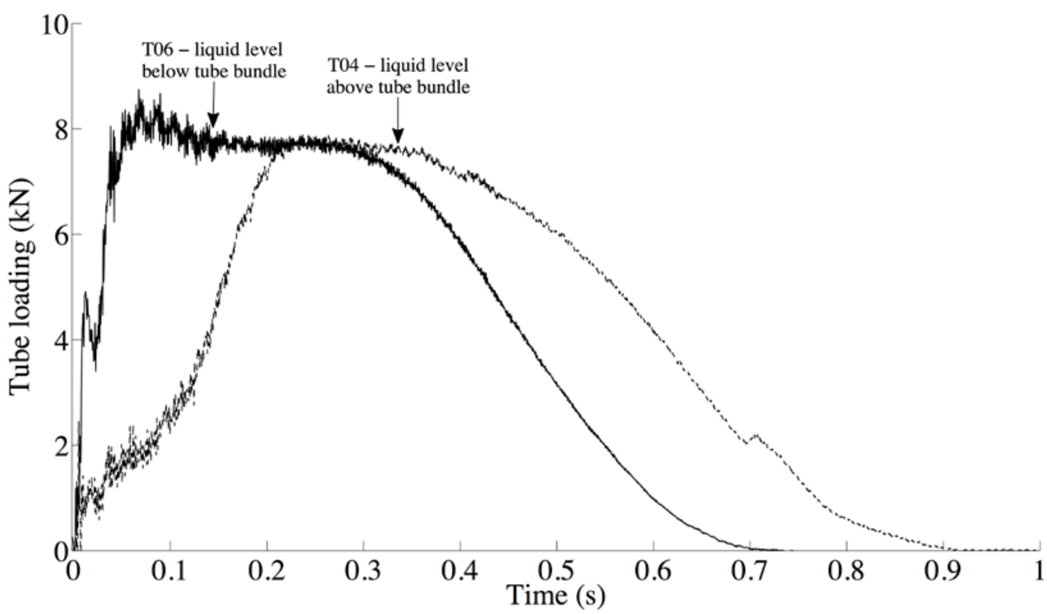

Figure 7-2. Comparison of the liquid level influence on tube loading (tests T04 & T06).

assuming that the pressure reduction of about 300kPa in test T06, shown in Fig. 6-24, is uniformly distributed over the cross-sectional flow area of 0.01864m^2, producing a computed acoustic load of 5.5kN on the tube bundle. The transient load measurement obtained in the initial 250ms of test T06 is shown in Fig. 7-3. The estimated ‘acoustic’ loading of 5.5kN is very close to the 5kN dynamic load measured by the load cells about 10ms following the opening of the rupture disc.

The sharp rise in the ‘acoustic’ load signal begins about 6ms into the blowdown, which coincides with the time during which the rarefaction wave passes through the tube bundle based on calculated propagation velocity timings, further confirming that the rapid pressure wave propagation effects are responsible for the sudden loading observed. The dynamic load amplitude decreases at about 14ms, following the acceleration of the vapour surrounding the test section caused by the sudden reduction in pressure, and begins to increase again at about 21ms, which was shown in Fig. 6-23 to be the time at which the flashing two-phase fluid accelerates through the tube bundle. This brief load of about 5kN during the initial transient stage of the blowdown is observed to be lower than the fluid drag load of about 8kN obtained during the subsequent acceleration of the two-phase fluid through the tube bundle. When the tube bundle is initially submerged in liquid in test T04, the rarefaction wave rapidly passes through the liquid

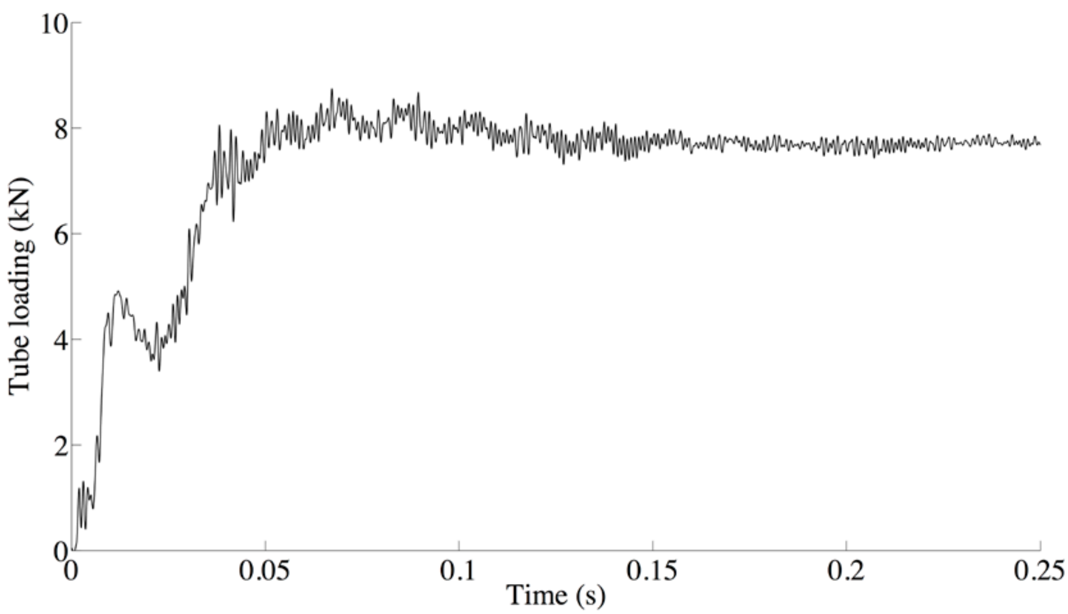

Figure 7-3. Transient acoustic load measured in the tube bundle (test T06).

and does not produce any significant 'acoustic' load measurement.

Figure 7-4 presents a direct comparison of the pressure drop measured across the tube bundle in tests T04 and T06, for which the transient drag loads were presented in Fig. 7-2. The transient pressure drop measurements contain upward spikes in the first 50ms of blowdown associated with the acceleration of the fluid above the tubes, after which the measured pressure drop is produced by the fluid acceleration from the bottom of the pressure vessel through the tube bundle towards the vacuum reservoir. As was shown in Fig. 7-2, the pressure drop in both tests in Fig. 7-4 during the 'quasi-steady' discharge phase of the blowdown is basically the same. The measurements shown in Figs. 7-2 and 7-4 demonstrate very similar trends, which confirms that a direct correlation exists between the transient two-phase tube loading and the transient pressure drop across the tube bundle, provided that the tube bundle geometry is the same and the fluid properties are similar.

In addition to investigating the effect of the location of the liquid free surface with respect to the tube bundle, the relative volume of liquid R-134a below the tubes before blowdown, or the ratio of liquid to vapour in the pressure vessel, was also studied in these experiments. Test T01 was carried out with a small initial liquid inventory of 0.8L, whereas test T08 was performed with the same pressure vessel dimensions and test section geometry as test

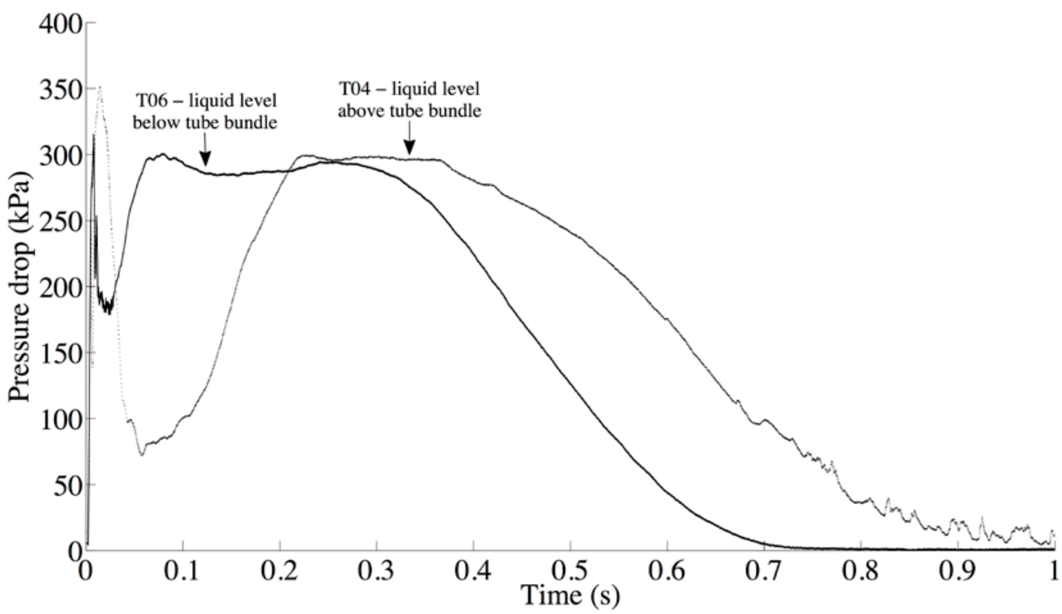

Figure 7-4. Comparison of pressure drop across the tube bundle for different initial liquid levels (tests T04 & T06).

T01, but with 14.3L of liquid R-134a. The respective liquid volume fills in tests T01 and T08 are 3% and 51%. Unfortunately, no direct measurement of tube loading is available for test T01, and the pressure drop measured across the tube bundle is relied on instead to provide a quantitative indication of the relative load magnitude between the tests. The relationship between the tube loading and pressure drop measurements was demonstrated to be a reliable indicator of the relative magnitudes in Figs. 7-2 and 7-4.

Figure 7-5 shows a comparison of the pressure drop measured across the tube bundle in tests T01 and T08. The pressure drop in test T08 reaches a maximum pressure that is greater than 300kPa. On the other hand, the pressure drop in test T01 only rises briefly as the two-phase mixture accelerates through the tubes, reaching a peak pressure drop of about 200kPa at 95ms. The pressure drop then decreases for the remainder of the transient. Thus, although the liquid level was observed not to significantly influence the amplitude of tube loading, Fig. 7-5 shows that the maximum load amplitude might not be attained if there is an insufficient initial liquid inventory below the tubes. This indicates that a minimum amount of liquid is required in order to sustain a vapour generation rate upstream of the tubes to produce the maximum pressure drop and tube loading during the blowdown transient.

The increase in the pressure below the tubes is caused by the expansion of the fluid in

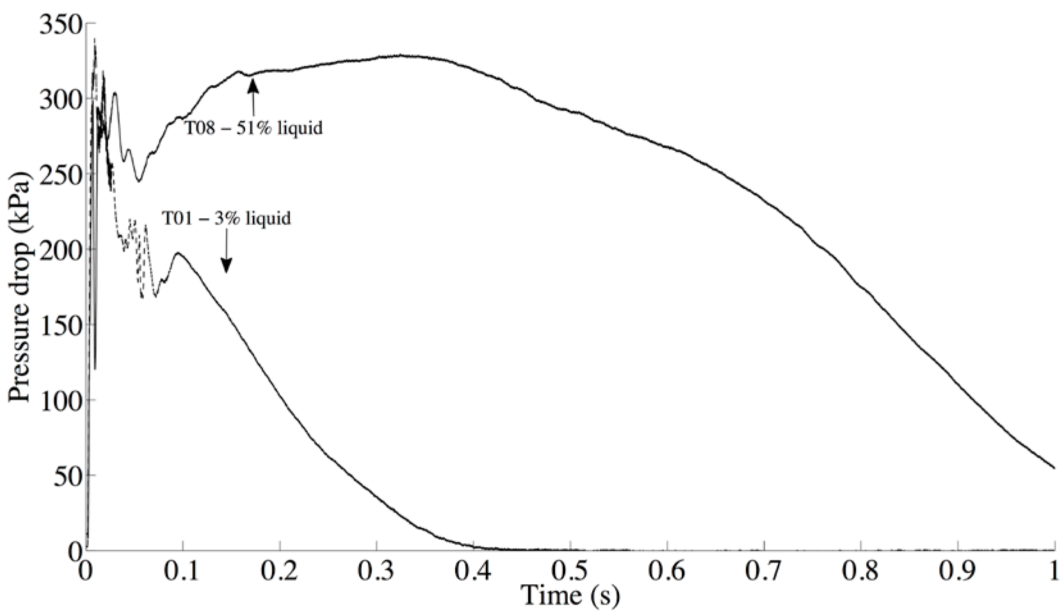

Figure 7-5. Comparison of pressure drop for different initial liquid inventories (tests T01 & T08).

this region when the rate of volumetric expansion exceeds the rate of volumetric discharge. The results presented in Figs. 7-4 and 7-5 demonstrate that under similar initial thermodynamic conditions, pressure vessel dimensions, and tube bundle geometries, the flow through the tube bundle will have the same maximum pressure drop regardless of the initial volume of liquid, provided that a maximum rate of vapour generation can be sustained during the transient blowdown discharge through the tube bundle. The maximum pressure drop across the tube bundle occurs when the fluid flow through the tube bundle is at its maximum because it has become choked.

7.2 Effect of the pressure vessel volume on tube loading

A comparison of tube load measurements obtained using different pressure vessel volumes is shown in Fig. 7-6. Test T05 was carried out using a 23.6L pressure vessel, and test T08 was performed with a longer section of pipe at the bottom of the vessel giving a total pressure vessel volume of 27.8L. The percentage of the vessel volume filled with liquid is about 51% in both tests. In test T05, this corresponds to a liquid column height of 650mm with the liquid level above the tube bundle, and in test T08 the liquid level height is 768mm with the liquid free surface inside the tube bundle. Since the region above the tubes is initially vapour in test T08, the pressure drop across the tube bundle rises quickly and produces a rapid rise in the transient tube loading in the first 50ms of the blowdown. Furthermore, given that test T08 was performed with 14.3L of liquid R-134a compared to 12.1L in test T05, the time duration during which the tube bundle is subjected to maximum loading is longer. The larger initial liquid inventory sustains a longer period of rapid vapour generation and choked two-phase flow through the tube bundle.

The amplitudes of the maximum tube bundle loads in the two tests compared in Fig. 7-6 is basically the same, which is not surprising given that the upstream thermodynamic conditions and the tube bundle geometry are unchanged. This produces similar mass flow rates through the tube bundle during the ‘quasi-steady’ discharge, which results in an equivalent magnitude of drag load on the tubes. The maximum load in test T05 is observed to be slightly higher than that

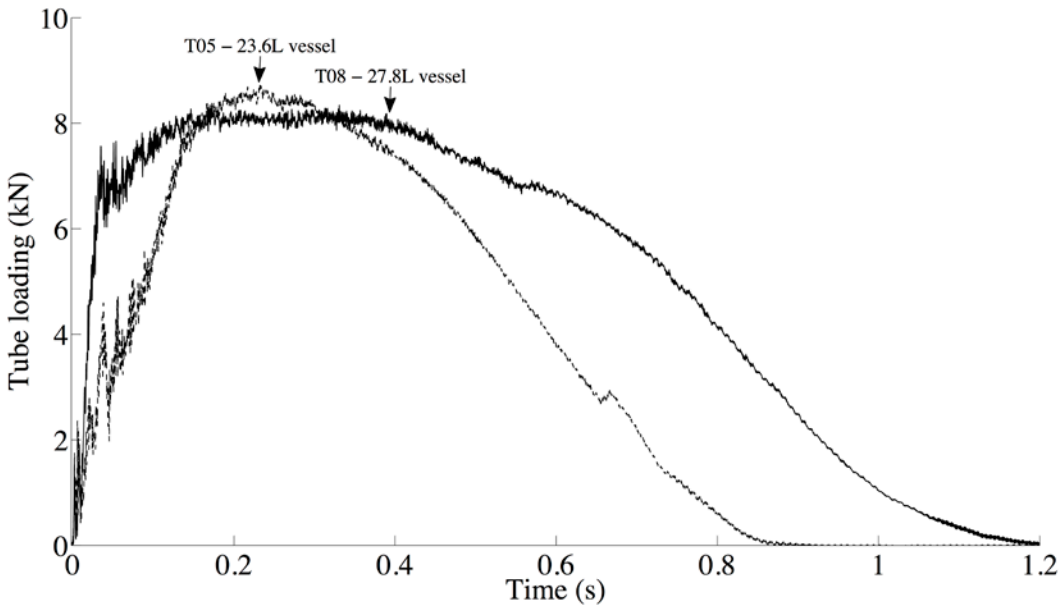

Figure 7-6. Comparison of tube loading for different pressure vessel volumes (tests T05 & T08).

in test T08, which can be attributed to the difference in the vapour generation rate between the two tests. High-speed flow visualisations in both experiments show that the rate of vapour generation is higher due to the presence of pre-existing vapour bubbles in the liquid bulk before blowdown, resulting in a higher pressure below the tubes during transient fluid expansion. This is also supported by transient pressure measurements obtained at the bottom of the pressure vessel. A comparison of the transient pressures in the first 250ms of both tests is presented in Fig. 7-7, showing the higher initial amplitude of pressure in test T05, and the subsequent comparable rates of increase in pressure due to liquid phase transition and fluid expansion in both tests T05 and T08.

7.3 Effect of the number of tube rows on tube loading

It was recognised based on the results presented and discussed in the previous sections that a parametric investigation of the variation in the transient tube loading with respect to the tube bundle geometry (number of tube rows) is essential in order to reveal the underlying physics of the phenomenon and develop a predictive methodology for dynamic tube bundle loading. It

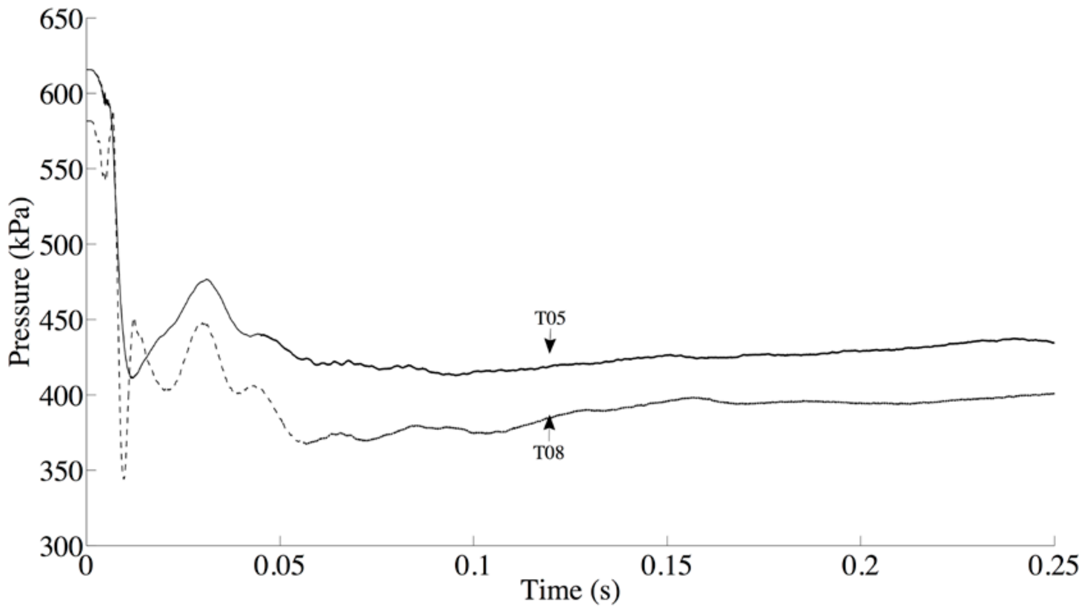

Figure 7-7. Comparison of initial transient pressure upstream of tube bundle (tests T05 & T08).

has been demonstrated that under similar initial thermodynamic conditions and tube bundle geometries, the tube bundle is subjected to the same maximum load amplitudes, which occur during the maximum quasi-steady two-phase blowdown discharge period through the tube bundle. By filling the 27.8L pressure vessel with about 50% liquid R-134a by volume, a sufficient liquid inventory is made available below the tubes to sustain the maximum observed rate of vapour expansion and consequently, maximum two-phase flow rate through the tube bundle.

Additionally, it was demonstrated that the maximum transient tube loads remain the same regardless of whether the initial liquid level is below or above the tube bundle. In fact, by having the region downstream of the tube bundle initially occupied by vapour, the maximum pressure drop across the tubes is established quicker, allowing for a longer duration of maximum quasi-steady drag loading. Thus, by charging the liquid in the pressure vessel so that the liquid surface level is inside the tube bundle and maintaining relatively uniform temperatures, the effect of the number of tube rows on the dynamic tube bundle load can be examined by varying the number of tube rows in the tube bundle. This corresponds to a liquid fill of about 50% for the 27.8L pressure vessel volume. The tube bundle test section was designed so that the number of rows of tubes can be modified between each test run. An example of tube load measurements obtained with different numbers of rows in the tube bundle is presented in Figure 7-8, which compares the transient tube loads obtained in tests T08 and T11, with 6 and 3 tube rows respectively, and all other initial conditions kept practically constant. The initial liquid volumes are 51% and 53% in tests T08 and T11 respectively. With this amount of liquid, the initial liquid surface level is inside the tube bundle in both tests.

The trends of the transient tube load measurements shown in Fig. 7-8 are observed to be very similar to each other. In particular, the rates of the change in the transient drag loading and the timing of the flow transition from the initial acceleration to the quasi-steady flow through the tubes are similar in both tests. The main difference between the two dynamic load measurements is the amplitude of the maximum tube loading, which is about 8.1kN for 6 tube rows and about 6.6kN for 3 tube rows. The duration of the transient loading also changes with the deeper tube bundle producing a greater flow resistance and a longer blowdown transient. This can be explained by the lower restriction imposed to the two-phase flow when the tube bundle contains a smaller number of rows of tubes.

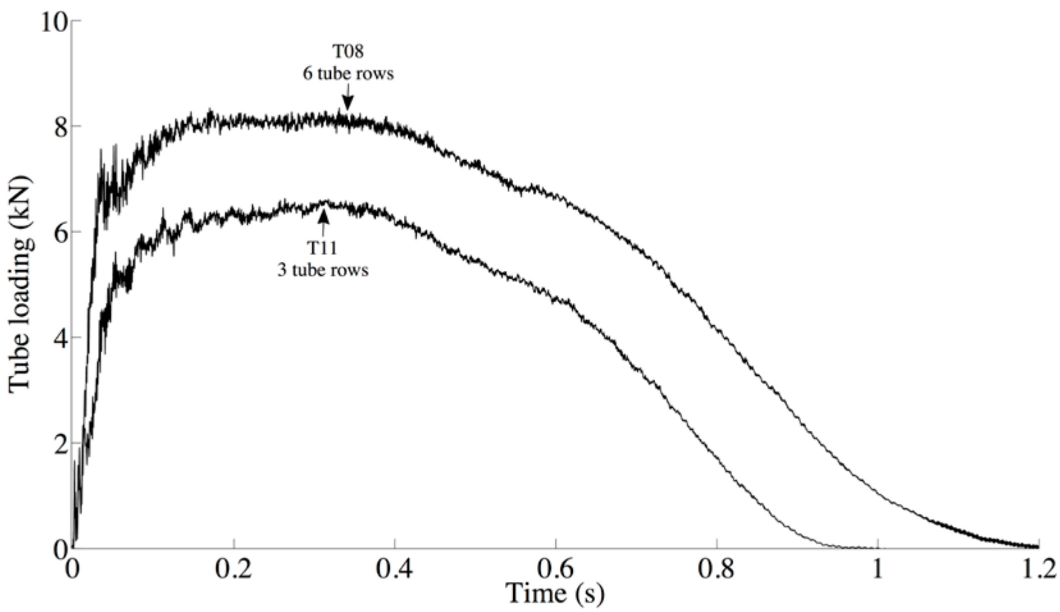

Figure 7-8. Comparison of tube bundle loading with different number of tube rows (tests T08 & T11).

7.4 Tube load drag coefficient

In Fig. 7-9, the dynamic tube bundle drag load in test T08, which was performed with 6 rows of tubes and 51% of the vessel initially filled with liquid, is compared to the transient pressure loading measured across the tube bundle. The dynamic pressure load across the tube bundle is computed simply by multiplying the pressure drop across the tube bundle by the cross-sectional flow area of the pressure vessel. Figure 7-9 demonstrates that after the first 55ms of the transient in which the acoustic and inertial effects downstream of the tube bundle are significant, the trends in the pressure drop measurement follow the load signal very closely for the entire remaining duration of the transient. Under steady-state conditions, the drag force exerted on a tube bundle, F_{drag}, is directly proportional to the pressure drop established across the full bank of tubes, Δp. The proportionality constant is a product of the cross-sectional flow area, A, and a drag coefficient, C_{drag}, as given by Eq. (7-1),

$$F_{drag} = C_{drag} \cdot A \cdot \Delta p\,. \tag{7-1}$$

In the present experiments, the drag coefficient corresponding to the pressure drop across the tube bundle with 6 rows of tubes was empirically determined through a series of experiments

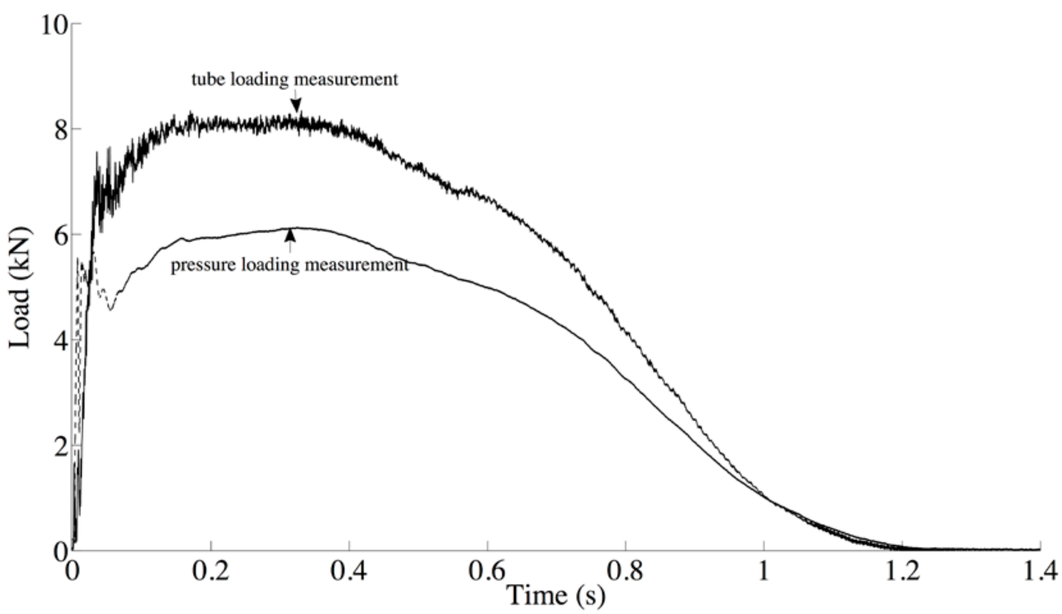

Figure 7-9. Comparison of pressure drag and tube bundle loading measurements (test T08).

to be 1.41. Hence, the dynamic load measured on the 6 row tube bundle during blowdown can be quantitatively related to the transient pressure drop across the tube bundle by simply multiplying the pressure drop by the pressure vessel hydraulic flow area and the empirical drag coefficient according to Eq. (7-1). The tube loading drag coefficient is numerically determined by matching the area under the tube load and pressure drop curves for the quasi-steady portion of the transient. The flow through the bundle is choked during this time, producing quasi-steady maximum amplitudes in both the load and pressure drop measurements. The measured pressure drop is corrected for hydrostatic head, which was typically very small and never greater than about 3% of the maximum pressure difference, depending on the initial level of liquid in the reservoir. This procedure used to determine the drag coefficient eliminates subjective bias, and provides a value that enables the transient pressure drop and tube load signals to agree very well with each other for the majority of the blowdown duration as shown in Fig. 7-10.

By determining the variation of the drag coefficient with the numbers of rows of tubes, the fluid drag loading on the tube bundle, which depends on the number of rows, the two-phase mass flow rate, and the tube bundle geometry, can be related to the transient pressure drop measured across the tube bundle for all of the experiments performed through an empirical drag coefficient per tube row. The overall empirical drag coefficient determined for the tube bundle

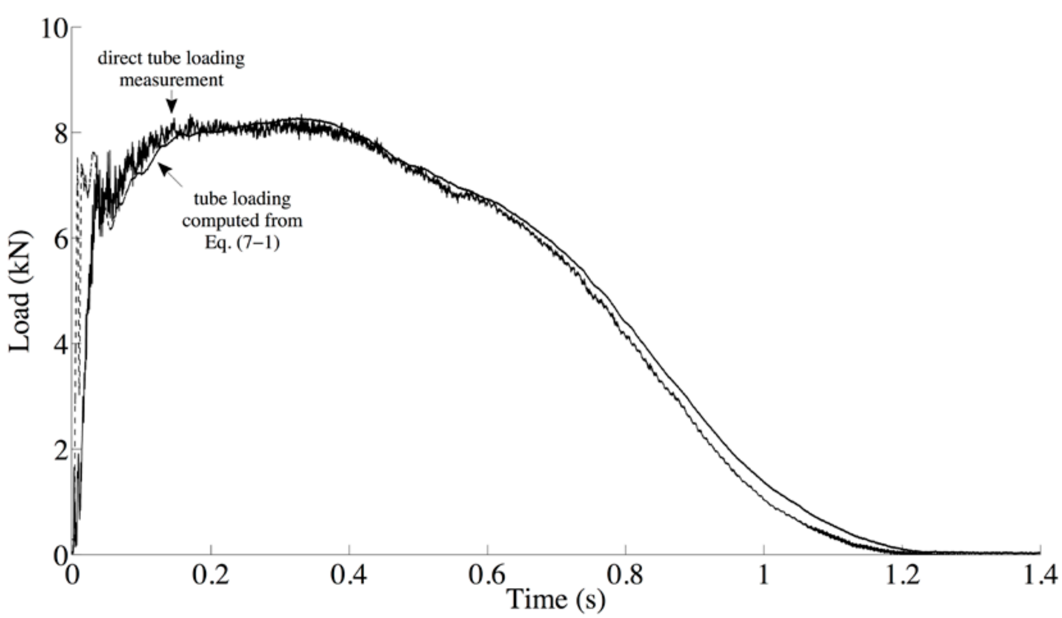

Figure 7-10. Comparison of tube loading measured and computed using empirical drag coefficient (test T08).

with different numbers of tube rows is shown in Table 7-1 and plotted in Fig. 7-11. The overall hydraulic drag on a tube bundle is proportional to the number of rows of tubes in the bundle. The mean drag for a single transverse row is determined by dividing the total pressure drop across the entire tube bundle by the number of rows of tubes.

If the number of rows of tubes in a staggered tube array is less than 10, the pressure drop per tube row may increase as the number of transverse rows is reduced [6]. This is because the flow losses in the first row of the tube bundle and the downstream wake effects and their associated losses become significant when the number of rows of tubes is 3 or less. Hence, the pressure drop per tube row in the first few rows can be significantly different from the rest of the bundle, and in steady-state incompressible flow drag calculations for tube bundles in cross-flow, correction factors are typically employed to determine the drag coefficient for the leading rows of tubes. For high velocity flows ($Re > 10^5$) the correction factor is about 50% for the 1st row, 17% for the 2nd row, and 2% for the 3rd transverse row of a staggered bank of tubes. The pressure drop across a tube bundle varies in the first 3 rows and becomes fully developed by about the 4th tube row. The pressure drop per tube row is then expected to increase proportionally with the number of transverse tube rows. This relationship is shown by the dashed line in Fig. 7-11. As expected, the drag coefficient for 2 and 3 rows does not fall on the line since the flow through such shallow tube arrays is not typical of deeper tube arrays. The relationship between the drag coefficient and the number of tube rows, which was determined empirically in the present blowdown experiments, is given by Eq. (7-2) below,

$$C_{drag} = 1.17 + 0.04z \,, \tag{7-2}$$

where z is the number of rows of tubes.

Table 7-1. Empirical tube load coefficient values from two-phase blowdown experiments.

Number of tube rows	2	3	4	5	6	6	6	6
Drag coefficient	1.230	1.285	1.328	1.370	1.405	1.410	1.408	1.405

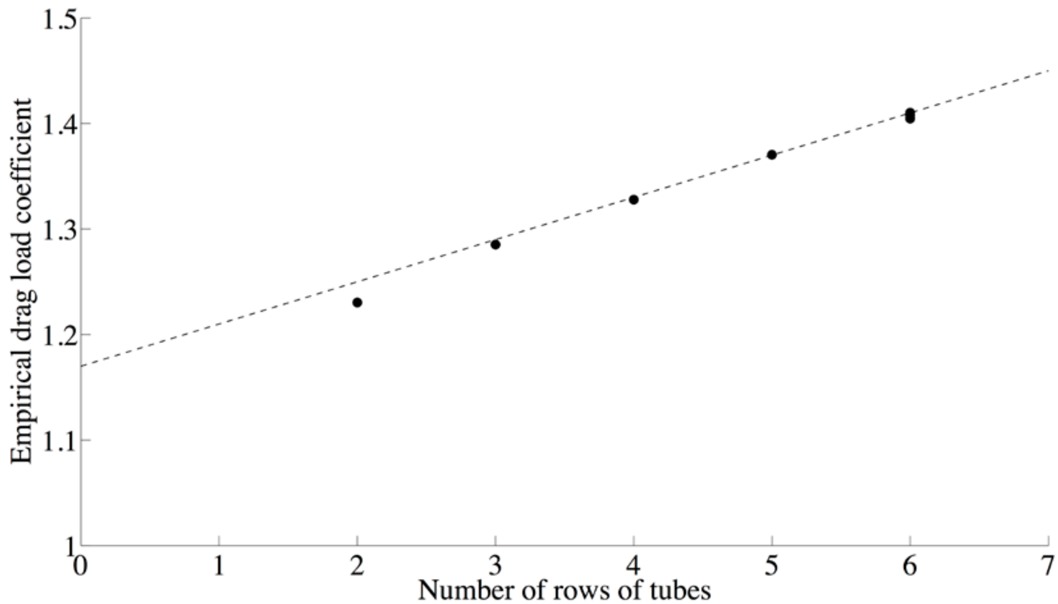

Figure 7-11. Tube bundle drag load coefficient.

The predicted drag loads based on the measured pressure drop obtained using Eq. (7-2) are compared to the measured dynamic loads for tests T12, T11, T09, and T08, with 2, 3, 5, and 6 rows of tubes respectively, in Fig. 7-12. All of the tests were performed with similar initial conditions and liquid levels. The results show that the empirical drag coefficient accurately scales the pressure drop and loads for the all of tests for which the tube bundle contained at least 3 tube rows. For the experiment performed with only 2 rows of tubes in the bundle, the load amplitude during the quasi-steady period of the transient is slightly over-predicted, which is expected since the flow in this tube bundle configuration is not representative of the flow in deeper bundles.

7.5 Comparison with steady state flows

There has been much work in the fields of heat transfer, fluid dynamics, and flow-induced vibrations of tube banks investigating the drag of a tube within a bundle in cross-flow. The hydraulic drag is generally formulated as a function of pressure drop and empirical drag coefficients. These depend on the spacing between the tubes, the number of transverse rows, and

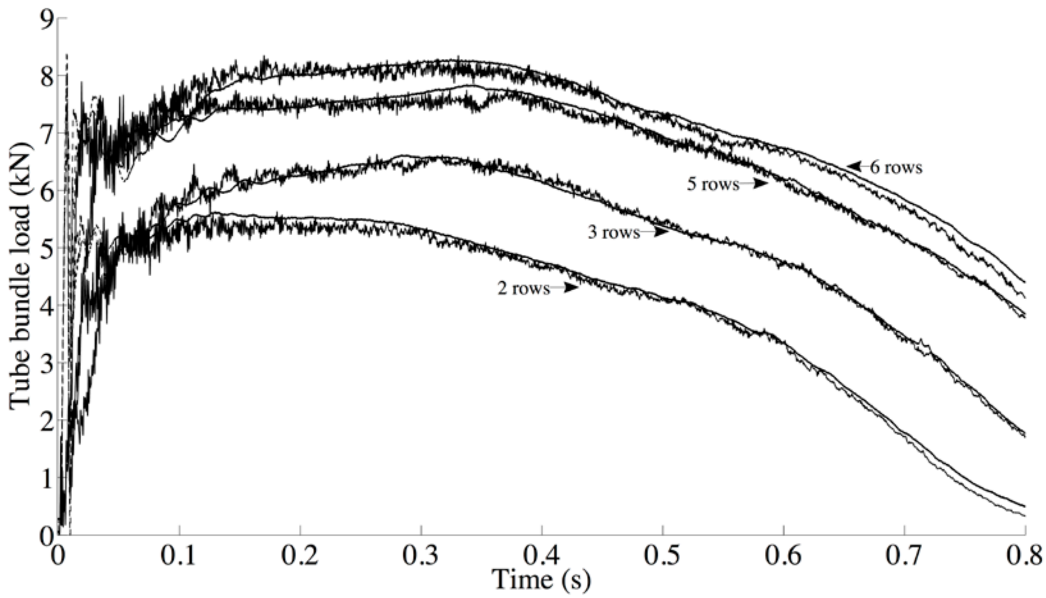

Figure 7-12. Comparison of load predicted from pressure drop to measured load (tests T08, T09, T11, & T12).

the fluid properties. Two-phase drag coefficients for tube bundles are empirically determined from experimental investigations, with the most widely adopted correlation presented by Ishihara et al. [31]. The correlation uses two-phase friction multipliers for the liquid and vapour phases, which do not approach the natural limits for single-phase liquid and vapour flows and contain an unrealistic step discontinuity between the liquid and vapour friction multipliers at Re = 2000. Furthermore, the two-phase friction multipliers only depend on an empirical two-phase turbulence correction parameter, which does not account for void fraction or mass flow rate.

Generally, the accuracy of the two-phase pressure drop correlations for tube bundles presented in the literature is limited by the range of mass flow, fluid properties, and tube bundle geometries in the experiments for which the models were developed. The predictive capabilities of currently available models are not yet fully resolved, and the prediction of two-phase pressure drop across tube bundles continues to be the focus of much experimental and theoretical research [32, 33]. Under steady incompressible flow conditions, the acceleration component of the pressure drop can be estimated by determining the rate of change of the momentum. When compressibility and phase change effects are included due to boiling and depressurisation, changes in state can produce rapid increases in velocity with reduction in fluid density.

Therefore, the rate of change of momentum may not be constant through the various rows of the tube bundle. It is evident then that even the case of two-phase steady flow through a tube bundle with heat and mass transfer is very difficult to model. Thus, the need to approximate the transient two-phase pressure drop in the present blowdown experiments using simplifying assumptions is stipulated by the complex nature of the dynamic flow development through the tube bundle.

A conservative 'single-phase' treatment of the flow using averaged fluid properties offers a starting point for the analysis of the transient pressure drop across the tube bundle during blowdown. The idealisation models the flow through the tube bundle as a single-phase vapour with a uniform average density and velocity. The assumption is conservative, in that the choked flow velocity of a single-phase gas is higher than that of a two-phase mixture. This steady-state idealisation is justified based on the experimental observations, which suggest that the maximum quasi-steady discharge occurs during the rapid vapour generation stage in which the vapour phase is visually observed to slip past the relatively static liquid phase. When the pressure drop across the tube bundle begins to decrease after the quasi-steady portion of the transient, the flow patterns downstream of the tube bundle show entrained liquid streams that were not present during the preceding quasi-steady discharge. Hence, the pressure drop across the tube bundle appears to be highest after the initial fluid acceleration when the two-phase discharge void fraction is high, during which the highest velocities and tube loads were observed.

There are several available predictive tools in the literature dealing with steady-state pressure drop through a tube bundle for an incompressible fluid. An attempt is made here to develop a methodology to relate the rapid transient flow through the tube bundle to the steady-state tools available in the literature. In particular, three models that provide predictions of pressure drop through tube arrays in practical heat exchanger designs were investigated and compared to the present transient blowdown test results. These are the Martin, Zukauskas, and Idelchik pressure drop models [5, 6, 15]. An average Reynolds number is calculated for the transient 'quasi-steady' blowdown stage based on an estimated average blowdown mass flux and an average inter-tube velocity. From this, a steady-state tube bundle pressure drop coefficient is estimated assuming single-phase vapour flow, as given by Eq. (7-3),

$$\Delta p = \frac{1}{2}\rho u^2 \xi z \, , \tag{7-3}$$

where Δp is the pressure drop across the tube bundle, ρ is the fluid density, u is the mean velocity at the minimum cross-section in the tube bundle, ξ is an empirically based steady-state pressure drop coefficient that depends on the tube bundle geometry and the flow Reynolds number, and z is the number of rows of tubes in the bundle.

For high Reynolds numbers, the skin friction coefficient of the pressure drop is negligible since the form drag is mainly responsible for the losses, and shear effects due to thermal variations are also negligible. The full details of the pressure drop calculations are provided in Appendix F. Figure 7-13 presents a comparison of the 3 steady-state pressure drop models with the transient two-phase pressure drop measured during the blowdown in test T04, which was performed using a tube bundle containing 6 rows of tubes. As demonstrated in section 6.7, the peak in the pressure drop measurement in the first 50ms of the blowdown is associated with the acceleration and flashing of the liquid downstream of the tube bundle (refer to Fig. 6-20), which does not affect the loading on the tubes. The subsequent acceleration of the fluid upstream of the tubes through the tube bundle produces a rise in the pressure drop beginning at about 76ms, as well as a simultaneous rise in the tube loading (refer to Fig. 4-5).

The results demonstrate that the Martin and Zukauskas models provide the closest

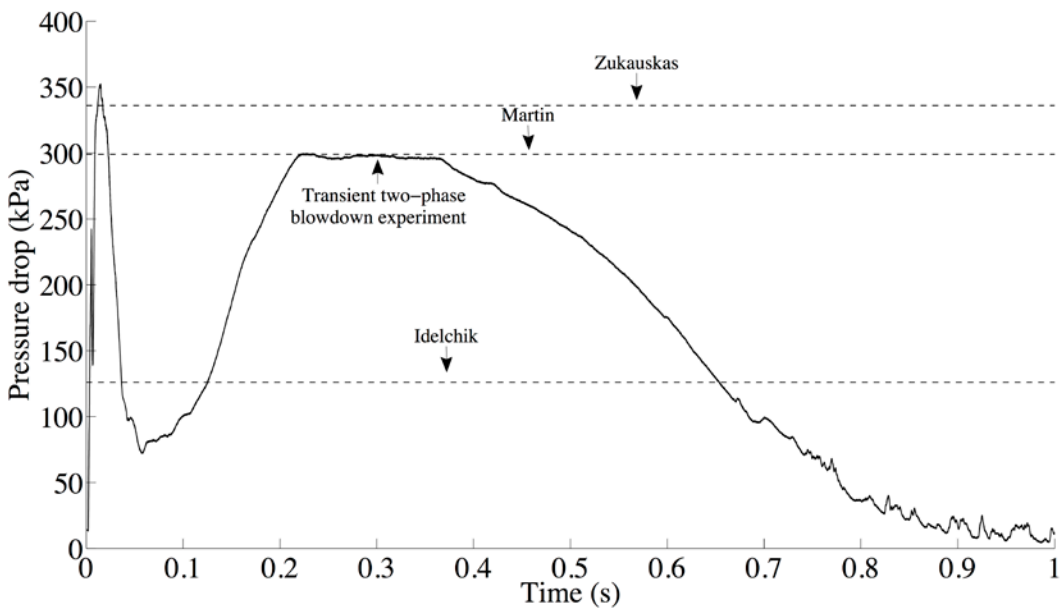

Figure 7-13. Comparison of transient two-phase pressure drop with theoretical steady-state single-phase predictions (test T04).

predictions to the quasi-steady two-phase pressure drop associated with the maximum amplitude of tube loading measured in test T04. The Martin model provides a very accurate prediction of the pressure drop during the quasi-steady stage of the transient based on the assumptions of choked saturated vapour flow with thermodynamic properties obtained from the experimental quasi-steady conditions downstream of the tube bundle (125kPa). The Zukauskas and Idelchik predictions are similarly based on the assumption of choked vapour flow with upstream thermodynamic conditions (425kPa) used in the calculations. The Idelchik model significantly under-predicts the pressure drop, while the Zukauskas prediction provides a suitably conservative upper bound. These pressure drop computations suggest that steady-state empirical tools available in the literature may be adequate to use as a starting point for conservatively predicting the transient pressure drop across a tube bundle during a steam generator Main Steam Line Break.

8. Summary and conclusions

An experimental laboratory project was undertaken to study the effects of a simulated blowdown on steam generator tube loading. The purpose of the research was to develop a better understanding of the transient two-phase tube loading and its prediction such that structural tube failures can be avoided in industrial steam generators. The tube array had a normal triangular geometry and a pitch ratio of 1.36 and the working fluid was refrigerant R- 134a, which boils at near standard pressure and temperature. Experiments were conducted varying the initial liquid levels and the number of tube rows in the tube array. Pressure, temperature, and high-speed video images during the blowdown were obtained to study the details of the fluid transients and their effects on the tube loading.

Commissioning tests showed that the shock produced by the initiation of the blowdown and the associated sudden drop in fluid temperature degraded the measurements to the point that the quantitative signal output was of little value. It was considered important in this experimental investigation to correct these measurement issues and eliminate the spurious signal sources. A program of instrumentation development was therefore initiated to generate reliable measurement capabilities for the blowdown research. Remedial measures were developed, which proved to be effective in eliminating the spurious effects in the output data for the duration of the transients.

By acquiring a physical understanding of the transient two-phase tube loading aspects of the experiments, the development of a predictive methodology for dynamic tube loading during two-phase blowdown was enabled. The two-phase transient experiments indicated a significant amount of thermal non-equilibrium between the liquid and vapour phases during the transients. Upon sudden depressurisation, the rapid phase transition from liquid to vapour and the associated volumetric expansion initially overcomes the volumetric flow discharge rate, which results in temporary pressure recoveries. The rates of vapour generation and fluid expulsion are then observed to equalise at about 100 – 200ms into the transient, producing a ‘quasi-steady’ flow condition that persists for several hundred milliseconds of the transient during which the flow is choked. When the liquid inventory in the reservoir is no longer capable of sustaining a vapour generation rate that matches the rate of discharge, a decrease is observed in the pressure as it proceeds towards the equilibrium conditions of the containment system. The blowdowns were typically observed to last for about 1 second.

Large-amplitude pressure spikes observed in the first few milliseconds of the blowdowns due to the propagation of pressure waves at acoustic velocities were observed to produce tube loads that were smaller in magnitude than those measured during the 'quasi-steady' fluid discharge phase of the blowdowns. The pressure drop across the tube bundle controls the maximum flow rate of the two-phase fluid, which apparently exits the tube bundle at the critical flow rate. The two-phase flow through the bundle appears to become choked very rapidly, and the maximum amplitude of tube loading was observed to occur during this 'quasi-steady' flow discharge stage of the blowdown. The pressure drop measured across the tube bundle correlates very well with the tube loading measurements. The tube loads can be estimated according to an empirically determined drag coefficient once the pressure drop is known.

A comparison of the measured transient pressure drop across the tube bundle with existing steady-state methodologies permits the generalisation of the current experimental results to other tube array patterns and pitch ratios not tested in this study. The complexity of the thermodynamic phenomena that occur during the blowdown process necessitates the evaluation of the two-phase pressure drop across the tube bundle using simplified modelling tools. It appears that formulating the transient two-phase pressure drop using well-documented pressure drop models available in the literature for steady-state single-phase flow in tube banks subjected to cross-flow may provide suitable conservative estimates of the maximum pressure drop.

References

[1] E. Reichelt, “Resolution of Generic Safety Issue 188: steam generator tube leaks or ruptures concurrent with containment bypass from Main Steam Line or Feedwater Line breaches,” Office of Nuclear Regulatory Research – U.S. Nuclear Regulatory Commission, NUREG-1919, August 2009.

[2] X. Sireta, “An experimental and theoretical study of the blowdown of the secondary side of a steam generator,” Transactions of the American Nuclear Society, vol. 31, pp. 392-394, 1978.

[3] S. P. Kalra and G. Adams, “Thermal hydraulics of steam line break transients in thermal reactors – simulation experiments”, Transactions of the American Nuclear Society, vol. 35, pp. 297-298, 1980.

[4] C. F. Forrest, “Flaw tolerance of steam generator tubes under accident conditions,” Regulatory Research and Support Program – Atomic Energy Control Board, AECB Project No. 2.273.1, August 1995.

[5] R. K. Shah and D. P. Sekulic, Fundamentals of heat exchanger design. John Wiley & Sons, 2003.

[6] A. Zukauskas, “Heat transfer from tubes in cross-flow,” Advances in Heat Transfer, vol. 18, pp. 87-159, 1987.

[7] B. L. Smith, “Assessment of CFD codes used in nuclear reactor safety simulations,” Nuclear Engineering and Technology, vol. 42, iss. 4, pp. 339-364, 2010.

[8] P. Saha, A. Ghosh, T. K. Das, and S. Ray, “Numerical simulation of pressure wave time history inside a steam generator in the event of Main Steam Line Break and Feedwater Line Break transients,” Transient Phenomena in Nuclear Reactor Systems, ASME HTD-vol. 245/ NE-vol. 11, pp. 131-140, 1993.

[9] V. Bhasin, H. S. Kushwaha, S. C. Mahajan, and A. Kakodkar, “Structural analysis of steam generator internals following Feed Water/Main Steam Line Break: DLF approach,” Bhabha Atomic Research Centre – Government of India Atomic Energy Commission, BARC/1993/E/026, October 1993.

[10] P. R. Chappidi, M. D. Kannapel, N. Vaidya, and A. K. Singhal, “Steam Line Break and primary tube leak analysis of a Model-F generator with ATHOS3-MOD1,” CFD

Research Corporation – Electric Power Research Institute, CFDRC Report 4036/6, June 1993.

[11] R. G. Sauvé, M. Tabatabai, D. Savoia, and M. J. Kozluk, “Bruce ‘B’ steam generators flow induced vibration analysis blowdown conditions transient fatigue evaluation,” Ontario Hydro Technologies, OHT Report No. A-NSG-96-90-P, August 1996.

[12] R. Beaton and C. D. Fletcher, “TRAC-M simulations of MB-2 Steam Line Breaks,” Information Systems Laboratories – U.S. Nuclear Regulatory Commission, ISL-NSAD-TR-03-09, March 2003.

[13] O. J. Mendler, K. Takeuchi, and M. Y. Young, “Loss of Feed Flow, Steam Generator Tube Rupture and Steam Line Break thermohydraulic experiments,” Westinghouse Electric Corporation – U.S. Nuclear Regulatory Commission, NUREG/CR-4751, October 1986.

[14] W. J. Krotiuk, “Pressurized Water Reactor steam generator internal loading following a Main Steam or Feedwater Line Break,” Office of Nuclear Regulatory Research – Safety Margins and Systems Analysis Branch, SMSAB-02-05, May 2004.

[15] I. E. Idelchik, Handbook of hydraulic resistance. Hemisphere Publishing Corporation, Washington, DC, 1986.

[16] F. J. Moody, Introduction to unsteady thermofluid mechanics. Wiley, New York, NY, 1990.

[17] L. Wolf, “Experimental results of coupled fluid-structure interactions during blowdown of the HDR-vessel and comparisons with pre- and post-test predictions,” Nuclear Engineering and Design, vol. 70, iss. 3, pp. 269-308, 1982.

[18] H. Tinoco, “Three-dimensional modeling of a Steam-Line Break in a Boiling Water Reactor,” Nuclear Science and Engineering, vol. 140, iss. 2, pp. 152-164, 2002.

[19] J. C. Jo, “Numerical simulation of pressure transients in a PWR Main Steam Line system due to quick operations of pressure relief valve,” Proceedings of the ASME 2009 Pressure Vessels and Piping Conference, Prague, Czech Republic, pp. 35-43, July 2009.

[20] J. C. Jo and F. J. Moody, “Transient thermal-hydraulic responses of the nuclear steam generator secondary side to a Main Steam Line Break,” Journal of Pressure Vessel Technology, vol. 137, iss. 4, August 2015.

[21] O. Hamouda, An experimental rig and investigation of steam generator tube loading during Main Steam Line Break. M.A.Sc. Thesis, McMaster University, Hamilton, ON, February 2011.

[22] H. Städtke, Gasdynamic aspects of two-phase flow. Wiley-VCH, Weinheim, 2006.

[23] S. Levy, Two-phase flow in complex systems. Wiley-Interscience, New York, NY, 1999.

[24] V. M. Fthenakis, U. S. Rohatgi, and B. D. Chung, "A simple model for predicting the release of a liquid-vapor mixture from a large break in a pressurized container," Journal of Loss Prevention in the Process Industries, vol. 16, iss. 1, pp. 61-72, January 2003.

[25] G. B. Wallis, "Critical two-phase flow," International Journal of Multiphase Flow, vol. 6, iss. 1-2, pp. 97-112, February 1980.

[26] V. P. Carey, Liquid-vapor phase change phenomena. Taylor & Francis, Bristol, PA, 1992.

[27] P. Deligiannis and J. W. Cleaver, "Blowdown from a vented partially full vessel," International Journal of Multiphase Flow, vol. 22, iss. 1, pp. 55-68, 1996.

[28] W. S. Winters Jr. and H. Merte Jr., "Experiments and nonequilibrium analysis of pipe blowdown," Nuclear Science and Engineering, vol. 69, pp. 411-429, 1979.

[29] A. R. Edwards and T. P. O'Brien, "Studies of phenomena connected with the depressurisation of water reactors," Journal of British Nuclear Energy, vol. 9, pp. 125-135, 1970.

[30] M. Alamgir, C. Y. Kan, and J. H. Lienhard, "An experimental study of the rapid depressurization of hot water," Journal of Heat Transfer, vol. 102, pp. 433-438, 1980.

[31] K. Ishihara, J. W. Palen, and J. Taborek, "Critical review of correlations for predicting two-phase flow pressure drop across tube banks," Heat Transfer Engineering, vol. 1, iss. 3, pp. 23-33, 1980.

[32] L. Consolini, D. Robinson, and J. R. Thome, "Void fraction and two-phase pressure drops for evaporating flow over horizontal tube bundles," Heat Transfer Engineering, vol. 27, iss. 3, pp. 5-21, 2006.

[33] G. Ribatski and J. R. Thome, "Two-phase flow and heat transfer across horizontal tube bundles – a review," Heat Transfer Engineering, vol. 28, iss. 6, pp. 508-524, 2007.

List of publications from this research

1. O. Hamouda, D. S. Weaver, and J. Riznic, "An experimental rig and investigation of steam generator tube loading during Main Steam Line Break," Proceedings of The 14th International Topical Meeting on Nuclear Reactor Thermalhydraulics, NURETH-14, Toronto, ON, September 25-30, 2011, paper no. NURETH14-261.

2. O. Hamouda, D. S. Weaver, and J. Riznic, "Preliminary calibration tests for an experimental study of steam generator tube loading during blowdown," Proceedings of The Canadian Society for Mechanical Engineering International Congress CSME 2012, June 4-6, 2012, Winnipeg, MB.

3. O. Hamouda, D. S. Weaver, and J. Riznic, "Commissioning tests for an experimental study of steam generator tube loading during blowdown," Proceedings of the ASME 2013 Pressure Vessels & Piping Division Conference PVP 2013, July 14-18, 2013, Paris, France, paper no. PVP2013-97809.

4. O. Hamouda, D. S. Weaver, and J. Riznic, "An experimental study of steam generator blowdown tube loading: preliminary results," Proceedings of The Canadian Society for Mechanical Engineering International Congress CSME 2014, June 1-4, 2014, Toronto, ON.

5. O. Hamouda, D. S. Weaver, and J. Riznic, "Instrumentation development and validation for an experimental study of steam generator tube loading during blowdown," Proceedings of the ASME 2014 Pressure Vessels & Piping Conference PVP 2014, July 20-24, 2014, Anaheim, CA, paper no. PVP2014-28137.

6. O. Hamouda, D. S. Weaver, and J. Riznic, "Transient loading on nuclear steam generator tubes during a two-phase blowdown," Proceedings of the 25^{th} CANCAM, London ON, May 31 – June 4, 2015.

7. O. Hamouda, D. S. Weaver, and J. Riznic, "An experimental study of steam generator tube loading during blowdown," Proceedings of the ASME 2015 Pressure Vessels & Piping Conference PVP 2015, July 19-23, 2015, Boston, MA, paper no. PVP2015-45250.

Appendix A. Design details of experimental rig and instrumentation

The basic concept of the design is to have a static fluid reservoir holding liquid R-134a at the appropriate temperature and pressure conditions, a sectional model test section containing a bundle of steam generator tubes, a pressure control device to suddenly release the pressure on the fluid reservoir, and a vacuum tank of sufficient volume that the blowdown transient is not controlled by rising downstream pressure. The volume of liquid in the reservoir determines to some extent the length of the blowdown transient and also the required volume of the vacuum tank receiver. Calculations indicated that the liquid-to-receiver volume ratio should be of the order of 60 or larger for the maximum design pressure of about 690kPa. Calculations and practical considerations such as available space and cost led to a design based on 6-inch standard schedule-40 pipe and a 1000 litre vacuum tank. All of the components of the experimental facility were custom made at McMaster University except for standard off-the-shelf components and specially custom made parts by outside suppliers.

A.1. Pressure vessel

The pressurised liquid reservoir is made from standard 6-inch schedule-40 pipe with welded steel flanges. The total length of the bottom reservoir is 18 inches, with a welded standard 6-inch blanking flange dividing the pipe into sections approximately 4 inches and 14 inches long. This way, the capacity of the liquid reservoir can be changed by about 4.6L by simply turning the reservoir over. The transition sections containing the sight windows are identical. The inside cross-section is 5.437x5.437 inches, which gives the same cross-sectional area as the 6-inch standard pipe used for the liquid reservoir. Each side is fitted with a 1.25-inch thick tempered quartz glass window, specially ordered and produced by Specialty Glass Products of Willow Grove, PA, USA, with a sighting area of 3x7.5 inches. Thus, there are 8 windows, each of which is sealed with neoprene gaskets between the window and its frame, and between the window and clamping plate. Drawings of the pressurised liquid reservoir components are provided in Figs. A-1 and A-2.

A.2. Tube bundle test section

The test section contains a tube bundle consisting of 0.5-inch diameter tubes in a normal triangular geometry with a pitch ratio of 1.36. The test section was designed to accommodate anywhere from 0 to 6 rows of tubes. When there are no tubes mounted in the test section, the drilled side walls are replaced by blank side walls. The tube array geometry, pitch ratio and tube diameter are similar to those used in CANDU steam generators. The frame holding the tube bundle is supported by four piezoelectric load cells, which measure the dynamic load on tube bundle during the blowdown. The test section casing was designed so that the load cells were

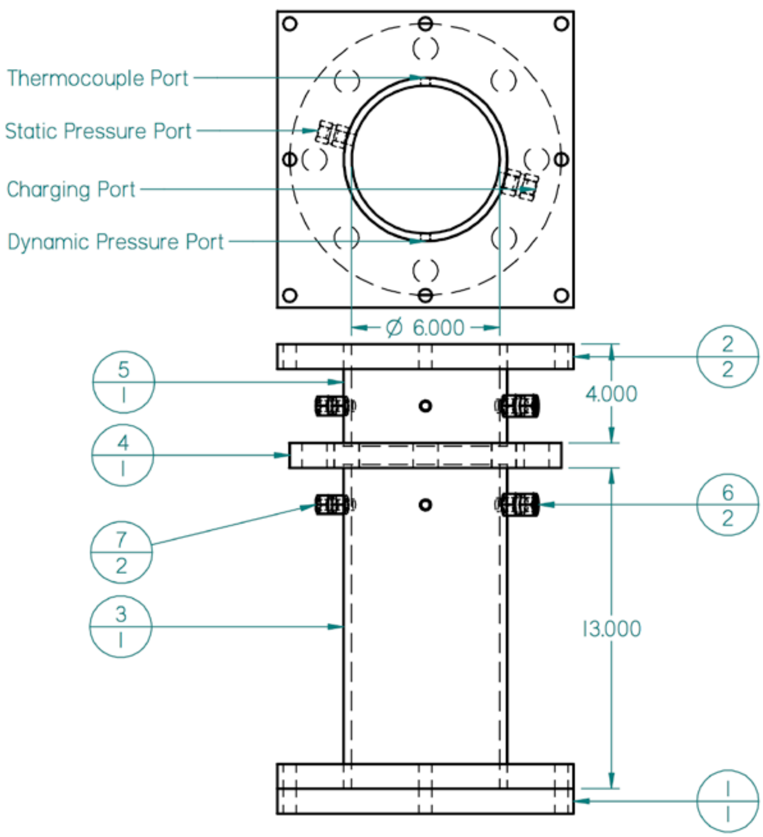

Item Number	Title	Quantity
1	Blanking Flange	1
2	Pipe Flange	2
3	6" Schedule 40 Pipe	1
4	Std. 6" Blank Flange	1
5	6" Schedule 40 Pipe	1
6	3/8 NPT Hex Coupling	2
7	1/4 NPT Hex Coupling	2

ALL DIMENSIONS IN INCHES

Figure A-1. Pressurised liquid reservoir.

sealed from the R-134a using O-rings. The design transfers the entire blowdown load on the tube bundle to the load cells, while sealing the latter from contact with the R-134a. It was necessary to ensure that the load cells were sealed from the working fluid, since their performance and durability is not guaranteed when submerged in or exposed to any liquid. This posed a significant challenge from a design perspective, and the constructed test section is the product of several design iterations and intricate machining work. The tube bundle geometry and load measurement methodology is illustrated in Fig. A-3.

A.3. Pressure relief section

The device used for suddenly releasing the test section pressure to produce the blowdown is clearly a very important part of the design. The design criteria were that the flow area should

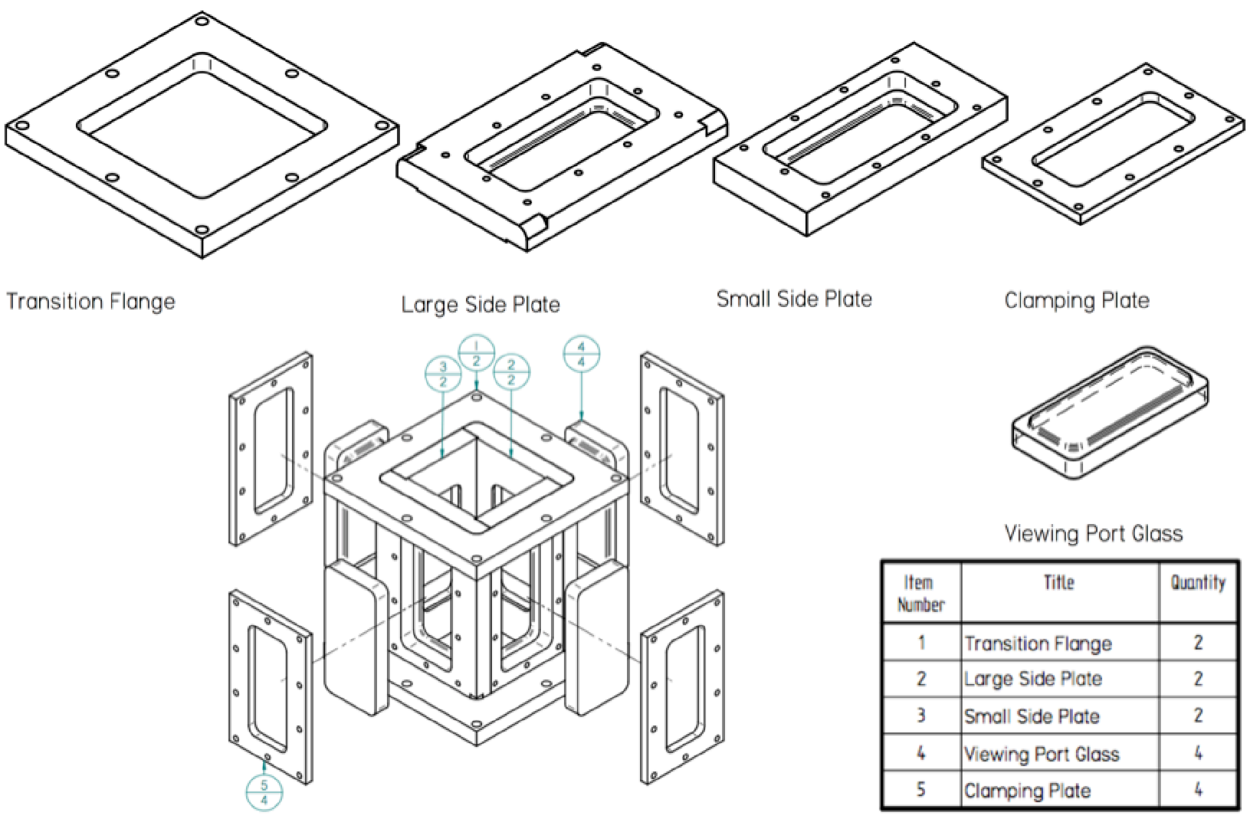

Item Number	Title	Quantity
1	Transition Flange	2
2	Large Side Plate	2
3	Small Side Plate	2
4	Viewing Port Glass	4
5	Clamping Plate	4

Figure A-2. Transition section.

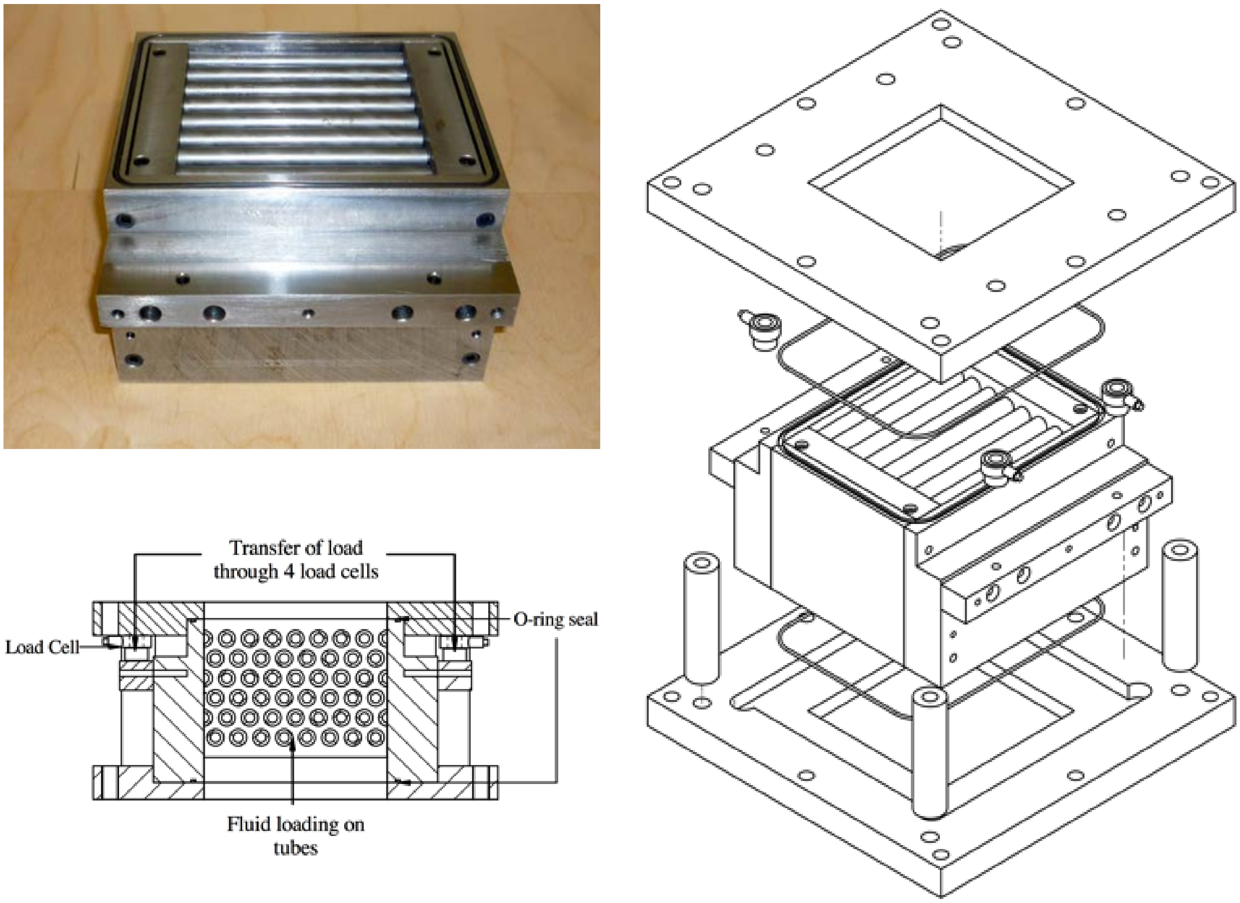

Figure A-3. Tube bundle test section.

be as close as possible to that of the 6-inch diameter pipe serving the device, that the pressure difference across the device at which pressure release occurs should be controllable, and that the device should go from closed to fully open in as short a time as possible. It was decided that a rupture disc assembly was the best choice. The determining factor was the opening time of the order of milliseconds, more than ten times faster than quick opening valves of the same size. Aluminum rupture discs (6” Poly-SD) supplied by Fike Canada, Inc. were chosen, which are non-fragmenting, and always open completely with a predictable opening pattern. The disc holder is fixed between standard 6-inch flanges in the standard pipe between the transition section and the vacuum tank. An assembly drawing and photographs are shown in Fig. A-4.

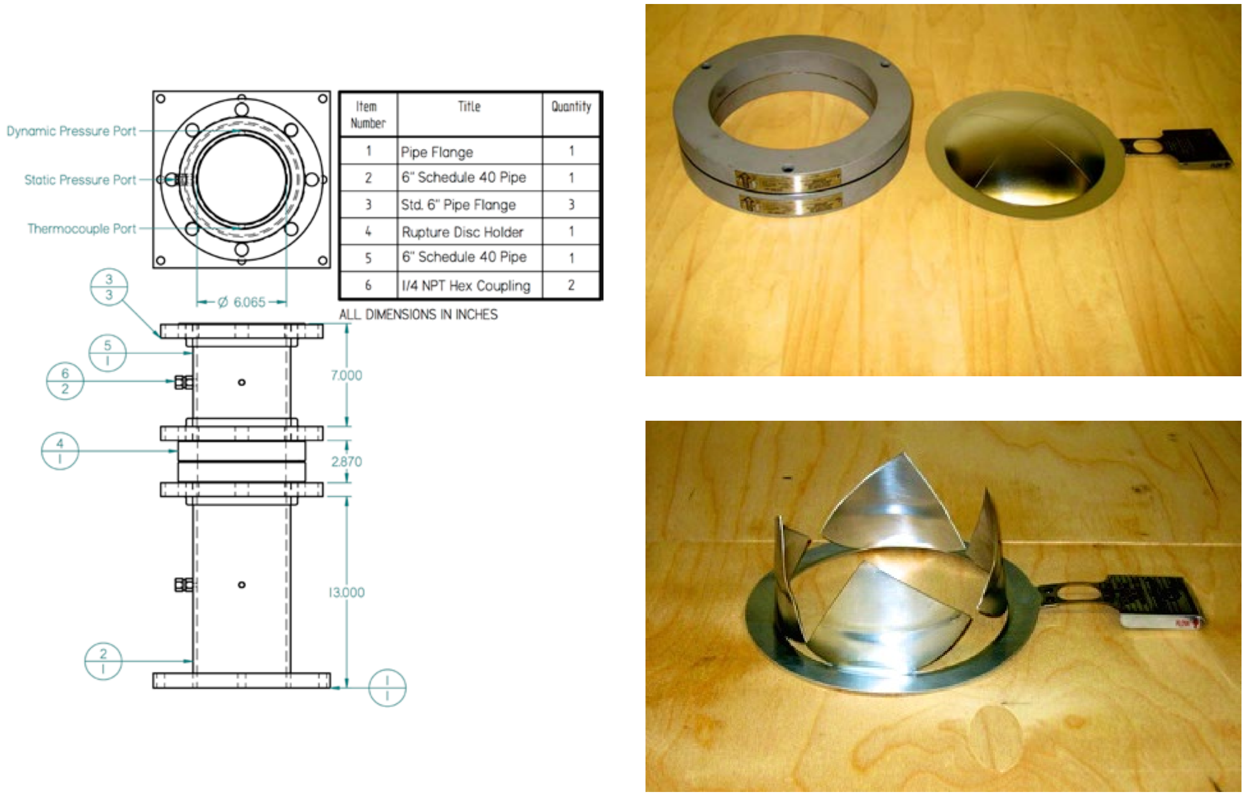

Figure A-4. Pressure relief section (left), new rupture disc (top right), open rupture disc (bottom right).

A.4. Vacuum reservoir

The primary design criteria for the vacuum tank receiver was that it should provide an expansion ratio of 60 or greater for the liquid R-134a in the reservoir, and that it should withstand dynamic pressures at least equal to the maximum pressure in the reservoir of 690kPa. The vacuum tank was built by Steel Fab in Oakville, Ontario to ASME Code, with a volume capacity of about 908L and design pressures from vacuum to 1.38MPa. A design drawing of the vacuum tank is provided in Fig. A-5.

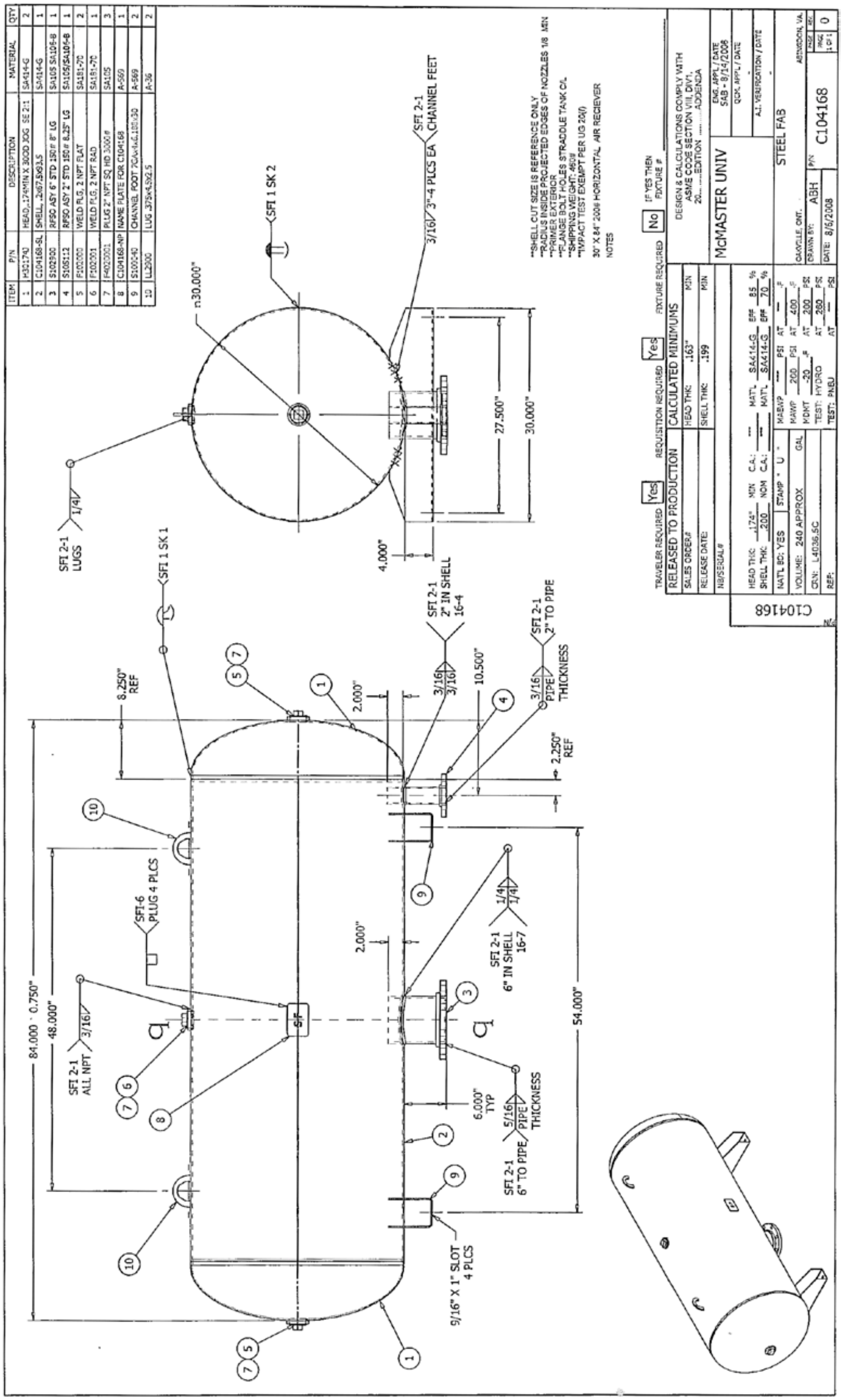

Figure A-5. Vacuum tank design.

A.5. Instrumentation

During the initial stages of an experimental run, the entire blowdown rig pressure is brought down to a vacuum, in order to purge any gases and create the necessary low pressure in the vacuum tank. A vacuum level of about 99.9% is established, which corresponds to about 70Pa, within measurement uncertainty. The section of the rig below the rupture disc is then pressurised by charging it with liquid R-134a, and the pressure is monitored using static pressure sensors. The pressure is adequately maintained this way to ensure that the blowdown does not occur unexpectedly, and is instead triggered by adjusting the pressure in a controlled manner to the prescribed rupture disc pressure difference. Once the necessary pressure to open the rupture disc is reached, a blowdown is initiated. The instruments are set to continuously capture and buffer data during pressurisation, and the data logging process is triggered by the pressure wave initiated by the opening of the rupture disc. The transient fluid pressures and temperatures are monitored at three locations along the pressurised pipe, and the dynamic fluid drag load is measured on the tube bundle directly. Sight glasses upstream and downstream of the test section permit visual observation of the blowdown event and its recording using high-speed imaging. The following sections describe the selection of instruments used to acquire data in these experiments.

A.5.1. Thermocouples

Sheathed exposed-junction fine-wire Chromel-Constantan thermocouples supplied by Omega (model EMQSS) were chosen to provide temperature measurements. The thermocouples are protected by 15.24cm long 0.25mm diameter stainless steel sheaths, with exposed junctions of 25μm diameter wires at the end for fast temperature response. A significant challenge associated with this design of thermocouple was creating a seal at the mounting location in the walls of the blowdown rig, due to the fragility of the thermocouple sheath and the exposed junction. In order to achieve the required seal, 0.125-inch stainless steel tube fittings were mounted onto the walls, and the threads were sealed normally using regular pipe joint sealant.

Blank Teflon ferrules for 0.125-inch compression fittings were used instead of regular stainless steel bored ferrules, which were previously drilled using a 0.27mm drill to provide minimal clearance so that the thermocouple sheaths could be inserted carefully all the way through. The tube fittings were then mounted with the thermocouples in place, causing the Teflon ferrule to compress evenly onto the sheaths, creating a relatively soft non-destructive press fit that prevents leakage flow. Despite being subjected to rapid and substantial changes in fluid flow rate during the blowdown transients, the thermocouples all performed very reliably, and were not damaged by the accelerating fluid in any of the experimental runs.

A.5.2. Pressure transducers

The dynamic pressure transducers chosen for this study were high-sensitivity acceleration compensated piezoelectric dynamic pressure sensors supplied by Dytran (models 2200 and 2300), with a measurement range of 690 – 1720kPa, and sensitivity ranging between 2.9 – 7.25mV/kPa. Dynamic pressure sensors of this type are well suited for fast transient blowdown measurements since they respond very rapidly to changes in pressure with a rise time as fast as 2μs. However, they do not measure static pressures. The integrated acceleration compensation acts in the axial direction of the sensors to minimise the effects of acceleration during measurements where the sensor may be subjected to vibration. As such, it was expected that the sensors would not pick up vibration signals from the rig during the transient blowdowns, and would only be sensitive to pressure changes.

It was discovered during commissioning tests, however, that the alleged acceleration compensation was not sufficient, and that the transducer performance was seriously degraded by the initial shock loading during blowdown. Therefore, the sensors were mounted in custom-designed and built vibration isolation designs in order to eliminate spurious vibration-induced measurements in the signals. The sensors were also thermally shielded with silicone rubber insulating coatings to prevent erroneous pressure readings resulting from transient temperature effects. Due to the high relative stiffness of the sensor elements compared to the coating layers, the silicone rubber was found not to significantly alter the sensitivity of the sensors. Details of the pressure transducer development are provided in Appendix B.1.

For the static pressure measurements, silicon-based strain gage pressure sensors supplied by Measurement Specialties (model U5100) were selected. These sensors measure down to zero absolute pressure and are therefore appropriate for the entire range of experimental pressures, starting from the vacuum point. The use of static pressure sensors provided a desirable back up to the dynamic pressure transducers, since the latter had given so much trouble during commissioning tests due to thermal and mechanical shock. The static pressure sensors offer reasonable dynamic capabilities, with a time constant of about 0.16ms, yielding a response time of approximately 0.8ms. In addition, the sensors are digitally calibrated and temperature compensated through an internal signal conditioner that uses an integral temperature sensor, which is MEMS-based (Micro-Electro-Mechanical Systems), with a temperature range of -40°C to 125°C.

Given the reasonable dynamic capability of the static sensors, as well as the built-in thermal and mechanical shock compensation, a static pressure sensor was mounted at every dynamic pressure measurement location in the rig, such that instrumentation tests could be developed by substantiating the pressure traces against each other at all points along the rig. The complete transient measurement of pressure is obtained by using the dynamic pressure transducer signals for the initial stages of the transient, characterised by the propagation of high-frequency pressure waves, and the static pressure sensor signals for the remainder of the transient, which approaches quasi-steady state.

A.5.3. Load cells

The load cells chosen to measure dynamic loading on the tube bundle were piezoelectric quartz washer-type force sensors supplied by PCB (model 202), with a capacity of 44.5kN and a sensitivity of about 112mV/kN. The four load cells were pre-loaded by custom fabricated cylindrical spacers mounted directly on the model tube bundle test section. The signals were monitored individually but summed to determine the total transient drag load on the tubes. The discharge time constant for this type of load cell is long enough to allow load measurements to be performed over a very wide frequency range, from quasi-static to 40kHz.

The load cells were mounted between two flat smooth polished parallel surfaces, pre-loaded in compression, and measured compressive loads for the entire durations of the blowdown transients. The stiffness of each load cell is about 5GN/m, which is comparable to a solid piece of steel of similar dimensions. This high stiffness, coupled with the relatively negligible stiffness of the O-rings used to seal the test section tube bundle, allows practically the entire load applied onto the tubes during the transient blowdown to be registered by the sensors. Commissioning tests showed that there were many problems with the original configuration and an experimental development program was initiated to overcome the problems. Details are provided in Appendix B.2.

A.5.4. Data acquisition system

Two separate cards were used for data acquisition. The dynamic pressure and load signals were obtained using an 8-channel dynamic signal acquisition card supplied by National Instruments (model PCI-4472), which has a 24-bit resolution and a 102.4kHz maximum simultaneous sampling rate for 8 analogue channels. Since the quasi-steady behaviour of the transient was of interest in this study, the data acquisition card was DC-coupled, bypassing its cut-off frequency, and two couplers (Kistler model 5134) were used to provide excitation power and signal conditioning for the piezoelectric sensors. With a -3dB cut-off frequency of 0.036Hz, and a discharge time constant of 4.42s, it was possible using these power supplies to capture relatively slower events, limited only by the low cut-off frequencies of the sensors. For temperature and static pressure measurements, a 16-channel analogue input data acquisition card (model PCI-6221) and a connector block (model SCC-68) supplied by National Instruments were used. This provided a 16-bit resolution and a 250kHz sampling rate, divided over the 6 channels needed for the thermocouples and static pressure sensors. The connector block has an embedded temperature sensor with an accuracy of ±0.3°C, which is used for cold-junction compensation of the thermocouple measurements. Signal processing for all measurements was performed using LabVIEW software, and data analysis was performed using MATLAB software.

In order to avoid artificial instrument phase distortion, the measurements were all accurately synchronised to a hardware-timed clock, shared simultaneously between all of the measurement channels. The data collection system acquires simultaneous data samples from each individual instrument connected to the central data acquisition board at a rate of 30kHz. This provides a smooth signal for data analysis, which allows proper investigation of high-frequency phenomena. An elaborate dynamic sensor-activated triggering system was also incorporated, which initiates data recording upon the detection of rising pressure immediately downstream of the rupture disc. This way, complete data collection is ensured for each test.

A.5.5. High-speed cameras

Visualisations of the transient flow through the sight glasses located below and above the tube bundle test section were recorded using 2 high-speed cameras (Photron FastCam models SA4 and SA5). Time-synchronised high-speed imaging was established so that fluid phenomena could be physically compared to the measurements. This enables better interpretation of the blowdown physics, which is especially important for determining the fluid drag loading behaviour by observing the acceleration of the liquid surface and fluid bulk, and monitoring the velocity of the discharging fluid during blowdown. A photograph of the experimental facility, showing the high-speed camera system set-up, is provided in Fig. A-6.

A.5.6. Accelerometer

An accelerometer supplied by PCB (model 352A24) was mounted on the blowdown rig for each test in order to measure the rig vibration, and validate the inertial measurements of the load cells due to the vibrations. The accelerometer has a measurement range of $\pm 490 m/s^2$, and a nominal sensitivity of 10mV/(m/s^2). By comparing the frequency content of the accelerometer and load cell signals, the vibration component of the signal can be determined and removed from the load measurements, yielding a mean measurement of the transient fluid drag loading on the tube bundle.

A.5.7. R-134a scale

During R-134a charging into the rig, there is no direct indicator of the quantity of R-134a inserted aside from visually observing the liquid level through the sight windows. In order to obtain a quantitative measure of the amount of working fluid contained in the pressurised reservoir, the R-134a supply cylinder was placed on top of a digital scale with a measurement range of 50kg, supplied by Yellow Jacket (model 68802), throughout the charging process. The readout on the scale displays the mass of R-134a discharged into the pressurised reservoir system. Knowing the reservoir volume and the liquid and vapour densities, the volume occupied by the liquid and vapour phases can be determined from the total mass of R-134a discharged into the reservoir. The results were consistent with liquid volume calculations of the hydrostatic pressure head based on the collected pressure and temperature data.

Figure A-6. Photograph of experimental facility showing instrumentation and high-speed cameras.

Appendix B. Instrumentation shock and vibration isolation

The sudden opening of a rupture disc, and the resultant pressure relief of the pipe section upstream, imposes severe impulsive loads on the associated structural system, which produce transient structural responses due to the propagation of stress waves and vibrations. In the current experimental facility, the structural loads are generated by stress wave propagation, which subjects the experimental rig to a sudden axial shock loading. As a result, shock and vibration induced artefacts were apparent in the dynamic tube loading and pressure signals obtained in preliminary commissioning tests.

The magnitude of the sudden axial load on the rig can be estimated by determining the longitudinal force, F, which is exerted on the pipe upon sudden disc rupture. Figure B-1 presents simplified free-body diagrams of the experimental rig, immediately before rupture, at time $t = 0$, and after a certain time Δt has elapsed, which is equivalent to the time required for a stress wave to travel the distance between the rupture disc and the load cells. In Fig. B-1, the pressurised reservoir is modelled as a uniform pipe, with a cross-sectional area A_i of 186.4cm^2. The pipe reservoir is initially filled with stagnant pressurised R-134a, at a pressure p_i of about 600kPa. On the opposite side of the rupture disc, the vacuum region is initially at vacuum pressure, p_∞, which can be approximated as 0kPa. The cylindrical pipe shown in Fig. B-1 below the rupture disc is subjected at the bottom end to an internal pressure p_i and an external pressure p_{atm}. As shown in Eq. (B1), the net pressure differential on the pipe, p_d, is the difference between the internal pressure and the atmospheric pressure,

$$p_d = p_i - p_{atm} . \tag{B1}$$

In order to satisfy equilibrium, there must be a force that counteracts this pressure difference, and the two forces must be equal for the cylinder to remain in static equilibrium. When a closed cylinder is subjected to internal pressure, three mutually perpendicular principal stresses are created in the cylinder walls. These are the circumferential stress, the radial stress, and the longitudinal stress. The radial forces applied to the straight pipe walls by the internal pressure differential create the circumferential stresses. Similarly, at the closed pipe ends, the

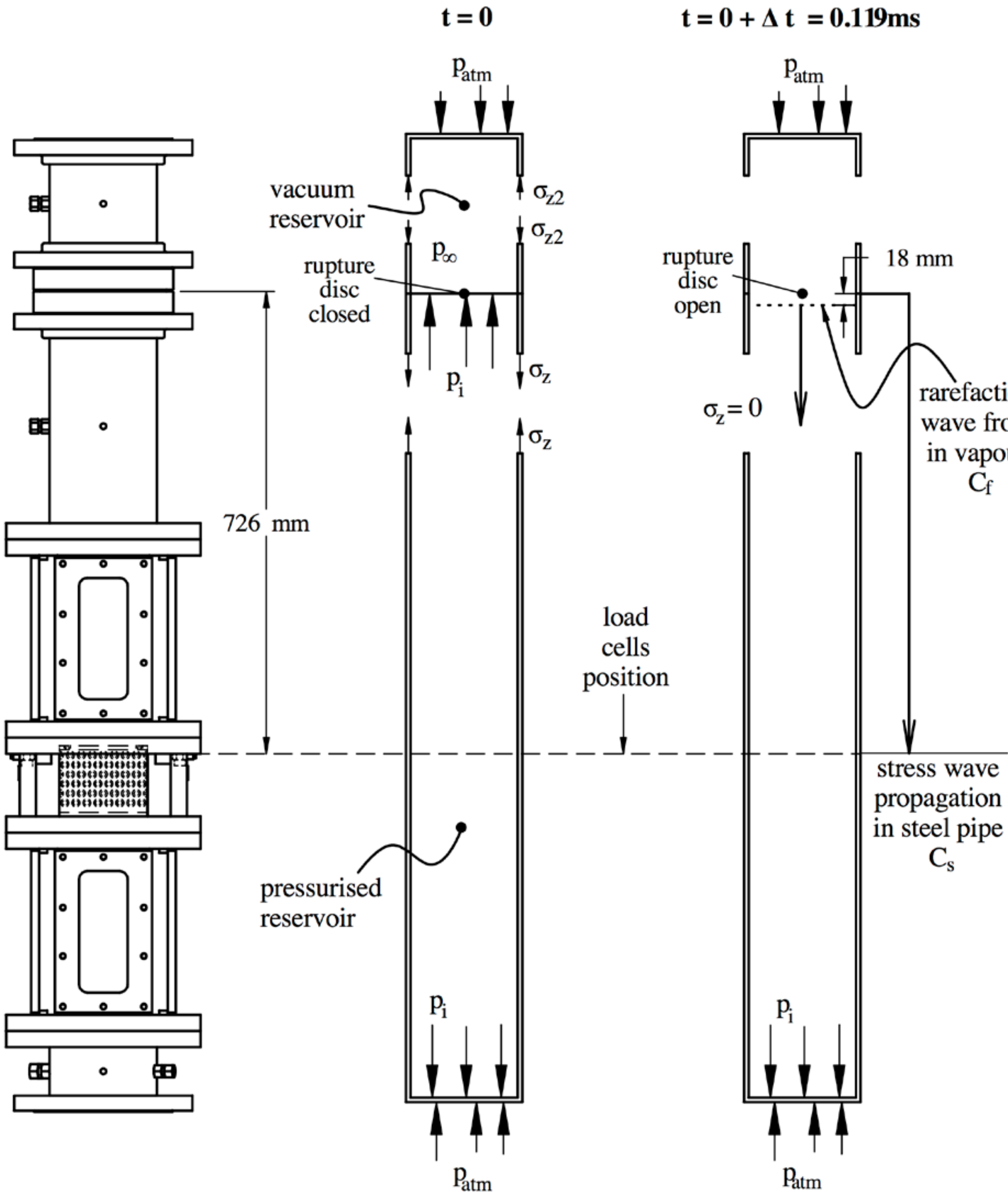

Figure B-1. Longitudinal thrust shock due to a sudden disc rupture.

static pressure force stretches the pipe walls longitudinally, which develops longitudinal stresses on the same pipe wall along the axis of the pipe. When the inside diameter is more than 20 times the pipe wall thickness, the pipe can be accurately assumed as ‘thin-walled’. In this case, the circumferential and longitudinal stresses across the pipe wall are constant, and the radial stress is relatively negligible compared to the two other principal stresses. The Schedule-40 6-inch pipes employed in the experimental rig have an inside diameter of 6.07 inches and a thickness of 0.28 inches, yielding a thickness to diameter ratio of 0.046, which is less than 0.05 and therefore qualifies the pipe to be modelled as a thin-walled cylinder. Therefore, prior to disc rupture, the net internal pressure force is equal to the longitudinal stress force as given by Eq. (B2),

$$p_d A_i = \sigma_z A_p \, , \tag{B2}$$

where σ_z is the longitudinal stress, A_i is the inside cross-sectional pipe area, and A_p is the steel transverse area of the pipe.

Following the instantaneous disc rupture, the removal of the pressure boundary between the pressurised and vacuum regions suddenly relieves the longitudinal stress in the pipe wall, $\sigma_z = 0$, which was balancing the pressure load at the bottom. Thus, a rarefaction stress wave propagates down the pipe at the speed of sound in the solid medium, c_s, which is about 6100m/s for steel. This reaches the location of the load cells, a distance l_s of 0.726m away, in a time Δt, calculated in Eq. (B3),

$$\Delta t = \frac{l_s}{c_s} = \frac{0.726m}{6100\, m/s} = 0.119ms \, . \tag{B3}$$

In this time, the distance l_f travelled by the rarefaction wave along the axis of the pipe through the vapour medium, at a sonic velocity c_f, is given by Eq. (B4),

$$l_f = c_f \Delta t = 150\, m/s \times 0.119ms = 18mm \, . \tag{B4}$$

Since the speed of propagation of the stress wave in the pipe is so much faster than the rarefaction wave in the vapour, the pressure in the pipe at the load cells has not changed when the balancing stress in the pipe has disappeared. The resulting unbalanced ‘shock load’, F, can be estimated by Eq. (B5) as

$$F = p_d A_i = (600 - 100)\, kPa \times 186.4cm^2 = 9.32kN \, . \tag{B5}$$

Hence, the sudden axial force exerted on the rig is estimated to be about 9.32kN, which is equivalent to a shock loading of about 0.95 tonnes. Due to this sudden shock loading on the load cells, preliminary attempts to measure the transient tube bundle loads were unsuccessful. The load cell signals were apparently saturating immediately following blowdown initiation, producing overall transient measurements that were essentially useless. Figure B-2 shows an example of the dynamic fluid loading on the tube bundle measured during a preliminary commissioning test. The load signal shown in Fig. B-2 is the instantaneous summation of the measurements of the 4 load cells mounted in the test section. Almost immediately after rupture, the effects of the initial shock loading on the sensors are manifested through a steep dynamic load change, followed by large-magnitude oscillations. The large periodic signal fluctuations continue for much of the duration of the blowdown. Figure B-3 shows vibration measurements obtained by an accelerometer mounted at the test section, as well as FFT plots of the dynamic load and vibration signals, both of which contain similar frequency content, with a primary natural frequency of 33.6Hz. The oscillations in the load signals were therefore determined to be vibration signals occurring at the lowest axial natural frequency of the test section.

Qualitatively, after the initial 150ms, the mean load signal trend in Fig. B-2 follows that of the pressure drop measured across the tubes. Since the oscillations in the signals are

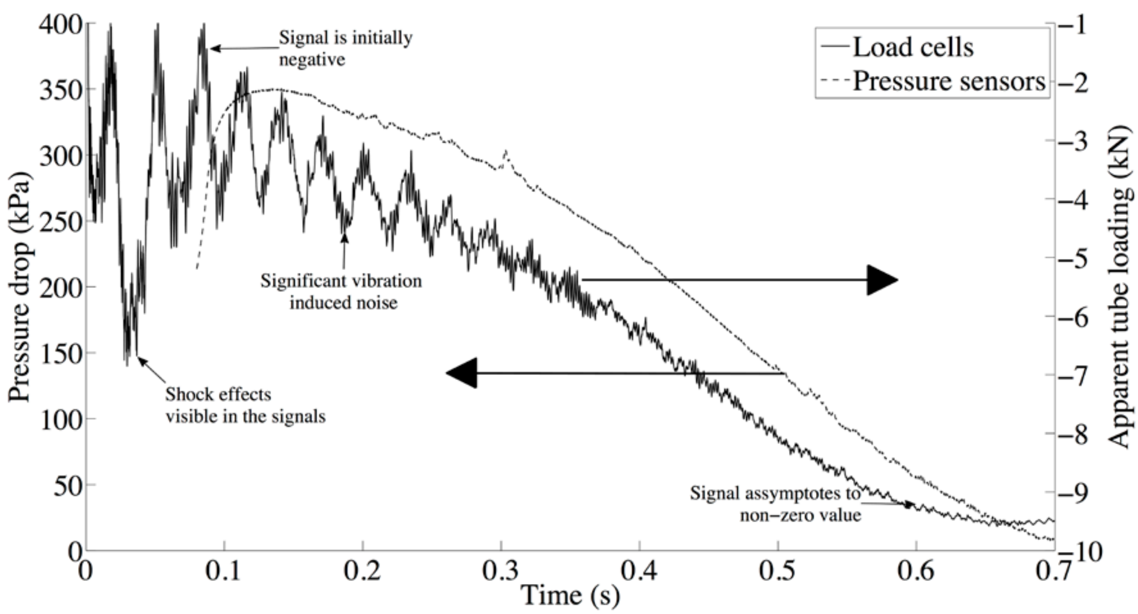

Figure B-2. Spurious dynamic load measurement on the tube bundle during commissioning.

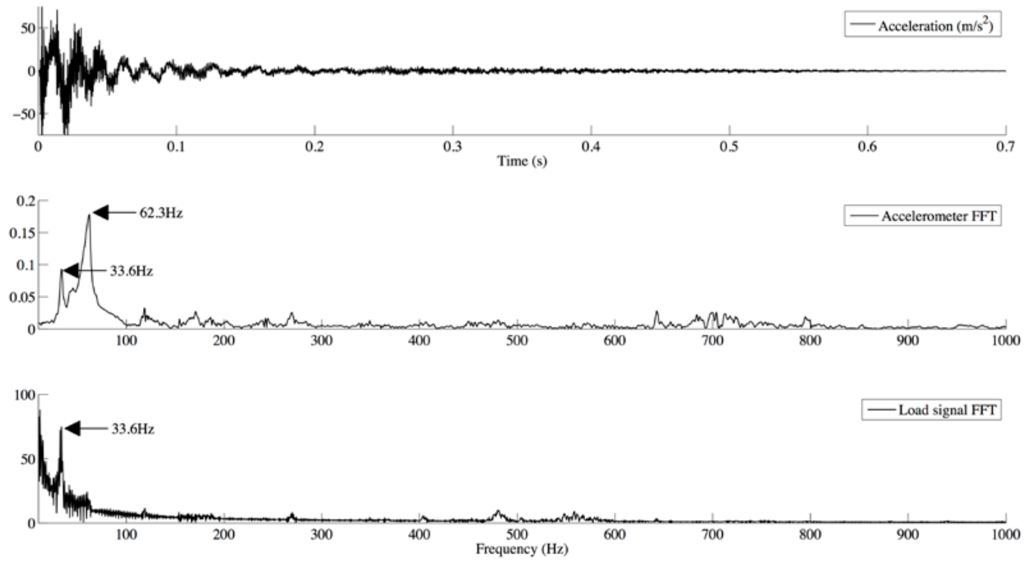

Figure B-3. FFT analysis of accelerometer and load signals.

understood to represent the test section fundamental axial mode of vibration, as confirmed by the accelerometer measurements in Fig. B-3, one might simply ignore them and take the mean value of the signal as the tube loading. However, looking at the tube loading measurements in Fig. B-2, the direction of the loading is opposite to that expected, and there seems to be a significant shift of the static zero load signal at the beginning of the measurement. In addition, the measured loads in Fig. B-2 must asymptote to zero at the end of the blowdown under no load conditions, but instead asymptote to about -9kN.

It appears from the logical load distribution following the initial shock that the zero is shifted by the amount of the steady-state zero load signal, which is about 9kN. Interestingly, this corresponds to the estimated shock loading on the rig from Eq. (B5). The measured signal is also negative, when the upward drag load on the tubes should register a positive load. It is therefore plausible, based on explainable physics, that by simply shifting the whole measured load signal upwards by 9kN, a true dynamic measurement of the blowdown drag load would be presented. However, the effect of the shock load renders the load cell output signals to be of no quantitative value.

The shock-induced response in the load cell signals shown in Fig. B-2 appears almost immediately after the rupture disc opened, in about 0.1 – 0.2ms. The wave speed calculations in Eqs. (B3) and (B4) suggest that the registered response in this time period is not due to fluid acoustic phenomena, but rather an artefact of the structural stress wave propagation in the pipe walls. The calculated timing of the propagation of the stress wave from the point of the rupture disc to the load cells of 0.119ms is in agreement with the measurements. Upon close examination of the original test section design, the load cells were found to respond sensitively and undesirably to external loads applied beyond the tube bundle location, indicating problems with load cell cross-sensitivity, load path transfer, and test section design. The sum of the 4 individual load cell signals gave the correct load in static tests, but the individual load readings were not the same, and were very sensitive to any eccentricity in the loading. Design changes were needed to ensure accurate load measurement, and the test section was therefore modified to rectify these issues.

When a rarefaction wave passes along a pipe, the relief on the internal pressure causes the pipe to suddenly contract in diameter, and similarly, a positive pressure pulse would produce a sudden pipe expansion. These rapid pipe movements subject the pressure transducers to significant accelerations. During preliminary commissioning tests, high frequency dynamic pressure oscillations were observed in the pressure transducer signals immediately following the opening of the rupture disc. This raised the question of whether the acceleration compensation in the sensors was capable of handling the shock loads generated in these experiments. Figure B-4 shows an example of erroneous pressure signals obtained during a commissioning test.

It is not surprising that this type of impulsive excitation should cause vibrations in the rig. Not so obvious is that it should cause significant ‘ringing’ in the signals of dynamic pressure transducers, allegedly damped against vibrations. The pipe wall vibration, which can cause the quartz element and some other components inside the piezoelectric transducers to act as seismic masses, were found to produce significant measurement errors in the pressure signals. These are especially visible in the first few milliseconds after rupture, as shown in Fig B-4, and cannot be physically explained by transient fluid pressure phenomena.

The breathing mode frequency of the pipe in the present experimental rig, f_0, was estimated to be about 5.3kHz according to Eq. (B6),

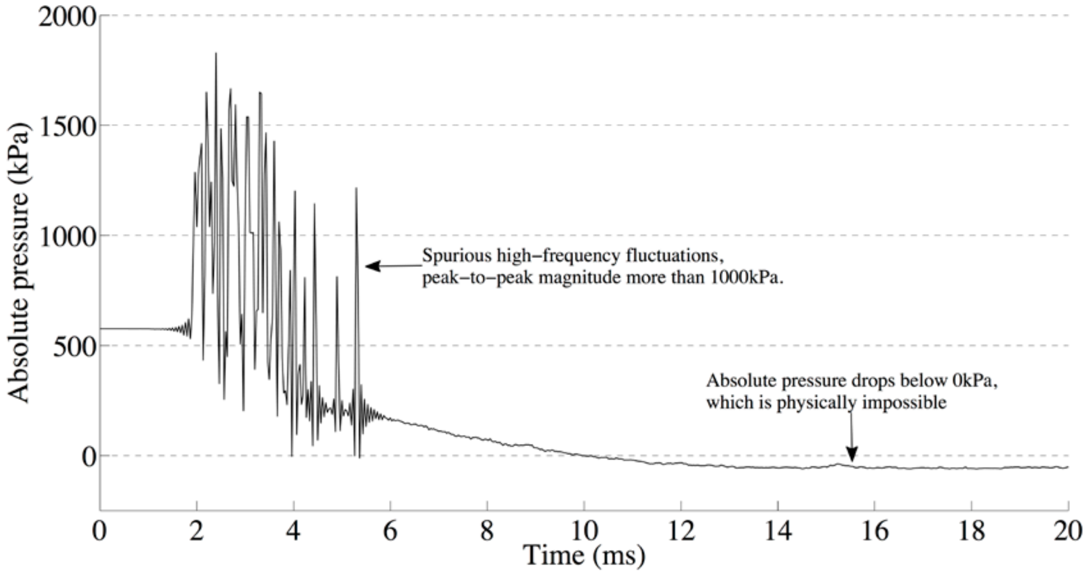

Figure B-4. Erroneous sample transient pressure measurement during commissioning.

$$f_0 = \frac{1}{2\pi R}\sqrt{\left(\frac{E}{\mu\left(1-\upsilon^2\right)}\right)}, \tag{B6}$$

where R is the cylinder radius, E is the modulus of elasticity, μ is the density of the pipe shell material, and υ is the Poisson's ratio. This calculated 5.3kHz frequency of the axisymmetric pipe breathing mode, which is supported by accelerometer measurements, matches the frequency of the oscillations seen in the dynamic pressure signals in Fig. B-4, which indicates that the radial pipe vibrations are the most probable cause of the high-frequency noise. Since these vibrations act in the direction parallel to the measurement axis of the pressure transducer, they produce inertial effects that appear as periodic fluctuations in the pressure signals. These may also affect the transducer calibration since the pressure asymptotes to a value below 0kPa absolute pressure in Fig. B-4, which is physically impossible. The following sections describe the design strategies used in the implementation of successful isolation devices for measurements of transient blowdown pressures and loads.

B.1. Pressure transducer shock and vibration isolation

The dynamic pressure transducers selected in this study appeared well suited for this type of application, being acceleration compensated by design. However, their performance was unsatisfactory due to significant levels of oscillatory noise in the signals. There are several factors that may be contributing to these measurement distortions. The main problem is that the blowdown produces transient temperature and acceleration effects in addition to the rapid changes in pressure, such that these concurrent effects compete with the desired pressure measurements in the signals.

The shock generated by the opening of the rupture disc appears to be responsible for the 'ringing' behaviour, which is seen in the measurements as high frequency pressure spikes. Furthermore, the thermal shock sensitivity of the pressure transducers may be contributing a thermal output due to transient temperature effects during rapid depressurisation. A suddenly depressurising fluid simultaneously undergoes a significant transient drop in temperature. This subjects the rig and all of its components, including pressure sensors, to a rapid thermal shock, which can cause misleading pressure signals. Dynamic pressure transducer specifications provided by manufacturers usually include a steady-state thermal drift correction coefficient, but there is typically no documentation available on the effect of abrupt temperature changes on pressure measurements. Although less likely, vibration causing flexure of the sensor lead wires during pressure measurements may also create distortions in the signal output.

Despite their allegedly being vibration compensated, it seems that the sensor integrated acceleration compensation is insufficient. The shock loading produced by the initial pressure release at blowdown consistently corrupted the dynamic pressure transducer signals. Since these effects cannot be easily quantified, they must be anticipated and minimised in order to ensure correct data measurement. A vibration isolation design was therefore designed and implemented to provide accurate and reliable dynamic pressure measurement capability. Vibration isolation is a technique by which the undesirable effects of vibration are minimised. The magnitude of vibration response can be significantly lowered by effectively reducing the transmission of the excitation forces to the vibrating system. The essential idea is to embed the vibrating mass in a flexible material (isolator) attached to the vibration source, so that for specific excitation conditions, a lower amplitude of system dynamic response is obtained. In practice, elastomeric suspension is commonly used for vibration isolation applications, which also adds damping.

The transducer mass vibrates at the natural frequency of the system, and the required spring 'isolator' stiffness can be selected to allow for sufficient force transmission reduction. Since a low system natural frequency is desired, the spring support must have low stiffness, and the vibrating mass must be relatively large. The developed vibration isolation design was achieved by moulding an elastomeric material, which provides the soft support, between the pressure transducer and a threaded metal ring mounted onto the pipe wall. An assembly drawing of the shock isolator design components is shown in Fig. B-5. The pressure transducer is fixed in a brass ring, which significantly adds to the vibrating mass supported by the elastomer. The design requirements were that the elastomer must not react chemically with R-134a, should provide acceptable shock isolation to the transducer in both radial and transverse directions, and is able to withstand the static pressures in the rig before commencing blowdown. Thermal insulation from the pipe walls is a bonus.

The device is assembled by moulding the elastomeric material in a specially designed aluminum fixture with dowel pin locators. A thin layer of lubrication is initially applied to the aluminum surfaces to prevent adhesion during assembly. The brass ring identified as component

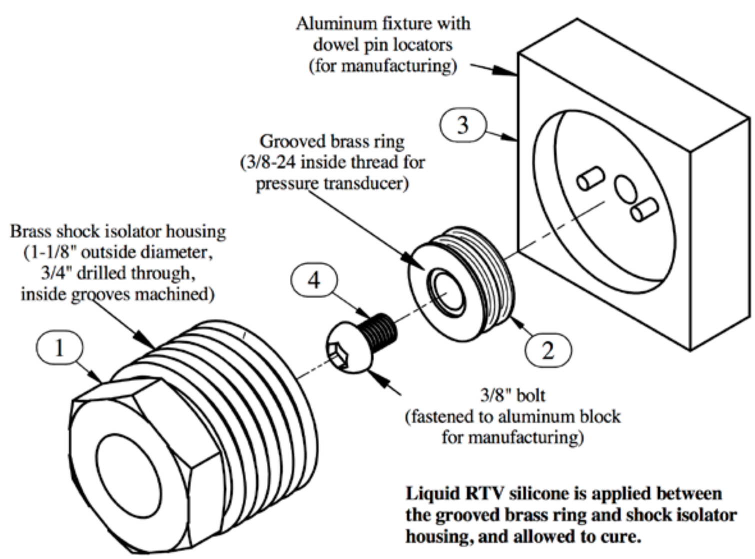

Figure B-5. Shock isolation device manufacturing procedure.

2 in Fig. B-5 is then placed in the aluminum fixture, component 3, and is prevented from rotating by the dowel pin locators. The ring is bolted into place by component 4, which fills the smooth flat sealing surface in the brass ring later required for creating the pressure transducer seal. The isolator housing, component 1, is then placed in the aluminum fixture, after which liquid RTV silicone is applied between this housing and the brass ring and allowed to cure. The inside of the housing and the exterior of the brass ring are grooved in order to provide maximal surface area for elastomer adhesion during curing. Pressure transducer isolation prototype devices were manufactured and tested under nitrogen blowdown conditions. The design shown in Fig. B-6 permits the installation of the pressure transducers such that the pressure sensing face is flush with the inside walls of the pipe. This is important in order to capture accurate dynamic pressure signals from the propagating pressure waves immediately following the initiation of the blowdown transients.

Sudden thermal changes produce temperature gradients that can also affect the response of piezoelectric pressure transducers. If the thermal deformation is large enough to exert a physical load on the quartz crystal inside the sensor, the pressure transducer registers a response, even when the pressure remains constant. In some cases, thermal shock can cause a very significant divergence of the transducer response from the desired measurement of the real

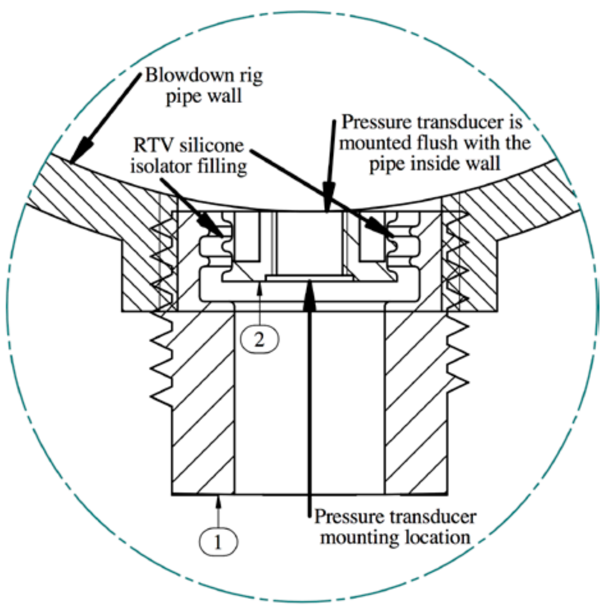

Figure B-6. Pressure transducer shock isolator prototype device.

pressure variation. In the present blowdown experiments, the transient temperature drop is large, up to 80°C, and can therefore cause erroneous pressure readings. The thermal shock phenomenon was tested by dipping the pressure transducers from room temperature into an ice water bath and observing the output response. Theoretically, a pressure sensor that is gently dipped from room temperature into a container of ice water should not indicate any significant change in pressure. The process is essentially isobaric, assuming that the hydrostatic pressure is negligible, and any detectable signals emitted from the sensor would therefore be artefacts of thermal shock. The static pressure sensors, which are digitally temperature-compensated, were tested in this way, and no visible thermal-induced response was registered. However, the output response of the dynamic pressure transducers under similar test conditions showed substantial susceptibility to thermal shock.

Different ways of minimising the temperature effects were investigated, and it was found that the application of a thin layer of thermal insulation (RTV silicone) on the pressure sensing face of the sensors was the most effective method. Temperature effects on dynamic sensors with and without insulation coatings applied for a sudden isobaric thermal shock were quantified, and a sample set of results is presented in Fig. B-7, which plots spurious pressure signals against the logarithm of time. Figure B-7 shows that the spurious pressure signal can be as high as 120kPa, which is almost 20% of the sensor full measurement range, for a mere temperature drop of 20°C. Importantly, this peak in thermal response begins within a few milliseconds of immersion. The effect of the insulation is to substantially increase the time taken for the transducer to be affected by the thermal shock, by as much as two orders of magnitude, as well as to greatly reduce the spurious pressure amplitude. The effect of delaying the thermal effects shown in Fig. B-7 is important since the dynamic pressures of interest are typically measured in the first tens of milliseconds.

By insulating the sensors, the delay is sufficient that the measurements obtained are reliable and accurate, before heat transfer produces any degradation in the signals. All of the pressure transducers were insulated against thermal shock and calibrated dynamically. The thin surface coating of RTV silicone sealant and the shock isolation adapters were effective in eliminating both the mechanical and thermal shock effects on the pressure transducers. The success of the developed shock isolation strategies is demonstrated in Fig. B-8. The signals

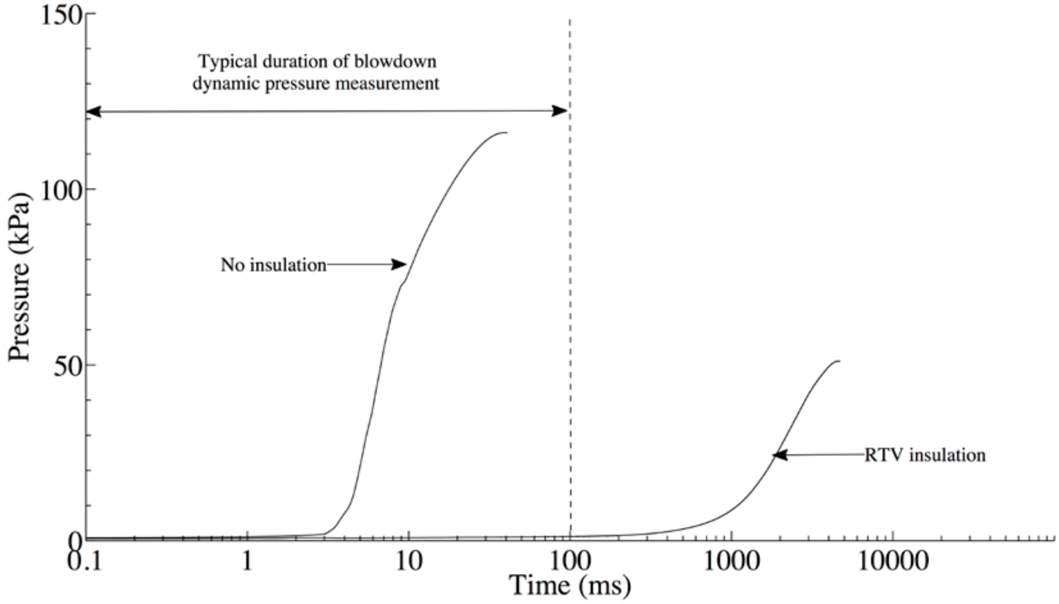

Figure B-7. A comparison of the output response of pressure transducers with and without insulation coatings dipped gently into a container of ice-water.

shown were collected above the rupture disc (location 3 in Fig. 3-1) during a N_2 blowdown test. The signals were provided by each of a static pressure sensor, a dynamic pressure transducer mounted directly into the pipe, and a dynamic pressure transducer that was shock and vibration isolated using the adaptor shown in Fig. B-6.

The proximity and identical axial positioning of the sensors means that the pressure signals should essentially be the same, allowing for some phasing error due to the spatial distribution of the initial spherical wave propagating from the rupture point, before the two-dimensional planar wave profile is fully established. The results in Fig. B-8 show that the pipe wall acceleration effect produces an artificial sharp dip in pressure 2 – 3ms after blowdown initiation in the un-isolated sensor signal. This undesired response in the direct wall mounting configuration is consistent with previously obtained results in which mechanical shock was unaccounted for. The pressure signals collected from the other two sensors show very good agreement. The dynamic pressure sensor captures local pressure perturbation details, while the overall pressure magnitudes match the static sensor measurements very well.

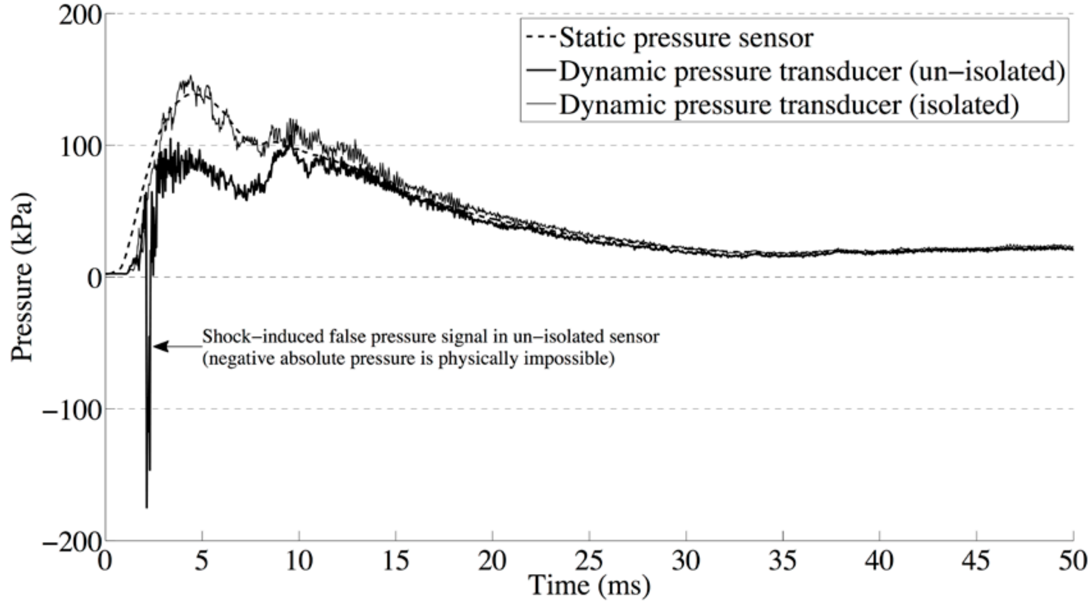

Figure B-8. Shock isolation in dynamic pressure measurements during N_2 commissioning test.

The static pressure sensor's dynamic capability is good for studying quasi-steady blowdown drag loading. Although this sensor does not capture local high-frequency pressure perturbations, it provides an accurate average pressure trace for the full transient duration. The sudden pressure dip in the un-isolated sensor seems to produce errors in the ensuing signal, and the pressures about 5 – 10ms immediately following the spike do not agree with the dynamic pressures measured by the other sensors. The results presented in Fig. B-8 clearly illustrate the importance of addressing thermal and mechanical artefacts in the measurements. A sensor that provides spurious signals induced by undesired effects will apparently suffer from a loss of accuracy that cannot be determined beforehand.

B.2. Test section and load cell shock isolation

Preliminary measurements of dynamic loads on the tube bundle during blowdown indicated parasitic loading on the load cells. Large shock-loads associated with the sudden blowdowns produced problems with load cell measurements, and did not allow proper investigations of fluid drag loading to be performed. Inertial effects produced by the vibration of the experimental rig further distorted the load signals by introducing periodic oscillations that were determined using accelerometers, and the mean dynamic loads remained unexplainable in terms of fluid drag loading phenomena. In order to accurately determine the transient drag loading on the tube bundle in the presence of the blowdown rig shock loading, it is important to mechanically isolate the test section such that the shock loading does not induce significant signal distortion.

The test section design relies on O-rings between the flanges and the tube bundle frame for fluid sealing and mechanical load isolation. The expectation is that the fluid drag load is transmitted totally through the load cells, and no load is transmitted through the O-rings. The purpose of this design was to seal the internal fluid reservoir from the exterior of the rig, to ensure that the load cells were not exposed to the R-134a, and to provide a soft enough support to the tube bundle such that mechanical isolation is achieved and the entire dynamic fluid load is transferred exclusively through the load cells.

The only logical explanation found for the transient load results such as the measurement shown in Fig. B-2 was the presence of alternate mechanical load paths, which result in shock loading on the load cells, and produce undesirable effects in the signals. The existence of alternate load paths is made possible by the relatively small design clearances that are stipulated for standard industrial static O-ring seals (0.127mm). If this clearance is compromised in any way, then the two metal surfaces may come into contact. Although this maintains a satisfactory seal, and no change in system behaviour is observed, the alternate structural load path created would interfere with the desired load path for tube loading measurement. Even though such behaviour may be repeatable under similar loading conditions, it cannot be accurately calibrated for, and is extremely sensitive to shock loading as well as external loading applied beyond the tubes, therefore making it unreliable for dynamic tube load measurement. There are several factors that may influence the designed clearance, including machining tolerances, dimensional mismatch, abrupt shock load accelerations, excessive O-ring compression due to load cell preloading, additional load exerted by the test section gravity weight, or steel flange deformation during mechanical fastening and loading.

If any of the loading on the tubes is transferred anywhere other than at the load cells, the readings would be incorrect. Therefore, it is important in this design that the load is not transferred at the O-rings. In the original design, the gravity weight of the tube bundle pre-loaded the load cells in compression, and the drag loading on the tubes from the blowdown flow produced a tensile force on the load cells. Upon further consideration, it was thought that the load cells might be better suited for measuring compressive forces. The test section was therefore inverted to the orientation shown in Fig. B-9, with the load cells pre-loaded in compression between the flange and the test section frame. During the blowdown transient, the upward fluid drag loading produces further compressive loading on the load cells.

Following several design iterations intended to address the above issues by mechanically isolating the tube bundle test section from the blowdown shock, a modified test section was devised. The original thread-mounted load cells were substituted by washer-type load cells, creating a sliding contact surface, which minimises cross loading of the load cells. The modified design also implements shallower O-ring grooves and larger O-rings (nominal thickness 4.76mm), intended to provide larger clearances of about 2mm, about 16 times the clearance of the original depth, in order to prevent metal surfaces from coming into contact at any time during experimental rig operation. This was found to provide an impermeable seal with sufficient softness. In order for the design to perform satisfactorily, the entire blowdown load must be transmitted through the load cells only, with the O-rings isolating the tube bundle frame from extraneous loading that may interfere with the measurements, as illustrated in Fig. B-9. Another

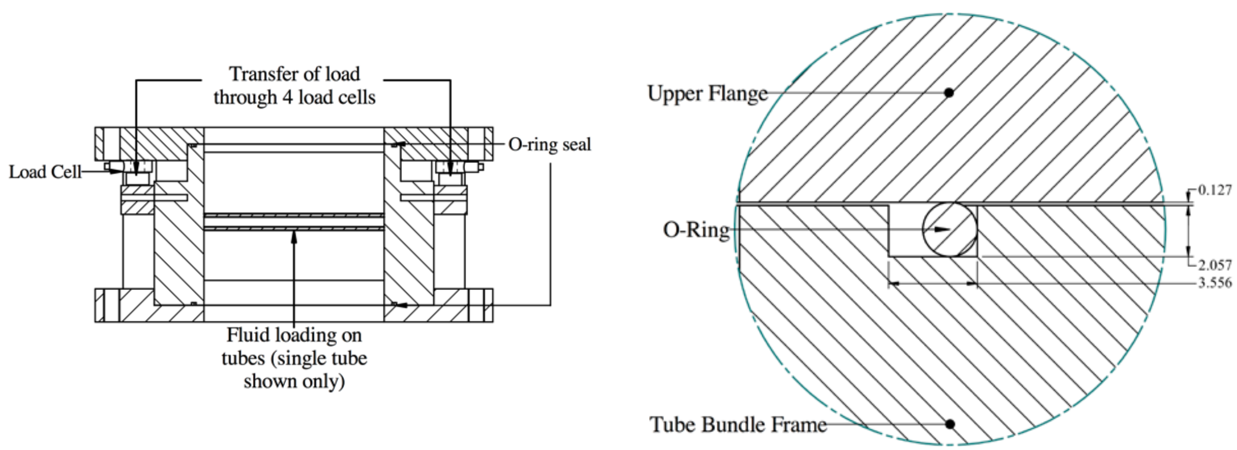

Figure B-9. Load measurement design showing the original O-ring clearance design details (all dimensions in mm).

feature of the modified test section design is that the tube bundle can be easily removed and replaced either by a tube bundle of different geometry, or by blank solid walls without any tubes in between. When the blank test section walls are inserted in the region formerly occupied by the tube bundle, the tube bundle obstruction to the blowdown flow is removed, and the pressurised reservoir section of the rig, below the rupture disc, essentially becomes a hollow pipe with constant cross-sectional flow area.

An experiment that is carried out with blank test section walls, using a significant volume of liquid, would validate the response of the load cells to a virtually non-existent drag load. Basically, the shock loading on the rig remains the same, but since there are no tubes in the test section, and therefore no restriction to the flow, the drag loading measurement should be almost zero, allowing for friction drag on the test section walls. Blowdown tests were therefore performed with varying volumes of liquid R-134a, with the tube bundle removed from the test section, in order to investigate the modified test section design and load cell response to the blowdown shock and open pipe zero drag load conditions.

Figure B-10 shows dynamic load measurements obtained from two tests performed with the tube bundle removed from the test section. The measurements show relatively large immediate shock loads in the original test section design configuration, and minimal output from

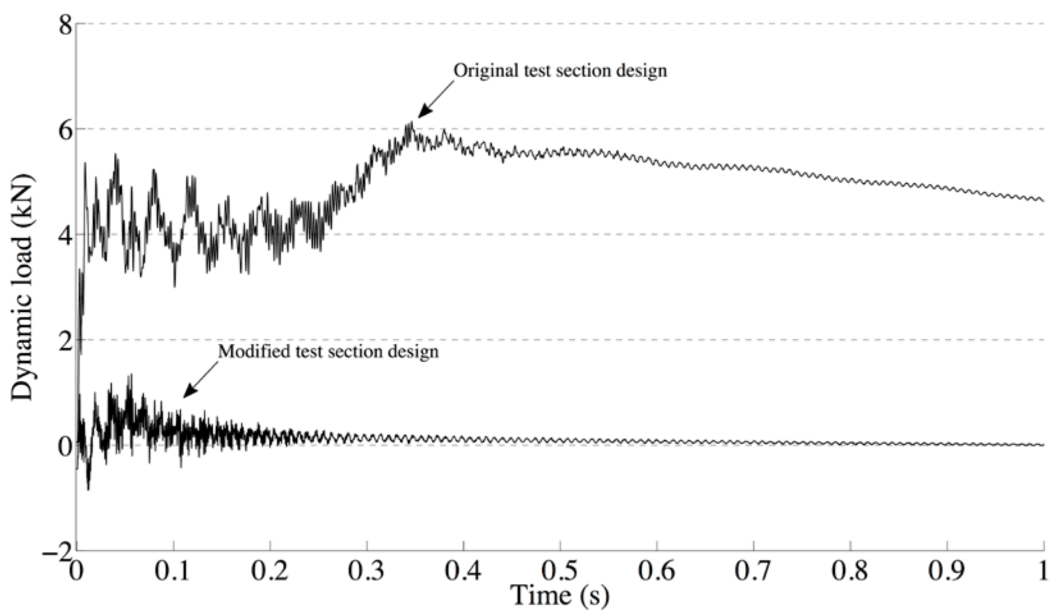

Figure B-10. Zero load signal comparison for empty test section using original and modified designs.

the modified shock-isolated configuration. The results demonstrate the elimination of undesired shock effects and problematic high-frequency ringing in the load cell signals. The periodic 'ringing' in the load measurements is caused by the structural rig dynamics, which represent the natural modes of vibration of the tube bundle test section assembly, and are supported by accelerometer measurements obtained in the test section. These signal oscillations can therefore be ignored, and the mean value of the signal can be taken as the dynamic tube loading. The results show that by adapting the test section design to achieve improved performance under blowdown conditions, mechanical shock effects in the measurements have been largely resolved.

Appendix C. Instrument calibration

C.1. Pressure transducers

The pressure sensors were calibrated with a pneumatic pressure-vacuum hand pump (Ralston Instruments model DPPV) using a precision pressure calibrator as the pressure reference. The test pump generates pressures from vacuum to 700kPa, and allows for precise pressure adjustment within ±7Pa. The dynamic pressure transducers are difficult to calibrate because of their relatively short discharge time constants (1.8s), and their sensitivities were determined through a dynamic pressure calibration technique. A calibration device was built to provide controlled repeatable static and dynamic pressures for simultaneous pressure instrumentation calibration. Using this device, all of the pressure sensors were calibrated against known static and dynamic pressures. The calibration device basically consists of a small plenum chamber that can be opened and shut using a quick-acting solenoid valve controlled by an electrical switch. A photograph of the pressure calibration system with the pressure sensors installed is shown in Fig. C-1.

Figure C-1. Plenum chamber for pressure sensor calibration and response characterisation.

The plenum configuration shown in Fig. C-1 enables the determination of sensor response to known static pressures as well as dynamic pressure changes. Figure C-2 shows a sample pressure measurement from each of a static and dynamic pressure sensor, for a 138kPa dynamic drop in pressure in the plenum chamber. Using this calibration technique, the dynamic and pressure sensors were all calibrated against various known pressures. Each dynamic pressure data point was obtained by averaging 3 independent measurements, and the sensitivity was then determined from a range of 7 pressure data points from 34 – 240kPa, amounting to 21 measurements in total for each individual sensor. All of the sensors displayed linear repeatable dynamic response. An example calibration chart for one of the dynamic pressure transducers used for the experimental blowdown measurements is shown in Fig. C-3. The calibrated sensitivity of 7.52mV/kPa is within 7% of the factory provided reference sensitivity of the individual pressure transducer, 7.05mV/kPa, and within 4% of the nominal specified sensitivity of the dynamic pressure transducers, 7.25mV/kPa.

C.2. Thermocouples

The thermocouples were calibrated against a thermistor embedded in the data acquisition connector block, with a specified accuracy of ±0.3°C. During the blowdown experiments, the thermocouples measure rapid transient temperatures in the accelerating liquid and vapour mixture, which boils off from a subcooled liquid phase to a dry vapour phase in less than one second. During this time, the measurement at the thermocouple junction location is a representation of the instantaneous local flow regime. Experimental observations suggest that the temperature measurements after the initial rapid transient phases of the blowdowns tend to indicate saturated thermodynamic conditions. The randomness of the non-equilibrium flashing phenomenon is also manifested through irregular increases in temperature, deviating from the saturated temperature curve in the form of upward spikes. Since the temperature measurement will depend on the response time properties of the thermocouple, which is a function of the temperature difference between the liquid and vapour phases, the fluid flow rate past the thermocouple junction, and the fluid heat transfer properties, it is difficult to establish with

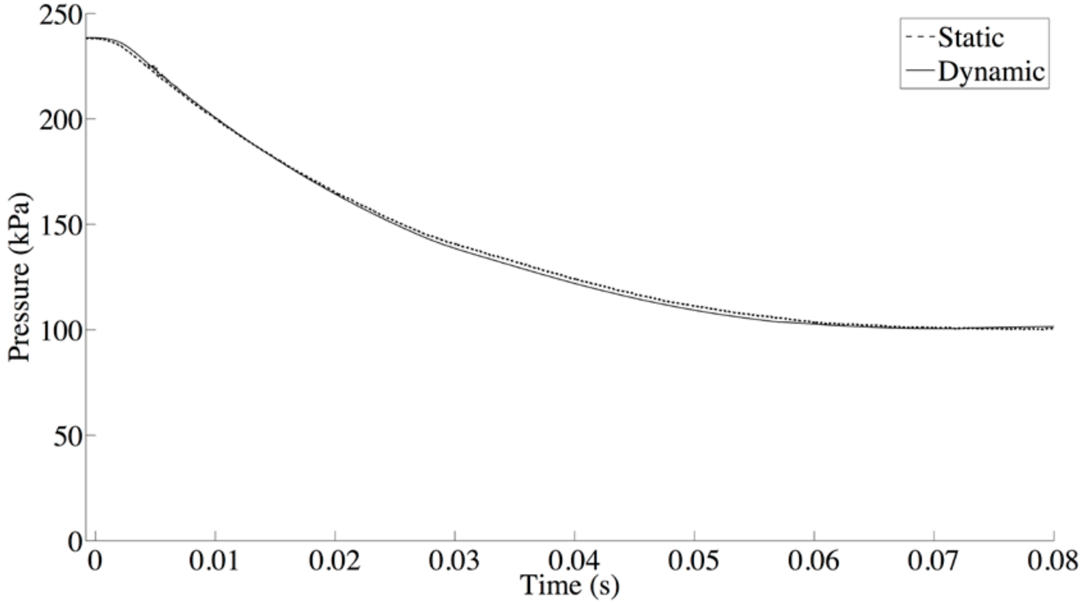

Figure C-2. Calibrated static and dynamic pressure sensors for a 138kPa drop in pressure.

confidence a measurement uncertainty that accounts for all of the factors involved. Given the rapid transient nature of the experiments, and the wide range of accelerating flow regimes encountered during this relatively short period of time, the above mentioned method of temperature calibration was regarded to be sufficient, and the thermocouple measurements were deemed to be satisfactory.

C.3. Load cells

The average overall loading on the tube bundle was calibrated in a manner that allowed the signals from the load cells to be correlated with the actual physical loading on the tubes. Since the load cells are designed to measure rapidly changing forces, it was desirable to calibrate them dynamically. The calibration tests were performed by placing a known load statically on the tube bundle, allowing the dynamic signal to discharge completely, and then removing the load and capturing the resultant output signal. This dynamic calibration procedure begins with the suspension of known loads of up to 40kg from the tube bundle on braided high-strength

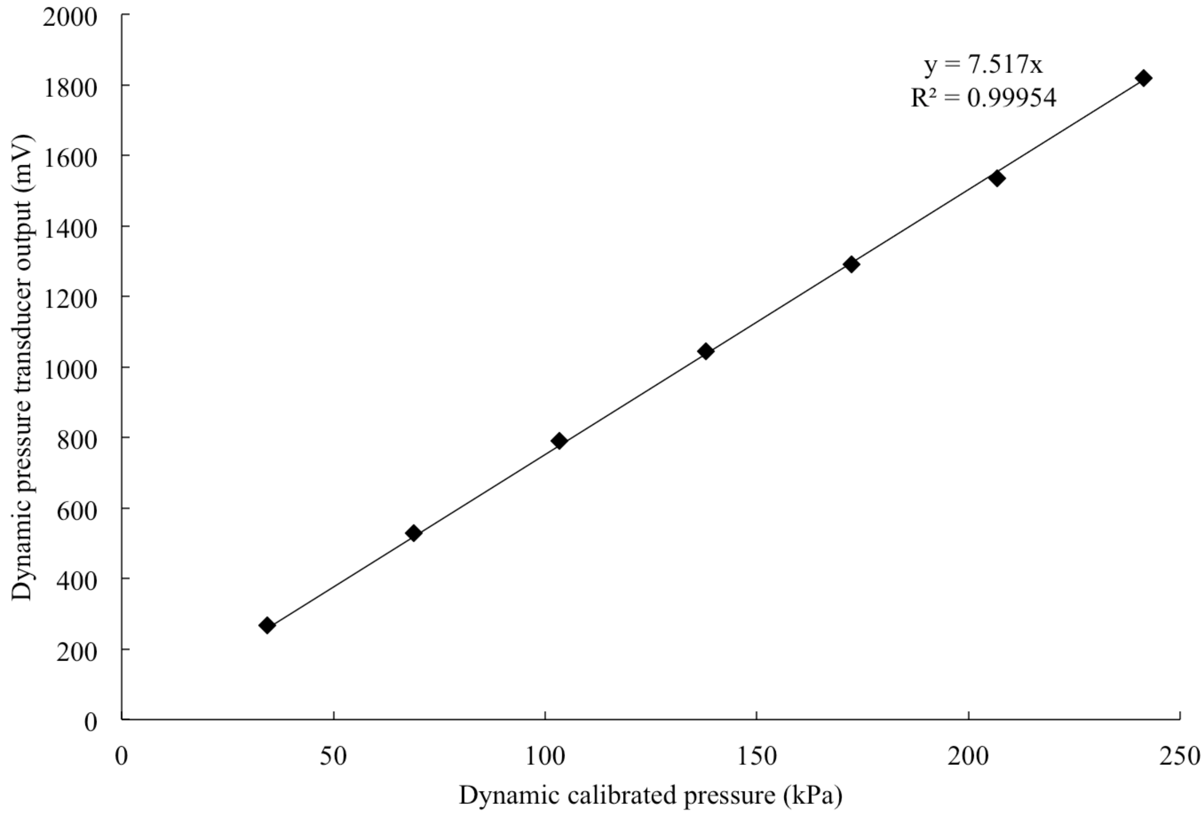

Figure C-3. Sample dynamic pressure calibration chart, 34-240kPa range (nominal sensitivity 7.25mV/kPa).

wires. When the wires are suddenly cut and the weights fall to the ground, the load on the tube bundle is released dynamically, producing a sharp and clean dynamic load signal. Since the test section perceives the load removal as a sudden upwards oriented load, the signal polarity is the same as that expected when the test section is loaded upwards towards the vacuum reservoir during the transient experiments by blowdown fluid cross-flow through the tube bundle. The procedure can be performed accurately in a controlled and repeatable fashion. For illustration purposes, a sample calibration trace of the total summed signal of the four load cells and individual load cell readings for a 31.8kg dynamic load are provided in Fig. C-4.

The frequency content of the dynamic load signal from the calibration run presented in Fig. C-4 is shown in Fig. C-5. The summed signal contains inertial oscillations at frequencies of about 15Hz and 56Hz, which represent the axial modes of vibration of the tube bundle in the load measurement axis. The individual load cell signals provide information on the cross-sectional load distribution on the tube bundle, whereas the total signal provides the amplitude of

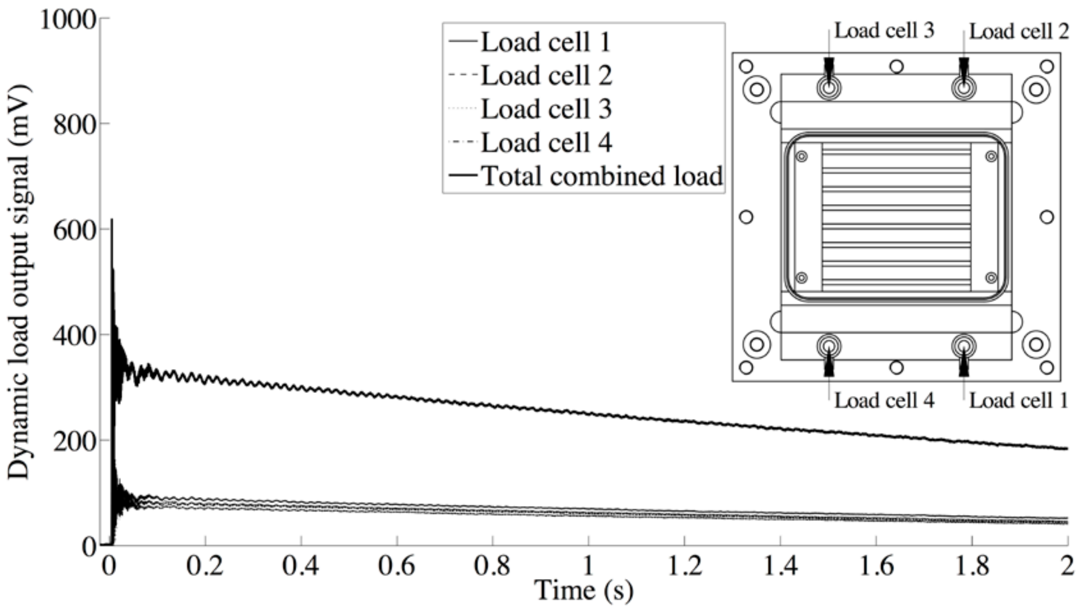

Figure C-4. Sample calibration test with 31.8kg unloading of the tube bundle.

loading on the tubes. In the context of the experimental drag loads measured, the total summed signal is required to determine the dynamic loading on the tube bundle, and an equal distribution of the total load across the four load cells provides confidence in the load measurement design in terms of load eccentricity on the tubes.

Figure C-6 shows the calibration chart constructed for the load cells installed in the tube bundle test section assembly. The results include repeatability tests that were performed at 13.6kg, 22.7kg, and 31.8kg. The calibrated sensitivity of the test section load signal, 0.1104mV/N, agrees within 2% of the factory specification of the load cells, 0.1124mV/N. This yields an additional measure of confidence that the entirety of the load is measured through the load cells only, without any alternate load path. The calibration results of the dynamic load measurements such as the one shown in Fig. C-4 were found to be highly repeatable, and the linearity of the calibration curve in Fig. C-6 demonstrates the relatively high degree of precision and sensitivity of the tube loading measurements.

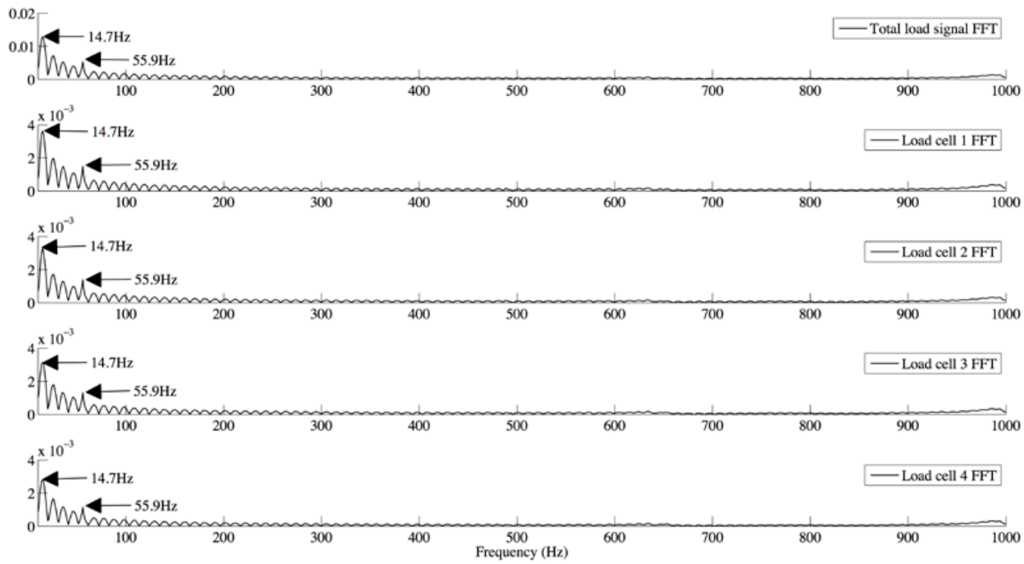

Figure C-5. Frequency content of sample calibration run using 31.8kg weight.

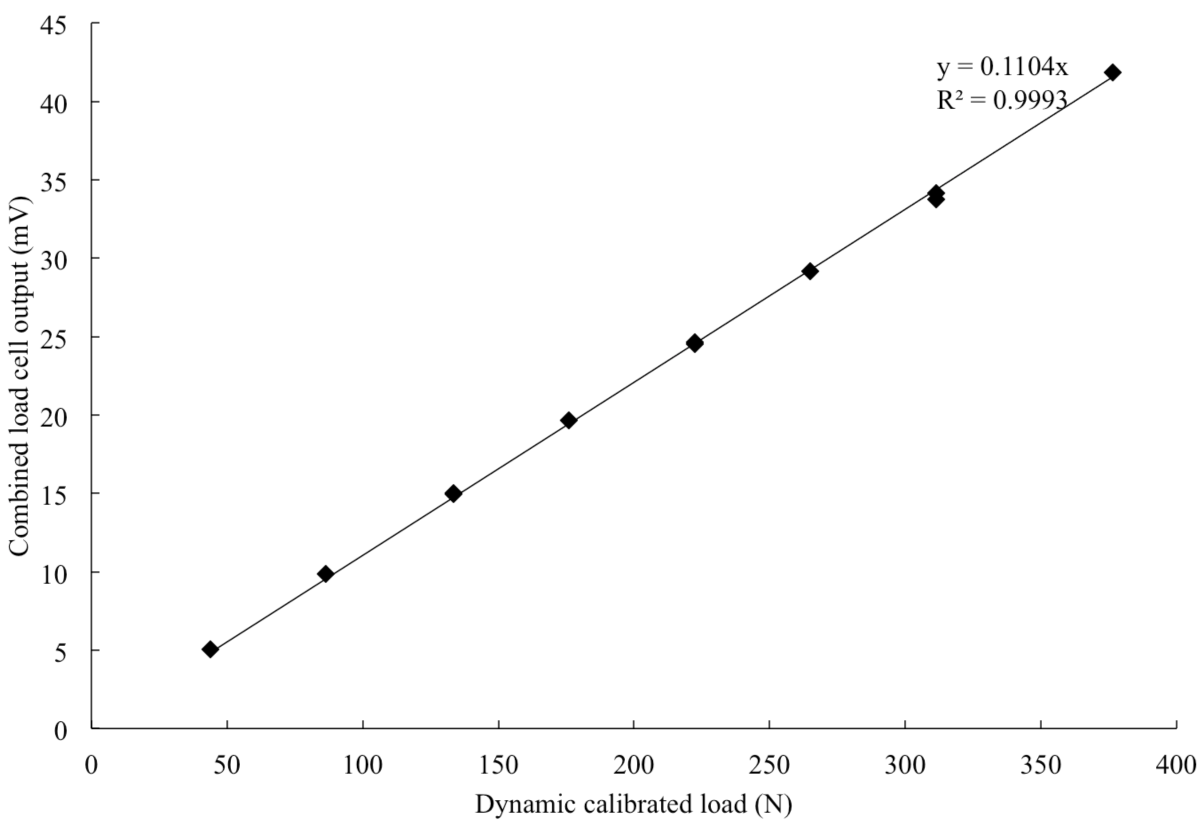

Figure C-6. Test section tube bundle load calibration.

Appendix D. Uncertainty analysis

Physical measurement uncertainties can be determined through an analysis of the individual contributing factors. The overall uncertainty, Δ, of a specific measurement is determined from Eq. (D1) as

$$\Delta = \sqrt{\sum_{i=1}^{n} \left(\delta_i\right)^2}\,, \tag{D1}$$

where δ_i refers to an individual uncertainty for any particular measurement parameter. The sensor uncertainties, which are usually specified by the manufacturer, as well as additional uncertainties introduced by calibration procedures and the data collection system are all considered and incorporated in this analysis. Independent measurements obtained from multiple tests suggest an accuracy level that is much better than specified by the manufacturers.

D.1. Pressure measurement uncertainty

The uncertainty associated with pressure calibration is ±6.9Pa. The static pressure sensor measurement uncertainties are caused by output signal inaccuracies due to signal non-linearity, hysteresis, and repeatability effects, which are specified by the manufacturers to provide a maximum uncertainty of ±2.07kPa. In addition, the static pressure sensors have a specified long-term stability uncertainty of ±2.07kPa. The dynamic pressure transducers have a specified signal non-linearity of ±17.2kPa and an electrical noise resolution of ±27.6Pa. The total uncertainty in the pressure measurements calculated from Eq. (D1) for the static pressure sensors and the dynamic pressure transducers is

$$\delta p_{static} = \sqrt{\left(6.9\times10^{-3}\right)^2 + \left(2.1\right)^2 + \left(2.1\right)^2} = \pm 3.0 kPa,$$
$$\delta p_{dynamic} = \sqrt{\left(6.9\times10^{-3}\right)^2 + \left(17.2\right)^2 + \left(27.6\times10^{-3}\right)^2} = \pm 17.2 kPa.$$

Simultaneous independent measurements collected from the dynamic and static sensors during calibration agreed very well with each other, to within about ±2.5kPa (refer to Fig. C-2), suggesting that the actual measurement uncertainties are much smaller than the values obtained in the above calculations. The average deviation observed on the dynamic pressure transducers over a set of 21 calibration tests was between 0.5 – 1.5%, with a maximum deviation of 4.3% obtained for a small dynamic pressure reduction of 34.5kPa. The maximum uncertainty in the pressure amplitude during dynamic calibration was found to be 1.9kPa (0.7mV).

D.2. Temperature measurement uncertainty

Aside from the cold-junction compensation uncertainty of ±0.3°C, there are several factors that can directly contribute towards errors in the thermocouple measurements. These include isothermal error between the cold-junction thermistor and the actual cold junction formed by the thermocouple at the screw terminals of the connector block, variations in ambient temperature, heat dissipation within the connector block module, and conduction along the thermocouple wires. The thermocouple signals, being in the millivolts range, are also susceptible to external sources of noise. Furthermore, additional errors are introduced by temperature gradients within the thermocouples and metal impurities across the wires. The overall uncertainty, which implicitly accounts for the above factors, is specified by the manufacturer as ±0.85°C. Therefore, from Eq. (D1), the temperature uncertainty is

$$\delta T_{thermocouple} = \sqrt{(0.3)^2 + (0.85)^2} = \pm 0.9°C.$$

Calculated saturation pressures based on the measured temperatures showed consistently good agreement with independent pressure measurements (refer to Fig. 4-4), confirming the small error margins in the measurements, and the quantitative quality of the data. Since the two measurements are independent, the difference between them where the pressures should match (saturation pressure) gives a good indication of the real error of both measurements. Generally, the average difference between the measurements was observed to be about ±2kPa.

D.3. Tube loading measurement uncertainty

The weights used to calibrate the tube bundle loading were verified using an electronic scale with an uncertainty of ±0.018kg, which translates to a weight uncertainty of ±0.18N. The individual signal resolution of the load cells is ±0.89N, and the signal linearity is specified by the manufacturer as ±0.44kN. Since the total tube bundle load is determined by summing the output signal of four identical load cells in parallel, the total tube bundle load measurement uncertainty can be determined by calculating the combined uncertainty of the four load cells. The individual load cell uncertainty and the tube loading uncertainty are, respectively,

$$\delta F_{sensor} = \sqrt{\left(0.18\times10^{-3}\right)^2 + \left(0.89\times10^{-3}\right)^2 + \left(0.44\right)^2} = \pm 0.44kN,$$
$$\delta F_{total} = \sqrt{4\times\left(0.44\right)^2} = \pm 0.9kN.$$

The actual load measurement uncertainties observed during dynamic load calibration were much smaller than the uncertainties calculated above. The non-linearity uncertainty quoted by the manufacturers is for the full measurement range, which is about 180kN. The maximum loads measured in these tests were about 10kN, which is only 5% of the measurement span. The linearity of the sensors in this range is expected to be much closer to that obtained during calibration (refer to Fig. C-6). The average deviation during calibration was observed to be about 1.5% and a maximum deviation of 4% occurred when calibrating using a small dynamic load of 43.9N. The maximum amplitude of the tube loading uncertainty during calibration was found to be 5.8N (0.6mV). The linearity during calibration was observed to be about ±3.5mV, which translates to a load measurement uncertainty of ±0.032kN, almost 14 times less than the values obtained from the calculations above.

D.4. Dynamic response characteristics

The transient nature of the blowdown phenomena investigated in this study necessitates that the instrumentation system dynamics must satisfy the response time and accuracy requirements of the measurements. When an input that is to be measured varies rapidly with time, the sensor output signal will generally not follow the specified linear calibration with perfect accuracy. This is because the sensors cannot respond instantly to a changing stimulus, and there will always be a finite phase lag inherently associated with dynamic measurements that approach an instantaneous step change. The dynamic characteristics of sensor response must therefore be verified in order to quantify the time-dependent error involved.

The frequency bandwidth for measurements of valid accuracy can be determined through the high and low frequency response characteristics of the instrumentation system. The frequency response specifies how fast a sensor, modelled as a first-order system, can react to changes in input. A commonly used frequency limit is the -3dB cut-off frequency, at which the output signal drops to about 70.7% of the ‘flat’ range. Thus the upper cut-off frequency characterises how fast a sensor reacts, and the lower frequency characterises the slowest changing input that a sensor can accurately measure.

D.4.1. Low-frequency response

Direct-current coupled sensors accurately respond to static steady-state input at a frequency, f, of 0Hz. Dynamic piezoelectric sensors however do not posses this type of true static response, and cannot measure events that occur at a dynamic rate below a specified lower cut-off frequency. This behaviour is characterised by the discharge time constant, τ, of the sensors, which is the time taken for the sensor output voltage to discharge 63% of its initial value immediately following the application of a long-term, steady input change. The data acquisition system electronics may introduce additional low-frequency limitations, or time discharge constants, and the system behaviour will reflect the combined effect of the sensor as well as system low-frequency characteristics. For a transient input that lasts for less than 10% of the smallest discharge time constant, the total discharge time can be determined from Eq. (D2),

$$\tau_{total} = \frac{\tau_{sensor} \times \tau_{electronic}}{\tau_{sensor} + \tau_{electronic}}. \qquad \text{(D2)}$$

As a general 'rule of thumb', the relationship between the cut-off frequency and the discharge time constant is provided in Eq. (D3) for the f_{-3dB} cut-off frequency (70.7%), and in Eq. (D4) for the $f_{-5\%}$ cut-off frequency (95%),

$$\tau = \frac{1}{2\pi f_{-3dB}} = \frac{0.16}{f_{-3dB}}, \tag{D3}$$

$$\tau = \frac{3}{2\pi f_{-5\%}} = \frac{0.5}{f_{-5\%}}. \tag{D4}$$

In order to achieve adequate low-frequency sensor performance, which guarantees less than 10% output signal discharge at the end of an input square wave, the width of the input signal pulse must not be greater than 10% of the measurement system discharge constant.

D.4.2. High-frequency response

Assuming there are no electronic limitations, the high-frequency response of a sensor is governed by its lowest resonant frequency, f_n. As the natural frequency of the sensor is approached, the sensitivity begins to rise rapidly and non-linearly, and the mechanical structure within the sensor therefore imposes a high-frequency limit in which the response is linear and sufficiently accurate. If a sensor is modelled as a single degree-of-freedom mass-spring system with no damping, general dynamic 'rules of thumb' can be applied for determining acceptable rise-time response.

The rise time of a sensor is generally defined as the time required by a sensor to respond from 10% to 90% of a steady-state input signal upon exposure to an instant step change. The upper frequency limit at which the sensor sensitivity will begin to deviate by greater than +5% occurs at approximately 20% of the resonant frequency. At 33% of the resonant frequency, the non-linearity error can be as high as 10%. Therefore, in order to guarantee less than 10% signal overshoot, the rise time of the input signal, t_r, must be at least 2.5 times the sensor natural period.

In addition to sensor high-frequency limitations, all electronic measurement systems impose high-frequency limitations. Generally, signal aliasing will occur at frequencies higher than half the sampling frequency, and anti-aliasing filters will have cut-off frequencies just below this frequency, also known as the Nyquist frequency. In order to avoid excessive signal compromise, the rise time of the input signal must be at least 0.45 divided by the -3dB cut-off frequency of a low-pass signal conditioner. By combining the rise times of the measurement components as the sum of the square root, an overall assessment of the rise time capability of a given measurement system can be performed. For valid high-frequency response, the rise time of an input pulse signal should be at least 5 times longer than the combined rise time of the system, which is governed by sensor as well as electronic limitations.

D.4.3. Dynamic measurement uncertainty

The dynamic characteristics of the data collection and instrumentation system used in this study are summarised in Table D-1. Based on these frequency characteristics, the acceptable frequency limits of the desired physical measurements can then be calculated according to the discussions in the previous sections. The results of these calculations are presented in Table D-2, which indicates the longest pulse that can be accurately measured (low-frequency response limitation) and the shortest valid signal rise time (high-frequency limitation). By identifying the frequency bandwidth in which each instrumentation component performs with the desired level of accuracy, the interpretation of the dynamic measurements can be made with confidence in the calibrated linear sensitivities.

The transient pressure measurements were obtained by combining the signals of the static and dynamic sensors, offering an extended measurement frequency range, with validity established for signals from steady-state up to rise times as fast as 0.2ms. This is demonstrated in the sample calibration test result provided in Fig. C-2, in which both static and pressure sensors are observed to respond accurately to a transient pressure input of 80ms duration. The thermocouple dynamic calculations suggest a minimum valid signal rise time of about 40ms. The dynamic response of the thermocouple depends on the temperature gradient established at the

Table D-1. Summary of signal acquisition system dynamic characteristics.

Instrumentation system component	**Low frequency characteristics**			**High frequency characteristics**		
	f_{-3dB} (Hz)	**$f_{-5\%}$ (Hz)**	**τ (s)**	**f_n (kHz)**	**$f_{cut\text{-}off}$ (kHz)**	**t_r (μs)**
Dynamic pressure transducers (2200V1)	0.08	0.25	2.0	300	60	8
Static pressure sensors (U5100)	0	0	∞	N/A	1	450
Thermocouples (EMQSS)	0	0	∞	N/A	0.053	8438
Dynamic load cells (202A)	0.00008	0.00025	2000	65	13	38
Accelerometer (352A24)	0.32	1	0.5	30	8	56
Dynamic data acquisition card (4472)	0	0	∞	N/A	13.605	33
Power supply & signal conditioner (5134A)	0.036	0.1125	4.44	N/A	30	15
Static data acquisition card (6221)	0	0	∞	N/A	700	0.6

thermocouple junction, which is highly dependent on the heat transfer properties of the adjacent fluid, based on the fluid flow rate and thermal inertia. The calculations are based on

Table D-2. Frequency limitations of sensor measurements (to within 90% accuracy).

Measured property	Longest pulse		Shortest rise time	
	(Hz)	(ms)	(Hz)	(ms)
Dynamic pressure	7	138	2632	0.19
Static pressure	0	∞	217	2.3
Temperature	0	∞	12	42
Dynamic load	2	443	1923	0.26
Vibration	22	45	1515	0.33

manufacturer data provided for 20m/s air flow at room temperature and pressure. Measurements performed in a highly dynamic two-phase fluid environment in the current study suggest a thermocouple response time about an order of magnitude higher. However, due to the dependence of the response on the fluid properties and the highly transient and irregular nature of the blowdown temperature measurements, it is difficult to quantify the thermocouple response with more precision. Some question therefore remains as to whether the superheated liquid temperature measurements, which display a rapid temperature departure from the saturated vapour temperature, represent the actual liquid temperature, or somewhere in between the vapour and liquid temperatures.

The dynamic load frequency characteristics establish a dynamic measurement validity range for load changes lasting for as long as about half a second, to as short as about 0.3ms. Since the load cell frequency characteristics are inherently related to the parent structure to which they are mounted (the tube bundle test section), the actual dynamic response for tube loading measurements may differ from the calculations which consider the load cells as independent units. Nevertheless, the calculations indicate a broad range of satisfactory dynamic performance for the purposes of the experimental tube load measurements in this study. The accelerometer validity range is calculated to be 22 – 1515Hz, which is suitable for accurately capturing the frequency content of the structural rig vibrations measured, generally observed to be in the range of about 30 – 200Hz.

Appendix E. Experimental conditions

Experiment	R-134a Initial Conditions				Volume (L)			Liquid level height (mm)	Number of tube rows
	Liquid		Vapour						
	Pressure (kPa)	Temperature (°C)	Pressure (kPa)	Temperature (°C)	Liquid	Reservoir	Percentage fill		
T01	600.3	13.9	597.8	19.1	0.8	27.8	3	45	6
T07	604.7	17.3	600.7	19.7	2.4	23.6	10	129	0
T06	599.8	18.8	594	19.8	4.9	23.6	21	265	6
C01	554	19.3	551	23.2	4.5	20.7	22	241	0
C04	575	18	573	21.1	5.2	23.6	22	279	6
T03	593.2	16	585.5	17.9	5.4	23.6	23	290	0
C03	569	17.6	566	20	5.5	23.6	23	295	6
T02	605	18.2	596.6	19.6	9.3	23.6	39	499	0
T09	586.4	17.7	575.5	18.4	13.7	27.8	49	734	5
T05	615.7	17.7	605	19.5	12.1	23.6	51	650	6
T10	598.7	15.4	588	17.7	14.2	27.8	51	761	4
T08	581.6	18.3	570.2	18.7	14.3	27.8	51	768	6
T11	595.6	15.9	583.8	18.1	14.6	27.8	53	784	3
T12	556.9	14.1	546.8	17.2	14.9	27.8	54	799	2
C02	579	16.3	572	21.7	11.5	20.7	56	617	0
C05	572	17.6	564	21.8	14.6	23.6	62	783	6
T04	612.1	21.1	598.1	20.1	15.4	23.6	65	828	6

Appendix F. Tube bundle pressure drop calculations

F.1. Zukauskas pressure drop calculation

Tube diameter $d = 0.0127$ m

Relative transverse pitch $a = \dfrac{0.0173}{0.0127} = 1.36$

Relative longitudinal pitch $b = \dfrac{0.015}{0.0127} = 1.18$

Number of rows of tubes $z = 6$

Mean bulk fluid physical properties:

Vapour density $\rho = 20.7\ \text{kg/m}^3$

Vapour viscosity $\mu = 11.1\ \mu\text{Pa} \cdot \text{s}$

Vapour velocity $u = 146$ m/s

Reynolds number:

$$\text{Re} = \frac{\rho u d}{\mu} = 3.46 \times 10^6$$

Euler number for an infinite staggered bank of tubes:

$$k_1 = 1.218 - 0.297\left(\frac{a-1}{b-1}\right) + 0.0265\left(\frac{a-1}{b-1}\right)^2 = 1.023$$

For $a = 1.25$

$$\frac{\text{Eu}}{k_1} = 0.245 + \frac{0.339 \times 10^4}{\text{Re}} - \frac{0.984 \times 10^7}{\text{Re}^2} + \frac{0.132 \times 10^{11}}{\text{Re}^3} - \frac{0.599 \times 10^{13}}{\text{Re}^4} = 0.246$$

For $a = 1.5$

$$\frac{\text{Eu}}{k_1} = 0.203 + \frac{0.248 \times 10^4}{\text{Re}} - \frac{0.758 \times 10^7}{\text{Re}^2} + \frac{0.104 \times 10^{11}}{\text{Re}^3} - \frac{0.482 \times 10^{13}}{\text{Re}^4} = 0.204$$

Linearly interpolating for $a = 1.36$:

$$\frac{\text{Eu}}{k_1} = 0.227$$

Euler number per tube row for 6 rows:

$$\mathrm{Eu}_z = C_z \mathrm{Eu} = 1.115 \cdot 0.227 = 0.254$$

Total pressure drop:

$$\Delta p = \mathrm{Eu}_z \frac{\rho u^2}{2} z = 336 \text{ kPa}$$

F.2. Martin pressure drop calculation

Tube diameter $d = 0.0127$ m

Ratio of transverse pitch to tube diameter $X_t^* = \dfrac{0.0173}{0.0127} = 1.36$

Ratio of longitudinal pitch to tube diameter $X_l^* = \dfrac{0.015}{0.0127} = 1.18$

Ratio of diagonal pitch to tube diameter $X_d^* = \dfrac{0.0173^2 + 0.015^2}{0.0127} = 1.8$

Number of rows of tubes $N_r = 6$

Correction for small tube bundles $\phi_{t,n} = \dfrac{1}{2X_t^{*2}}\left(\dfrac{1}{N_r} - \dfrac{1}{10}\right) = 0.018$

Mean bulk fluid physical properties:

Vapour density $\rho = 6.41$ kg/m^3

Vapour viscosity $\mu = 9.95\ \mu\text{Pa}\cdot\text{s}$

Vapour velocity $u = 146$ m/s

Reynolds number:

$$\text{Re} = \frac{\rho u d}{\mu} = 1.19\times10^6$$

Hagen number for turbulent flow in staggered tube bundles:

$$\text{Hg}_{turb,s} = \left\{\left[1.25 + \frac{0.6}{\left(X_t^* - 0.85\right)^{1.08}}\right] + 0.2\left(\frac{X_l^*}{X_t^*} - 1\right)^3 - 0.005\left(\frac{X_t^*}{X_l^*} - 1\right)^3\right\}\times\text{Re}^{1.75} + \phi_{t,n}\,\text{Re}^2 = 1.33\times10^{11}$$

Hagen number for Re > 250,000:

$$\text{Hg}_{turb,s,corr} = \text{Hg}_{turb,s}\left(1 + \frac{\text{Re} - 250,000}{325,000}\right) = 5.2\times10^{11}$$

Hagen number for laminar flow in tube bundles:

$$\mathrm{Hg}_{lam} = 140\,\mathrm{Re}\frac{\left(X_l^{*0.5} - 0.6\right)^2 + 0.75}{X_t^{*1.6}\left(4X_t^* X_l^* / \pi - 1\right)} = 1.35\times10^8$$

Total Hagen number per tube row for staggered tube bundles:

$$\mathrm{Hg} = \mathrm{Hg}_{lam} + \mathrm{Hg}_{turb,s,corr}\left[1 - \exp\left(1 - \frac{\mathrm{Re} + 200}{1000}\right)\right] = 5.21\times10^{11}$$

Total pressure drop for flow normal to tube bundle:

$$\Delta p = \frac{\mu^2}{\rho g}\frac{N_r}{d^2}\mathrm{Hg} = 299\ \mathrm{kPa}$$

F.3. Idelchik pressure drop calculation

Tube diameter $d = 0.0127$ m

Transverse pitch $S_1 = 0.0173$ m

Tube bundle geometric resistance $\overline{s} = \dfrac{0.0173 - 0.0127}{0.015 - 0.0127} = 2.02$

Number of rows of tubes $z_p = 6$

Mean bulk fluid physical properties:

Vapour density $\rho = 20.7\ \text{kg/m}^3$

Vapour viscosity $\mu = 11.1\ \mu\text{Pa} \cdot \text{s}$

Vapour velocity $u = 146$ m/s

Reynolds number:

$$\text{Re} = \frac{\rho u d}{\mu} = 3.46 \times 10^6$$

Resistance coefficient for staggered smooth-walled tube bundle:

$$\zeta = \left(1.88 - S_1/d\right)\left(\overline{s} + 1\right)^2 \text{Re}^{-0.27} \left(z_p + 1\right) = 0.571$$

Total hydraulic pressure drop:

$$\Delta p = \zeta \frac{\rho u^2}{2} = 126\ \text{kPa}$$